

U.S. DEPARTMENT OF COMMERCE  
National Technical Information Service

AD-A023 068

# Research on Materials for High Power Laser Windows

Massachusetts Inst. of Tech.

Prepared For  
Air Force Cambridge Research Labs.

December 1975

## KEEP UP TO DATE

Between the time you ordered this report—which is only one of the hundreds of thousands in the NTIS information collection available to you—and the time you are reading this message, several *new* reports relevant to your interests probably have entered the collection.

Subscribe to the **Weekly Government Abstracts** series that will bring you summaries of new reports as soon as they are received by NTIS from the originators of the research. The WGA's are an NTIS weekly newsletter service covering the most recent research findings in 25 areas of industrial, technological, and sociological interest—invaluable information for executives and professionals who must keep up to date.

The executive and professional information service provided by NTIS in the **Weekly Government Abstracts** newsletters will give you thorough and comprehensive coverage of government-conducted or sponsored re-

search activities. And you'll get this important information within two weeks of the time it's released by originating agencies.

WGA newsletters are computer produced and electronically photocomposed to slash the time gap between the release of a report and its availability. You can learn about technical innovations immediately—and use them in the most meaningful and productive ways possible for your organization. Please request NTIS-PR-205/PCW for more information.

The weekly newsletter series will keep you current. But *learn what you have missed in the past* by ordering a computer **NTISearch** of all the research reports in your area of interest, dating as far back as 1964, if you wish. Please request NTIS-PR-186/PCN for more information.

WRITE: Managing Editor  
5285 Port Royal Road  
Springfield, VA 22161

## Keep Up To Date With SRIM

SRIM (Selected Research in Microfiche) provides you with regular, automatic distribution of the complete texts of NTIS research reports *only* in the subject areas you select. SRIM covers almost all Government research reports by subject area and/or the originating Federal or local government agency. You may subscribe by any category or subcategory of our WGA (**Weekly Government Abstracts**) or **Government Reports Announcements and Index** categories, or to the reports issued by a particular agency such as the Department of Defense, Federal Energy Administration, or Environmental Protection Agency. Other options that will give you greater selectivity are available on request.

The cost of SRIM service is only 45¢ domestic (60¢ foreign) for each complete

microfiche report. Your SRIM service begins as soon as your order is received and processed and you will receive biweekly shipments thereafter. If you wish, your service will be backdated to furnish you microfiche of reports issued earlier.

Because of contractual arrangements with several Special Technology Groups, not all NTIS reports are distributed in the SRIM program. You will receive a notice in your microfiche shipments identifying the exceptionally priced reports not available through SRIM.

A deposit account with NTIS is required before this service can be initiated. If you have specific questions concerning this service, please call (703) 451-1558, or write NTIS, attention SRIM Product Manager.

This information product distributed by

**NTIS**

U.S. DEPARTMENT OF COMMERCE  
National Technical Information Service  
5285 Port Royal Road  
Springfield, Virginia 22161

110101  
11-78-0027  
ADA023068

# RESEARCH ON MATERIALS FOR HIGH POWER LASER WINDOWS

N. J. GRANT, H. K. BOWEN, R. M. CANNON,  
F. A. MCCLINTOCK, R. M. N. PELLOUX,  
J. B. VANDER SANDE

FINAL TECHNICAL REPORT  
FOR THE PERIOD 1 MAY 1972 THROUGH 30 APRIL 1975

DECEMBER, 1975

CENTER FOR MATERIALS SCIENCE AND ENGINEERING  
MASSACHUSETTS INSTITUTE OF TECHNOLOGY  
CAMBRIDGE, MASSACHUSETTS 02139

APPROVED FOR PUBLIC RELEASE; DISTRIBUTION UNLIMITED.

SPONSORED BY  
DEFENSE ADVANCED RESEARCH PROJECTS AGENCY  
ARPA ORDEK NO. 2055

AIR FORCE CAMBRIDGE RESEARCH LABORATORIES  
AIR FORCE SYSTEMS COMMAND  
UNITED STATES AIR FORCE  
HANSOM AFB, MASSACHUSETTS 01731

REPRODUCED BY  
NATIONAL TECHNICAL  
INFORMATION SERVICE  
U. S. DEPARTMENT OF COMMERCE  
SPRINGFIELD, VA. 22161



ASPA Order Number

2055

Contract Number

F19628-72-C-0304

Program Code Number

3 D 10

Principal Investigator:

N. J. Grant

(617) 253-5638

Name of Contractor:

Massachusetts Institute of  
Technology

AFCRL Project Scientist:

Harold Posen

(617) 861-3532

Effective Date of Contract

1 May 1972

Contract Expiration Date

30 April 1975

ACCESSION BY	
BY	DATE
BY	DATE
EXEMPTIONS	
JUSTIFICATION	
BY	
DISTRIBUTION/AVAILABILITY CODES	
CLASS	AVAIL. DES. W. SPECIAL
A	



UNCLASSIFIED

SECURITY CLASSIFICATION OF THIS PAGE (When Data Entered)

REPORT DOCUMENTATION PAGE		READ INSTRUCTIONS BEFORE COMPLETING FORM
1. REPORT NUMBER AFCRL-TR-76-0027	2. GOVT ACCESSION NO.	3. RECIPIENT'S CATALOG NUMBER
4. TITLE (and Subtitle) RESEARCH ON MATERIALS FOR HIGH POWER LASER WINDOWS		5. TYPE OF REPORT & PERIOD COVERED Final Report 1 May 1972 - 30 April 1975
7. AUTHOR(s) N.J. Grant, H.K. Bowen, R.M. Cannon, F.A. McClintock, R.M.N. Pelloux, J.B. Vander Sande		6. PERFORMING ORG. REPORT NUMBER
9. PERFORMING ORGANIZATION NAME AND ADDRESS Massachusetts Institute of Technology Division of Sponsored Research 77 Massachusetts Avenue, Cambridge MA 02139		8. CONTRACT OR GRANT NUMBER(s) F19628-72-C-0304
11. CONTROLLING OFFICE NAME AND ADDRESS Air Force Cambridge Research Laboratories Hanscom AFB, Massachusetts 01731 LQO/Harold Posen/Monitor		10. PROGRAM ELEMENT, PROJECT, TASK AREA & WORK UNIT NUMBERS ARPA Order No. 2055 61101D 678100
14. MONITORING AGENCY NAME & ADDRESS (if different from Controlling Office)		12. REPORT DATE Dec., 1975
		13. NUMBER OF PAGES 324
		15. SECURITY CLASS. (of this report) UNCLASSIFIED
		15a. DECLASSIFICATION/DOWNGRADING SCHEDULE
16. DISTRIBUTION STATEMENT (of this Report) Approved for public release; distribution unlimited.		
17. DISTRIBUTION STATEMENT (of the abstract entered in Block 20, if different from Report)		
<p style="text-align: center;"><b>PRICES SUBJECT TO CHANGE</b></p>		
18. SUPPLEMENTARY NOTES Research was sponsored by Defence Advanced Research Projects Agency, ARPA Order No. 2055		
19. KEY WORDS (Continue on reverse side if necessary and identify by block number)		
Alkali halides	Fracture Toughness	Grain Boundary Migration
Lasers	ZnSe	Impurity Drag
Recrystallization	Flaw Analysis	Grain Boundary Diffusion
Fatigue	Proof Testing	
	Subgrains	
20. ABSTRACT (Continue on reverse side if necessary and identify by block number)		
<p>Microstructural investigation of forged KCl and KBr showed that the subgrain size depends reciprocally on the forging stress and only indirectly on impurities, temperature, or orientation. Additives significantly reduce the grain boundary mobility and inhibit secondary or dynamic recrystallization which can destroy the strengthening caused by these fine subgrains. Divalent dopants inhibit the mobility much more than</p>		

Unclassified

SECURITY CLASSIFICATION OF THIS PAGE(When Data Entered)

monovalent ones. A theoretical analysis of the impurity drag caused by the electrostatic interaction with the divalent impurities is in reasonable agreement with the experimental grain boundary mobilities. Theoretical calculations of the impurity effect on grain boundary diffusion were also done.

Design methods using strength statistics have been studied. A computer program was developed for converting fracture load data to strength distributions from which possible flaw concentrations can be found. However, failure rate predictions cannot be made using strength distributions since sufficient data cannot be obtained and extrapolation is difficult because strength distribution curves do not follow an extreme value distribution if failure is due to coalescing subsurface flaws. A proof testing technique using a liquid nitrogen jet was developed and non-destructive flaw detection methods are considered as alternatives.

Fracture toughness and fatigue tests were done on forged KCl and on ZnSe. For ZnSe  $K_{IC}$  was found to be  $0.75 \text{ MN}/\text{m}^{3/2}$ ; this corresponds to a crack half-length of  $90 \mu\text{m}$  at a working stress of  $45 \text{ MN}/\text{m}^2$ , much less than the typical window coating thickness. For KCl  $K_{IC}$  depends on temperature and strain rate and varies in the range of  $0.33$  to  $0.77 \text{ MN}/\text{m}^{3/2}$ . Corrosion fatigue crack growth was observed although initiation of fatigue cracks from a smooth surface is difficult even at a stress amplitude approaching the yield stress in tension.

# CONTENTS

	page
A. INTRODUCTION	5
B. SUBSTRUCTURE FORMATION IN HOT FORGED KCl and KBr M. F. Yan, R. M. Cannon and H. K. Bowen.	7
C. IMPURITY DRAG THEORY IN GRAIN BOUNDARY MIGRATION OF KCl M. F. Yan, R. M. Cannon and H. K. Bowen.	47
D. SPACE CHARGE CONTRIBUTION TO GRAIN BOUNDARY DIFFUSION M. F. Yan, et al.	103
E. DESIGN OF LASER WINDOWS USING FLAW ANALYSIS F. A. McClintock and W. F. Hahn.	139
App. E.1. STATISTICAL DETERMINATION OF SURFACE FLAW DENSITY IN BRITTLE MATERIALS J. R. Matthews, F. A. McClintock and W. J. Shack.	179
App. E.2. USERS MANUAL FOR FLAW STATISTICS PROGRAM; GENERATION OF $g(S)$ CURVES J. R. Matthews.	193
App. E.3. PROOF TESTING OF BRITTLE MATERIALS BY THERMAL SHOCK. F. A. McClintock and J. R. Matthews.	244
F. FRACTURE TOUGHNESS AND FATIGUE R. M. N. Pelloux	275
G. TRANSMISSION ELECTRON MICROSCOPY OF ALKALI HALIDES J. B. VanderSande	310
H. RESULTANT PUBLICATIONS AND THESES	322

## A. INTRODUCTION

The mechanical properties of infrared transmitting windows had not been considered the limiting factor in their application until the recent requirement for windows in high power laser systems. Of the several classes of candidate materials the alkali halides exhibit the lowest optical absorption at the longer wavelengths; however their poor mechanical properties and hygroscopicity may limit their usefulness. Water absorption may be avoided by application of appropriate protective coatings. The problem of low strength, reflected in poor mechanical stability under loading and thermally induced stresses, has been addressed here and by others by applying various strengthening techniques such as solid solution strengthening, strain hardening, texture hardening, grain boundary hardening, precipitation hardening, radiation hardening and surface protection. However, the requirement of good optical transmissivity at infrared wave lengths restricts the appropriate strengthening mechanisms to those processing techniques that do not contribute to optical scattering or absorption.

This research effort has included work on strengthening of the alkali halides by hot forging and texture hardening and studies of the brittle fracture, fracture toughness and fatigue failure of these materials. The



present report includes work on the substructure formation during forging and attendant studies of grain boundary mobility and diffusion which contribute to understanding the secondary recrystallization problems in the forged halides. Additional work has been initiated to provide a capability of doing TEM on the halides to compliment these studies. The problems of measuring and adequately characterizing the fracture strength distributions and of proof testing these materials have been considered with regard of the problems of designing with these brittle materials. Finally, the fracture toughness and fatigue behavior of KCl have been investigated.

This research has been carried out primarily by graduate students. Because of the extensive nature of this investigation, several research teams have worked together; polycrystalline material prepared under the same processing conditions have been used for most of the mechanical testing. The various individual efforts have been directed by Professor H. K. Bowen, Professor R. M. Cannon, Professor F. A. McClintock, Professor R. M. N. Pelloux, and Professor J. B. VandeSande.

## B. SUBSTRUCTURE FORMATION DURING HOT FORGED KCl & KBr.

### B.1 INTRODUCTION

Substructures developed by forging KCl, KBr or other alkali halides have been shown to provide sufficient improvements in the mechanical properties of these materials that they are potentially useful as laser windows. These microstructures are largely deformation structures, although subsequent recrystallization or even concurrent recrystallization can contribute in part to the final microstructures. This section summarizes the results of the forging study with particular emphasis on the factors contributing to the microstructural development during forging or creep of potassium halides.

B.2 EXPERIMENTAL PROCEDURE. Crystals of KCl or KBr of various dopant or impurity levels were used. High purity single crystals of KCl and KBr were purchased from Optovac\*. Strontium-doped and bromine-doped KCl crystals were obtained from Raytheon† and AFCRL\*\*, respectively.

---

\* Brookfield, Mass.

† D. Readey, Waltham, Mass.

\*\* H. Posen, Bedford, Mass.

Calcium and strontium-doped KCl crystals were also grown in our laboratory from Fisher reagent grade powders by the Czochralski method while under a nitrogen atmosphere. The Sr or Ca doped crystals had dopant concentrations between 40 and 1000 ppm (molar). Most of the crystals were forged in the  $\langle 100 \rangle$  direction although a few pure KCl and KBr crystals were forged in the  $\langle 110 \rangle$  or the  $\langle 111 \rangle$  direction.

The forgings were done in compression using a closed steel die with a Grafoil\* die liner on each face. Specimens were usually forged to a true strain of 80 - 140% and at a strain rate in the range 0.05 to 0.2 min<sup>-1</sup>. Samples were forged over the range of 180 to 740°C for KCl ( $T/T_m = 0.43$  to 0.97) and of 21 to 705°C for KBr ( $T/T_m = 0.29$  to 0.97) to observe changes in the microstructure. Samples were hot ejected from the die and quenched in the ambient atmosphere to try to preserve the deformation structures. Polishing and controlled etching by alcohol diluted water revealed grain boundaries and substructures. Grain sizes were reported as the average linear intercept.

---

\* Union Carbide pyrolytic graphite paper 0.01 inch thick.

The starting crystals typically had diameter to height ratios,  $D/H$ , of 1 to 2, so that by the end of the forging  $D/H$  was typically 10 or more. This causes a significant hydrostatic constraint to develop because of friction between the punch faces and sample. Flow stresses were corrected for this effect using the approximate relation from Hill<sup>1</sup>

$$\sigma_y = \frac{P}{(1 + \frac{\mu}{3} \frac{D}{H})} \quad (1)$$

where  $\sigma_y$  is the flow stress, and  $P$  is the average forging pressure. The coefficient of friction  $\mu$  was taken as 0.12 for the Grafoil\* liners. A typical stress-strain curve during forging, Figure B-1, shows that after about 40% strain the flow stress approached a constant value. The increase in the apparent stress at the end of the test resulted from contact with the die wall.

The hardness or flexural strength was measured for a few samples to indicate the effects of the deformation. The experimental details were described in more detail previously.<sup>2</sup>

---

\* Union Carbide Pyrolytic graphite paper 0.01 inch thick.



B.3 RESULTS. For essentially all of the test conditions, the results indicated a steady state condition was achieved in which the stress no longer varied with increasing strain. The microstructures described were all taken from specimens forged to reach the steady state conditions.

Deformation Microstructures. The examination of the microstructures of the forged crystals all revealed two consistent features. First, as shown in Figure B-2, there is a strong crystallographic texture retained in the deformed pieces. The textures, as have been discussed previously, were all consistent with deformation textures expected from the theoretical work of Chin<sup>3</sup>. Crystals forged in the  $\langle 100 \rangle$  direction retained that texture after forging. Crystals initially oriented in either the  $\langle 110 \rangle$  or the  $\langle 111 \rangle$  direction tended to rotate to give a final orientation of  $\langle 110 \rangle$  as predicted.

In addition, as shown in Fig. B-3, all the crystals exhibited a relatively equiaxed subgrain structure after forging. There was no evidence of blocky subgrains as have been seen in some studies such as reported by Poirier<sup>4</sup> for NaCl or by Clauer et al<sup>5</sup> for molybdenum. The difference in this case is believed to

be related to the fact that the severe geometrical constraint from the very small height to diameter ratio requires slip on several systems, including the secondary systems. In contrast, on single crystals with larger height to diameter ratios, slip can be restricted to one or two slip systems leading to blocky subgrains with a bimodal size distribution.

Stress Dependence of the Subgrain Size. The range of steady state flow stresses can be seen in Fig. B-4 in which the normalized flow stress  $\sigma/E$  is plotted against the homologous temperature at which the experiments were done. It can be seen that the data for the undoped KBr and KCl are essentially identical on this plot. However, the controlling creep or deformation mechanism was different over the range tested. At the low stress, high temperature end the deformation is expected to satisfy a power law creep relation. Most of the stress range is in the exponential creep region. Even at the high stresses it appeared to still be in the range where steady state creep was obtained; however, at the lowest temperatures and highest stresses the behavior is very closely approaching non-steady state yielding behavior. In NaCl Blum<sup>6</sup> and Burke<sup>7</sup> estimated the transition stress between the power law and exponential creep regimes to

be about 300 and 1200 psi, respectively which would be  $\sigma/E$  of about 0.17 to 0.40. The flow stresses for the KCl samples doped with divalent impurities were higher as expected.

As has been found in many other materials, the steady state subgrain size is primarily a function of the applied stress. The results of the tests on KCl from this program as well as samples from Kulin et al<sup>8</sup> from Klausutis et al<sup>9</sup> and from Koepke et al<sup>10</sup> are plotted on Fig. B-5 which shows the subgrain size vs. the steady state flow stress. This graph includes samples of pure KCl as well as samples doped with Sr or Ca in the 100 - 500 ppm range, and also a point from the sample of 2KBr - 1KCl. The results plotted from other laboratories include data on undoped KCl as well as for materials doped with a few percent monovalent impurities of either bromine or rubidium or with small levels of divalent europium. The results are consistent in that the divalent impurities invariably were much more potent hardeners than the monovalent impurities. However, for a given temperature and strain rate the monovalent doped materials were harder than the pure materials. As can be seen a single curve satisfactorily fits the stress subgrain size data for all of the various materials.

Consequently the effects of impurity and temperature only indirectly, through the effective flow stress, influence the subgrain size. A similar curve is shown for the KBr samples in Fig. B-6 in which the behavior is essentially identical.

For lithium fluoride Streb and Reppich<sup>11</sup> have reported a small dependence of the subgrain size on the strain rate, however all of the present tests were done with similar strain rates and so no indication of a strain rate dependence could be found in the present results. It can be seen that a simple inverse relation between subgrain size and stress exists over the range of conditions tested. This is perhaps surprising since it includes materials tested in undoped materials at low stresses in the power law creep region and at high stresses in the exponential regions. Further, the mode of hardening, whether from divalent impurities which induce electrostatic effects, or monovalent impurities, or simply from the development of dislocation networks appears not to significantly affect the subgrain size relation. Finally, it can be seen that even the crystal orientation had no discernable effect on the subgrain size; results for  $\langle 100 \rangle$   $\langle 111 \rangle$  and  $\langle 110 \rangle$  tests are all shown and these have been done at both relatively high



and low temperatures. Particularly at the higher temperatures virtually no difference in the actual flow stress for a given temperature and strain rate could be found for the  $\langle 100 \rangle$ ,  $\langle 111 \rangle$ , or the  $\langle 110 \rangle$  oriented crystals. This further suggests that because of the strong geometrical constraints on the samples that both primary and secondary slip were required in all of the forgings.

These results are compared with those of other studies reported in the literature, particularly for NaCl, in Fig. B-7. The present results are shown to agree particularly well with the results of Burke and Sherby on NaCl polycrystals. The subgrain sizes measured in other single crystal experiments appear to be slightly higher than those found in the present study. This is likely due to the tendency to get simpler, blockier subgrains when only duplex slip occurs for  $\langle 100 \rangle$  crystals with a larger height to diameter ratio; the behavior for highly constrained single crystals is apparently more like that of polycrystals.

An attempt to normalize the stress subgrain curves for the various materials by using  $\sigma/E$  produced two unexpected results. Unlike the  $\sigma/E$  vs.  $T/T_m$  plot, the normalization using  $\sigma/E$  did not bring the curves for KCl

and KBr together. Perhaps more surprisingly, because of the strong temperature dependence of  $E$  for the alkali halides the plots of  $d$  vs  $(\sigma/E)$  became much steeper and in fact more nearly fit a relation of  $d \propto (\sigma/E)^{-2}$ .

Strength of Forged Crystals. The results of hardness tests and flexure tests on various forged crystals are shown in Table B-1. Significant strengthening from the subgrains can be seen. In addition the difference between the  $\langle 100 \rangle$  and the stronger  $\langle 110 \rangle$  and  $\langle 111 \rangle$  samples is at least in part due to texture hardening because of the higher secondary yield stresses.

The low temperature strengthening which results from these subgrains in forged KCl and KBr is consistent with experience with metals. However, Abson and Jonas<sup>12</sup> have recently suggested that the relatively perfect subboundaries formed at higher temperatures may be less effective barriers to slip than the tangled cell walls which form at lower temperatures and higher stresses in metals. This may partially explain the fact that the room temperature strain to fracture in hot-forged KCl is larger than would be expected for a fine grain size polycrystal with only two active slip systems, since the pile up stresses which develop are not as large if the boundaries are imperfect barriers to slip.

Subgrain Structures. Microstructures from specimens tested over the entire range of stress and temperature have been examined by optical or scanning microscopy of polished and etched surfaces. All of the samples show similar characteristic features although the size of the various features depends on the forging stress. Although the structures tend to be equiaxed, as can be seen in Fig. B-8 there appear to be two different ranges of subgrain boundary misorientation angle. In Fig. B-8a it can be seen that some of the boundaries have a relatively lower misorientation angle than others. This can be appreciated by examination of the triple junctions. When a low angle sub-boundary intersects a higher angle one the dihedral angle between the two high angle boundaries is very much greater than  $120^\circ$ ; this indicates that the surface energy of the lower angle boundaries is very much smaller than that of higher angle sub-boundaries. However, both of these boundaries are low angle sub-boundaries resulting from the deformation and are not high angle, or recrystallized grain boundaries. There is a tendency for patches of these lower boundaries to fall within a larger subgrain which are surrounded by the higher angle types of boundaries. This is indicated in Fig. B-8b,

which is from a pure sample forged at low temperature and high stress so that the mean subgrain size is of the order of a few microns.

Fig. B-9 also shows this feature. Two high angle boundaries resulting from recrystallization during annealing while cooling can be seen along the top and the extreme right of the figure. Within the unrecrystallized area, higher angle sub-boundaries can be seen. Examination of the triple junctions where these intersect the high angle grain boundaries again reveals the dihedral angle of the high angle grain boundaries is also very much greater than  $120^\circ$ . Measurements of the dihedral angle allow an estimate of the relative surface energy of the sub-boundary compared to that of the high angle boundary as about  $1/3$ . Comparing this with the expected misorientation angle - grain boundary energy curve as measured for KCl tilt boundaries by Class and Machlin<sup>13</sup> suggests that the higher angle sub-boundaries typically have a misorientation angle of about  $1-2^\circ$ . Further, it can be seen that within these higher angle subgrains are lower angle sub-boundaries which cause a dihedral angle that is also very much greater than  $120^\circ$  at intersections with the high angle sub-boundaries; this demonstrates the large



difference in the relative misorientation angles of the two types of sub-boundaries.

Under the proper circumstances the lower angle subgrain boundaries can be resolved into individual etch pits, as in Fig. B-10. Counting the etch pits in this micrograph gives a misorientation angle of the lower angle sub-boundaries of the order of  $0.01^\circ$ . In addition, the free dislocation density within the subgrains was found to be about  $10^6 \text{ cm}^{-2}$  from this Figure. It must be emphasized that resolving any of the boundaries into etch pits proved to be very difficult; usually etching only revealed the light, but continuous subgrain boundaries shown in previous micrographs. Some of the scatter in the subgrain size-stress plot undoubtedly relates to the difficulty in resolving all of the lower angle sub-boundaries; the result is that the mean grain size reported tends to be an average between the finer cell size delineated by the small angle sub-boundaries and a larger size which might be obtained by counting only those grains surrounded by higher angle sub-boundaries. Measuring either of these extremes is difficult because there is not always a clear distinction between these two types of grains. However, it is generally found that the size of the small angle subgrains or cells is

particularly uniform. This can be seen in Fig. B-11 which is taken out of focus which tends to accentuate the small angle boundaries compared to the higher angle sub-boundaries; this gives a visual picture of a much greater uniformity of the subgrain or cell size than is indicated in some of the other figures where the low angle boundaries are less clearly resolved.

Recrystallization Microstructures. For the specimens forged at higher temperatures similar features are observed but an additional complication occurs. From the microstructure of a specimen forged at 650°C, Fig. B-12, it can be seen that there is a tendency to form both higher and lower angle sub-boundaries. In addition, however, high angle boundaries can also be seen such as the one running across the top of the micrograph. Thus, there are two types of sub-boundaries as well as high angle grain boundaries present in some of the high temperature specimens. This apparently results from actual recrystallization during forging. It has been previously found that during annealing of forged samples isolated, recrystallized grains (such as shown in Fig. B-19) appear and grow into the matrix of subgrains. The subgrains do not coarsen during annealing at temperature without an applied stress and the subgrain

size during straining remains at a fixed value determined by the applied stress. However, in specimens forged at high temperatures isolated, new grains occasionally nucleate and grow into the strained surroundings. However, since deformation is continuing, substructure immediately begins to develop within the new grain. The new substructure slowly intensifies and after sufficient strain it becomes comparable with that in the surrounding matrix leaving only an isolated high angle boundary as evidence of the process.

An example is shown in Fig. B-13 which shows a new grain which has nucleated and grown into the surrounding matrix. However, in the lower part of the grain new substructure has already developed indicating that appreciable strain has occurred since the grain grew through that region. It appears as though the substructure is less developed in the left half of the grain than in the right half. This suggests that the grain grew sporadically with rapid but jerky movement of the boundary so that the left part of the grain grew somewhat later than the right half. Sporadic or jerky movement of the boundaries is also consistent with the irregular shape of the high angle boundary which presumably results from growth of the different segments

at different times. Fig. B-14 presents a similar recrystallized grain except that in this case there has been sufficient strain since the new grain appeared so that visible substructure has developed throughout; however, the misorientation angles, inferred from the etching of the subgrains, may still be slightly less than those of the sub-boundaries in the matrix surrounding the new grain. Apparently after sufficient strain there is relatively little difference in the material inside and outside the grain boundary except that there are regions near the high angle boundary which have a finer subgrain size; this may be due to higher stresses near the boundary caused by the misorientation across it.

For materials without dopants in which the boundary mobility can be very high at high temperatures, it is frequently impossible to obtain samples forged at high temperatures without evidence of dynamic recrystallization having occurred during forging. An extreme example taken from a KCl specimen deformed at about 700°C is shown in Fig. B-15 in which there are almost no areas which have not experienced some recrystallization. Isolated patches of well developed subgrains exist but high angle boundaries can be found laced through-out the sample. A wide variation in the degree of substructure

development exists indicating that the passage of high angle boundaries and the destruction of the subgrains behind them is a recurring process. At high enough temperatures, above about 700°C for undoped KBr and 580°C for undoped KCl, it appears as though steady state substructures are never reached, but instead the steady state creep behavior involves continual dynamic recrystallization. The temperature above which this occurs will undoubtedly be influenced by the specific strain rate, and will be appreciably raised by impurities which retard grain boundary mobility.

Fig. B-16 summarizes schematically the types of microstructural features found in the deformed halides. Both higher angle and lower angle subgrains are found. There is a tendency for the low angle subgrains to form an array of small cells within subgrains bounded by higher angle sub-boundaries. However, the clear situation shown in the schematic is rarely so neatly seen in the actual specimens and in some cases it would be virtually impossible to define two distinct subgrain sizes corresponding to these two extremes. In addition, particularly in samples forged at higher temperatures, isolated, sometimes round high angle boundaries sometimes also occur. These apparently resulted from

recrystallization during forging but with new substructure soon developing again in the recrystallized strain free areas. This dynamic recrystallization must occur on a small scale so that it is effectively occurring continuously throughout the sample for we have not seen evidence of discontinuous or abrupt changes in the flow stress during forging at a constant strain rate. There is clear evidence that the presence of impurities such as strontium which inhibit high angle boundary mobility restrict the amount or extent of dynamic recrystallization at a given temperature and stress. This makes it possible to forge doped samples to higher temperatures and still obtain purely deformation structures than can be done with pure samples.

The cause of nucleation of the isolated high angle grains is not understood at the present time, either during annealing of forged samples or in dynamic recrystallization during deformation. Localized regions of apparently higher strain or finer subgrain size, such as shown in Fig. B-17, can be found occasionally in some samples; these may be, in part, the cause or at least the location of nucleation. Similar bands such as shown in Fig. B-18 which extends across the sample and also indicates strain localization or a higher density of subgrain boundaries can also be seen occasionally

in specimens. It is not clear exactly how these contribute to formation of new grains, but because of the higher local strain energy density these may be the type of place where high angle boundaries would develop. New grains probably do not nucleate in the classical way, but rather the process more likely involves the development of isolated subgrain boundaries which have higher misorientation angles than their neighbors. It has been found in other studies that the mobility of sub-boundaries tends to decrease as the misorientation angle increases until a certain critical misorientation angle is reached at which the mobility then begins to increase again with additional misorientation between the two grains. The result is that high angle boundaries are generally very much more mobile than sub-boundaries particularly if the sub-boundaries are made up of more than one set of dislocations as would be the case for the present samples. Consequently, any sub-boundary which develops a higher misorientation angle than its neighbors is potentially more mobile, and it might be supposed that a critical misorientation is reached at which point it becomes sufficiently mobile to move easily. Then nucleation only requires that at some point there is a variation in strain energy density on either side



of the boundary such that it starts to move preferentially in one direction. As it does this it leaves behind it a region of reduced strain energy density and can effectively become a nuclei for growth of a high angle grain boundary and effectively the start of secondary recrystallization.

In samples annealed after forging in which isolated grains have grown, three types of grain shapes can be found as are shown in Fig. B-19a,b, and c. Frequently, roundish, rather smooth grain boundaries are found particularly after annealing at intermediate temperatures where the grain boundary is thought to be moving in the low velocity, impurity drag limited mode based on the mobility studies reported in the next section. Occasionally very irregularly shaped grains such as that in Fig. B-19b are found. Irregularly shaped grains such as these also frequently result from concurrent recrystallization which occurs during forging. In mobility studies such grain shapes are much more frequently seen where the measured grain growth rates indicate the boundaries to be in the break-away region rather than in the low velocity limits. This behavior is thought to result because various portions of the boundary alternately move at low and at high velocity

extremes and that the average speed measured is between these two extremes. Essentially what is envisioned is that a portion of the boundary locally starts to move fast enough to break-away from its impurity cloud and moves along dragging behind it an increasing region of high angle boundary until the restraint from the back tension of the lateral portion of the grain boundary or until a local region of higher impurity or lower driving force cause that part of the boundary to slow down and fall from the high speed to the low speed part of the mobility curve. However, for samples with a high enough driving force, it is possible for the entire boundary to start to move at high velocity and to stay in the high velocity limit. This would be particularly likely for samples forged at low temperatures giving fine subgrain sizes or particularly if there are a significant number of additional dislocations within the grains caused by room temperatures strain, or polishing damage. In this case the boundary should move smoothly and uniformly and if there is a tendency as there is in KCl to form straight boundaries then straight sided grains should result as are seen in Fig. B-19c. It is not certain whether the grains in KCl prefer to be straight sided because of anisotropic grain

boundary energy, or because of orientation differences in the intrinsic boundary mobility.

B.4 SUMMARY. The results of our study show that a stable deformation texture is formed during forging and that the coarseness or subgrain size is determined primarily by the effective flow stress which in turn is influenced by the temperature, strain rate, and the impurities which are present. The effect of impurities is primarily felt indirectly through their effect on the flow stress. However, at higher stresses recrystallization can occur during forging leading to more complex microstructures with regions having less well developed subgrain structures and with occasional high angle boundaries being present. The presence of impurities which reduce the mobility of these high angle boundaries profoundly effect the amount of dynamic recrystallization which occurs during deformation at higher temperatures. As yet we have not systematically evaluated or investigated the development of the substructure during the transient period. It is found that it takes approximately 40-50% strain to reach a steady state flow stress, this indicates of course that it takes nearly this much strain to reach a completely steady

state deformation structure for a given condition. It is anticipated that the misorientation angles between subgrains must increase during this period. It is less certain whether it continues to increase during the steady state period. We intend to look at these features and to examine the time and strain dependence of sub-structural development during the transient, to try to characterize misorientation difference found between subgrains as a function of strain, and to consider the misorientation and texture relations for forged samples deformed to various strains. The misorientation angles and the extent of preferred texture found in samples in which dynamic recrystallization occurs will also be further studied.

B.6 REFERENCES FOR SECTION B

1. Hill, R., (1950), "Plasticity", Oxford University Press, London.
2. Bowen, H. K., Singh, R. N., Posen, H., Armington, A. and Kulin, S. A., (1973), "Fabrication and Properties of Polycrystalline Alkali Halides", Mat. Res. Bull., 8, 1380.
3. Chin, G. Y., (1973), "A Theoretical Examination of the Plastic Deformation of Ionic Crystals, :1", Met. Trans, 4, 329.
4. Poirier, J. P., (1972), "High Temperature Creep of Single Crystalline Sodium Chloride II: Investigation of the Creep Structure", Phil. Mag., 26, 713.
5. Clauer, A. H., Wilcox, B. A. and Hirth, J. P., (1970), "Dislocation Substructure Induced by Creep in Molybdenum Single Crystals", Acta. Met. 18, 381.
6. Blum. W., (1973), "Activation Analysis of the Steady State Deformation of Single and Polycrystalline Sodium Chloride", Phil. Mag., 28, 245.
7. Burke, P. M. (1968), "High Temperature Creep of Polycrystalline Sodium Chloride", Ph.D. Thesis, Stanford University.
8. Kulin, S. A., Neshe, P. P. and Kreder, K., (1974), "Development of Polycrystalline Alkali Halides by Strain Recrystallization for Use as High Energy Infrared Laser Windows", Technical Report, AFML-TR-74-17., ManLabs, Inc., Cambridge, Mass.
9. Klausutis, N., Nikula, J., Adamski, J., Collins, C., Bruce, J., and O'Connor, J., (1974), "Properties of Hot Forged RbCl-KCl Alloys of Low Rubidium Concentrations", Proceedings of the Fourth Annual Conference on Infrared Laser Window Materials, p. 611, Nov. 18-20, 1974., Eds. C. R. Andrews and C. I. Strecker.

10. Koepke, B. G., Anderson, R. H., Bernal G., E., and Stokes, R. J., (1974), "Room Temperature Grain Growth in Potassium Chloride", J. Appl. Phys., 45, 969.
11. Streb, G. and Reppich, B., (1973), "Steady State Deformation and Dislocation Structure of Pure and Mg-Doped LiF Single Crystals", Phys. Stat. Solid. (2), 16, 493.
12. Abson, D. J. and Jonas, J. J., (1970), "The Hall-Petch Relation and High Temperature Subgrains", Met. Sci. J., 4, 24.
13. Class, W. H. and Machlin, E. S., (1966), "Crack Propagation Method for Measuring Grain Boundary Energies in Brittle Materials", J. Am. Ceram. Soc., 49, 306.
14. Schuh, F., Blum. W, and Ilschner, B., (1970), "Steady State Creep Rate, Impurities and Diffusion in the Rock-Salt Structure", Proc. of Brit. Ceram. Soc., No. 15, 143.

TABLE B-1

## Yield and Fracture Strengths of Alkali Halides

<u>Material</u>	<u>Vickers Hardness (Kg/mm<sup>2</sup>)</u>	<u>Grain Size (μ)</u>	<u>Yield Strength* (psi)</u>	<u>Fracture Strength (psi)</u>
KCl Single Crystal {100}	10	-	300	400
KCl Polycrystal {100}	10.3	12	2700	6000
KCl Polycrystal {110}	15.5	8	4500	9000
KCl Polycrystal {111}	12.5	6	4500	7000
KBr Polycrystal {100}	9.5	-	2500	5000
KCl <sub>.33</sub> Br <sub>.67</sub> Single Crystal {100}	21.5	-	-	1350
KCl <sub>.33</sub> Br <sub>.67</sub> Polycrystal {100}	21.4	300	-	2460

---

\* Yield Stress at 0.1% Strain.



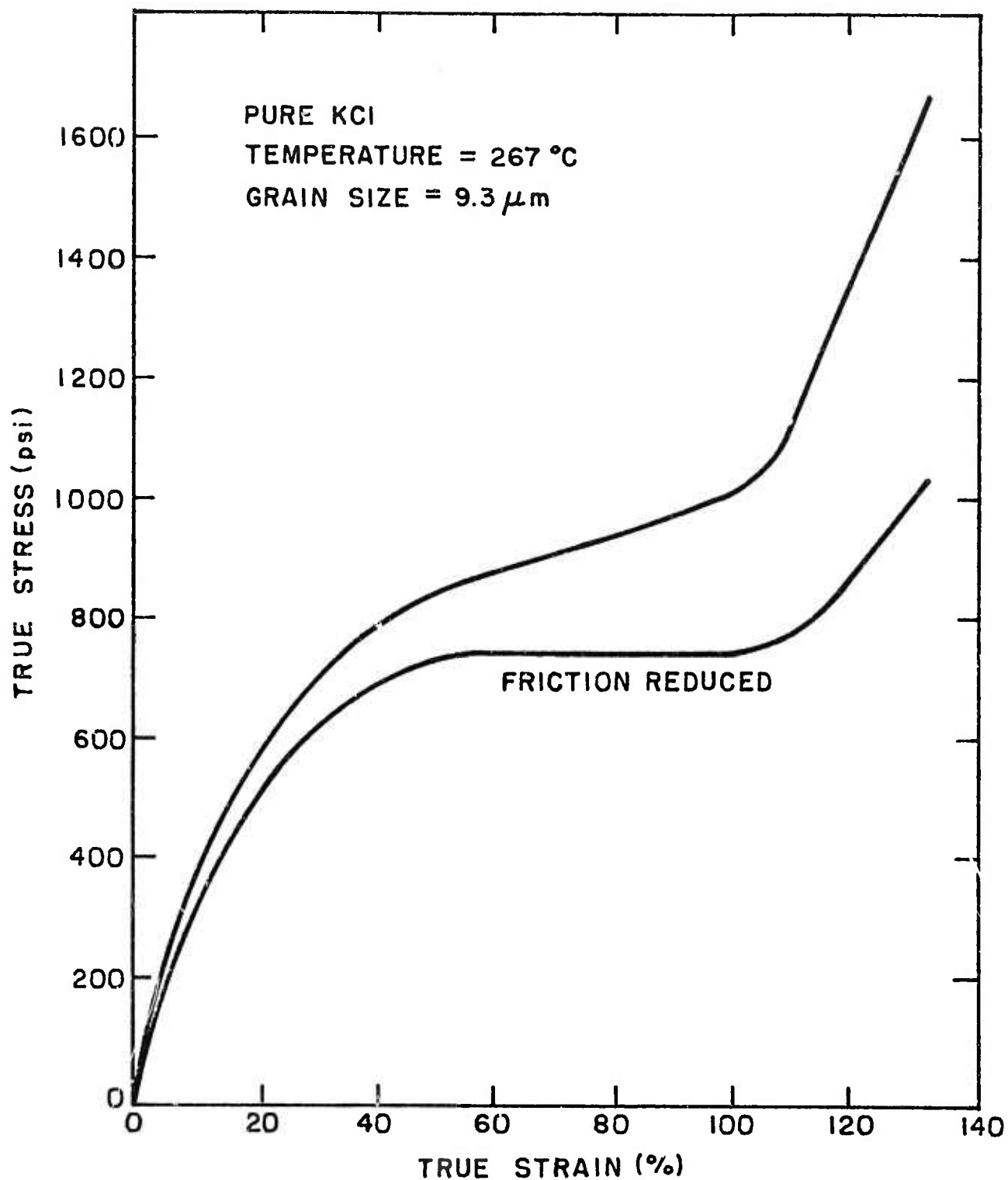


Figure B-1. Stress-strain relation during hot forging of "pure" KCl. The increase in stress after the steady state region results from die wall constraint.

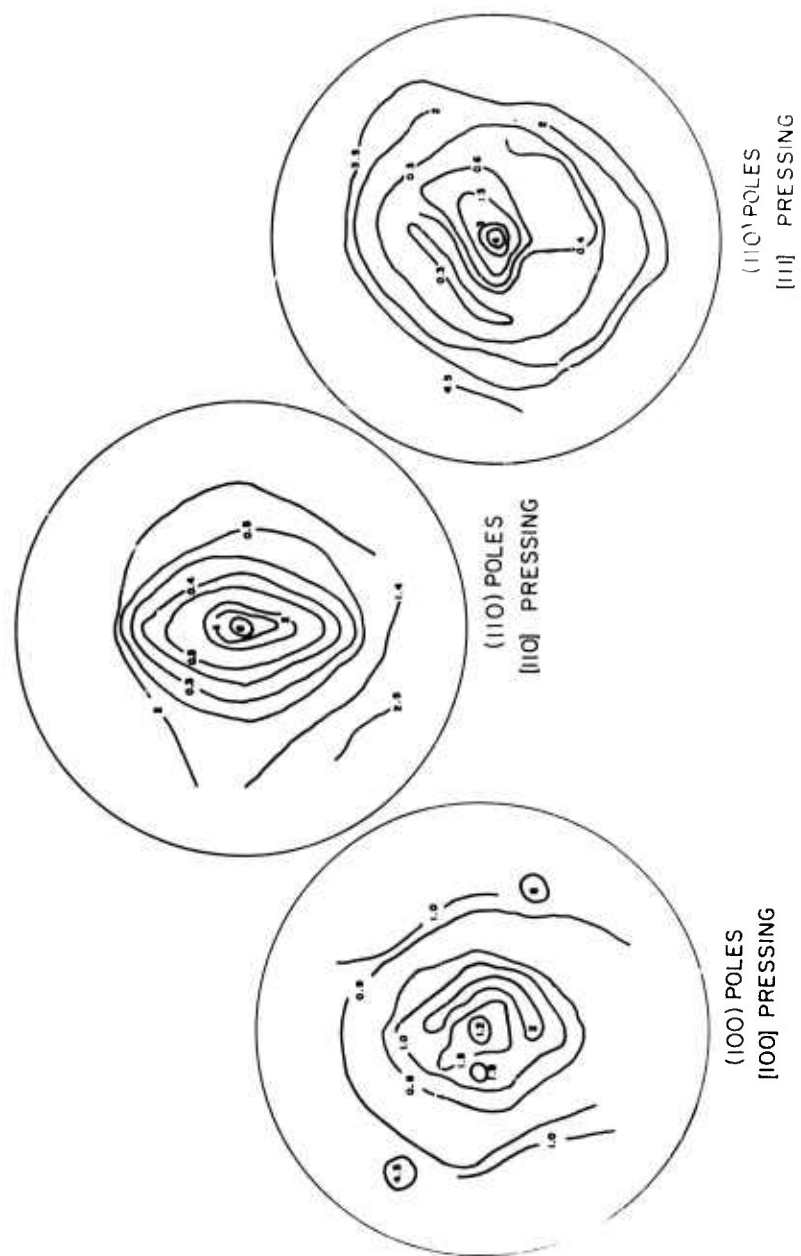


Figure B-2. Pole figures for hot worked KCl showing the forging texture which develops.



2100x

Figure B-3. Subgrains in Ca doped KCl  
forged at 242°C and 3640 psi.

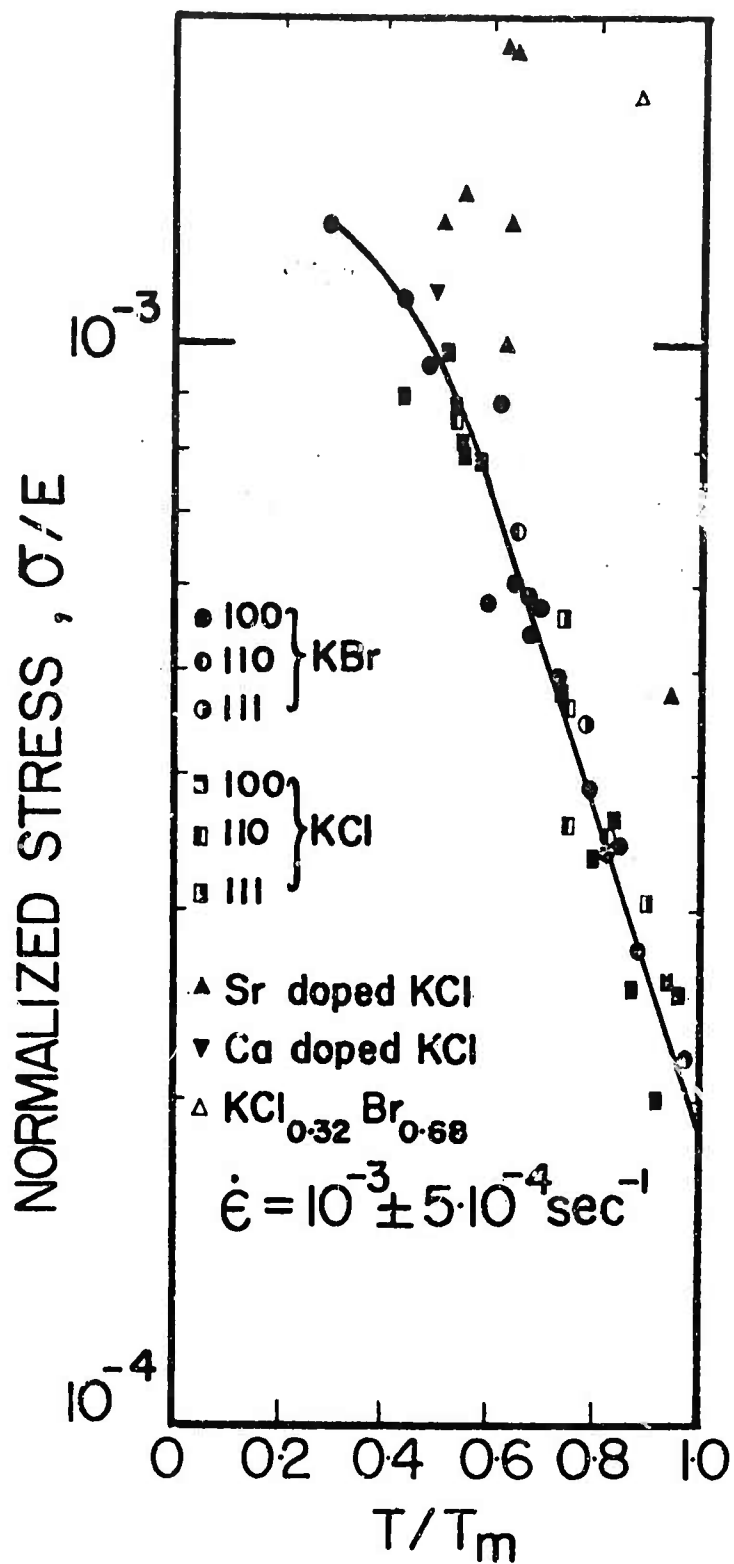


Figure B-4. Normalized steady state stress-temperature curve for the KCl and KBr forgings.

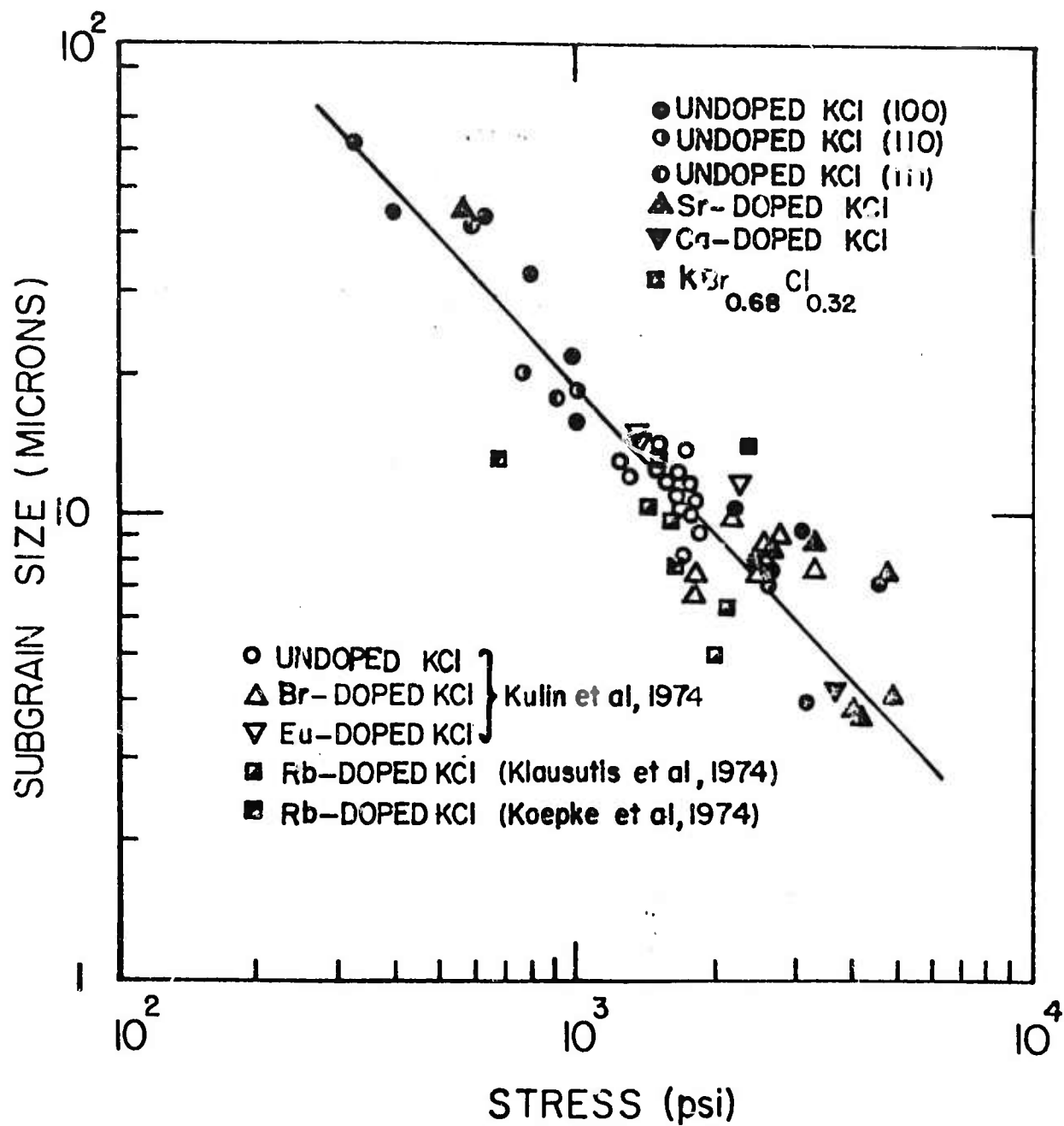


Figure B-5. Subgrain size versus forging stress for KCl.

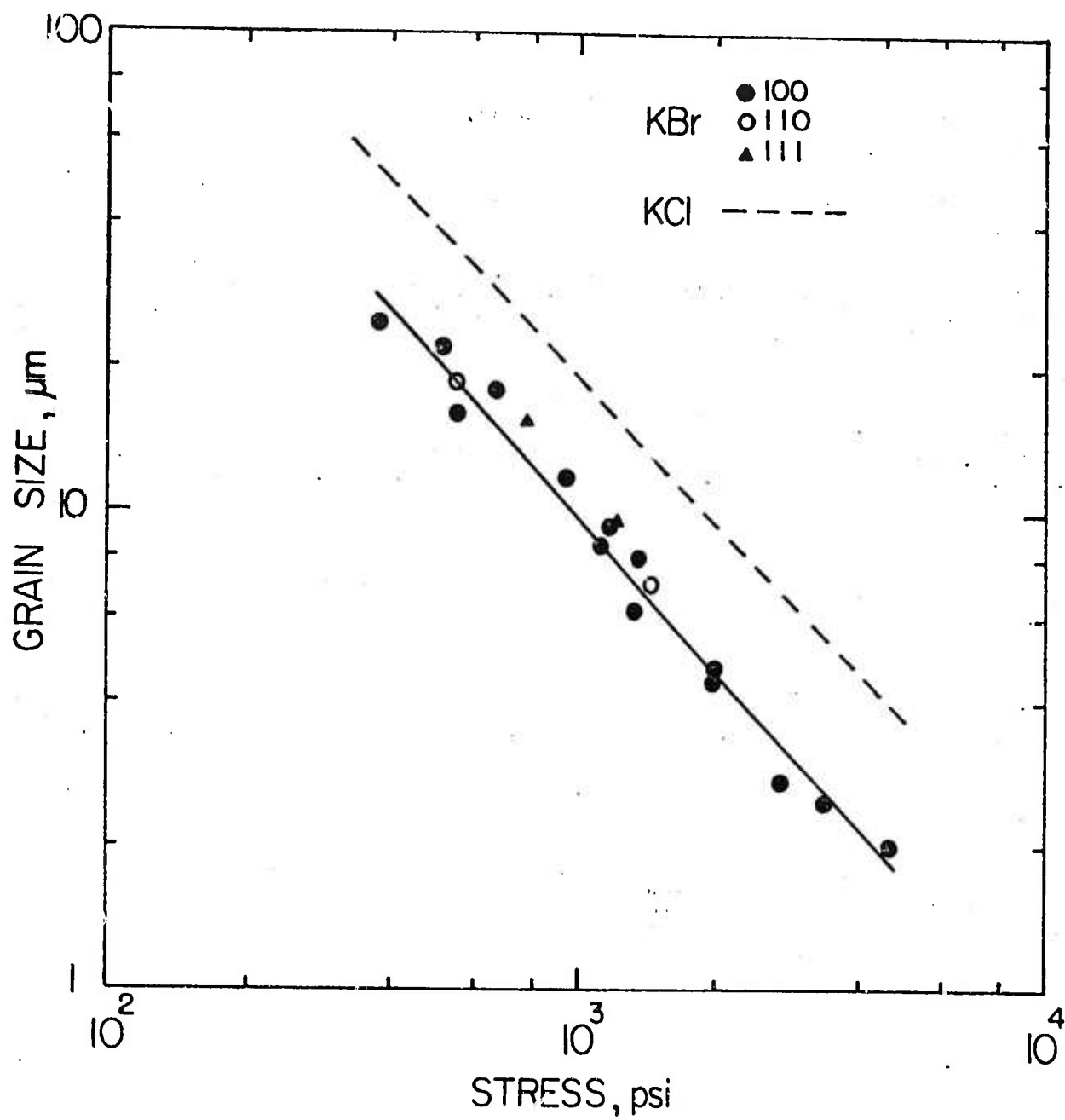


Figure B-6. Subgrain size versus forging stress for KBr.

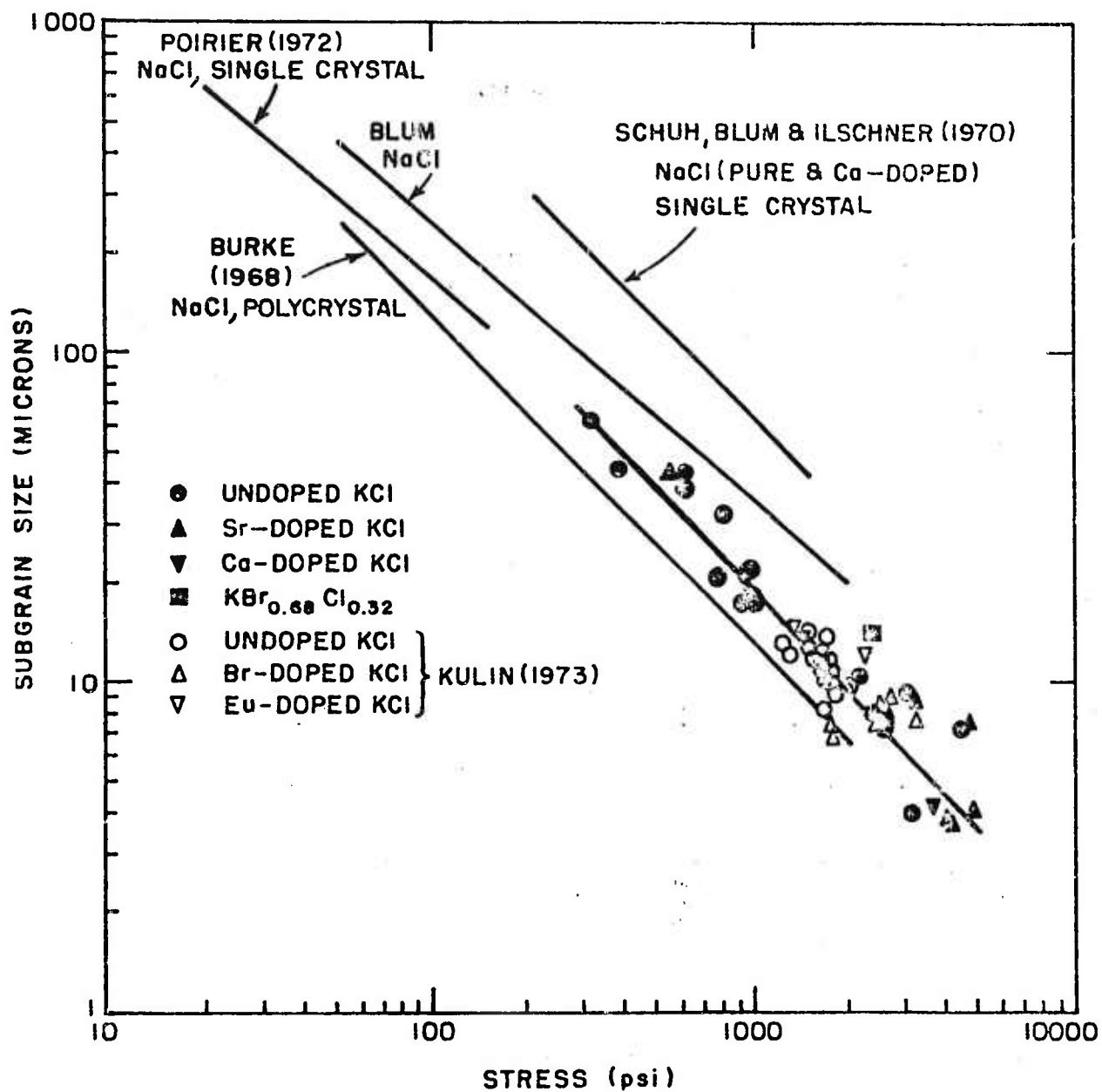
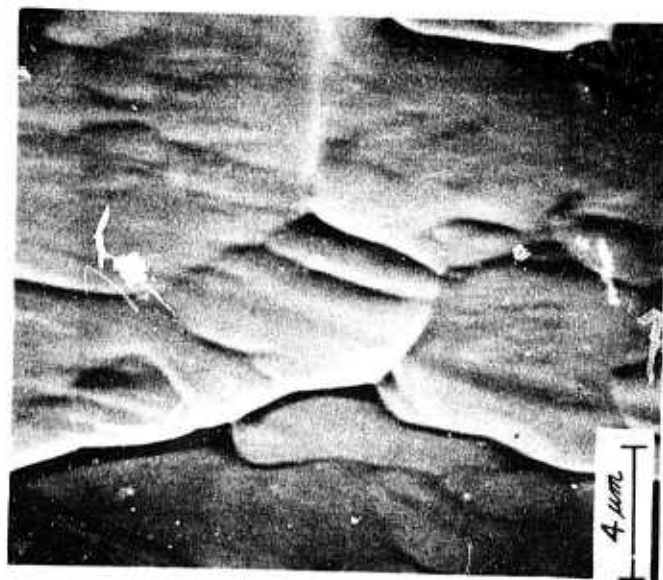
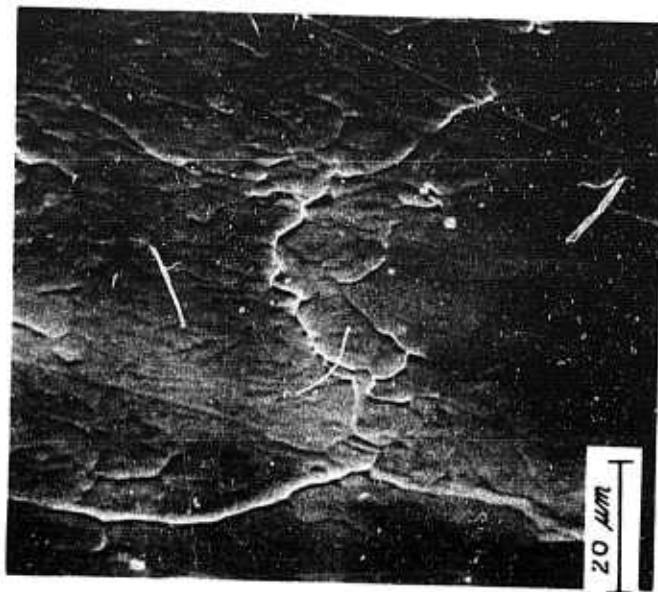


Figure B-7. Subgrain size versus forging stress for KCl and KBr compared with similar curves from NaCl creep studies, data of Blum as reported by Streb and Reppich.<sup>11</sup>



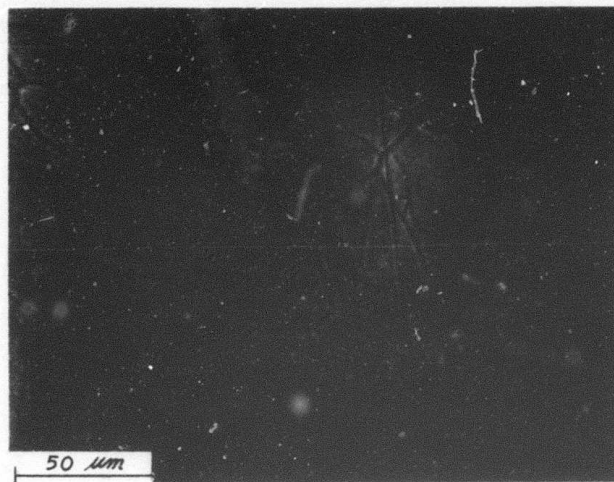


5100x a)



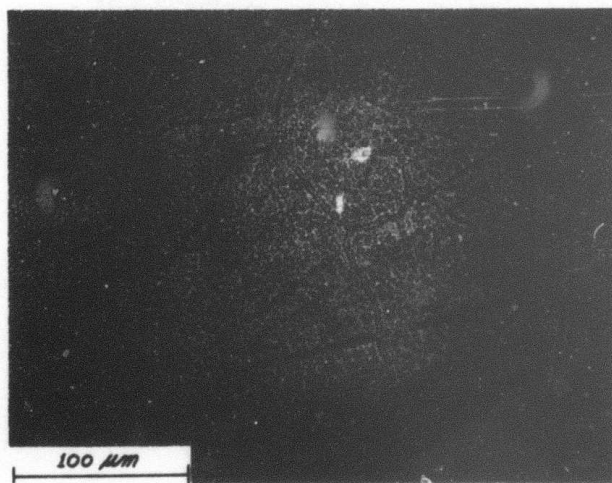
1000x b)

Figure B-8. SEM of Ca doped KCl forged at 242°C and 3640 psi.  
Note the high and low angle subgrain boundaries.



500x

Figure B-9. High angle boundaries and two types of sub-boundaries. Examination of triple junctions shows significant differences in energy for the three different types of boundary. Pure KCl forged at 505°C at 970 psi in the  $\langle 110 \rangle$ .



320x

Figure B-10. Resolution of low angle subgrain boundaries into individual etch pits. Pure KCl forged at 670°C and 575 psi in the  $\langle 111 \rangle$ .

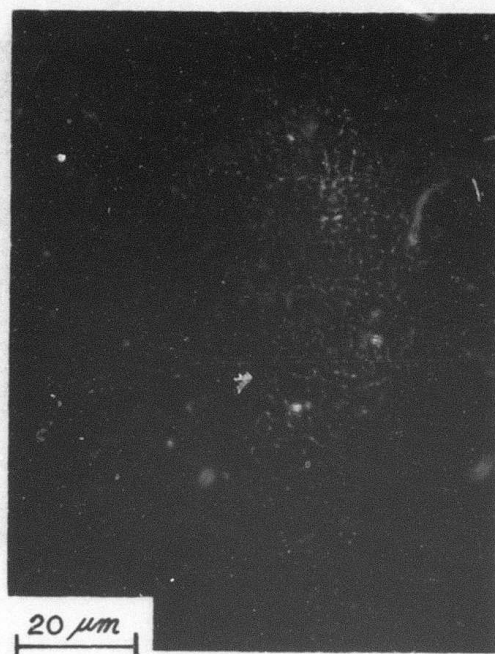
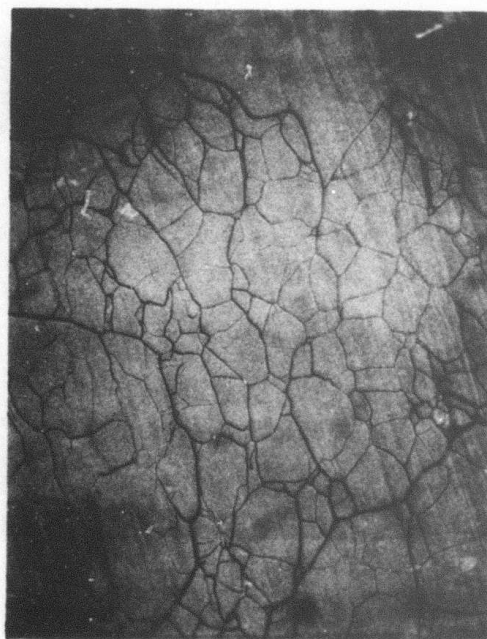


Figure B-11. Photomicrograph taken slightly out of focus to emphasis small subgrains. Pure KBr forged at 21°C and 4660 psi.



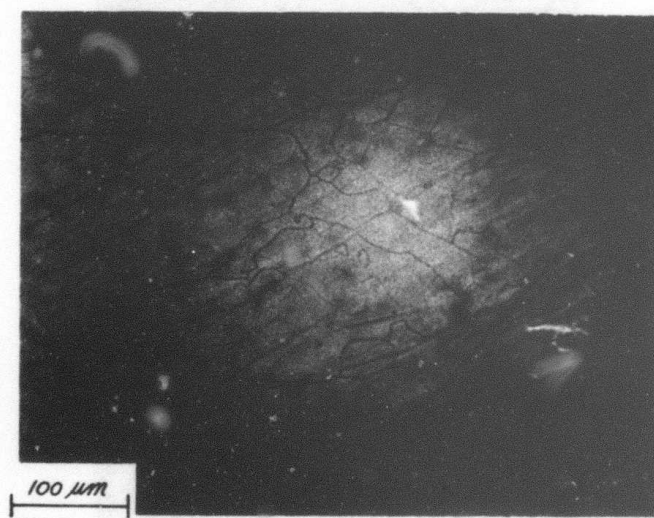
100x

Figure B-12. Pure KCl deformed at high temperature, 635°C, and 390 psi, showing high angle boundaries in addition to subgrains.



50x

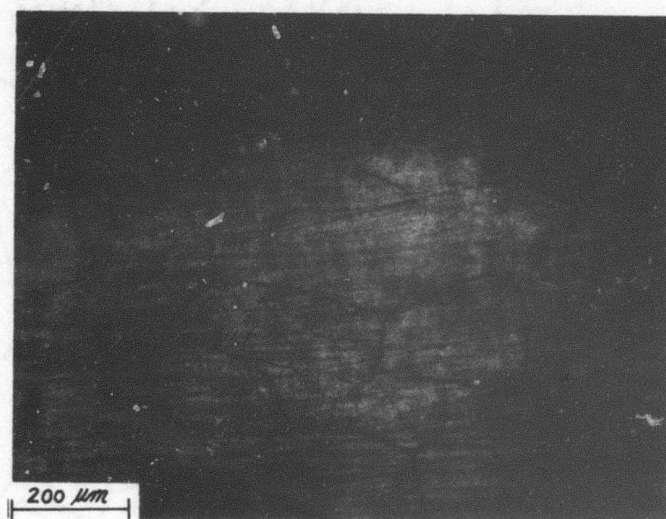
Figure B-13. Evidence of dynamic recrystallization. Pure KCl forged at 504°C and 750 psi in the  $\langle 110 \rangle$ .



200x

Figure B-14. High angle boundary resulting from recrystallization. Pure KCl forged at 504°C and 750 psi in the  $\langle 110 \rangle$ .





100x

Figure B-15. Dynamic recrystallization leads to high angle grain boundaries and variation in the subgrain development. Pure KCl forged at 504°C and 750 psi in the  $\langle 110 \rangle$ .

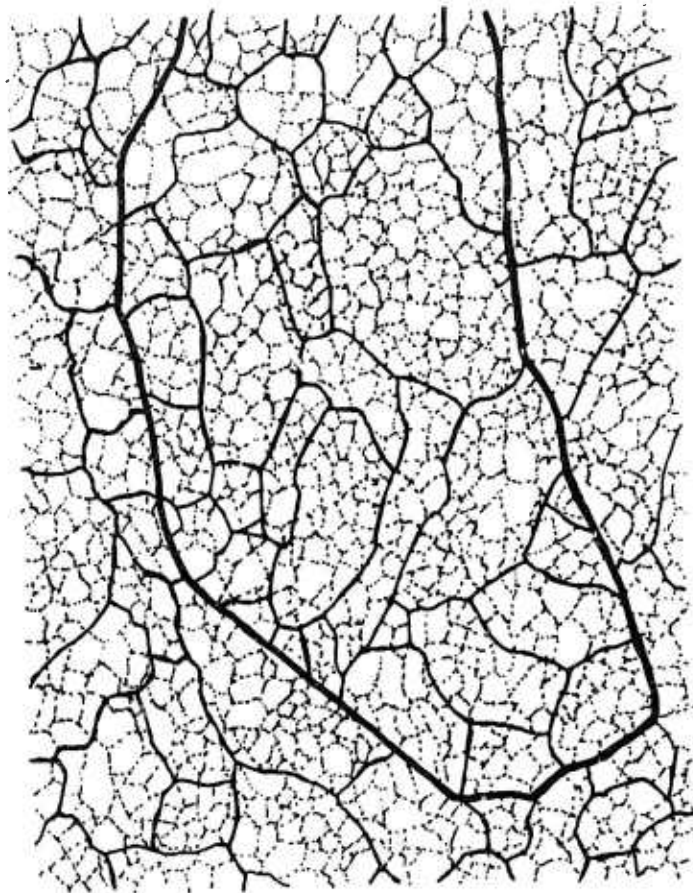
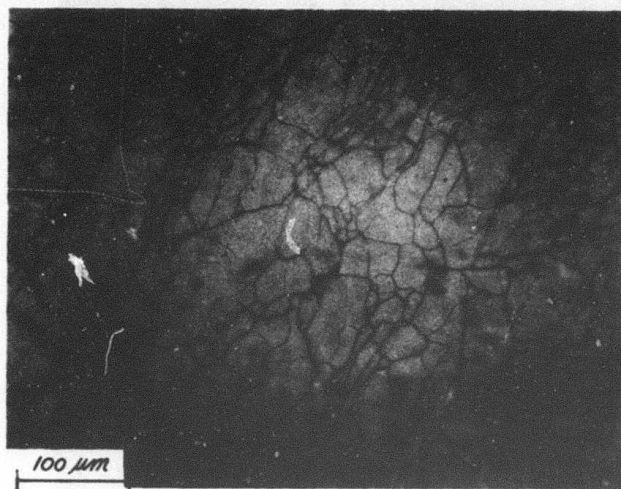
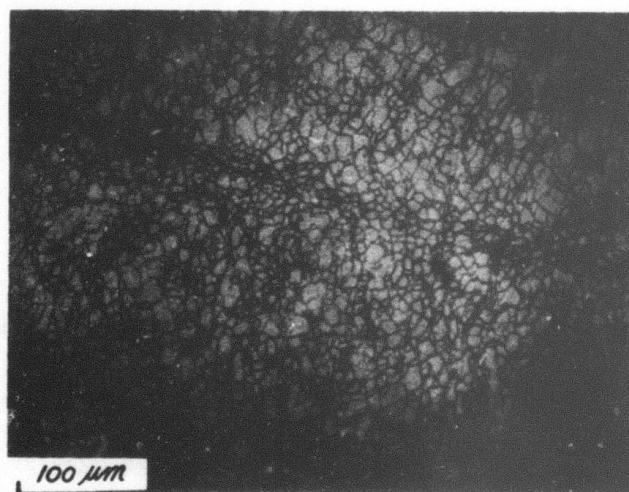


Figure B-16. Schematic showing a simplified picture of the microstructure in forged KCl and KBr with high and low angle sub-boundaries and an occasional high angle boundary from dynamic recrystallization at higher forging temperatures.



200x

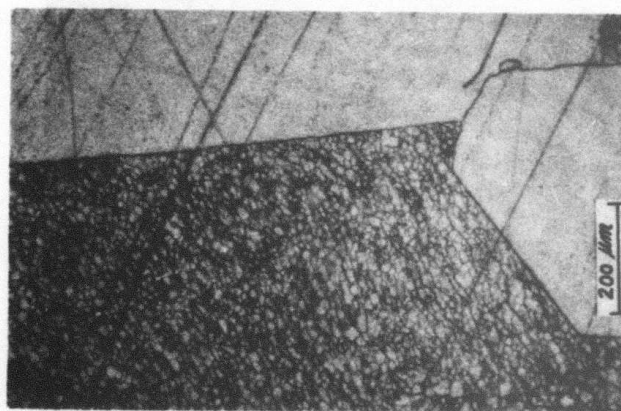
Figure B-17. Banded structure from local regions of higher subgrain density. Pure KCl forged at 504°C and 1160 psi in  $\langle 111 \rangle$ .



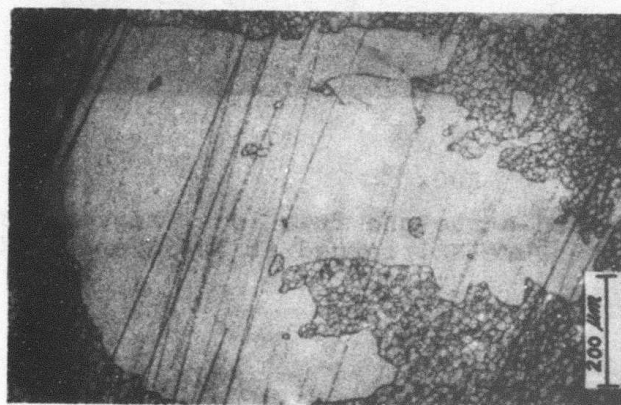
200x

Figure B-18. Bands of fine subgrains. Sr doped KCl forged at 396°C and 3280 psi.





100x a)



100x b)



200x c)

Figure B-19. Various morphologies of recrystallized grains found in forged and annealed KCl.

## C. IMPURITY DRAG THEORY IN GRAIN BOUNDARY MIGRATION OF KCl

### C.1 Experimental Work and Results

Grain boundary migration mobilities of undoped and Ca-, Sr- and Br- doped KCl were measured by the secondary grain growth in the hot deformed samples. Only the samples deformed in the  $\langle 100 \rangle$  direction were used for grain growth experiments. The hot-forged samples were annealed within  $0.5^\circ\text{C}$  of the desired temperature and under a dried nitrogen atmosphere. The annealed samples showed several big (mostly isolated) grains grown among the small grains as shown in Figure C-1. The grain boundary energy and misorientation angle of the subgrains was evaluated indirectly. Measurements of Class and Machlin (1966) showed that the grain boundary energy for twist boundaries  $>10^\circ$  was about  $110 \text{ erg/cm}^2$ . The growing grains must have high angle boundaries as suggested by the etching patterns. Therefore, we assumed that the grain boundary energy of the grain was  $110 \text{ erg/cm}^2$ . The dihedral angle between the growing grain boundary and the surrounding subgrain boundary was about  $160^\circ$ . Therefore, the grain boundary energy of the subgrains is about  $1/3$  that of the growing grains, i.e. about  $37 \text{ erg/cm}^2$ . This value of the grain boundary energy corresponds to  $1\text{-}3^\circ$  misorientated boundaries, as extrapolated from the data of Class and Machlin, (1966). The small grain to grain misorientation indicated here is also consistent with the strong texture found from x-ray analysis, Bowen et al (1973), Section B.

In computing the grain growth velocity, the area of the largest grain was chosen because of geometrical and grain growth incubation time considerations. The grain growth velocity,  $V$ ,

is given by

$$V = \frac{(A/\pi)^{1/2} - r}{t} \quad (C-1a)$$

where A is the area of largest grain found;

r, the neighboring small grain radius; and

t, the annealing time.

The driving force,  $\Delta F$ , for the motion of high angle boundaries is due to the surface energy of the neighboring subgrain boundaries,

$$\Delta F = S_V \gamma_{GB} = \frac{2\gamma_{GB}}{L} \quad (C-1b)$$

where  $S_V$ , the surface area per unit volume is related to L, the average length of grain intercepts, Underwood (1970), and where  $\gamma_{GB}$  was estimated above as  $37 \text{ erg/cm}^2$ .

Each value of grain boundary mobility data plotted in Figure C-2 is computed from

$$M \equiv \frac{V}{\Delta F} = \left( \frac{(A/\pi)^{1/2} - r}{t} \right) \left( \frac{2\gamma_{GB}}{L} \right)^{-1} \quad (C-1c)$$

Several features of the grain boundary mobility data are noted:

1. The apparent activation energy for boundary migration in undoped KCl at the temperature range investigated is about 35.4 kcal/mole. The boundaries in Ca- and Sr-doped KCl also have the same mobility activation energy above some transition temperature.

2. The 45 molar ppm Sr-doped and 95 molar Sr-doped KCl have the same boundary mobility at low temperatures. The 135 molar ppm Ca-doped samples have a lower mobility. However, all doped

samples have the same mobility activation energy of 18.6 kcal/mole.

3. The grain boundary mobility in KCl with 5 molar % KBr is at least an order of magnitude higher than that in samples with divalent impurities of a much lower dopant level. However, the boundary mobility in Br-doped KCl is lower than that of the undoped samples. This shows that the Br dopant can limit the boundary mobility to a certain extent. The activation energy in the mobility data of Br-doped KCl is about 9 kcal/mole.

4. The present mobility data and their extrapolations are higher than those observed by Gibbon (1968) and Kitazawa (1974) for KCl and Sun and Bauer (1970 a) for NaCl.

5. However, mobilities extrapolated from our data for doped and undoped samples are well below the room temperature mobility reported by Koepke et al (1974).

## C.2 MODEL AND BASIC ASSUMPTIONS

Since it was shown that the divalent cation impurities have pronounced effects in restraining the boundary mobility of KCl, the previous report proposed that the electrostatic interaction between the divalent impurity and the charged grain boundary accounts for the mobility drag mechanisms. Based on the general model developed by Cahn (1962), Lucke and Stuwe (1962), we attempt to develop, in the present report, an impurity drag theory for the grain boundary mobility of an ionic system.

The essential feature of the impurity drag model by Cahn (1962) and Lucke and Stuwe (1962) is to assume an interaction energy between impurity atoms and grain boundary. From the chemical potential of the impurity species in the boundary region, the flux equations of the impurity atoms are formulated. Solutions of the flux equations

give the impurity distributions in the neighborhood of a moving grain boundary. The drag force on a moving boundary is then calculated from the impurity distribution profiles and the interaction force between impurity atoms and the boundary.

This one dimensional model assumes:

- (A) A dilute solution of impurity in the matrix, thus the chemical potential for the impurity alone.  $\mu = RT \ln C\gamma$ , where  $C$  is the dopant concentration and  $\gamma$  is the activity coefficient.
- (B) There exists an interaction energy,  $U$ , between the dopant and the grain boundary which is assumed to have the following properties:
  - (1) it is not a function of velocity
  - (2) it is not an explicit function of local dopant concentration; and
  - (3) it is a function of the spatial coordinates in the frame of reference of the moving boundary.
- (C) The Einstein relation between the diffusion coefficient and the mobility of the impurity atoms is valid.
- (D) A steady state for the grain boundary, i.e.

$$\frac{\partial C}{\partial t} = v \frac{\partial C}{\partial X} \quad (C-1d)$$

where  $V$  is the boundary velocity.

- (E) The diffusion coefficient is a function of spatial distance from the moving boundary.

We can now write the chemical potential of the dopant as:

$$\mu = RT \ln C\gamma + U(x) + \mu_0 \quad (C-2)$$

where  $\mu_0$  is an additive constant potential term. The flux,  $J$ , of the dopant as observed from the frame of reference of the moving boundary is,

$$\begin{aligned} J &= \frac{DC}{RT} \nabla \mu \\ J &= -D \frac{dc}{dx} - \frac{DC}{RT} \frac{dU}{dx} \end{aligned} \quad (C-3)$$

But the equation of continuity requires that,

$$\nabla \cdot J + \frac{\partial C}{\partial t} = 0$$

Thus,

$$\begin{aligned} \frac{dJ}{dx} &= - \frac{\partial C}{\partial t} \\ &= -V \frac{\partial C}{\partial x} \end{aligned} \quad (C-4)$$

with the steady state assumption.

Combining (C-3) and (C-4) we get,

$$\frac{d}{dx} \left[ D \frac{dC}{dx} + \frac{DC}{RT} \frac{dU}{dx} + VC \right] = 0 \quad (C-5)$$

After integration we have expression,

$$D \frac{dC}{dx} + \frac{DC}{RT} \frac{dU}{dx} + VC = \text{constant} \quad (C-6a)$$

At  $x = \infty$ ,  $\frac{dC}{dx} = 0$  and  $\frac{dU}{dx} = 0$  and the concentration is that in the bulk,  $C_\infty$ , thus the integration constant is  $VC_\infty$  and equation (C-6a) becomes,

$$D \frac{dC}{dx} + \frac{DC}{RT} \frac{dU}{dx} + V(C - C_\infty) = 0 \quad (C-6b)$$

### C.3 NATURE OF IMPURITY-GRAIN BOUNDARY INTERACTION ENERGY, $E(x)$

In the previous discussion of grain boundary migration in metals, e.g. Cahn (1962), Lucke and Stuwe (1962), Gordon and Vandermeer (1965), the interaction energy

was generally assumed to be due to mechanical or strain field interaction. In the present study of ionic materials, we propose that the interaction energy is mainly due to the electrostatic interactions between the space charge cloud and the moving grain boundary. The origin of the space charge cloud is essentially from the difference in formation energies of the cation and anion vacancies and the presence of vacancy sources and sinks at surfaces. The space charge potential,  $\phi$ , must satisfy the Poisson's equation  $\frac{d^2\phi}{dx^2} = -\frac{4\pi\rho}{\epsilon}$ , where  $\rho$  is the distribution in the charge density and  $\epsilon$  is the static dielectric constant. It is composed of two major components, namely free Sr ions,  $[\text{Sr}_K^\bullet]$  and free K vacancies  $[\text{V}_K']$  and the contribution of free Cl vacancies,  $[\text{V}_{\text{Cl}}^\bullet]$ , is not significant in the Sr-doped KCl, at extrinsic temperatures. Furthermore, the relative contributions of  $[\text{Sr}_K^\bullet]$  and  $[\text{V}_K']$  also vary with temperature. At temperatures above the isoelectric temperature, the  $[\text{V}_K']$  constitutes the bulk of the charge density whereas at temperatures below the isoelectric temperature, the charge density is mainly due to the  $[\text{Sr}_K^\bullet]$  impurity cloud.

When the grain boundary migrates, the space charge potential will be affected by the variations of the impurity distribution, which is a function of the boundary velocity. This will influence energy,  $U$ , between the dopant and a moving boundary. An estimation of the velocity dependence can be made by considering the extreme case of such a high boundary velocity that the total Sr impurity profile breaks down to a uniform distribution,



whereas the vacancies, because of their relatively high diffusivities, can adjust themselves to the distribution profiles of the minimum energy. The space charge potential distributions for this high velocity boundary, as shown in Appendix (C-I), do not deviate significantly from the potential distributions for a stationary boundary. Based on those results, we use the space charge potential associated with a static grain boundary as the interaction energy between the impurity cloud and a moving boundary.

#### C.4 TRANSPORT MECHANISMS OF Sr IONS IN THE SPACE CHARGE POTENTIAL

Due to the Electric Field. In a space charge potential, the unassociated Sr impurities,  $Sr_K^+$ , which are positively charged, experience an electrostatic force in the field direction.

One is tempted to relate the diffusivity of the strontium  $D_{Sr}$ , and the mobility of Sr ions,  $M_{Sr}$ , by the Einstein relation,

$$\frac{M_{Sr}}{D_{Sr}} = \frac{e}{kT} \quad (C-7)$$

However, based on the Sr diffusion data in a cleaved NaCl crystal under a uniform electric field, Chemla (1956) reported that  $M_{Sr}/D_{Sr}$  is much less than  $e/kT$ . Howard and Lidiard (1964) studied the kinetics of Sr transport in a field and concluded that

$$\frac{M_{Sr}}{D_{Sr}} = \frac{e}{kT} \frac{10W_3}{W_1 + 3.5W_3} \quad (C-8)$$

where  $W_3$  is the dissociation frequency of the vacancy-impurity complex and  $W_1$  is the jumping frequency of the associated vacancy from one nearest neighbor position of Sr to another. Consequently, the Sr flux under the field in the space charge potential is

$$J_E = \frac{n_{Sr} C}{kT} \cdot \frac{10W_3}{W_1 + 3.5W_3} \frac{d\phi}{dx} \quad (C-9)$$

Due to the Electric Field Gradient. In the space charge region, the electric field is highly non-uniform, varying from about  $10^6$  volt/cm at the surface to  $10^2$  volt/cm or less at about  $50 \text{ \AA}$  in the bulk. The field gradient causes an attractive force on the dipole in the  $(Sr_K^+ V_K^-)^*$  complexes. However, the interactions between the electric field and the dipoles are neglected in the space charge theory of Kliever and Koehler (1965). As shown in Appendix (C-II) further refinement of the space charge theory with the consideration of dipole-field interaction, results in no significant modifications in the space potential nor the electric field. However, the dipole concentration is enhanced in the space charge region and the dipole distributions are significantly affected by the dipole orientations, as indicated in Appendix C-II.

With the notations defined in Appendix C-II, and for the grain boundary normal in the  $[100]$  direction, the total interaction energy between the electric field and the Sr dopants

$$U_{\text{dipole}} = -\frac{1}{2} \frac{ea}{2} (N_1 - N_3)E \quad (\text{C-10a})$$

$$= \frac{a}{4} (N_1 - N_3) \frac{de\phi}{dx}$$

which at equilibrium is

$$= \frac{aC_{\infty}p_{\infty}}{6} \sinh \left( \frac{a}{2kT} \frac{de\phi}{dx} \right) \frac{de\phi}{dx} \quad (\text{C-10b})$$

and the dipole flux,

$$J_{\text{dipole}} = -M_o \nabla U_{\text{dipole}}$$

$$= -M_o \frac{a}{4} (N_1 - N_3) \frac{d^2 e\phi}{dx^2} \quad (\text{C-11})$$

where  $M_o$  is the dipole mobility.

Due to Flux of Cation Vacancies. When a grain boundary migrates, the vacancies, because of their relatively high diffusivities, maintain the distribution profile by the vacancy fluxes towards the moving boundary. The Sr transport, which depends on the association with cation vacancies, is facilitated by the vacancy fluxes. In the reference frame of the moving boundary, the vacancy flux is  $([V_K'(x)] - [V_K'(\infty)])V$ , where  $V$  is the boundary velocity,  $[V_K'(x)]$  is the vacancy concentration at the location,  $x$ , away from the boundary and  $[V_K'(\infty)]$  is the vacancy concentration in the bulk. A Sr flux of the magnitude as the vacancy flux is then required to maintain the charge density,  $\rho$ , and the space potential,  $e\phi$ , in the boundary region. However, a quantitative measure of the vacancy flux contribution to Sr transport requires the simultaneous solution of the flux equations for vacancies and impurities, as well as the Poisson's equation which couples the defect concentrations.

The above discussions identify the electric field, the field gradient and the cation vacancy flux as the driving force for the Sr transport. However, these discussions also fail to suggest a quantitative measure of the Sr mobility in a given force field. In view of these difficulties, we relate the atomic mobility to the diffusivity by the Einstein relation, and the net force field for Sr transport is assumed to be the space charge electric field. Consequently, the total Sr flux,  $J_{Sr}$  due to the diffusion down a concentration gradient and the drift in a space charge electric field is

$$J_{Sr} = -D_o \frac{dc}{dx} - \frac{D_o}{kT} \frac{de\phi}{dx} . \quad (C-12)$$

#### C.5 NUMERICAL CALCULATIONS OF Sr DISTRIBUTION

The impurity distribution,  $C(x)$ , about a moving grain boundary can be evaluated from the flux Equation (C-6) which has a solution in the integrated form, as given in Cahn (1962)

$$C(x) = C_\infty V \int_{-\infty}^x \left[ \exp\left(\frac{U(\xi) - U(x)}{kT}\right) \cdot \exp\left(\int_x^\xi \frac{dn}{D(n)}\right) \right] \frac{d\xi}{D(\xi)} \quad (C-13)$$

As discussed in section D of this report, the diffusion coefficient,  $D(x)$ , of Sr ions is

$$D(x) = \frac{D_o p_\infty}{p_\infty + (1 - p_\infty) \exp\left(\frac{-e\phi - e\phi_\infty}{kT}\right)} \quad (C-14)$$

and the interaction energy,  $U(x)$ , between the impurity atoms and the charged grain boundary is

$$U(x) = e\phi(x) - e\phi_\infty . \quad (C-15)$$

With further algebraic manipulations, it can be shown that

For  $x < 0$

$$C(x,V)/C_{\infty} = \frac{2m}{\ell^2} \left(\frac{\ell+1}{\ell-1}\right)^m \exp\left(-\frac{2m(1-p_{\infty})}{\ell}\right) \cdot \int_1^{\ell} \frac{\left(\frac{y-1}{y+1}\right)^m (p_{\infty}y^2 + 1 - p_{\infty}) \exp\left(\frac{2m(1-p_{\infty})}{y}\right) dy}{(y+1)(y-1)} \quad (C-16)$$

For  $x > 0$

$$C(x,V)/C_{\infty} = \frac{2m}{\ell} \left(\frac{\ell-1}{\ell+1}\right)^m \exp\left(\frac{2m(1-p_{\infty})}{\ell}\right) \cdot \left\{ \left(\frac{\eta+1}{\eta-1}\right)^{2m} \exp\left(-\frac{4m(1-p_{\infty})}{\eta}\right) \cdot \int_1^{\eta} \frac{\left(\frac{y-1}{y+1}\right)^m (p_{\infty}y^2 + 1 - p_{\infty}) \exp\left(\frac{2m(1-p_{\infty})}{y}\right) dy}{(y+1)(y-1)} - \int_{\eta}^{\ell} \frac{\left(\frac{y+1}{y-1}\right)^m (p_{\infty}y^2 + 1 - p) \exp\left(-\frac{2m(1-p_{\infty})}{y}\right) dy}{(y+1)(y-1)} \right\} \quad (C-17)$$

where

$$\ell = \exp[(e\phi(x) - e\phi_{\infty})/2kT] = \ell(x) \quad (C-18a)$$

$$\eta = \exp[(e\phi(o) - e\phi_{\infty})/2kT] = \text{a constant} \quad (C-18b)$$

$$m = V/(D_0 p_{\infty}/\delta) \quad (C-18c)$$

$V$  = actual boundary velocity

$D_0 p_{\infty}$  = the bulk Sr diffusivity

Physically,  $D_0 p / \delta$  is the velocity at which the Sr ions move across the space charge layer by random walk, and  $m$  is the normalized boundary migration velocity with respect to the diffusion velocity.

The singularity, at  $y = 1$ , in the integrands of Eqs. C-16 and C-17, can be removed by proper partial integrations. Furthermore, it can be shown that the integrals are convergent.

The numeral integrations, using Simpson's method, were performed in a PDP-11 computer of Digital Corporation. Typical distribution profiles of a grain boundary moving in 50-ppm Sr-doped KCl at velocities of  $0.01 < m < 2$  are shown in Figures C-3 and C-4. The coordinate system of the moving frame of reference of the boundary is adopted for these curves. Several features are noted:

- (A) The profile is assymetrical; and the degree of assymetry increases with velocity.
- (B) For  $T < T_0$  (Figure C-3) the interaction energy between the boundary and the Sr ions is attractive and Sr absorption to the moving boundary is observed. As velocity increases, the absorption decreases. Furthermore, the maximum of concentration profile trails slightly the moving boundary.

(C) For  $T > T_0$  (Figure C-4) the  $[Sr_K^{\bullet}]$  tends to avoid the grain boundary because of the interaction energy with the boundary. As the velocity increases, there is a  $[Sr_K^{\bullet}]$  pile up on the leading side of the boundary. The maximum of the  $[Sr_K^{\bullet}]$  pile-up can be twice the bulk concentration and occurs at about  $20 \text{ \AA}$  ( $\delta$  to  $2\delta$ ) from the boundary.

#### C.6 NUMERICAL CALCULATIONS OF IMPURITY DRAG

Having calculated the distribution of  $[Sr_K^{\bullet}]$  around a moving boundary, we proceed to the calculation of the impurity drag due to the space charge cloud.

The drag force due to  $[Sr_K^{\bullet}]$  ions on a per unit volume basis is,

$$\frac{\Delta F}{\Delta X} = - N_V (C(x) - C_{\infty}) \frac{dU}{dx} \quad (C-19)$$

where  $U$  is the Sr-boundary interaction energy; and  $(-\frac{dU}{dx})$  is the force of interaction;  $N_V$  is the number of atoms per unit volume;  $C(x)$  is the concentration at the location  $x$ ; and  $C_{\infty}$  is the bulk  $[Sr_K^{\bullet}]$  concentration. Therefore the total drag due to  $[Sr_K^{\bullet}]$  is,

$$F = - N_V \int_{-\infty}^{\infty} (C - C_{\infty}) \frac{dU}{dx} \cdot dx \quad (C-20)$$

By methods of numerical integration, the impurity drag exerted on a moving grain boundary can be calculated. The



mobilities of the grain boundary, defined as velocity per unit drag, for a slow moving boundary ( $m = 0.1$ ) were calculated for different temperatures and dopant levels and are shown in Figure C-5.

In general, the calculated mobilities are within a factor of 10 of the experimentally measured data. Since the input data for the calculations are solely from the diffusion and association activation energies in the literature, and with no adjustable parameters, a close fit between the experimental data and the theory is encouraging. The activation energies for grain boundary migration in the various temperature ranges are essentially those we predicted in the previous report.

According to Cahn (1962), the total drag force,  $F$ , experienced by a moving grain boundary with velocity,  $V$ , can be approximated as

$$F = \lambda V + \frac{\alpha C_{\infty} V}{1 + \beta^2 V^2} \quad (C-21)$$

where  $\lambda^{-1}$  is the intrinsic boundary mobility,  $\alpha^{-1}$  is the mobility per unit impurity concentration in the impurity controlled low velocity region; and  $\beta^{-1}$  is the drift velocity of the impurity atoms across the grain boundary and it is also the boundary velocity at which the impurity drag reaches the maximum.

Furthermore, as shown in Cahn (1962), the quantities  $\alpha$  and  $\beta$  are related to the impurity-boundary interaction energy,  $U(x)$ , and the impurity diffusivity,  $D(x)$ ,

$$\alpha = 4N_VKT \int_{-\infty}^{\infty} \frac{\sinh^2 U(x)/2kT}{D(x)} dx \quad (C-22)$$

$$\frac{\alpha}{\beta^2} = \int_{-\infty}^{\infty} \frac{N_V}{kT} \left( \frac{dU}{dx} \right)^2 D(x) dx \quad (C-23)$$

where  $N_V$  is the number of atoms per unit volume. In the context of space charge interaction between the impurity cloud and the grain boundary, the interaction energy,  $U(x)$ , and the Sr impurity diffusivity,  $D(x)$ , are given in Eqs. (C-15) and (C-14) respectively. The quantities,  $\alpha$  and  $\beta$  are evaluated from Eq. (C-22) and Eq. (C-23), as shown in Appendix C-III.

The intrinsic boundary mobility,  $\lambda^{-1}$ , is estimated, based on the maximum mobility data in the undoped samples of Gibbon (1968) and Yan et al (1974), Fig. C-2, at the high and low temperature regions respectively, to be

$$\lambda^{-1} = 4.64 \times 10^{-6} \exp(-7.63 \text{ kcal/RT}) \left( \frac{\text{cm}}{\text{sec}} \right) \left( \frac{\text{dyne}}{\text{cm}^2} \right)^{-1} \quad (C-24)$$

In the low velocity limit, the grain boundary mobilities,  $(\lambda + \alpha C_\infty)^{-1}$ , are shown in Fig. C-6 ) as a function of temperature and with the dopant concentrations as parameters. The peaking mobilities at the isoelectric temperatures are due to the vanishing space potential.

The calculated values of  $\beta^{-1}$ , the boundary velocities at which the impurity cloud exerts the maximum drag, are compared with the experimental velocity data, as shown in Fig. (C-7). The comparison suggests that the experimental migration velocities are in the neighborhood of the breakaway velocities.

A more rigorous test of the theory can be made by comparing the experimental velocity data with those resulted from the experimental driving force as predicted in Eq. (C-21). Since the drag force must be balanced by the driving force in order to maintain the steady state boundary motion, we can solve the cubic equation, Eq. (C-21), of the boundary velocity for a given driving force. The solutions of boundary velocities under the driving force of  $10^5$  dynes/cm<sup>2</sup>, which corresponds to an average of 7.3  $\mu$ m for the linear grain size intercepts, are shown in Figs. (C-8)-(C-10). The drag force has a local maximum of  $\Delta F_{\max} \approx \frac{C_\infty \alpha}{2} \beta^{-1}$  at the boundary velocity,  $v_{\max} \approx \beta^{-1} (1 + \frac{4\lambda}{C_\infty})^{1/2}$  and also a local minimum of  $\Delta F_{\min} \approx 2 (\lambda \alpha C_\infty)^{1/2} \beta^{-1}$  at  $v_{\min} = (\frac{C_\infty \alpha}{\lambda})^{1/2} \beta^{-1}$ . When the experimental driving force,  $\Delta F$ , is  $F_{\min} < \Delta F < F_{\max}$ , there exist three possible velocity solutions for Eq. (C-21), as indicated in Figs. (C-8)-(C-10) in some

temperature range. When the experimental boundary velocities are compared with the predicted velocities we observe that:

1. For samples with Sr concentrations of 50 and 100 ppm, the experimental boundary velocities at low temperatures are within an order of magnitude of the predicted low velocity region.

2. In the high temperature range, when the experimental driving force,  $\Delta F$ , exceeds the local maximum drag force,  $F_{\max}$ , only a high velocity solution is predicted from Eq. (C-21). However, the experimental velocities, in this temperature range, are intermediate between the predicted high velocities and those extrapolated from the low velocities predicted at low temperatures. This suggests that the experimental velocity data at high temperatures are in the stage of break-away.

3. For the samples with a Sr concentration of 1 ppm, most of the experimental data are in the break-away stage and the anomalously high boundary velocities of Koepke et al (1974) are in the predicted high velocity region.

#### C.7 STRAIN FIELD INTERACTION WITH THE SPACE CHARGE POTENTIALS

In the previous discussions, we consider the space charge potential as the only interaction energy between the grain boundary and the impurity cloud. This assumption may be justified by the relatively modest effects of the monovalent dopant, Br, as compared with the divalent dopant, Sr, in inhibiting the grain boundary mobility. However the strain field interactions between impurity atoms and the grain boundary became important

at the isoelectric temperature, at which the effects of the space charge potential interactions vanish. Furthermore, Kitazawa (1975) reported that both the ionic radii and the ionic charge of the impurity dopants have important effects in limiting the grain boundary mobility of KCl.

Auger Electron Spectroscopy studies of Johnson et al. (1974) on the intergranularly fractured surface of alumina, sintered to 100% T.D., with 0.1-0.2 a/o Mg dopant and 40-50 atomic ppm Ca in the bulk, showed a strong segregation of 3 a/o Ca and only a modest concentration of 0.2-0.4 a/o Mg at the grain boundary along the fractured surfaces. Whereas both the Mg and Ca ions have the same ionic charge, the ionic radii of  $Mg^{2+}$  and  $Ca^{2+}$  are 144% and 209% respectively of the  $Al^{3+}$  radius. Based on the elastic strain energy induced in a lattice by a solute ion of different radius, and the equilibrium segregation theory of McLean (1951), Johnson et al. (1974) calculated the dopant concentrations segregated to the grain boundary and found a reasonable fit to the experimental data.

Given the individual importance of the strain field interaction as well as the space charge electrostatic interaction between the dopant impurity and the grain boundary, the strain field and the space charge potential also couple with each other in enhancing the impurity segregation and in limiting the grain boundary mobility. With the inclusion of the strain field interaction energy,  $U_s$ , between the

unassociated Sr ions and the grain boundary, the free energy,  $F$ , per unit area of the half of the crystal is

$$F = \int_0^L dx \left[ n_+ F^+ + n_- F^- + n_B \{F^+ + F^- - B\} + n_{1b} \{F^+ - B_+\} + n_f U_S + \frac{1}{2} \rho \phi \right] - TS \quad (C-25)$$

and the associated Poisson's equation is

$$\frac{d^2 \phi}{dx^2} = \frac{-4\pi e}{\epsilon} (n_f + n_- - n_+) \quad (C-26)$$

After the minimization of the free energy with the usual constraint of constant impurity content, we get

$$n_+/N = \exp\left(\frac{F^+ - e\phi}{kT}\right) \quad (C-27a)$$

$$n_-/N = \exp\left(\frac{-F^- + e\phi}{kT}\right) \quad (C-27b)$$

$$n_f/N = C_\infty (1 - p_\infty) \exp\left(-\frac{e\phi - e\phi_\infty + U_S}{kT}\right) \quad (C-27c)$$

It can be shown that the Poisson's equation becomes

$$\frac{d^2 z}{ds^2} = \frac{1}{2} \left[ e^z - e^{-(U_S(x) - U_S(\infty)/kT)} e^{-z} \right] \quad (C-28)$$

where

$$Z \equiv (e\phi - e\phi_{\infty})/kT \quad (C-29a)$$

$$S = X/\delta \quad (C-29b)$$

$$\delta = \left[ \frac{\epsilon kT}{8\pi N e^2} e^{(F^+ - e\phi_{\infty})/kT} \right]^{1/2} \quad (C-29c)$$

Physically,  $C_{\infty}(1-p_{\infty})/\exp(-(F^+ - e\phi_{\infty})/kT)$  is the ratio of the free Sr concentration to the free cation vacancy concentration. This ratio is always less than one at all temperatures and is approaching one at the extrinsic, low temperature.

We arbitrarily assume that the strain field interaction energy,  $U_S$ , takes the following form

$$U_S(X) = \begin{cases} U_0(1 - \frac{X}{na}) & ; \quad X \leq na \\ 0 & X > na \end{cases} \quad (C-30)$$

where  $a$  is the lattice constant,  $6.293\text{\AA}$ , for KCl, and  $n$  is an integer, say 2.

In the neighborhood of the isoelectric temperature,  $T_0$ , the ratio  $Z = (e\phi - e\phi_{\infty})/kT \ll 1$ , and Eq.(C-28) can be reduced to

$$\frac{d^2 Z}{dS^2} = \frac{1}{2} \left[ 1 + Z - (1-Z) e^{-(U_S(s) - U_S(\infty))/kT} \right] \quad (C-31)$$



With the assumption of  $U_S$  in Eq (C-30), and the boundary conditions of

a)  $Z(0) = -e\phi_\infty/kT$

b)  $Z$  and  $dZ/dS$  are continuous at  $X = na$

this can be solved numerically.

The space charge potentials,  $e\phi$ , at several degrees below the isoelectric temperature are shown in Fig.(C-11) for both an attractive impurity strain field interaction energy,  $U_0 < 0$ , and a repulsive interaction energy,  $U_0 > 0$ . For  $U_0 < 0$ , whereas the impurity atoms are segregated to the grain boundary region by the attractive strain field, the space charge potential tends to be negative and repulsive to the impurity segregation in the boundary region in order to maintain a stable impurity distribution. Since the space potentials,  $e\phi$ , are constrained to a zero surface potential and a positive bulk potential,  $e\phi_\infty$ , the space charge potential, after reaching the minimum and negative value, passes through the zero potential again before attaining the positive bulk potential. Similarly, for  $U_0 > 0$ , the space charge potential reaches the maximum value before attaining the bulk potential.

The concentrations of the unassociated Sr impurities and the unassociated cation vacancies due to the coupled effects of strain field and the space charge potential

are shown in Fig. (C-12). The maximum and the minimum in the concentration ratios are related to the similar features in the space charge potentials.

At temperatures not within the immediate neighborhood of the isoelectric temperature, since the approximation  $(e\phi - e\phi_{\infty})/kT \ll 1$  does not hold everywhere in the boundary region, numerical solutions for the Poisson's equation are required. Computer calculations of the coupled effects of the strain field and space charge electric field are in progress at the time of this report preparation.

Appendix C-I: Space Charge Potential Distribution  
in a Moving Grain Boundary

In this appendix, we discuss the effects of the grain boundary motion on the space charge potential. While the distribution profile of a given species of impurities or vacancies is governed by the individual flux equation, of the type similar to Eq. (C-6b), all these distribution profiles are coupled and related to the space potential by the Poisson's equation. The solutions of the space potential as a function of the boundary velocity involve 4 coupled differential equations, as suggested in Brown (1960), instead of solving the complicated mathematics, we consider the extreme case of such a high boundary velocity that the total Sr impurity profile breaks down to a uniform distribution, while the vacancies, because of the relatively high diffusivities, can adjust themselves to the distribution profiles of the minimum energy. The uniform Sr distribution suggests that

$$n_i(x) = n_f(x) + n_b(x) = \bar{C} \quad (\text{CI-1})$$

$$\delta n_f(x) = -\delta n_b(x) \quad (\text{CI-2})$$

where  $n_f$  and  $n_b$  are the density of unassociated ( $\text{Sr}_K^{\cdot}$ ) and associated ( $\text{Sr}_K^{\cdot} \text{V}_K^{\cdot}$ )\*, respectively.

With the condition, (CI-2), and after the minimization of the free energy, as discussed in Kliever and Koehler (1965),

we obtain

$$\delta n_f \left\{ -(F^+ - B_+) + e\phi - kT \ln \left( \frac{N}{n_f} \cdot \frac{n_b}{12N} \right) \right\} = 0$$

$$\frac{n_b}{n_f} = 12 \cdot \exp(-(F^+ - B_+ - e\phi)/kT) \quad (\text{CI-3})$$

where  $F^+$  is the cation vacancy formation energy and  $B^+$  is the binding energy of the  $(\text{Sr}_K^+ \text{V}_K^+)^*$  complexes. Combining Eqs. (CI-1) and (CI-3), we get

$$n_f = \frac{\bar{C}}{1 + 12 \cdot \exp(-(F^+ - B_+ - e\phi)/kT)} \quad (\text{CI-4})$$

With the expressions for cation and anion vacancies, as derived in Kliever and Koehler (1965), the Poisson's equation becomes

$$\frac{d^2\phi}{dx^2} = -\frac{4\pi Ne}{\epsilon} \left\{ \frac{\bar{C}}{1 + 12 \exp(-(F^+ - B_+ - e\phi)/kT)} + \exp\left(-\frac{F^+ + e\phi}{kT}\right) - \exp\left(-\frac{F^+ - e\phi}{kT}\right) \right\} \quad (\text{CI-5})$$

It can be shown that the bulk potential,  $e\phi_\infty$ , in this case of a migrating grain boundary, is identical to that in the case of a stationary boundary. Further algebraic manipulations reduce the Poisson's equation to

$$2\bar{c}(1-p_\infty)\frac{d^2(e\phi/kT)}{dS^2} = -\left\{\frac{\bar{c}}{1+12\exp(-(F^*-B_s-e\phi)/kT)} + \exp(-\frac{F^*-e\phi}{kT}) - \exp(-\frac{F^*-e\phi_\infty}{kT})\right\} \quad (\text{CI-6})$$

with  $S \equiv x/\delta$  (CI-7)

and  $\delta \equiv \left[\frac{\epsilon kT}{8\pi N e^2 \bar{c}(1-p_\infty)}\right]^{1/2}$  (CI-8)

where the Debye length,  $\delta$ , is identical to that in the case of stationary grain boundary in the extrinsic temperature range.

Upon the integration of Eq. (CI-6), and with the boundary conditions that  $d\phi/ds = 0$ ,  $\phi = \phi_\infty$  at  $S \rightarrow \infty$ , we get

$$\begin{aligned} \bar{c} \left[ \frac{d(e\phi - e\phi_\infty)/kT}{dS} \right]^2 = & \frac{1}{1+12\exp(-\frac{F^*-B_s-e\phi}{kT})} \left\{ \bar{c}(e\phi - e\phi_\infty)/kT - \bar{c} \ln \left[ \frac{1+12\exp(-\frac{F^*-B_s-e\phi}{kT})}{1+12\exp(-\frac{F^*-B_s-e\phi_\infty}{kT})} \right] \right. \\ & + \exp(-\frac{F^*}{kT}) \left[ \exp(-\frac{e\phi}{kT}) - \exp(-\frac{e\phi_\infty}{kT}) \right] \\ & \left. + \exp(-\frac{F^*}{kT}) \left[ \exp(\frac{e\phi}{kT}) - \exp(\frac{e\phi_\infty}{kT}) \right] \right\} \end{aligned}$$

(CI-9)

Numerical integrations of Eq. (CI-9) give the space potential distribution for a crystal in the temperature of 200-700°C. At temperatures above the isoelectric temperature, the calculated potential distributions are very similar to those given in Kliever and Koehler (1965) for a stationary, as shown in Figure (CI-1). This is expected because the vacancy cloud, which are free to adjust themselves to the minimum free energy distribution, constitute the majority of the charge density, which creates the space charge potential. However, at temperatures below the isoelectric temperature, the impurity cloud has a larger share of contributions to the potential, and the potential distribution for a mobile boundary is different by about 30% of that for a stationary boundary as indicated in Figure (CA-2).

Appendix C-II: Effects of Dipole Interactions  
in the Space Charge Potential Theory

The space charge theory, as formulated in Kliever and Koehler (1965), neglected the interactions between the bound charges, e.g. the  $(\text{Sr}_K^+ \text{V}_K^-)^*$  dipoles and  $(\text{V}_K^+ \text{V}_{\text{Cl}}^-)^*$  dipoles, and the electric field as created by the distribution of the free charges, e.g.  $\text{Sr}_K^+$ ,  $\text{V}_K^-$ ,  $\text{V}_{\text{Cl}}^-$ , in the neighborhood of the grain boundary. As shown in Jackson (1962), the interaction energy,  $U_{\text{dipole}}$ , of the polarizable dipoles of dipole moments,  $\vec{p}$ , in an electric field,  $\vec{E}$ , is given as

$$U_{\text{dipole}} = -\frac{1}{2} \vec{E} \cdot \vec{p} \quad (\text{CII-1})$$

For the crystal structure of KCl, the dipole moment of the  $(\text{Sr}_K^+ \text{V}_K^-)^*$  complexes can be in any of the 12 vectors,  $\vec{p}_i$ , of the type,  $ea/2$  (110); and each vector has a magnitude of  $ea/\sqrt{2}$ , where  $e$  is the electronic charge,  $1.6 \times 10^{-19}$  coulomb; and  $a$  is the lattice constant, 6.293 Å for KCl. We further assume that there are  $m_i(x)$  vacancy-impurity dipoles,  $(\text{Sr}_K^+ \text{V}_K^-)^*$ , with dipole moment,  $\vec{p}_i$ , at the location  $x$ .

However, the dipole moment of  $(\text{V}_K^+ \text{V}_{\text{Cl}}^-)^*$  complexes can only be in any of the 6 vectors,  $\vec{q}_j$ , of the type,  $ea/2$  (100); and each has a magnitude of  $ea/2$ . Similarly, we assume that there are  $n_j(x)$  vacancy-vacancy dipoles,  $(\text{V}_K^+ \text{V}_{\text{Cl}}^-)^*$ , with dipole moment,  $\vec{q}_j$ , at the location  $x$ .

The net dipole moment,  $p$ , of the  $m_i(x)$  and  $n_j(x)$  dipoles with moments,  $\vec{p}_i$  and  $\vec{q}_j$ , respectfully, when resolved in the direction of the electric field, which is normal to the planar



grain boundary, is

$$\begin{aligned}
 P &= \left( \sum_{i=1}^{12} \vec{p}_i m_i + \sum_{j=1}^6 \vec{q}_j n_j \right) \cdot \vec{E} / |E| \\
 &= \sum_{i=1}^{12} p_{ix} m_i + \sum_{j=1}^6 q_{jx} n_j
 \end{aligned} \tag{CII-2}$$

where  $p_{ix}$  and  $q_{jx}$  is the component of  $\vec{p}_i$  and  $\vec{q}_j$  moment in the field direction,  $\vec{x}$ .

The interaction energy,  $U_{\text{dipole}}$ , between all these dipoles and the electric field,  $E$ , is

$$\begin{aligned}
 U_{\text{dipole}} &= -\frac{1}{2} \vec{E} \cdot \left( \sum_{i=1}^{12} \vec{p}_i m_i + \sum_{j=1}^6 \vec{q}_j n_j \right) \\
 &= \frac{1}{2} \left( \sum_{i=1}^{12} p_{ix} m_i + \sum_{j=1}^6 q_{jx} n_j \right) \frac{d\phi}{dx}
 \end{aligned} \tag{CII-3}$$

where  $\phi$  is the potential associated with the field.

When the interaction energy term,  $U$ , is included, the free energy,  $F$ , of a crystal, of length  $2L$ , is

$$\begin{aligned}
 F &= 2 \int_0^L dx \left[ n_+(x) F^+ + n_-(x) F^- + \sum_{i=1}^{12} m_i(x) F^+ - B_+ - \vec{p}_i \cdot \vec{E} / 2 \right. \\
 &\quad \left. + \sum_{j=1}^6 n_j(x) (F^+ + F^- - B - \vec{q}_j \cdot \vec{E} / 2) + \frac{1}{2} \rho_f(x) \phi(x) \right] - T S_c
 \end{aligned} \tag{CII-4}$$

where  $n_+(x)$  is the number of cation vacancies with formation energy,  $F^+$ ;  $n_-(x)$  is the number of anion vacancies with formation energy,  $F^-$ ;  $B_+$  and  $B$  are the binding energies of

the  $(\text{Sr}_K^+ \text{V}_K^+)^*$  complexes and of the  $(\text{V}_K^+ \text{V}_{\text{Cl}}^+)^*$  complexes respectively; and  $\rho_f$  is the free charge density in the crystal.

The free energy of the crystal can be minimized by varying the 21 independent quantities of defects and impurities concentration, and with the following two constraints:

(1) Poisson's Equation:

$$\frac{d}{dx} (-\epsilon \frac{d\phi}{dx} + 4\pi p) = 4\pi e (n_{\text{f}} + n_- - n_+) \quad (\text{CII-5})$$

where  $n_{\text{f}}$  is the number of free Sr atoms.

(2) Impurity conservation:

$$\int_0^L \left[ \sum_{i=1}^{12} m_i(x) + n_{\text{f}}(x) \right] dx = \bar{C}NL \quad (\text{CII-6})$$

where  $\bar{C}$  is the average concentration of Sr impurities and  $N$  is the density of anion or cation sites in the crystal.

A variation of the free energy,  $F$ , as defined in Eq. (CII-4), gives,

$$\begin{aligned} \delta(F/2) &= \delta \int_0^L \left[ n_+ \omega F^+ + n_- \omega F^- + \sum_{i=1}^{12} m_i(x) \{ F^+ B_i^+ - \vec{p}_i \cdot \vec{E}/2 \} + \sum_{j=1}^6 n_j(x) \{ F^+ F^- B_j^- - \vec{q}_j \cdot \vec{E}/2 \} + \frac{1}{2} \rho_f(x) \phi(x) \right] \\ &\quad - \delta(TS_c) \\ &= \int_0^L F^+ \delta n_+(x) dx + \int_0^L F^- \delta n_-(x) dx + \int_0^L (F^+ B_i^+) \sum_{i=1}^{12} \delta m_i(x) dx + \int_0^L \{ F^+ F^- B_j^- \} \sum_{j=1}^6 \delta n_j(x) dx \\ &\quad - \delta \int_0^L \sum_{i=1}^{12} m_i(x) \vec{p}_i \cdot \vec{E}/2 dx - \delta \int_0^L \sum_{j=1}^6 n_j(x) \vec{q}_j \cdot \vec{E}/2 dx + \delta \left( \frac{1}{2} \rho_f(x) \phi(x) \right) dx \\ &\quad - \delta(TS_c) \end{aligned} \quad (\text{CI-7})$$

The following sections discuss the variations of the last 4 terms separately:

(B1) For the dipole interaction of  $(\text{Sr}_K^+ \text{V}_K^+)^*$  complexes with the electric field:

$$\begin{aligned}
 \text{We define } F_d &\equiv -\delta \int_0^L \sum_{i=1}^{12} m_i(x) \vec{p}_i \cdot \vec{E} / 2 \, dx \\
 &= \delta \int_0^L \sum_{i=1}^{12} m_i(x) \frac{p_{ix}}{2} \frac{d\phi}{dx} \, dx \\
 &= \int_0^L \frac{d\phi}{dx} \cdot \sum_{i=1}^{12} \frac{p_{ix}}{2} \delta m_i(x) \, dx \\
 &\quad + \int_0^L \sum_{i=1}^{12} \frac{p_{ix}}{2} m_i(x) \delta \left( \frac{d\phi}{dx} \right) \, dx \\
 &\equiv I_1 + I_2 \qquad \qquad \qquad (\text{CII-8})
 \end{aligned}$$

(B2) Similarly, for the dipole interaction of  $(V_K^i V_{Cl}^j)^*$  complexes with the electric field:

$$\begin{aligned}
 -\delta \int_0^L \sum_{j=1}^6 n_j(x) \vec{q}_j \cdot \vec{E}/2 \, dx &= \int_0^L \frac{d\phi}{dx} \sum_{j=1}^6 \frac{q_{jx}}{2} \delta n_j(x) \, dx \\
 &\quad + \int_0^L \sum_{j=1}^6 \frac{q_{jx}}{2} n_j(x) \delta \left( \frac{d\phi}{dx} \right) \, dx \\
 &\equiv J_1 + J_2 \quad (CII-9)
 \end{aligned}$$

(B3) For the electrostatic free energy term:

$$\begin{aligned}
 \text{Define } \delta F_e &\equiv \delta \int_0^L \frac{1}{2} \rho_f(x) \phi(x) \, dx \\
 &= \int_0^L \frac{1}{2} \rho_f(x) \delta \phi(x) \, dx + \int_0^L \frac{1}{2} \phi(x) \delta \rho_f(x) \, dx \\
 &= M + N \quad (CII-10)
 \end{aligned}$$

$$\begin{aligned}
 M &\equiv \int_0^L \frac{1}{2} \rho_f(x) \delta \phi \, dx \\
 &= \frac{-\epsilon}{8\pi} \int_0^L \frac{d^2 \phi}{dx^2} \delta \phi \, dx + \frac{1}{2} \int_0^L \frac{d}{dx} \left( \sum_{i=1}^{12} m_i p_{ix} + \sum_{j=1}^6 n_j q_{jx} \right) \delta \phi \, dx \\
 &= M_1 + M_2 \quad (CII-11)
 \end{aligned}$$

$$\begin{aligned}
 M_1 &\equiv \frac{-\epsilon}{8\pi} \int_0^L \frac{d^2 \phi}{dx^2} \delta \phi \, dx \\
 &= \frac{-\epsilon}{8\pi} \frac{d\phi}{dx} \delta \phi \Big|_0^L + \frac{\epsilon}{8\pi} \int_0^L \left( \frac{d\phi}{dx} \right) \frac{d\phi}{dx} \, dx \quad (CII-12a)
 \end{aligned}$$

after integration by parts.

For fixed potentials at the surface and in the bulk,

$$\delta\phi(0) = \delta\phi(L) = 0$$

$$\begin{aligned} \therefore M_1 &= \frac{\epsilon}{8\pi} \int_0^L \delta\left(\frac{d\phi}{dx}\right) \frac{d\phi}{dx} dx \\ &= \frac{\epsilon}{8\pi} \phi(x) \delta\left(\frac{d\phi}{dx}\right) \Big|_0^L - \frac{\epsilon}{8\pi} \int_0^L \phi(x) \delta\left(\frac{d^2\phi}{dx^2}\right) dx \quad (\text{CII-12b}) \end{aligned}$$

again after integration by parts.

We define  $\frac{d\phi}{dx} = 0$  in the bulk,  $L$ , due to the symmetry of the crystal.

$$\begin{aligned} M_1 &= -\frac{\epsilon}{8\pi} \phi(x) \delta\left(\frac{d\phi}{dx}\right) \Big|_0^L - \frac{\epsilon}{8\pi} \int_0^L \phi(x) \delta\left(\frac{d^2\phi}{dx^2}\right) dx \\ &= -\frac{\epsilon}{8\pi} \phi(x) \delta\left(\frac{d\phi}{dx}\right) \Big|_0^L - \frac{1}{8\pi} \int_0^L \phi(x) \left[ 4\pi \frac{d}{dx} \left( \sum_{i=1}^{12} p_{ix} \delta m_i + \sum_{j=1}^6 q_{jx} \delta n_j \right) \right. \\ &\quad \left. - 4\pi \delta \rho_f(x) \right] dx \quad (\text{CII-12c}) \end{aligned}$$

Since  $-\epsilon \frac{d\phi}{dx} \Big|_0^L + 4\pi \left( \sum_{i=1}^{12} p_{ix} m_i + \sum_{j=1}^6 q_{jx} n_j \right) \Big|_0^L = 4\pi \int_0^L \rho_f dx$

$$\begin{aligned} \therefore \epsilon \frac{d\phi}{dx} \Big|_{x=0} &= \int_0^L 4\pi \rho_f dx - 4\pi \left( \sum_{i=1}^{12} p_{ix} m_i(x) + \sum_{j=1}^6 q_{jx} n_j(x) \right) \Big|_0^L \\ &= \int_0^L 4\pi \rho_f dx + 4\pi \left( \sum_{i=1}^{12} p_{ix} m_i(0) + \sum_{j=1}^6 q_{jx} n_j(0) \right) \quad (\text{CII-13}) \end{aligned}$$

and we assumed that there is no net polarization term in the

bulk, 
$$\sum_{i=1}^{12} p_{ix} m_i(L) = \sum_{j=1}^6 q_{jx} n_j(L) = 0$$

$$\begin{aligned} M_1 = & -\frac{1}{2} \int_0^L \phi(0) \delta \rho_f(x) dx - \frac{1}{2} \phi(0) \delta \left( \sum_{i=1}^{12} p_{ix} m_i(0) + \sum_{j=1}^6 q_{jx} n_j(0) \right) \\ & + \frac{1}{2} \int_0^L \phi(x) \delta \rho_f(x) dx - \frac{1}{2} \int_0^L \phi(x) \frac{d}{dx} \left( \sum_{i=1}^{12} p_{ix} \delta m_i + \sum_{j=1}^6 q_{jx} \delta n_j \right) dx \end{aligned}$$

(CII-14a)

Since 
$$\int_0^L \phi(x) \frac{d}{dx} \left[ \sum_{i=1}^{12} p_{ix} \delta m_i + \sum_{j=1}^6 q_{jx} \delta n_j \right] dx$$

$$= \phi(x) \left( \sum_{i=1}^{12} p_{ix} \delta m_i + \sum_{j=1}^6 q_{jx} \delta n_j \right) \Big|_0^L - \int_0^L \left( \sum_{i=1}^{12} p_{ix} \delta m_i + \sum_{j=1}^6 q_{jx} \delta n_j \right) \frac{d\phi}{dx} dx$$

$$\therefore M_1 = \frac{1}{2} \int_0^L [\phi(x) - \phi(0)] \delta \rho_f(x) dx + \frac{1}{2} \int_0^L \left( \sum_{i=1}^{12} p_{ix} \delta m_i + \sum_{j=1}^6 q_{jx} \delta n_j \right) \frac{d\phi}{dx} dx$$

(CII-14 b)

$$\begin{aligned}
M_2 &\equiv \frac{1}{2} \int_0^L \frac{d}{dx} \left( \sum_{i=1}^{12} m_i p_{ix} + \sum_{j=1}^6 n_j q_{jx} \right) \delta \phi \, dx \\
&= \frac{1}{2} \left( \sum_{i=1}^{12} m_i p_{ix} + \sum_{j=1}^6 n_j q_{jx} \right) \delta \phi \Big|_0^L - \frac{1}{2} \int_0^L \left( \sum_{i=1}^{12} m_i p_{ix} + \sum_{j=1}^6 n_j q_{jx} \right) \frac{d \delta \phi}{dx} \, dx \\
&= -\frac{1}{2} \int_0^L \left( \sum_{i=1}^{12} m_i p_{ix} + \sum_{j=1}^6 n_j q_{jx} \right) \frac{d \delta \phi}{dx} \, dx \quad (CII-15)
\end{aligned}$$

$$\begin{aligned}
\delta F_e &= M + N \\
&= M_1 + M_2 + N \\
&= \frac{1}{2} \int_0^L (\phi(x) - \phi(0)) \delta \rho_f(x) \, dx - \frac{1}{2} \int_0^L \left( \sum_{i=1}^{12} p_{ix} \delta m_i + \sum_{j=1}^6 q_{jx} \delta n_j \right) \frac{d \phi}{dx} \, dx \\
&\quad - \frac{1}{2} \int_0^L \left( \sum_{i=1}^{12} m_i p_{ix} + \sum_{j=1}^6 n_j q_{jx} \right) \frac{d \phi}{dx} \, dx + \int_0^L \frac{1}{2} \phi(x) \delta \rho_f \, dx \\
&\hspace{15em} (CII-16)
\end{aligned}$$

Since we assign an arbitrary potential,  $\phi(0)$ , at the crystal surfaces, we have to include an electrostatic energy term,  $F_s$ , due to this surface potential and on the surface free charge,  $\sigma_s$ ,

$$\begin{aligned}
\delta F_s &= \delta \frac{1}{2} \phi(0) \sigma_s \\
&= -\frac{1}{2} \phi(0) \delta \int_0^L \rho_f \, dx \quad (CII-17)
\end{aligned}$$

Consequently, the total electrostatic energy,  $Fe_{tot}$ , due to the free charges,  $\delta Fe_{tot} = \delta Fe + \delta Fs$

$$= \int_0^L (\phi(x) - \phi(0)) \delta \rho_f dx - \frac{1}{2} \int_0^L \left( \sum_{i=1}^{12} m_i p_{ix} + \sum_{j=1}^6 n_j q_{jx} \right) \delta \left( \frac{d\phi}{dx} \right) dx \\ + \frac{1}{2} \int_0^L \left( \sum_{i=1}^{12} p_{ix} \delta m_i + \sum_{j=1}^6 q_{jx} \delta n_j \right) \frac{d\phi}{dx} dx \quad (CII-18)$$

We also note that only the potential difference with respect to the crystal surfaces appears in the expression of the crystal free energy, therefore a choice of zero surface potential,  $\phi(0) \equiv 0$ , results in no loss of generality.

(B3) The variation of the entropy term,  $Sc$ , is similar to the case discussed in Kliever and Koehler (1965). However, since the dipoles with different orientations,  $p_i$  or  $q_j$ , are considered as separate entities, the potassium vacancy must be in the unique nearest neighbor position of the Sr ion in order to form a  $(Sr_K V'_K)^*$  dihole of a specific moment. Similarly, a potassium vacancy must be in the unique nearest neighbor position of a chlorine vacancy to form a  $(V'_K V''_{Cl})^*$  dipole of a specific moment. With this consideration and based on the work of Kliever and Koehler (1965),

$$\delta Sc = k \int_0^L dx \left[ \delta n_f \ln(N/n_f) + \sum_{i=1}^{12} \delta m_i \ln(N/m_i) + \sum_{j=1}^6 \delta n_j \ln(N/n_j) \right. \\ \left. + \delta n_+ \ln(N/n_+) + \delta n_- \ln(N/n_-) \right] \quad (CII-19)$$



with the usual assumption of low impurities and defects concentrations,  $(n_f, m_1, m_2, n_+, n_-) \ll N$ , where  $N$  is the density of anion or cation sites in the crystal.

(F) Consequently, the variation of the crystal free energy can be expressed in terms of the variations of the 21 independent variables,  $n_f, m_1, m_2, \dots, m_{12}, n_1, n_2, \dots, n_6, n_+$  and  $n_-$ .

$$\begin{aligned}
 \delta F = & \int_0^L \sum_{i=1}^{12} \left( F_i^+ B_i + p_i \frac{d\phi}{dx} - kT \ln \left( \frac{N}{m_i} \right) + \alpha \right) \delta m_i(x) dx \\
 & + \int_0^L \sum_{j=1}^6 \left( F_j^+ F_j^- B + q_j x \frac{d\phi}{dx} - kT \ln \left( \frac{N}{n_j} \right) \right) \delta n_j(x) dx \\
 & + \int_0^L \left( e\phi + \alpha - kT \ln \frac{N}{n_f} \right) \delta n_f dx \\
 & + \int_0^L \left( F^- + e\phi - kT \ln \frac{N}{n_-} \right) \delta n_- dx \\
 & + \int_0^L \left( F^+ - e\phi - kT \ln \frac{N}{n_+} \right) \delta n_+ dx \quad (\text{CII-20})
 \end{aligned}$$

where  $\alpha$ , the Lagrange multiplier, is introduced for the conservation of impurity atoms.

The minimization of the free energy will assign  $\delta F$  to be

zero and we obtain the corresponding relations for the independent variables of the defects and impurities concentrations:

$$\frac{m_i}{N} = \exp[-(F^+ - B_+ + p_{ix} \frac{d\phi}{dx} + \alpha)/kT] \quad (\text{CII-21})$$

$$\frac{n_j}{N} = \exp[-(F^+ + F^- - B + q_{jx} \frac{d\phi}{dx})/kT] \quad (\text{CII-22})$$

$$\frac{n_f}{N} = \exp[-(\phi + \alpha)/kT] \quad (\text{CII-23})$$

$$\frac{n_+}{N} = \exp(-(F^+ - \phi)/kT) \quad (\text{CII-24})$$

$$\frac{n_-}{N} = \exp(-(F^- + \phi)/kT) \quad (\text{CII-25})$$

For a grain boundary normal in the (100) direction, a third of  $(\text{Sr}_K^+ \text{V}_K^-)$  dipole vectors have  $p_{ix} = ea/2$ , another third have  $p_{ix} = -ea/2$ , and the rest have  $p_{ix} = 0$ . We define  $m_1$  for the concentration of dipoles with  $p_{ix} = -ea/2$ ,  $m_2$  for  $p_{ix} = 0$ , and  $m_3$  for  $p_{ix} = ea/2$ . Thus Poisson's equation, Eq. (C-26) is simplified to

$$\left[ 1 + \frac{8\pi Ne^2}{\epsilon kT} \frac{a^2}{4} \frac{C_{\infty p_{\infty}}}{3} 2 \cosh\left(\frac{a}{2\delta} \frac{dz}{dS}\right) \right] \frac{d^2 z}{dS^2} = \sinh z \quad (\text{CII-26})$$

where the reduced distance  $S$  is given as

$$S \equiv x/\delta \quad (\text{CII-27})$$

$$\delta \equiv \left[ \frac{8\pi Ne^2}{\epsilon kT} \exp(-(F^+ - e\phi_{\infty})/kT) \right]^{-\frac{1}{2}} \quad (\text{CII-28})$$

and the reduced potential,  $Z$ , is given as

$$Z \equiv (e\phi - e\phi_{\infty})/kT \quad (\text{CII-29})$$

and the bulk potential,  $e\phi_{\infty}$ , is defined from the condition of charge neutrality in the bulk,

$$(1 - p_{\infty})C_{\infty} + \exp(-(F^{-} + e\phi_{\infty})/kT) - \exp(-(F^{+} - e\phi_{\infty})/kT) = 0 \quad (\text{CII-30})$$

The bulk potential,  $e\phi_{\infty}$ , and the Debye length,  $\delta$ , are similar to those defined in Kliever and Koehler (1965).

The numerical solutions of Eq. (C-27) for the space charge potential and the space charge electric field were performed. It was shown in Fig. (V-5), that the space charge electric field,  $E$ , when corrected for the dipole interactions is not significantly different from that derived in Kliever and Koehler (1965), in which the dipole interactions are neglected. However, the distributions of  $(\text{Sr}_K^{\cdot} \text{V}_K^{\cdot})^*$  dipoles, namely  $m_1$  and  $m_3$ , each with a net dipole moment resolved in the electric field direction, are non-uniform in the grain boundary region, Fig. (V-6).

With the dipole-field interaction, the net concentration of vacancy-impurity dipole complexes is always enhanced. The integrated enhancement,  $\Delta m$ , over both sides of the grain boundary region is given as

$$\Delta m = 2 \frac{C_{\infty} p_{\infty}}{3} \int_0^{\infty} \left\{ \left( \exp\left(\frac{ea}{2} \frac{d\phi}{dx}/kT\right) - 1 \right) + \left( \exp\left(-\frac{ea}{2} \frac{d\phi}{dx}/kT\right) - 1 \right) \right\} dx \quad (\text{CII-31})$$

$> 0$

Appendix C-III: Evaluation of the Quantities  $\alpha$  and  $\beta$

The quantities  $\alpha$  and  $\beta$  are evaluated in this appendix. According to Cahn (1962),

$$\alpha \equiv 4kTN_v \int_{-\infty}^{\infty} \frac{\sinh^2(U/2kT)}{D(x)} dx \quad (\text{CIII-1})$$

$$\frac{\alpha}{\beta^2} \equiv \frac{N_v}{kT} \int_{-\infty}^{\infty} \left( \frac{dU}{dx} \right)^2 D(x) dx \quad (\text{CIII-2})$$

For  $U \equiv e\phi - e\phi_{\infty}$  (CIII-3)

and  $D \equiv \frac{D_0 p_{\infty}}{p_{\infty} + (1-p_{\infty}) \exp(-\frac{e\phi - e\phi_{\infty}}{kT})}$  (CIII-4)

With the definitions of  $Z = (e\phi - e\phi_{\infty})/kT$  ;  $S = X/\delta$  and

$$\delta = \left[ \frac{\epsilon kT}{8\pi N e^2} \exp\left(\frac{F - e\phi_{\infty}}{kT}\right) \right]^{1/2} \quad \text{we get}$$

$$\alpha = 4N_v kT \int_{-\infty}^{\infty} \frac{\sinh^2 Z/2 \{p_{\infty} + (1-p_{\infty})e^{-Z}\}}{D_0 p_{\infty}} dx$$

$$= \frac{8kT\delta N_v}{D_0 p_\infty} \int_0^\infty \sinh^2(z/2) \{p_\infty + (1-p_\infty)e^{-z}\} dz$$

$$= -\frac{8kT\delta N_v}{D_0 p_\infty} \int_{-e\phi_0/kT}^0 \frac{\sinh^2(z/2) \{p_\infty + (1-p_\infty)e^{-z}\}}{2 \sinh z/2} dz$$

$$= \frac{4kTN_v\delta}{D_0 p_\infty} \left[ p_\infty (\exp(-\frac{e\phi_0}{2kT}) - 1) - (1-2p_\infty) (\exp(\frac{e\phi_0}{2kT}) - 1) + \frac{(1-p_\infty)}{3} (\exp(\frac{3e\phi_0}{2kT}) - 1) \right] \quad (\text{CIII-5})$$

$$= \alpha$$

Similarly,

$$\frac{\alpha}{\beta^2} = -kTN_v \left( \frac{D_0 p_\infty}{\delta} \right) 4 \left\{ \frac{1}{p_\infty^2} \left[ p_\infty (1 - \exp(-\frac{e\phi_0}{kT})) + (1-p_\infty) \ln((1-p_\infty) + p_\infty \exp(-\frac{e\phi_0}{kT})) \right] + \frac{1}{\sqrt{p_\infty(1-p_\infty)}} \left[ \tan^{-1} \sqrt{\frac{p_\infty}{1-p_\infty}} - \tan^{-1} \left( \sqrt{\frac{p_\infty}{1-p_\infty}} \exp(-\frac{e\phi_0}{2kT}) \right) \right] \right\} \quad (\text{CIII-6})$$

## C.8 References

- Cahn, J. W., (1972), "The Impurity-Drag Effect in Grain Boundary Motion," *Acta. Met.*, 10, 789.
- Class, W. H. and Machlin, E. S., (1966), "Crack Propagation Method for Measuring Grain Boundary Energies in Brittle Materials," *J. Am. Ceram. Soc.*, 49, 306.
- Gibbon, C. F., (1968), "Technique for Measuring Grain Boundary Mobility and its Application to Potassium Chloride," *J. Am. Ceram. Soc.*, 51, 273.
- Gordon, P. and Vendermeer, R. A., (1966), "Grain Boundary Migration," in Recrystallization, Grain Growth and Texture, A.S.M., Metals Park, Ohio, p. 205
- Johnson, W. C., Stein, D. F. and Rice, R. W. (1974), *Proceedings of the Fourth Bolton Landing Conference*.
- Kitazawa, K., (1974), Private Communication.
- Kitazawa, K., (1975), Private Communication.
- Kliwer, K. L. and Keohler, J. S., (1965), "Space Charge in Ionic Crystals, I: General Approach with Application to NaCl," *Phys. Rev.*, 140, A, 1226.
- Koepke, B. G., Anderson, R. H., Bernal G., E. and Stokes, R. J., (1974), "Room Temperature Grain Growth in Potassium Chloride," *J. Appl. Phys.*, 45, 969.
- Lidiard, A. B., (1955), "Impurity Diffusion in Crystals (Mainly Ionic Crystals with the Sodium Chloride Structure)," *Phil. Mag.*, 46, 1218.
- Lücke, K. and Stüwe, H.P., (1962), "On the theory of Grain Boundary Motion," in Recovery and Recrystallization of Metals, Ed. L. Himmel, AIME Symposium, Feb. 1962.
- McLean, D. (1951), "Grain Boundaries in Metals," Clarendon Press.
- Sun, R. C. and Bauer, C. L., (1970a), "Tilt Boundary Migration in NaCl Bicrystals," *Acta Met.*, 18, 639.
- Yan, M. F., Cannon, R. M., Bowen, H. K. and Coble, R. L., (1974), *Proceedings of the Fourth Annual Conference on Infrared Laser Window Materials*, Eds. Andrews, C. R. and Strecker, C. L., p. 639.

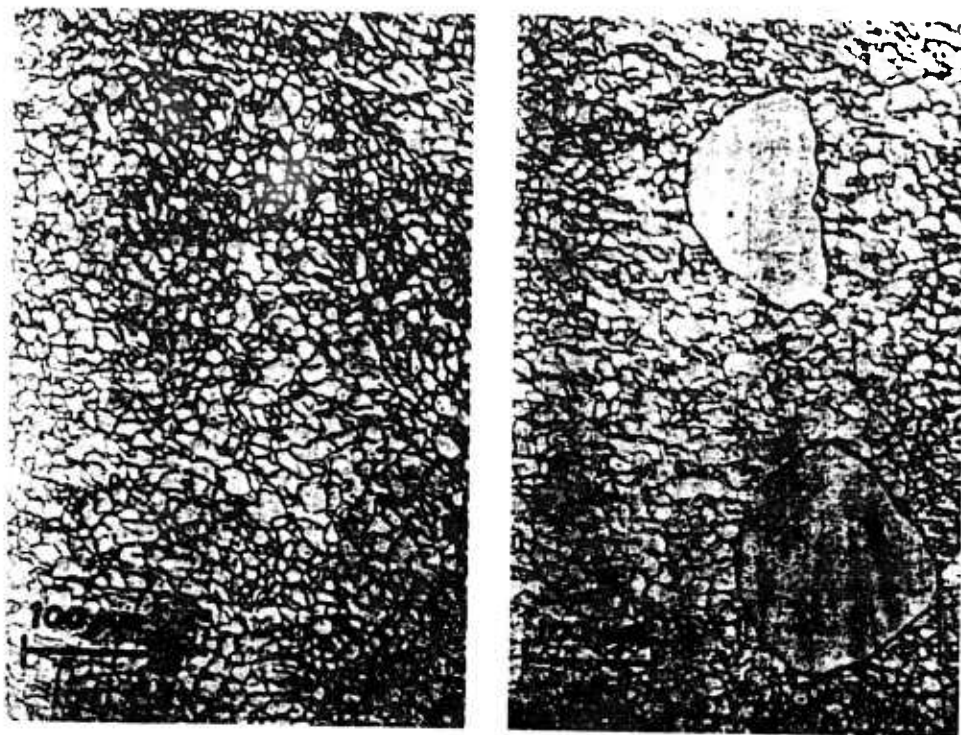


Figure C-1: Microstructures of hot-forged KCl 470 molar ppm  $\text{SrCl}_2$  in melt (a) before anneal and (b) after 1 hr anneal at  $448^\circ\text{C}$ .

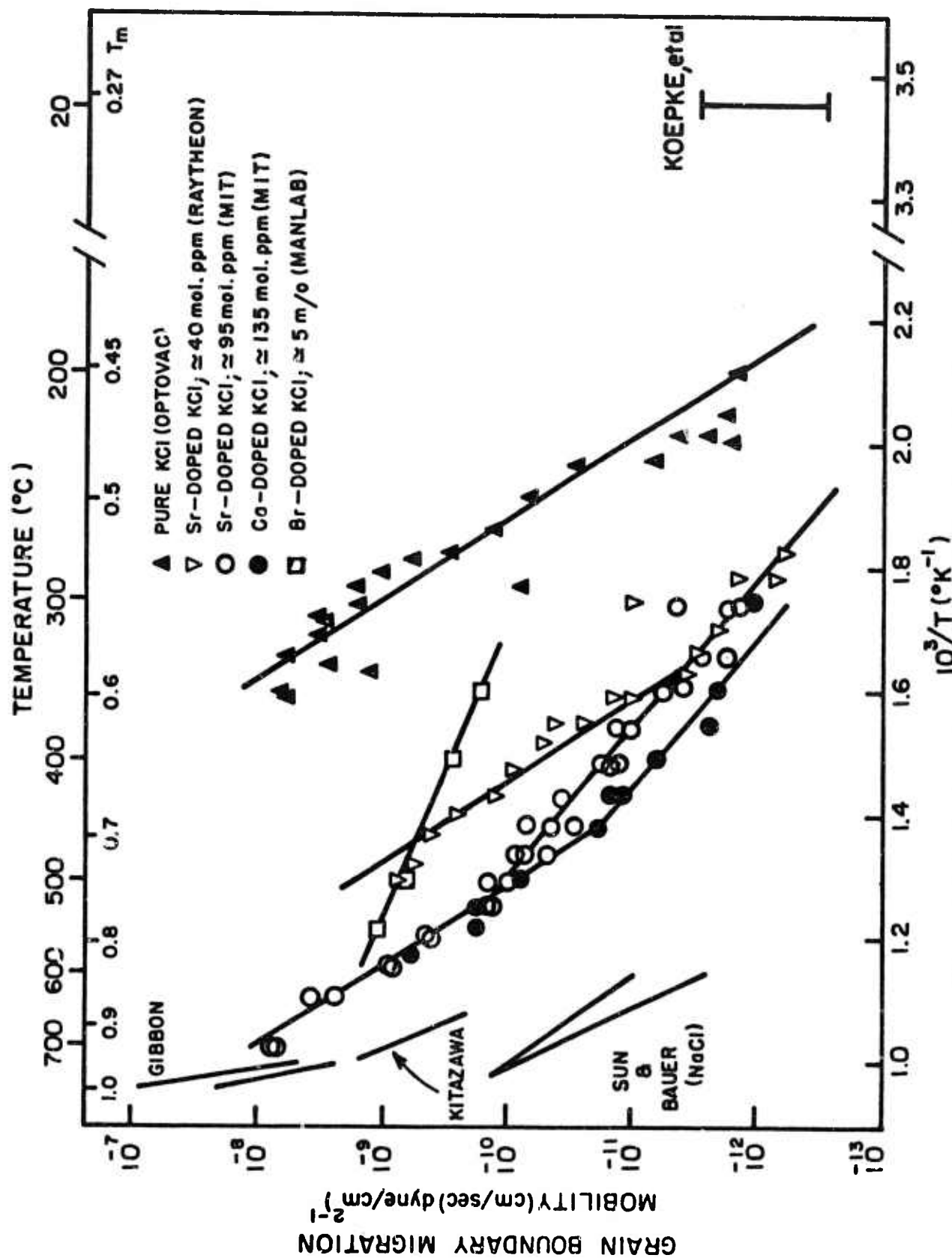


Figure C-2 Grain boundary mobility of hot forged KCl; sources of single crystal before forging are in parentheses. Typical driving force is about  $10^5$  dyne/cm<sup>2</sup> for mobility data in forged samples. Data of Gibbon (1968), Kitazawa (1974) are for KCl bicrystals; Koepke (1974), for hot forged KCl; Sun and Bauer (1970a) for NaCl bicrystals.



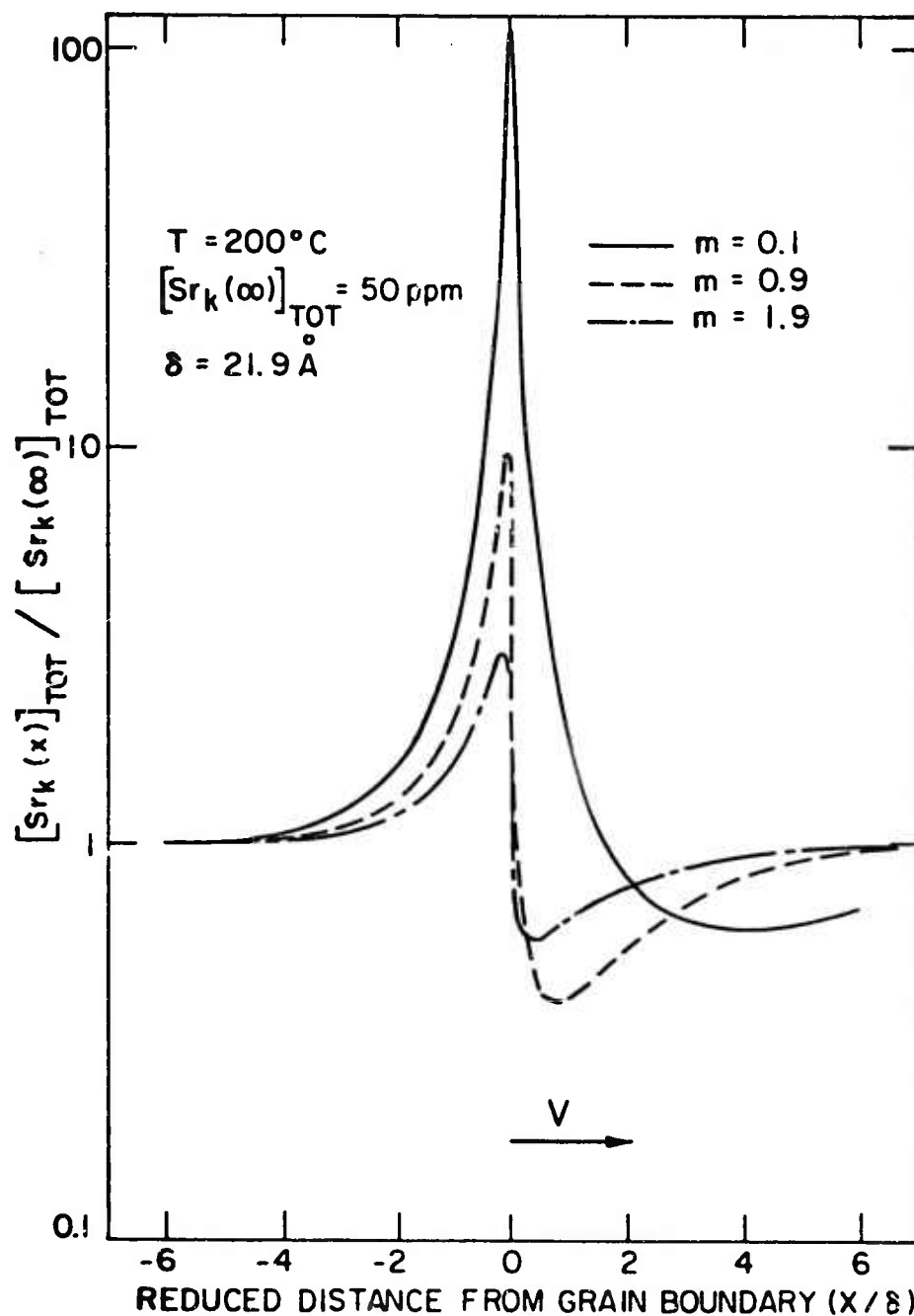


Figure C-3: Impurity distribution profiles in the neighborhood of a moving grain boundary.  $M$ , defined in Eq. (C-18c), is proportional to the boundary velocity. The impurity distribution profile becomes more asymmetrical as the velocity increases. At  $200^{\circ}\text{C}$ , which is below the isoelectric temperature, the boundary core is negatively charged and the impurity segregation occurs.

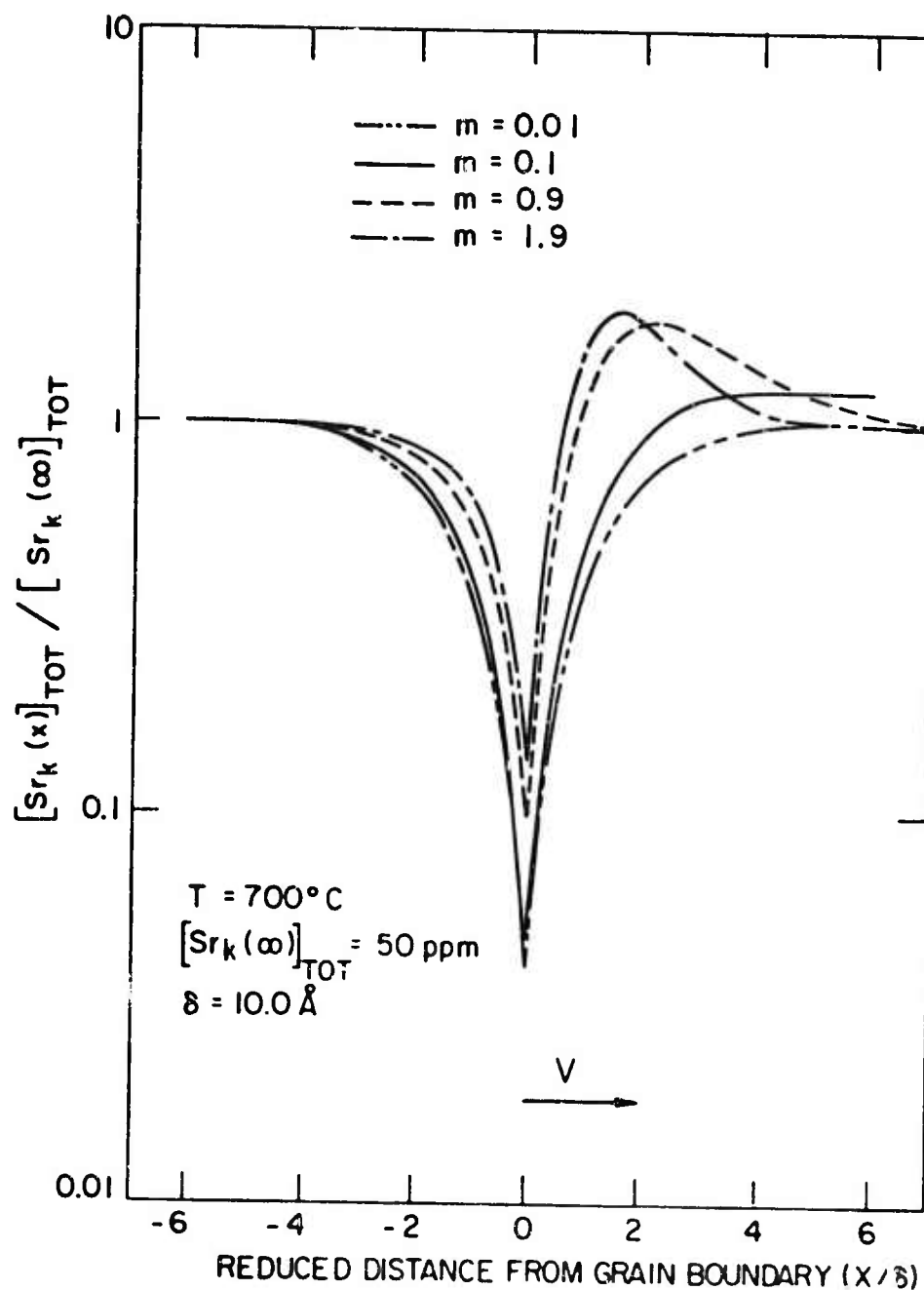


Figure C-4: Impurity distribution profiles in the neighborhood of a moving grain boundary.  $M$ , defined in Eq. (C-18c), is proportional to the boundary velocity. The impurity distribution profile becomes more asymmetrical as the velocity increases. At  $700^\circ\text{C}$ , which is above the isoelectric temperature, the boundary core is positively charged and the impurity is repulsed from the boundary.

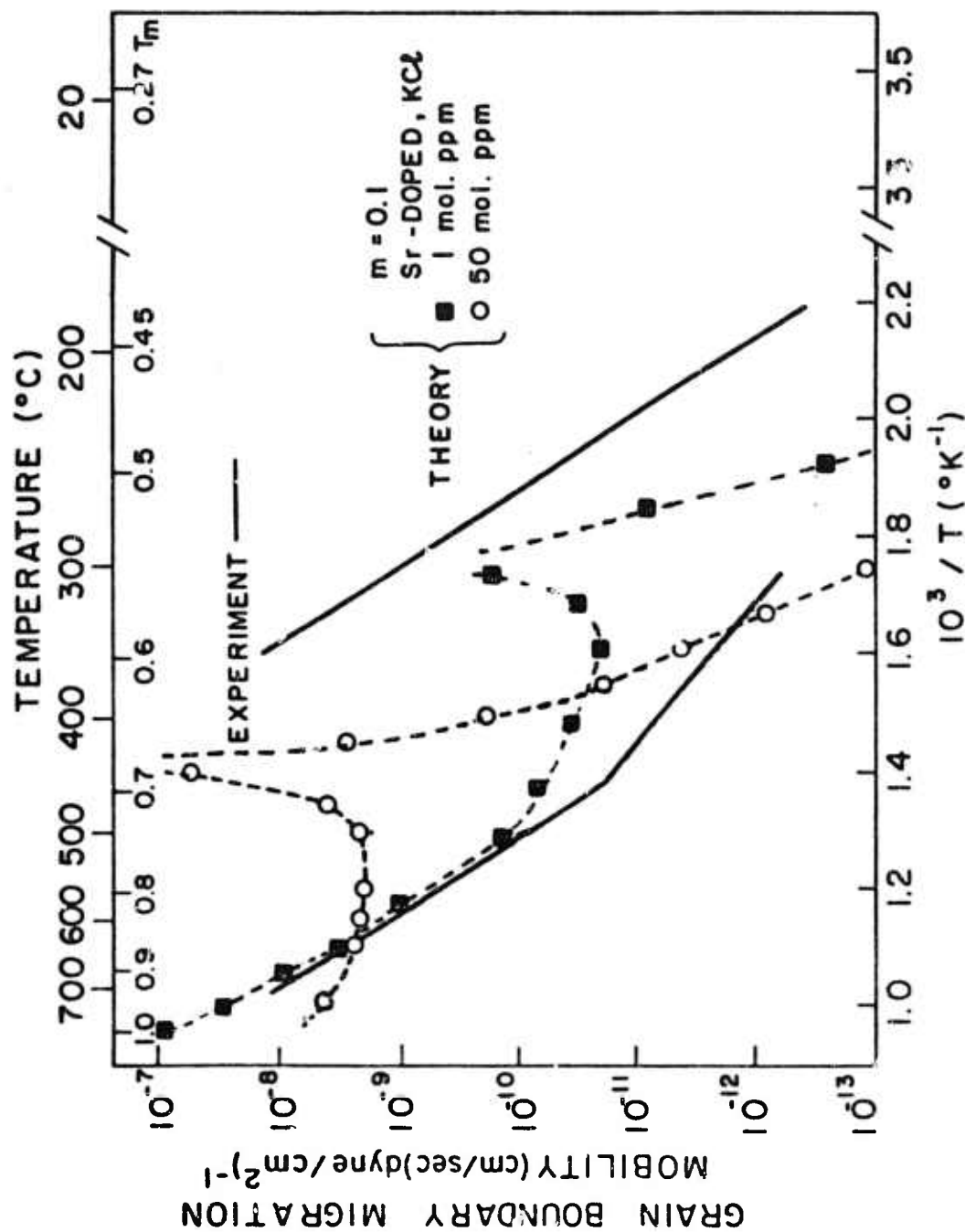


Figure C-5: Grain boundary mobility calculated from the impurity distribution profiles shown in Figs. C-3 and C-4.

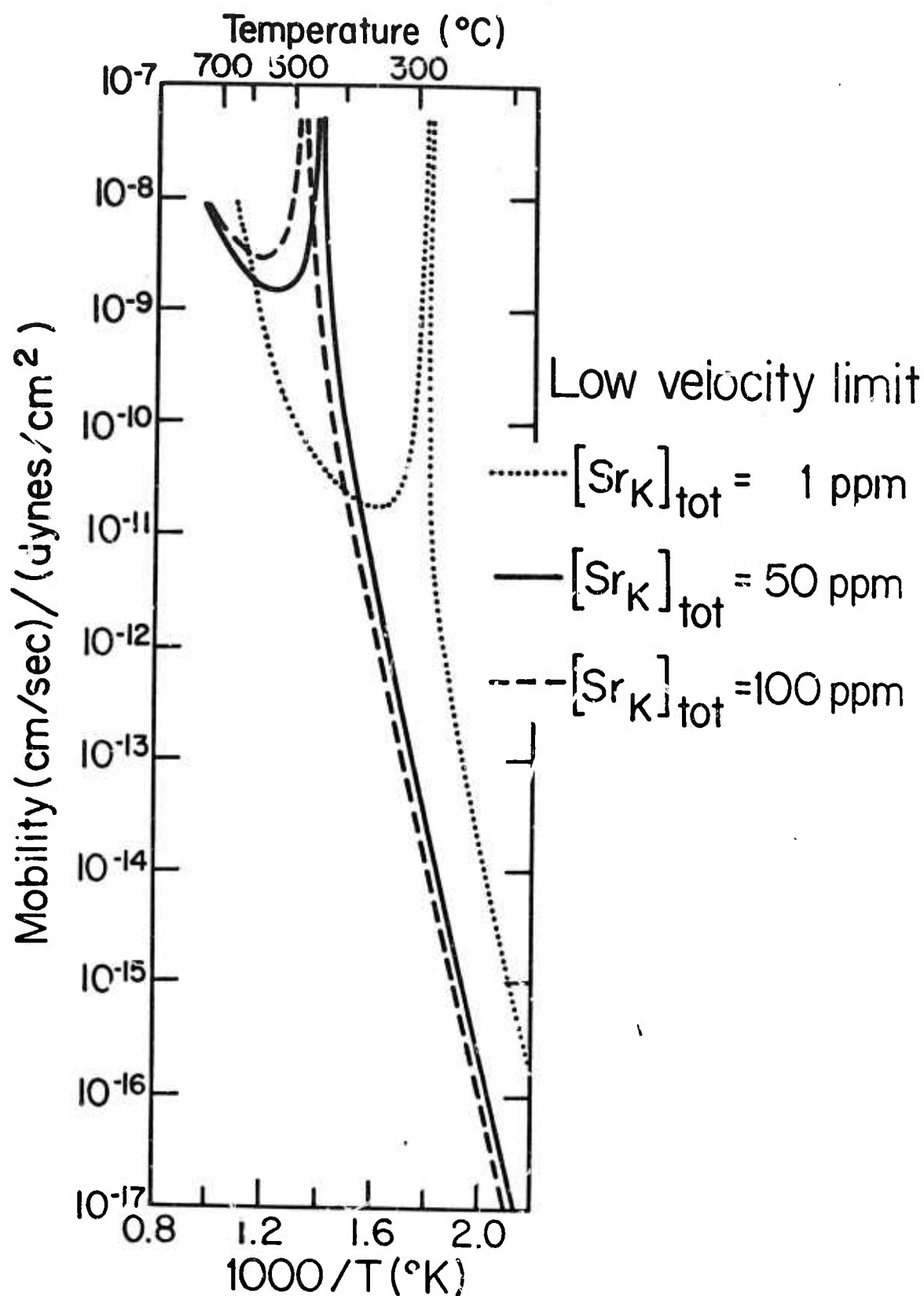


Figure C-6: Grain boundary mobility in the low velocity limit. The high mobilities at the isoelectric temperatures are due to the vanishing space charge potentials at these temperatures.

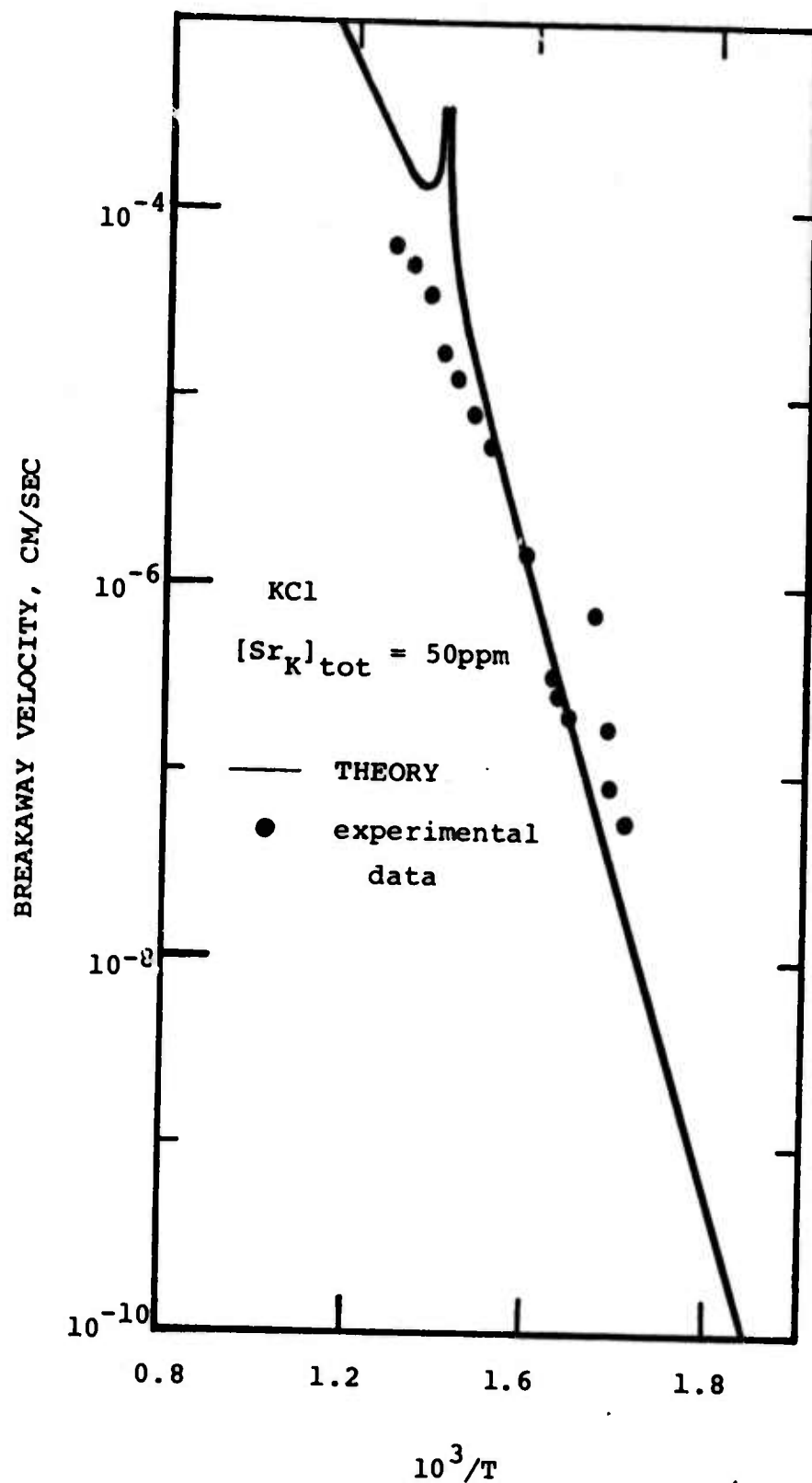


Figure C-7: The break-away velocity,  $\beta^{-1}$ , as calculated from Cahn's model.

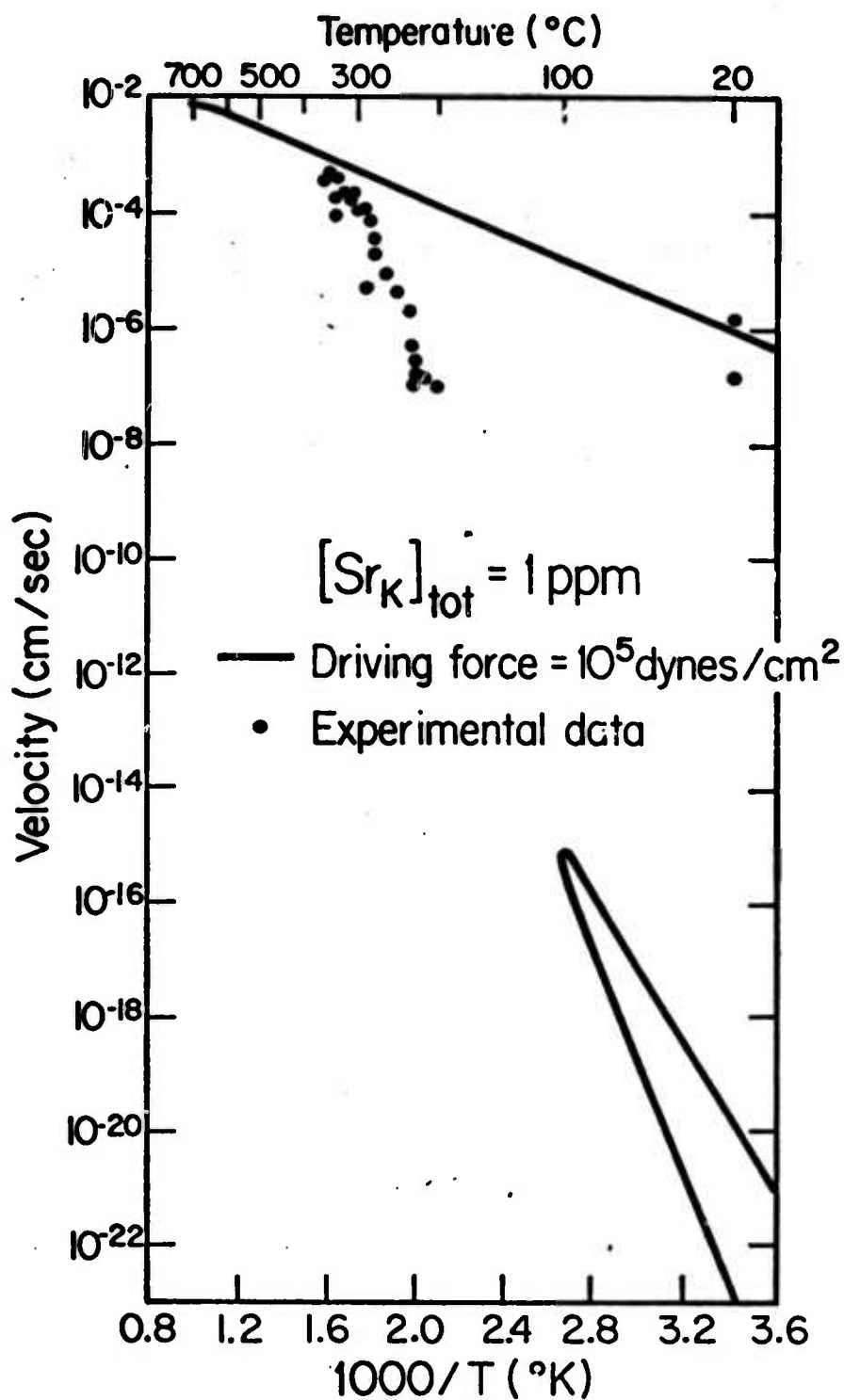


Figure C-8: The calculated grain boundary velocities under a driving force of 10<sup>5</sup> dyne/cm<sup>2</sup> in KCl with 1 ppm Sr impurity.

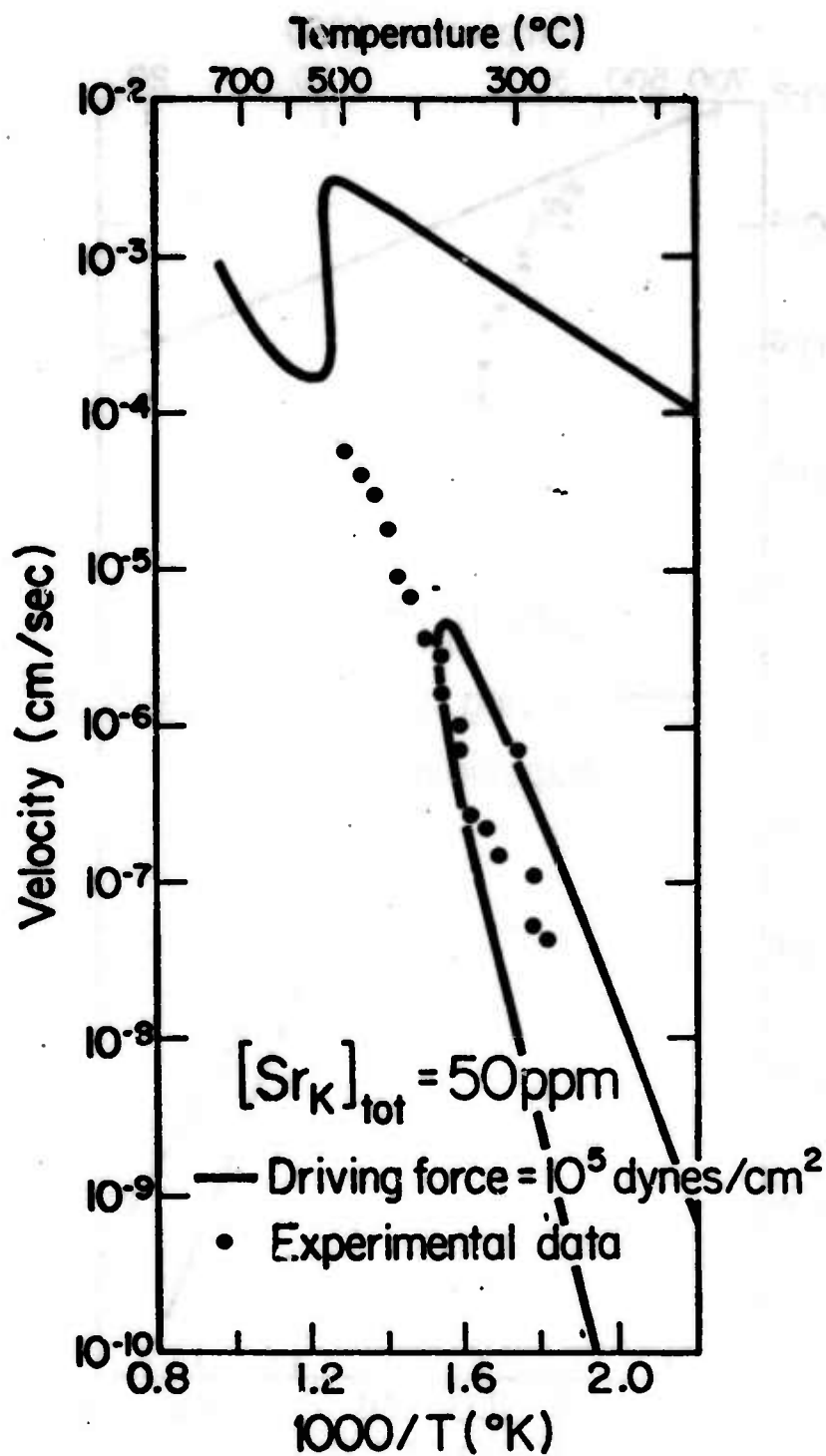


Figure C-9: The calculated grain boundary velocities under a driving force of  $10^5 \text{ dyne/cm}^2$  in KCl with 50 ppm Sr impurity.

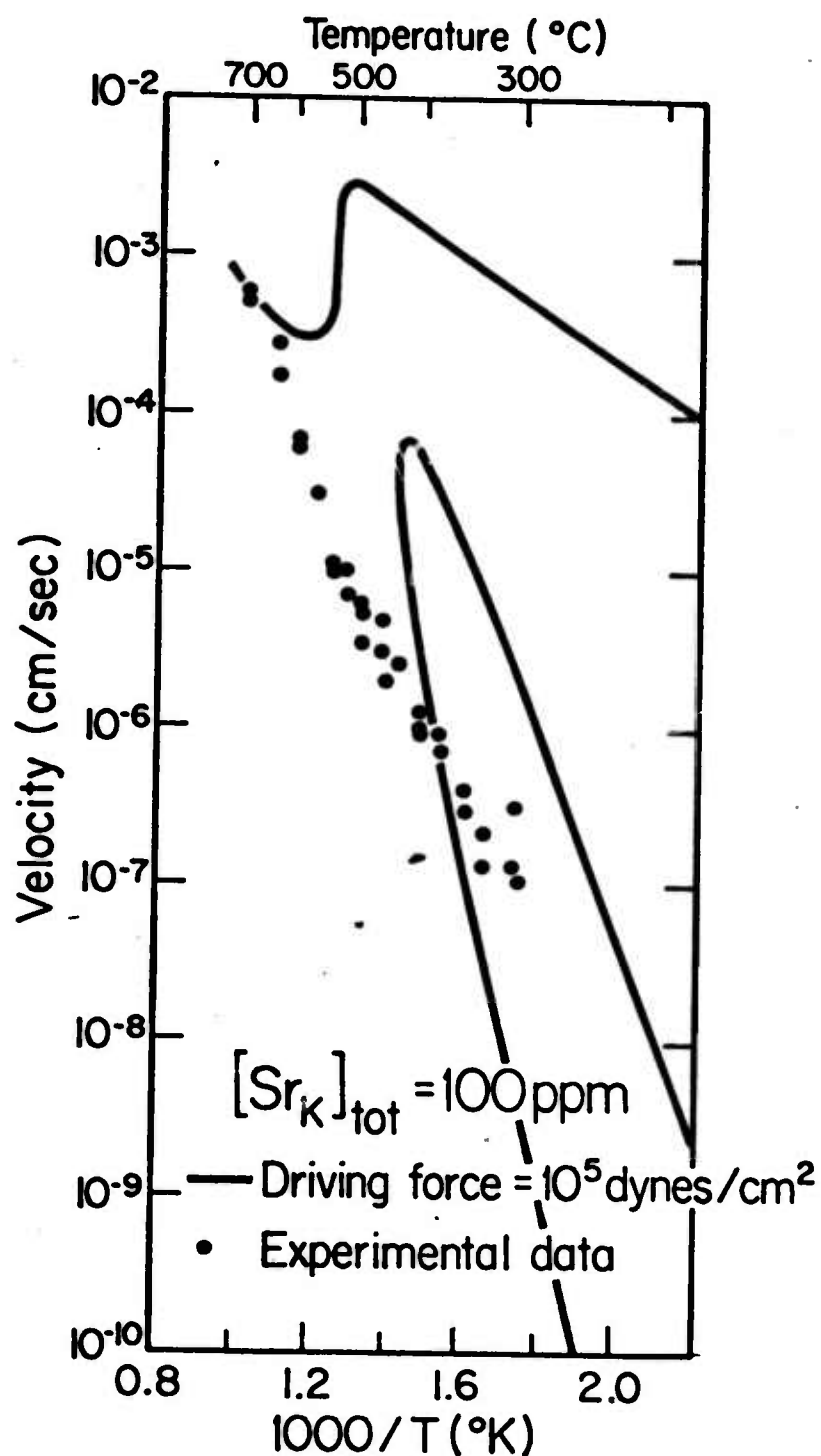


Figure C-10: The calculated grain boundary velocities under a driving force of  $10^5 \text{ dynes/cm}^2$  in KCl with 100 ppm Sr impurity.



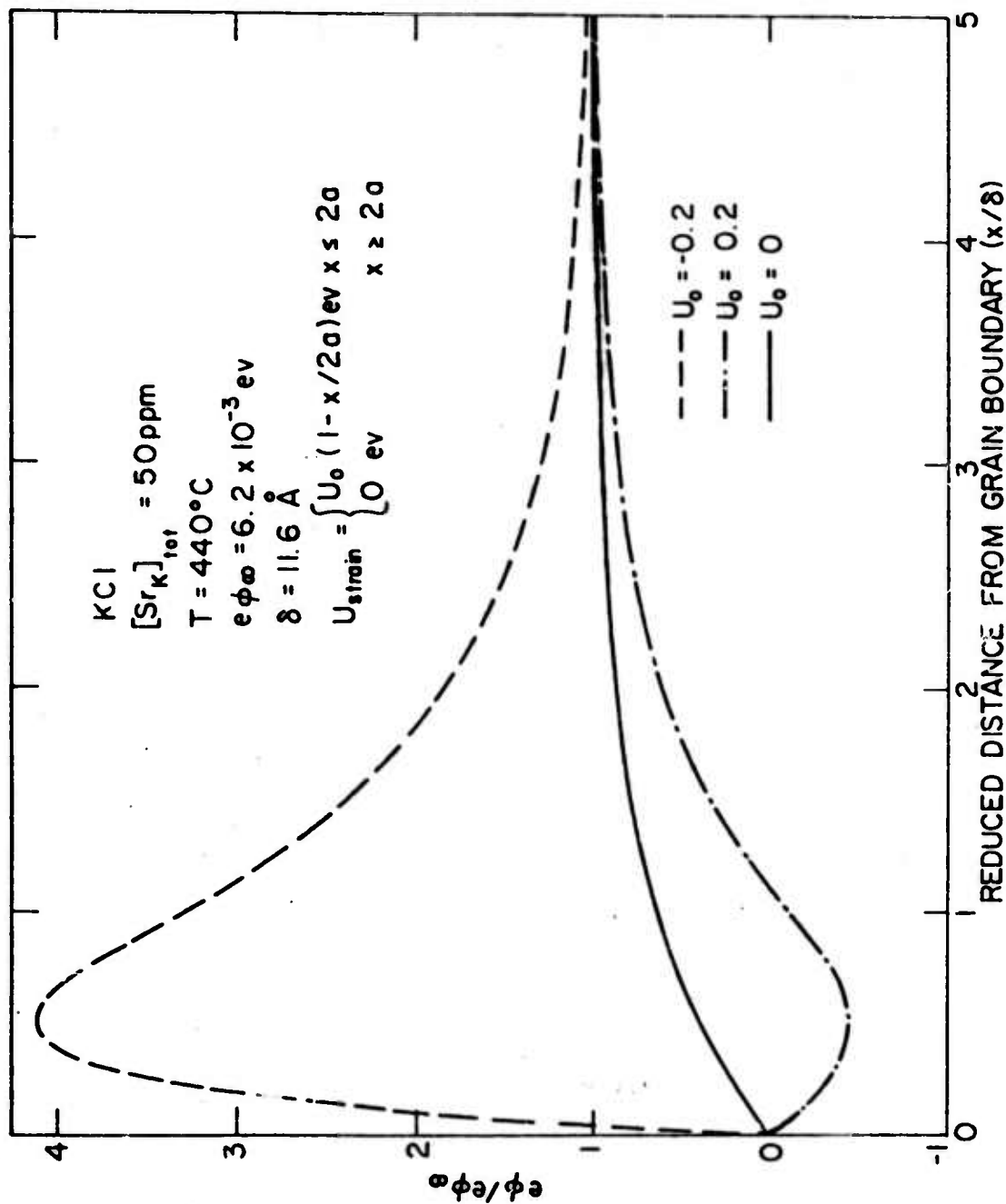


Figure C-11: Space charge potential distribution in the grain boundary region due to the impurity segregation which is originated from the strain field.

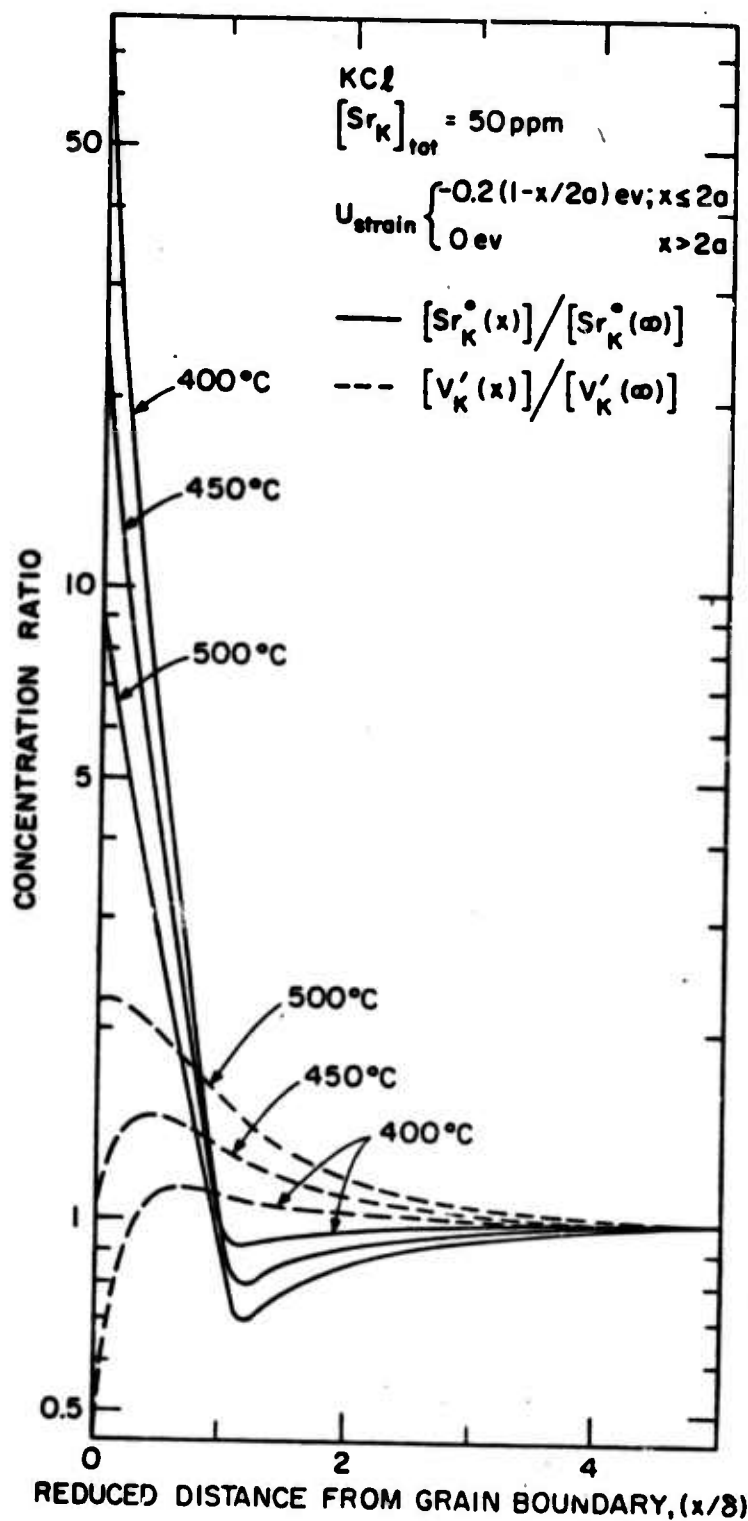


Figure C-12: Impurity and vacancy distributions in the grain boundary region due to the coupled effects of the electrostatic and strain field interactions between the impurity and the grain boundary.

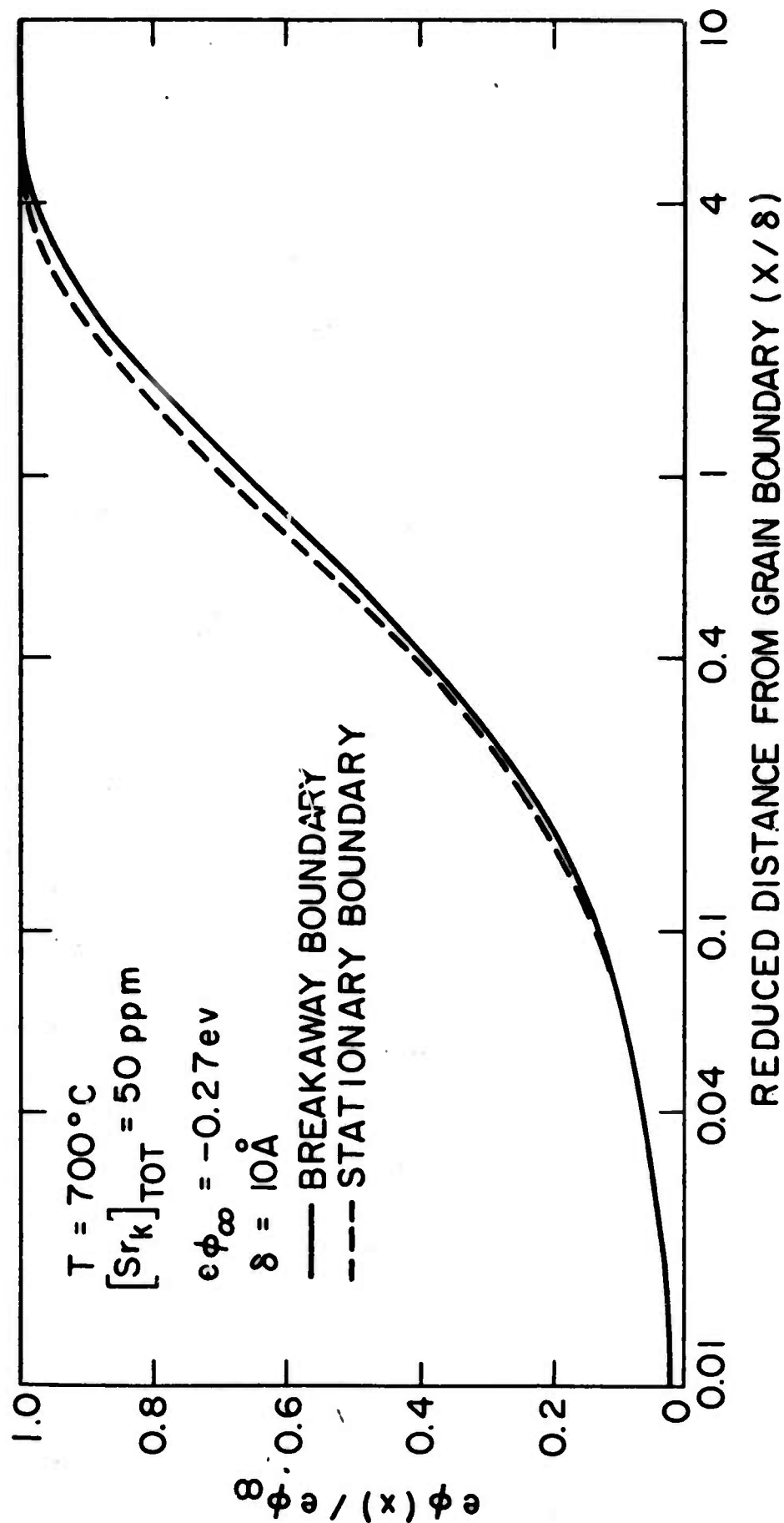


Figure C-I-1: The space charge potential distribution in a "break-away" grain boundary compared to the distribution in a stationary boundary. At temperatures above the isoelectric temperature, since most of the charge density is contributed by the vacancy, the velocity dependence of the space charge potential is negligible.

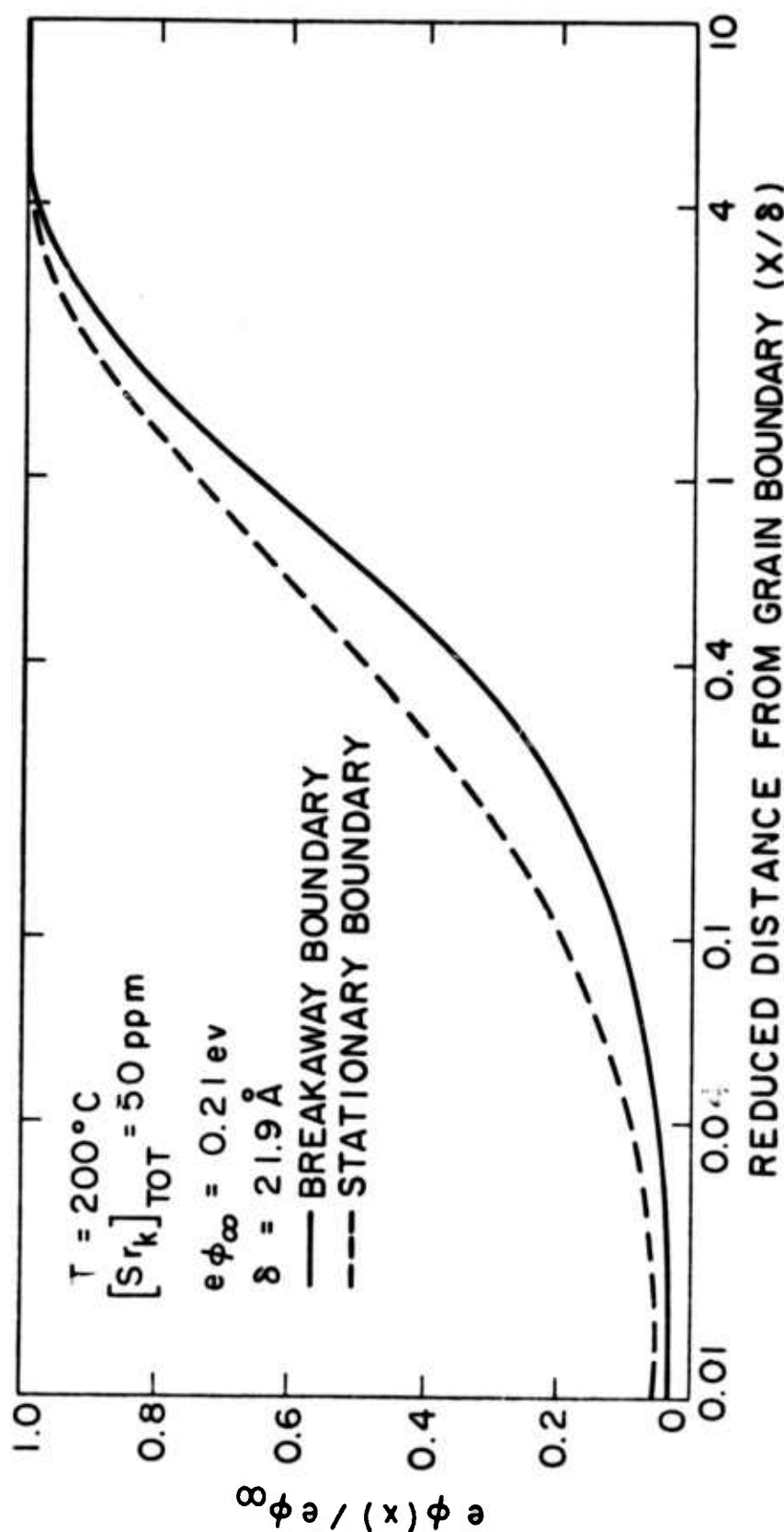


Figure C-I-2: The space charge potential distribution in a "break-away" grain boundary compared to the distribution in a stationary boundary. At temperatures below the isoelectric temperature, since most of the charge density is contributed by the impurity, the velocity dependence of the space charge potential is more pronounced.

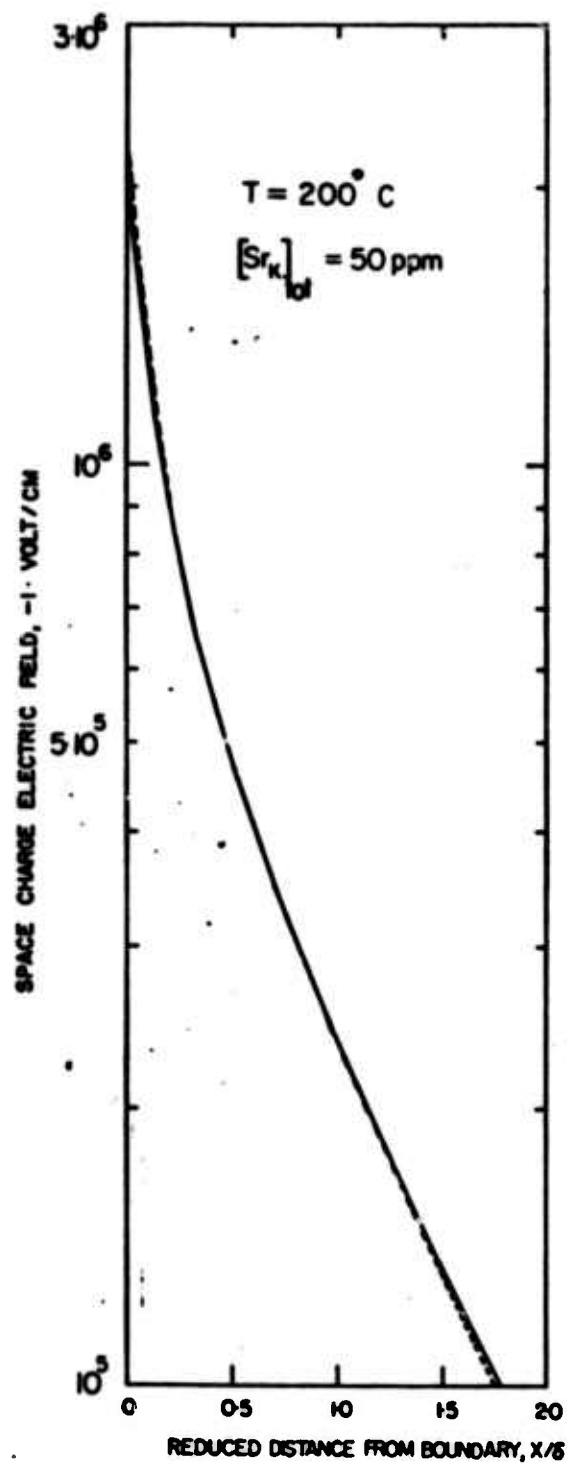


Figure C-II-1: Dipole interactions between impurity-vacancy complexes and the electric field have a negligible effect on the space charge electric field.

## D. SPACE CHARGE CONTRIBUTION TO GRAIN BOUNDARY DIFFUSION\*

M. F. Yan, R. M. Cannon, H. K. Bowen and R. L. Coble

### Abstract

The contributions of the space charge cloud to impurity and self diffusion in the grain boundary region of doped KCl are calculated and shown to be modest in magnitude ( $<10^3 D_i$ ) and limited in range (10 - 200 Å). Both enhancement and reduction in the charge cloud contribution to boundary diffusivities are predicted. Only for the ion on the sublattice opposite that of the principal impurity is appreciable diffusivity enhancement in the charge cloud ever indicated. Large boundary diffusion enhancements and wide boundary widths in "pure" and doped samples, often reported in the literature cannot be explained by the space charge contribution.

\*Work sponsored by Advanced Research Projects Agency through the Air Force Cambridge Research Laboratory (F19628-72-C-0304).

Accepted for publication by the American Ceramic Society.

## I. Introduction

The existence of space charge regions near lattice discontinuities (free surfaces, dislocations and grain boundaries) was first postulated by Frenkel<sup>1</sup>, and the charge distributions have been formulated by Frenkel<sup>1</sup>, Lehover<sup>2</sup>, Eshelby et al<sup>3</sup>, and Kliever and Koehler<sup>4</sup>. The conductance and diffusion in the space charge layer of alkali halides were considered by Lehover<sup>2</sup> and Burke<sup>5</sup>. In reviews by Kitazawa<sup>6</sup> and Kingery<sup>7</sup>, on preferential diffusion along grain boundaries and dislocations in ceramics, the possibilities of the space charge effects on diffusion were further discussed. Kinetic processes involving diffusion in the space charge regions have recently been studied; it was shown that the charge cloud of Sr ions accounts for most of the drag on a moving grain boundary of doped KCl<sup>8</sup>, and that the dislocation glide velocity in LiF at high temperature is controlled by the drag of the surrounding vacancy charge cloud.<sup>9</sup>

The purpose of this paper is to elucidate quantitatively the effects of the space charge cloud on diffusion in ionic materials. For illustrative purposes Sr and O impurity diffusion as well as K and Cl self diffusion in Sr and O doped KCl are studied in detail. The distributions of impurities and vacancies about grain boundaries as formulated by Kliever and Koehler<sup>4</sup>, are used in the calculations of the diffusivities in the space charge cloud.

## II. Theory

### (1) Formal Theory:

In ionic materials with predominantly Schottky type defects, e.g. KCl, both the impurity ions and the matrix ions diffuse only by associating with vacancies on the same sublattice. The diffusive flux of the ions,  $J$ , is the same as the flux of the associated vacancy-ion complexes,  $J_{\text{complex}}$ .

For a gas exchange tracer diffusion experiment in a semi-infinite bicrystal, as shown in Fig. 1, a uniform chemical potential is maintained in the bicrystal sample by keeping the same vapor pressure of the chemical species of the diffusing ions on both sides of the sample,  $y = 0$  and  $y = L$ . However, if the vapor phase at  $y < 0$  consists of the tracer isotope and the vapor phase at  $y > L$  consists of the major isotope, there exist concentration gradients of both isotopes parallel to the grain boundary in the bicrystal sample.

For simplicity, we treat the space charge effects only in the grain boundary region and neglect those at the surfaces. Since there is a strong electric field in the space charge regions of grain boundaries, a drift term due to the electric field as well as the usual diffusive term due to the concentration gradient is included in the flux equation of the vacancy-ion complexes,

$$\begin{aligned}
 J^{(i)} &= J_{\text{complex}}^{(i)}; \quad i = 1, 2 \\
 &= [-D_O \nabla (pC^{(i)}) - qBpC^{(i)} \nabla (e\phi(x) - e\phi_\infty)]; \quad i = 1, 2 \\
 &= [-\{D_O p \frac{\partial C^{(i)}}{\partial x} + D_O C^{(i)} \frac{\partial p}{\partial x} + qBC^{(i)} p \frac{\partial}{\partial x} (e\phi(x) - e\phi_\infty)\} \hat{x} \\
 &\quad - D_O p \frac{\partial C^{(i)}}{\partial y} \hat{y} - D_O p \frac{\partial C^{(i)}}{\partial z} \hat{z}]; \quad i = 1, 2
 \end{aligned} \tag{1}$$



where the quantity with a superscript,  $i = 1$ , denotes that of the tracer isotope and  $i = 2$ , for that of the major isotope;  $C$  is the local concentration of the ions;  $D_0$  is the diffusion coefficient of the vacancy-ion complexes;  $B$  is the effective mobility of these complexes in the space charge electric field;  $q$  is the effective charge number of the complexes;  $e$  is the absolute value of the electronic charge;  $p$  is the probability of association to form the complexes;  $\{\phi(x) - \phi_\infty\}$  is the potential difference between the bulk potential,  $\phi_\infty$ , and the potential at a distance  $x$  from a planar boundary or free surface, which is normal to the  $x$ -axis. In general,  $D_0$  is not affected by the space charge potential and therefore is not a function of location in the crystal.

It was shown in the Appendix that the total concentration of both isotopes  $C(x,y)$  is independent of  $y$ ,

$$C^{(1)}(x,y) + C^{(2)}(x,y) = C(x,y) = C(x) \quad (2)$$

and that the tracer isotope concentration,  $C^{(1)}(x,y)$ , can be expressed in terms of the total concentration,  $C(x)$ , as

$$C^{(1)}(x,y) = C(x) f(y)/C(\infty) \quad (3)$$

where  $f(y)$  is the tracer concentration at distance far from the grain boundary and  $C(\infty)$  is the total concentration of both isotopes in the bulk.

For diffusion parallel to the grain boundary, we only consider the  $y$ - component of the flux vector in Eq. (1); and the tracer diffusivity,  $D$ , is given as

$$D = D_0 p \quad (4)$$

The space charge enhancement to the tracer diffusion and conductance parallel to the boundary can be evaluated by integrating the y component flux,  $J_y$ , over both sides of the boundary,

$$\begin{aligned}
 \Delta J &= 2 \int_0^{\infty} [J_y(x) - J_y(\infty)] dx \\
 &= 2 \int_0^{\infty} [D_0 p(x) \frac{\partial C^{(1)}(x,y)}{\partial y} - D_0 p(\infty) \frac{\partial C^{(1)}(\infty,y)}{\partial y}] dx \\
 &= 2 \int_0^{\infty} [D_0 p(x) C(x) - D_0 p(\infty) C(\infty)] \frac{\partial f}{\partial y} dx \quad (5)
 \end{aligned}$$

This quantity is a measure of the conductance parallel to the boundary, but gives no information regarding the "effective" width or diffusivity for transport across the boundary or the space charge cloud.

However, for diffusion normal to the grain boundary, the ionic flux is the x-component of the flux vector in Eq. (1). Although the last two terms in this component,  $D_0 C^{(i)} \frac{\partial p}{\partial x}$  and  $-qBC \frac{\partial}{\partial x}(e\phi(x) - e\phi_{\infty})$ , will be of opposite signs, numerical calculations show that they can be of magnitude larger than the first term in the flux component,  $D_0 p \frac{\partial C^{(i)}}{\partial x}$ . The term  $\Gamma_0 C^{(i)} \frac{\partial p}{\partial x}$  can be derived from p, the association probabilities of different diffusing ionic species, discussed in the subsequent sections; and is proportional to the space charge electric field. Since this electric field<sup>4</sup> is an odd function with respect to the grain boundary,

$$- \frac{\partial (e\phi(x) - e\phi_{\infty})}{\partial x} = \begin{cases} +2kT \sinh \left( \frac{e\phi(x) - e\phi_{\infty}}{2kT} \right), & x > 0 \\ -2kT \sinh \left( \frac{e\phi(x) - e\phi_{\infty}}{2kT} \right), & x < 0 \end{cases} \quad (6)$$

the net flux due to the  $D_O C^{(i)} \frac{\partial p}{\partial x} - qBC^{(i)} p \frac{\partial}{\partial x} (e\phi(x) - e\phi_\infty)$  terms reverses direction on the opposite sides of the boundary.

Therefore it is likely that these fluxes have no net contribution to diffusion across the boundary. Consequently, Eq. (4) may also be approximately correct for some problems involving diffusion across the grain boundary.

Furthermore, for Eq. (4) to be applicable the diffusion of impurity ions, either parallel or normal to the boundary, is restricted to tracer diffusion or sufficiently small concentration gradients that the space charge is adequately characterized by the average impurity concentration near the boundary. A significant quantity of impurity introduced into the matrix by impurity diffusion will change the space charge potential and require a more complicated analysis. For the present purposes, the case of tracer diffusion may well illustrate the essential features of the problem. Besides, results for the self diffusion coefficients are also applicable to mass transport for ionic conduction, creep or sintering.

## (2) Sr Diffusion in Sr Doped KCl:

Since  $Sr^{2+}$  can only diffuse by associating with potassium vacancies,<sup>10</sup> the probability of association,  $p$ , is defined as

$$p = \frac{[(V_K' Sr_K^\bullet)^*]}{[(V_K' Sr_K^\bullet)^*] + [Sr_K^\bullet]} \quad (6)$$

and is a function of location in the crystal.<sup>+</sup>

---

<sup>+</sup> Kroger-Vink notation where ', •, \* indicate the effectively negative, positive and neutral charged species respectively.

We define  $p_{\infty}$  as the degree of association in the bulk. Since the space charge potential does not affect the associated complexes, which are neutral; the concentration of the complexes,  $[(V_K' Sr_K^{\bullet})^*]$ , is

$$[(V_K' Sr_K^{\bullet})^*] = C_{\infty} p_{\infty} \quad (7)$$

where  $C_{\infty}$  is the total Sr concentration in the bulk.

The space charge potential will strongly affect the equilibrium distribution of the charged, unassociated strontium. Since the grain size ( $> 10 \mu m$ ) is much larger than the Debye length ( $10^{-3}$  to  $10^{-1} \mu m$ ), it is reasonable to neglect effects of specimen size. The unassociated Sr concentration,  $[Sr_K^{\bullet}]$ , is<sup>4</sup>

$$[Sr_K^{\bullet}] = (1-p_{\infty}) C_{\infty} \exp \left( - \frac{e\phi(x) - e\phi_{\infty}}{kT} \right) \quad (8)$$

Combining Eqs. (4) - (6), we have the probability of association near the boundary

$$p(x) = \frac{p_{\infty}}{p_{\infty} + (1-p_{\infty}) \exp \left( - \frac{e\phi(x) - e\phi_{\infty}}{kT} \right)} \quad (9)$$

Combining Eqs. (2) and (7), we can express the ratio of the Sr diffusivity in the boundary region,  $D^{Sr}(x)$ , to that in the bulk,  $D^{Sr}(\infty)$ ,

$$\frac{D^{Sr}(x)}{D^{Sr}(\infty)} = \frac{D_O^{Sr} p(x)}{D_O^{Sr} p_{\infty}} = \frac{1}{p_{\infty} + (1-p_{\infty}) \exp \left( - \frac{e\phi(x) - e\phi_{\infty}}{kT} \right)} \quad (10)$$

The  $D^{\text{Sr}}(x)/D^{\text{Sr}}(\infty)$  ratio, plotted in Fig. 2, as a function of distance normalized with respect to the Debye length,  $\delta$ , shows a moderate enhancement of Sr diffusivity in the region near the boundary at temperatures above the isoelectric point, which is 440°C for 50 ppm Sr doped KCl. However, at temperatures below the isoelectric point, there is a significant reduction of Sr diffusivity near the boundary.

The Debye length,  $\delta$ , for extrinsic temperatures is given as<sup>4</sup>

$$\delta = \left[ \frac{\epsilon kT}{8\pi N e^2} \cdot \frac{1}{C_{\infty} (1-p_{\infty})} \right]^{1/2} \quad (11)$$

where  $\epsilon$  is the static dielectric constant and  $N$  is the density of anion or cation sites in the crystal. The diffusion and impurity-vacancy association data of Fuller et al<sup>11</sup> and the defect formation energies of Dreyfus and Norwick<sup>12</sup>, are given in Table (1). The calculated values of bulk potentials, Debye lengths and impurity-vacancy association probabilities are given in Table (2). This and subsequent calculations neglect  $\text{SrCl}_2$  precipitation in the matrix which may occur in heavily doped samples.<sup>13,14</sup>

In the space charge theory of Kliever and Koehler<sup>4</sup> the impurity-vacancy complexes are assumed to be electrically neutral and so to have no interaction with the space charge potential or the potential gradient; thus the concentration of the complexes,  $p(x) C(x)$ , is uniform across the boundary region, and  $p(x)C(x) = p(\infty)C(\infty)$ . Consequently, the presence of the space charge layers has no integrated enhancement of Sr diffusion

flux parallel to the grain boundary, as given in Eq. (5),  $\Delta J^{Sr} = 0$ .

However, the impurity-vacancy complexes are electric dipoles; the interaction between the dipole moments and the space charge electric field has a significant effect in the distribution of dipole complexes with different moment orientations. Furthermore, because of the high value of the electric field gradient, the distribution of dipole complexes is not uniform, i.e.  $C(x)p(x) \neq C(\infty)p(\infty)$ ; and it can be shown that the integrated enhancement to diffusion parallel to the grain boundary,  $\Delta J$ , as given in Eq. (5), is

$$\Delta J = 2 D_0 \frac{C_\infty p_\infty}{3} \int_0^\infty [(\exp(\frac{ea}{2} \frac{d\phi}{dx} / kT) - 1) + (\exp(-\frac{ea}{2} \frac{d\phi}{dx} / kT) - 1)] dx \quad (12)$$

where the space charge potential,  $\phi$ , differs by only a negligibly amount from the potential distribution in Kliewer and Koehler<sup>4</sup>, in which the complex dipole-electric field interaction is neglected.

Numerical integration shows that  $\Delta J$ , in Eq. (12), are  $0.133 \delta D^{Sr}(\infty) \frac{\partial f}{\partial y}$  and  $0.157 D^{Sr}(\infty) \frac{\partial f}{\partial y}$  for 200°C and 700°C respectively.

These values are at least an order of magnitude smaller than the integrated enhancement for the self diffusion of K and Cl ions as shown in the following sections.

(3) K Self Diffusion in Sr Doped KCl:

Since potassium ions diffuse by a vacancy mechanism, the  $p$ , as used in Section (1) for vacancy-ion association, is simply  $z[V_K']$  where  $z$  is the coordination number i.e. 12 for KCl and  $[V_K']$  is the concentration of potassium vacancies free from Sr association. The K diffusivity,  $D^K$ , is then given as

$$D^K = [V_K'] D_V^K \quad (12)$$

where  $D_V^K$  is the potassium vacancy diffusion coefficient.

Although the space charge potential has little effect on the vacancy diffusivity, it does determine the distribution of potassium vacancies in the vicinity of the grain boundary. The potassium vacancy concentration near the boundary is<sup>4</sup>,

$$[V_K'(x)]/[V_K'(\infty)] = \exp\left(\frac{e\phi(x) - e\phi_\infty}{kT}\right) \quad (13)$$

From Eqs. (11) and (12), the enhancement or reduction in K diffusion in the space charge region at temperatures above or below the isoelectric point have a similar trend as in the case of Sr diffusion and are shown in Fig. (3).

For the integrated enhancement of K flux, the  $C(x)$ , as in Eq. (5), is simply  $\{1 - [V_K'(x)]\}$ , and

$$\begin{aligned} \Delta J &= 2 \int_0^\infty \{D_V[V_K'(x)] \{1 - [V_K'(x)]\} - D_V[V_K'(\infty)] \{1 - [V_K'(\infty)]\}\} \frac{\partial f}{\partial y} dx \\ &= 4D^K(\infty) \delta \left\{ \left[ \exp\left(\frac{-e\phi_\infty}{2kT}\right) - 1 \right] + [V_K'(\infty)] \left( \frac{4}{3} - \frac{1}{3} \exp\left(\frac{-3e\phi_\infty}{2kT}\right) \right. \right. \\ &\quad \left. \left. - \exp\left(\frac{-e\phi_\infty}{2kT}\right) \right) \right\} \frac{\partial f}{\partial y} \quad (14) \end{aligned}$$

which gives values of  $-3.69\delta D^K(\infty) \frac{\partial f}{\partial y}$  at 200°C and  $+15.93\delta D(\infty) \frac{\partial f}{\partial y}$  at 700°C for 50 ppm Sr doped KCl.

#### (4) Cl Self Diffusion in Sr Doped KCl:

Due to the suppression of chlorine vacancies by Sr dopant, the Cl diffusivity is decreased in the extrinsic temperature region. However, the contribution due to potassium-chlorine vacancy pairs,  $(V_K' V_{Cl}^\bullet)^*$ , is then significant. The ratio of vacancy pair diffusion,  $D_p^{Cl}$ , to single anion vacancy diffusion in the bulk,  $D_S^{Cl}(\infty)$ , can be calculated from equations by Fuller<sup>15</sup> and with an assumption about the Sr impurity to K vacancy binding energy<sup>11</sup>. The  $D_p^{Cl}(\infty)/D_S^{Cl}(\infty)$  ratios for various Sr contents are shown in Fig. 4.

Since the vacancy pairs are neutral and with the effects of dipole moment-electric field interaction neglected, their contribution to diffusion is not affected by the space charge potential. At high temperatures, when the contribution of single vacancies,  $V_{Cl}^\bullet$ , to diffusion is significant, the space charge potential will affect the Cl diffusivity in a similar manner as to the K diffusivity. However, in this case, the ratio  $D_S^{Cl}(x)/D_S^{Cl}(\infty)$  is the reciprocal of that given in Eq. (12) for  $D^K(x)/D^K(\infty)$ .

When both the single anion vacancy and vacancy pair contributions are included  $D_{tot}^{Cl}$ , the Cl diffusivity in the region near the boundary can be expressed as

$$\frac{D_{tot}^{Cl}(x)}{D_{tot}^{Cl}(\infty)} = \frac{D_S^{Cl}(x)/D_S^{Cl}(\infty) + D_p^{Cl}(\infty)/D_S^{Cl}(\infty)}{1 + D_p^{Cl}(\infty)/D_S^{Cl}(\infty)} \quad (15)$$



This ratio is plotted for different temperatures in Fig. 5.

Because of a significant contribution of vacancy pairs to diffusion at low temperatures both the magnitude and the effective range of the space charge enhancement are significantly reduced.

The integrated enhancement for the Cl diffusion flux,

$$\Delta J = 2D_{\text{tot}}^{\text{Cl}}(\infty) \int_0^\infty \left\{ \frac{D_{\text{tot}}^{\text{Cl}}(x)}{D_{\text{tot}}^{\text{Cl}}(\infty)} (1 - [V_{\text{Cl}}^\bullet(x)]) - (1 - [V_{\text{Cl}}^\bullet(\infty)]) \right\} \frac{\partial f}{\partial y} dx$$

$$= \frac{4D_{\text{tot}}^{\text{Cl}}(\infty) \delta}{1 + D_{\text{p}}^{\text{Cl}}(\infty)/D_{\text{S}}^{\text{Cl}}(\infty)} \left[ (1 - [V_{\text{Cl}}^\bullet(\infty)]) \frac{D_{\text{p}}^{\text{Cl}}(\infty)}{D_{\text{S}}^{\text{Cl}}(\infty)} (e^{\frac{e\phi_\infty}{2kT}} - 1) \right. \\ \left. + [V_{\text{Cl}}^\bullet(\infty)] \left( \frac{4}{3} - \frac{e^{\frac{3e\phi_\infty}{2kT}}}{3} - e^{\frac{e\phi_\infty}{2kT}} \right) \right] \frac{\partial f}{\partial y} \quad (16)$$

is  $-2.08\delta D_{\text{tot}}^{\text{Cl}}(\infty) \frac{\partial f}{\partial y}$  at  $700^\circ\text{C}$  and  $+0.71\delta D_{\text{tot}}^{\text{Cl}}(\infty) \frac{\partial f}{\partial y}$  at  $200^\circ\text{C}$ , for 50 ppm Sr doped KCl.

#### (5) K Self Diffusion in O Doped KCl:

For KCl doped with divalent anion impurity, e.g.,  $\text{K}_2\text{O}$ , a negative bulk potential is always required. Physically it is due to the fact that the formation energy of anion vacancies is larger than that of cation vacancies. At intrinsic temperatures, the bulk potential approaches that of the pure KCl,  $-0.27$  eV. At extrinsic temperatures, the anion vacancy concentration at the surface, is always less than the impurity concentration. As temperature decreases, the surface concentration of anion vacancies is free to decrease; but because of the neutrality condition in the bulk, the anion vacancy concentration in the bulk is constrained by the

impurity concentration. Consequently, as temperature decreases, an increasingly negative bulk potential is required to maintain the increasingly larger concentration differential between the surface and the bulk.

With an analysis similar to that by Kliever and Koehler<sup>4</sup> but for anion divalent dopants, it can be shown that the bulk potential for the O-dopant KCl,  $e\phi_{\infty}(O)$ , and that for the Sr-doped KCl,  $e\phi_{\infty}(Sr)$  are related by

$$e\phi_{\infty}(Sr) + e\phi_{\infty}(O) = F^{+} - F^{-} \quad (17)$$

provided that the binding energy between  $O_{Cl}'$  and  $V_{Cl}'$  is the same as that between  $Sr_K^{\bullet}$  and  $V_K'$ , as shown in Fig. 6. Furthermore, the Debye length,  $\delta$ , for extrinsic temperatures is the same as that given in Eq. (10).

Based on the calculated values of the bulk potentials and the solutions of Poisson's equation, vacancy and impurity distributions were calculated; and from these, K diffusion due to single vacancies were evaluated by Eq. (12) and are shown in Fig. 7. Because of the large bulk potential, there is a strong enhancement of K diffusion in the space charge layer. In contrast to the case of K diffusion in Sr doped KCl, the enhancement in  $K_2O$  doped samples increases as the temperature decreases.

The integrated enhancement of K diffusion flux is also given by Eq. (14) and is  $+55.2\delta D^K(\infty) \frac{\partial f}{\partial y}$  at 500°C and  $+1543\delta D^K(\infty) \frac{\partial f}{\partial y}$  at 300°C, for 5 ppm  $K_2O$  doped KCl. Since the K diffusion in  $K_2O$  doped KCl is suppressed by this dopant, the bulk K diffusivity

is much less than that in Sr doped samples.

Similar to the case of Cl diffusion in Sr doped KCl, the vacancy pair contribution to K diffusion in K<sub>2</sub>O doped KCl will be significant, and the effective enhancement due to the space charge will be reduced. But since the enhancement factor ( $10^2 - 10^5$ ) is much larger than the  $D_P^K/D_S^K(\infty)$  ratio ( $1 - 10^2$ ), the effective enhancement remains rather significant; in contrast to the case of with Sr dopant.

#### (6) Cl and O Diffusion in O Doped KCl:

The Cl and O diffusivities in the boundary region of K<sub>2</sub>O doped KCl will be reduced by the space charge effects analogous to the previous cases. The integrated reduction in Cl diffusion flux is

$$\begin{aligned} \Delta J &= 2 D^{Cl}(\infty) \int_0^{\infty} \frac{D^{Cl}(x)}{D^{Cl}(\infty)} (1 - [V_{Cl}^{\bullet}(x)]) - (1 - [V_{Cl}^{\bullet}(\infty)]) dx \\ &= 4 D^{Cl}(\infty) \delta \left\{ \left( e^{\frac{e\phi_{\infty}}{2kT}} - 1 \right) + [V_{Cl}^{\bullet}(\infty)] \left( \frac{4}{3} - \frac{e^{\frac{3e\phi_{\infty}}{2kT}}}{3} - e^{\frac{e\phi_{\infty}}{2kT}} \right) \right\} \frac{\partial f}{\partial y} \quad (18) \end{aligned}$$

giving  $-3.73\delta D^{Cl}(\infty) \frac{\partial f}{\partial y}$  at 500°C and  $-3.99\delta D^{Cl}(\infty) \frac{\partial f}{\partial y}$  at 300°C for 5 ppm K<sub>2</sub>O doped KCl.

Similar to the case of Sr diffusion in Sr doped KCl, there is no integrated enhancement of O diffusion flux in O-doped KCl.

### III. Discussion

There have been several reports of boundary enhanced cation, anion and impurity diffusion in alkali halides. Anion diffusion has been typically found to be more enhanced than cation diffusion. Most of these experiments involved sintered samples e.g. Laurent

and Benard<sup>16</sup>, Cabane<sup>17</sup>, and some involved bicrystals eg. Geguzin et al<sup>18</sup> and Sabharwal et al<sup>19</sup>. The grain boundaries in the samples may have been preferentially contaminated during the processing.<sup>20</sup> Grain boundary diffusion for O and Br ions were observed in KBr; and O ions diffuse 100 times faster than Br.<sup>21</sup> However, enhanced grain boundary diffusion was not observed for either cation or anions in hot deformed and recrystallized CsI polycrystals.<sup>22</sup> Boundary enhanced Tl diffusion in KCl bicrystals was not observed except in bicrystals intentionally synthesized in the presence of water vapor.<sup>23</sup> Water-enhanced grain boundary electrical conduction in KCl was reported<sup>24</sup>; and cation grain boundary diffusion in NaCl was observed only if the Na-isotopes were accompanied by water contamination.<sup>25</sup> As a result, there appear to be no good experimental estimates of  $wD_b$  (the boundary width times the boundary diffusivity) for clean alkali halide boundaries, due in part to the relative insensitivity of diffusion measurement techniques in bicrystals.

There are conflicting reports about the grain boundary width in ionic materials. Boundary widths of 2-10 lattice spacings were estimated for MgO<sup>26</sup>, ZrO<sub>2</sub><sup>27</sup>, Al<sub>2</sub>O<sub>3</sub><sup>28</sup>. However, a boundary width  $\sim 1 \mu\text{m}$  was suggested for alkali halides.<sup>29</sup> When grain growth and diffusion data were compared, the boundary widths were estimated to be  $\sim 1 \mu\text{m}$  for NaCl,  $2 \mu\text{m}$  for MgO,  $150 \text{ \AA}$  for BeO and  $100 \text{ \AA}$  for Al<sub>2</sub>O<sub>3</sub>.<sup>30</sup> Boundary widths of 2 and  $75 \mu\text{m}$  were estimated for MgO<sup>31,32</sup> based on the same set of diffusion data.<sup>33</sup> Microhardness measurements of doped Al<sub>2</sub>O<sub>3</sub><sup>34</sup> and doped Y<sub>2</sub>O<sub>3</sub><sup>35</sup> showed an effective boundary width of  $10 - 20 \mu\text{m}$ ; but these are likely due to non-equilibrium solute segregation which occurred during cooling.

When the reported magnitude and extent of boundary-enhanced diffusion data are compared with those predicted by the space charge theory, several discrepancies, both qualitative and quantitative, are noted:

(1) Boundary enhanced K and Sr diffusivities are predicted at temperatures above the isoelectric point; whereas reduced K and Sr diffusivities are predicted at temperatures below the isoelectric point. The inversion from enhancement to reduction is also predicted for Cl diffusion. An exception to the predicted inversion is the diffusivity in  $K_2O$  doped KCl, which has no isoelectric point. However, no data on reduced boundary diffusivities have been reported, nor would they be easily measurable by direct diffusion experiments.

(2) The predicted magnitude of enhancement is much less than the reported value of  $10^3 - 10^6$  in the cases of observed boundary diffusion.

(3) The predicted boundary widths are in the range of 10 - 200 Å, depending on temperatures and impurities, much less than some reported values ( $\sim 1 \mu m$ ). Only a few results of temperature dependent widths have been inferred from sintering studies in  $Al_2O_3$ <sup>28</sup> and diffusion studies in ZnO bicrystals<sup>36</sup> and  $ZrO_2$  polycrystals.<sup>27</sup>

The present calculations give much lower values of Debye lengths and of the integrated diffusivity enhancements than for pure crystals. Inferred from the calculations of Lehovec<sup>2</sup>, the integrated Na diffusivity enhancements are  $20.2\delta D^{Na}(\infty)$  at 900°K and  $55.6\delta D^{Na}(\infty)$  at 600°K for pure NaCl. More importantly, the Debye lengths,  $\delta$ , for

pure NaCl are  $\sim 80 \text{ \AA}^+$  at  $900^\circ\text{K}$  and  $2000 \text{ \AA}$  at  $600^\circ\text{K}$ .<sup>2,4</sup> The nearly micron size value of the Debye length at  $600^\circ\text{K}$  is valid only if the divalent impurity concentration is less than 0.01 ppm so that the bulk cation vacancies are predominantly Schottky defects. Consequently, the present calculations give a more realistic estimate of the space charge effects for presently obtainable crystals.

The diffusivity calculations are based on the space charge theories formulated by Frenkel<sup>1</sup>, Lehovec<sup>2</sup>, Eshelby et al<sup>3</sup> and Kliever and Koehler<sup>4</sup>. In these theories, the effects of adsorbates and the energies of excess vacancies at the surfaces were neglected; Lifshitz and co-workers<sup>37,38</sup> observed that these surface properties will introduce the crystallographic orientation dependency in the potential and charge distributions in the space charge layer. Blakely and co-workers<sup>39,40</sup> made certain simplifying assumptions about the surface structures and were able to obtain a solution for the surface potential with the surface site density and binding energy as parameters. They suggested that the isoelectric temperatures in AgCl are independent of the surface site density.<sup>40</sup> Given further refinements in the theory, it is not likely to change certain essential features, e.g. the existence of the isoelectric point in divalent-cation doped KCl. But it is precisely these essential features of the theory that give the most interesting and unobserved predictions.

Furthermore, these space charge theories are formulated for ionic materials only. However, since many oxides, e.g. NiO, MgO,

$\text{ZnO}_2$ ,  $\text{ZrO}_2$ ,  $\text{UO}_2$ ,  $\text{Y}_2\text{O}_3$  and  $\text{Al}_2\text{O}_3$ , at high temperatures, are at least partially electronic conductors,<sup>41</sup> the present forms of space charge theory are not strictly applicable; and the difference in formation energies of electrons and holes should also be included in the evaluation of the bulk potential,  $e\phi_\infty$ , in these oxides.

In terms of the conceptual separation of at boundary, near boundary, and boundary associated phenomena<sup>7</sup>, the reported micron size boundary widths and many observed enhanced diffusivities in contaminated boundaries may be classified as the boundary associated phenomenon, and usually resulted from second phase films at the boundary. As calculated, the space charge enhanced diffusivity, a near boundary phenomenon, is usually rather modest.

For clean boundaries, without impurity films, enhanced diffusion can be expected in the "core" of the boundary as well as in the charge cloud. A significant openness or disorder exists in the core to accomodate the lattice mismatch. In addition, there will be excess ions of one sign at the boundary to balance the space charge cloud. The concentration of these excess ions per unit area,  $\Delta Q$ , will be:

$$\Delta Q = 4C_\infty^V \delta \left( \exp\left(\pm \frac{e\phi_\infty}{2kT}\right) - 1 \right) \quad (19)$$

where  $C_\infty^V$  is the vacancy concentration in the bulk, and the negative sign is for K ions and the positive sign is for Cl ions. The ratio of  $\Delta Q/C_\infty^V$  is proportional to the integrated enhancements of the self diffusivities in the charge cloud and is usually rather small. This total excess ion or defect concentration in the core is

probably very small compared to the effective defect concentration caused by the structural misfit. The mobilities of vacancies or interstitials in the core are different, and possibly significantly higher, than in the lattice. Therefore, no theoretical estimate of the core contribution to  $wD_b$  can be made based solely on space charge effects. Finally, because of the small contribution from the charge cloud, if significant enhancement of the grain boundary diffusivity is observed, it is likely due to enhanced diffusivity in the core, even for clean boundaries.

#### IV. Summary

The contribution from the space charge cloud to enhanced K, Cl, Sr and O diffusivities in alkali halides were calculated based on the present form of the space charge theory for ionic materials. The calculated diffusivities show only modest enhancements near the boundaries; and the range of enhancement is limited to 10 - 200 Å. Only for the ion on the opposite sublattice from the principle impurity is appreciable diffusivity enhancement in the space charge cloud ever indicated. Therefore, the space charge enhanced diffusion cannot explain the large enhancement and wide boundary width reported in some boundary diffusion data in ionic materials.



## Appendix

For the gas exchange diffusion experiment described in the text, whereas a uniform chemical potential is maintained throughout the bicrystal sample, a concentration gradient of the tracer isotope exists parallel to the grain boundary.

Since there is no potential gradient in the sample, both the x and y components of the net flux of the tracer and major isotopes vanish,

$$J_x = J_x^{(1)} + J_x^{(2)} = 0 \quad (A-1)$$

$$\text{where } J_x^{(1)} = -D_o p \frac{\partial C^{(1)}}{\partial x} - C^{(1)} \left( D_o \frac{\partial p}{\partial x} - q B p \frac{\partial}{\partial x} (e\phi - e\phi_\infty) \right) \quad (A-2)$$

$$J_x^{(2)} = -D_e p \frac{\partial C^{(2)}}{\partial x} - C^{(2)} \left( D_o \frac{\partial p}{\partial x} - q B p \frac{\partial}{\partial x} (e\phi - e\phi_\infty) \right) \quad (A-3)$$

$$\begin{aligned} J_y &= J_y^{(1)} + J_y^{(2)} \\ &= -D_o p \left( \frac{\partial C^{(1)}}{\partial y} + \frac{\partial C^{(2)}}{\partial y} \right) = 0 \end{aligned} \quad (A-4)$$

$$\text{or } C^{(1)}(x, y) + C^{(2)}(x, y) = C(x) \quad (A-5)$$

Where  $C(x)$  is the integration constant and the total concentration of the two isotopes are independent of  $y$ .

With the usual assumption that  $J_x$  and  $J_y$  are independent of each other and that the steady state is achieved, the equation of continuity requires that

$$\frac{\partial J_x^{(1)}}{\partial x} = \frac{\partial J_x^{(2)}}{\partial x} = \frac{\partial J_y^{(1)}}{\partial y} = \frac{\partial J_y^{(2)}}{\partial y} = 0 \quad (\text{A-6})$$

i.e.  $J_x^{(1)}$  and  $J_x^{(2)}$  are independent of  $x$ ; and  $J_y^{(1)}$  and  $J_y^{(2)}$  are independent of  $y$ .

By symmetry of the diffusion sample, the quantities  $C^{(1)}(x,y)$ ,  $C^{(2)}(x,y)$ ,  $p(x)$ ,  $\phi(x)$  are even functions of  $x$ . Therefore the fluxes,  $J_x^{(1)}$  and  $J_x^{(2)}$  are odd functions of  $x$ , and these fluxes vanish at  $x = 0$ ,

$$J_x^{(1)}(0,y) = J_x^{(2)}(0,y) = 0 \quad (\text{A-7})$$

It is obvious from Eqs. (A-3) and (A-4) that

$$J_x^{(1)}(x,y) = J_x^{(2)}(x,y) = 0 \quad (\text{A-8})$$

With Eq. (A-5), we observe that both  $C^{(1)}$  and  $C^{(2)}$  satisfy the same differential equation,

$$-D_0 p \frac{\partial C^{(i)}}{\partial x} - C^{(i)} (D_0 \frac{\partial p}{\partial x} - q B p \frac{\partial}{\partial x} (e\phi - e\phi_\infty)) = 0 \quad i = 1, 2 \quad (\text{A-9})$$

therefore  $C^{(1)}(x,y)$  and  $C^{(2)}(x,y)$  must have the same  $x$  dependence; in addition to the requirement stated in Eq. (A-5b). Consequently, it can be shown that

$$C^{(1)}(x,y) = C(x) f(y)/C(\infty) \quad (\text{A-10})$$

$$C^{(2)}(x,y) = C(x) [1 - f(y)/C(\infty)] \quad (\text{A-11})$$

where  $f(y)$  is the tracer concentration at distance far from the grain boundary,  $x = \infty$ .

Table 1: Data of KCl vacancy formation energies, impurity-vacancy binding energies, and Cl diffusion activation energies.

Quantity	enthalpy (eV)	entropy (k)
K-vacancy formation energy <sup>12</sup>	0.84	3.2
Cl-vacancy formation energy <sup>12</sup>	1.38	3.2
Schottky defect formation energy <sup>11</sup>	2.49	7.64
Sr-impurity-K vacancy binding energy <sup>11</sup>	-0.57	-1.88
O-impurity-Cl vacancy binding energy <sup>*</sup>	-0.57	-1.88
Cl-diffusion by vacancy pairs <sup>15</sup>	2.65	9.05
Cl-diffusion by Cl vacancy in pure KCl <sup>15</sup>	2.10	3.60

\* Assumed

Table 2: The calculated values of bulk potentials,  $e\phi_{\infty}$ , Debye lengths,  $\delta$ , and impurity-vacancy association probabilities,  $p_{\infty}$ , for doped KCl.

Impurity (concentration)	Temperature ( $^{\circ}\text{C}$ )	$e\phi_{\infty}$ (eV)	$\delta$ ( $^{\circ}\text{\AA}$ )	$p_{\infty}$
Sr (50 ppm)	700	-0.27	10.0	0.08
	600	-0.16	9.8	0.13
	300	0.13	13.9	0.72
	200	0.21	21.9	0.91
O (50 ppm)	500	-0.48	9.9	0.26
	300	-0.67	13.9	0.72
O (5 ppm)	500	-0.36	26.0	0.04
	300	-0.59	29.3	0.37

Table 3

$\Delta J$ , Integrated Enhancement in the Diffusion Flux of  
Impurity and Matrix Ions.

<u>Diffusant</u>	<u>Temperature</u>	<u><math>\Delta J / \frac{\partial f}{\partial y}^*</math></u>	
Sample: KCl with 50 ppm Sr.			
Sr	200°C	$0, (0.133\delta D^{Sr}(\infty))^{**}$	$0, (0.52aD^{Sr}(\infty))^*$
Sr	700°C	$0, (0.157\delta D^{Sr}(\infty))^{**}$	$0, (0.28aD^{Sr}(\infty))$
K	200°C	$-3.69\delta D^K(\infty)$	$-14.4aD^K(\infty)$
K	700°C	$+15.93\delta D^K(\infty)$	$+28.3aD^K(\infty)$
Cl	200°C	$+0.71\delta D_{tot}^{Cl}(\infty)$	$+2.77aD_{tot}^{Cl}(\infty)$
Cl	700°C	$-2.08\delta D_{tot}^{Cl}(\infty)$	$-3.70aD_{tot}^{Cl}(\infty)$
Sample: KCl with 5 ppm O.			
K	300°C	$+1543\delta D^K(\infty)$	$+7180aD^K(\infty)$
K	500°C	$+55.2\delta D^K(\infty)$	$+228aD^K(\infty)$
Cl	300°C	$-3.99\delta D^{Cl}(\infty)$	$-18.5aD^{Cl}(\infty)$
Cl	500°C	$-3.73\delta D^{Cl}(\infty)$	$-15.4aD^{Cl}(\infty)$
O	300°C	0	0
O	500°C	0	0
Sample: KCl without any aliovalent dopant.			
K	300°C	$57.11\delta D^K(\infty)$	$18253aD^K(\infty)$
K	500°C	$26.19\delta D^K(\infty)$	$444aD^K(\infty)$

\* a - lattice constant; \*\* Dipole attraction included.

## References

1. J. Frenkel, "Kinetic Theory of Liquids" Oxford University Press, N. Y. (1946).
2. K. Lehovec, "Space-Charge Layer and Distribution of Lattice Defects at the Surface of Ionic Crystals", J. Chem. Phys. 21 [7] 1123-1128 (1953).
3. J. Eshelby, C. Newey, P. Pratt and A. B. Lidiard, "Charged Dislocations and the Strength of Ionic Crystals", Phil. Mag. 8 [3] 75-89 (1958).
4. K. L. Kliewer and J. S. Koehler, "Space Charge in Ionic Crystals. I. General Approach with Application to NaCl", Phys. Rev. 140 [4A] 1226-1240 (1965).
5. P. M. Burke, "High Temperature Creep of Polycrystalline Sodium Chlorine", Ph.D. Thesis, Dept. of Materials Science, Stanford University, Calif. (1968).
6. K. Kitazawa, "Review: Preferential Diffusion Along Grain Boundaries and Dislocations in Ceramics", unpublished research, M.I.T. (1971).
7. W. D. Kingery, "Plausible Concepts Necessary and Sufficient for Interpretation of Ceramic Grain Boundary Phenomena", J. Amer. Ceram. Soc. 57 [1] 1-8 (1974) and 57 [2] 74-83 (1974).
8. M. F. Yan, R. M. Cannon, H. K. Bowen and R. L. Coble, "Grain Boundaries and Grain Boundary Mobility in Hot-Forged Alkali Halides", in Deformation of Ceramic Materials, Edited by R. E. Tressler and R. C. Brandt. Plenum Publishing Corp., N. Y. (1975).
9. R. A. Menezes and W. D. Nix, "High Temperature Dislocation Mobility in LiF", Mat. Sci. Eng. 16 [3/4] 57-73 (1974).

10. A. B. Lidiard, "Impurity Diffusion in Crystals (Mainly Ionic Crystals with the Sodium Chloride Structure)", *Phil. Mag.* 7 [46] 1218-1237 (1955).
11. R. L. Fuller, C. L. Marquardt, M. H. Reilly and J. C. Wells, Jr., "Ionic Transport in Potassium Chloride", *Phys. Rev.* 176 [3] 1036-1045 (1968).
12. R. W. Dreyfus and A. S. Norwick, "Energy and Entropy of Formation and Motion of Vacancies in NaCl and KCl Crystals", *J. Appl. Phys. Suppl.* 33 [1] 473-477 (1962).
13. M. I. Abaev, "Decomposition of a Solid Solution of Strontium in Sodium Chloride Crystal", *Sov. Phys. -Solid State* 13 [8] 1953-1956 (1972).
14. W. Spengler and R. Kaiser, "Precipitates in Annealed and Quenched NaCl:  $\text{Cd}^{++}$  Crystals", *Phys. Stat. Sol. (b)* 66, 107-116 (1974).
15. R. L. Fuller, "Diffusion of Chlorine Ion in Potassium Chloride", *Phys. Rev.* 142 [2] 524-529 (1966).
16. J. F. Laurant and J. Benard, "Autodiffusion des Ions Dans les Cristaux Uniques des Halogenures de Potassium et des Chlorures Alcalins", *J. Phys. Chem. Solids*, 3 [1] 7-19 (1957).
17. J. Cabane, "La Diffusion Intergranulaire et la Structure des Joints Intergranulaires dans les Halogenures Alcalins", *J. Chim. Phys.*, 59, 1123-1141 (1962).
18. Y. E. Geguzin, E. R. Dobrovinskaya, I. E. Lev, and M. V. Mozharov, "Cation Diffusion Along the Boundaries in Alkali Halide Bicrystals", *Sov. Phys. -Solid State* 8 [11] 2599-2603 (1967).
19. K. S. Sabharwal, J. Minkes and M. Wuttig, "Anion Grain-Boundary Diffusion in Sodium Chloride." *J. Appl. Phys.* 46 [4] 1839-1840 (1975).
20. B. J. Wuensch and B. J. Tiernan, to be published in *J. Amer. Ceram. Soc*

21. L. W. Barr and D. K. Dawson, "The Reaction of Oxygen with Potassium Bromide Single Crystals", p. 401-409 in "Reactivity of Solids". Edited by J. W. Mitchell et al Wiley Interscience, N. Y. (1968).
22. S. M. Klotsman, Z. P. Polikarpova, A. N. Timofeev, and I. S. Trakhtenberg, "Self-Diffusion of  $\text{Cs}^{134}$  and  $\text{I}^{131}$  in Single Crystals and Polycrystalline Samples of Cesium Iodide", Sov. Phys. -Solid State, 9 [9] 1956-1966 (1968).
23. R. J. Tiernan, "Calculation of Grain-Boundary Diffusion Parameters and Comparison with Experiment", J. Appl. Phys. 42 [13] 5596-5600 (1971).
24. G. Geschwind and E. Machlin, "Water-Enhanced Grain Boundary Conduction in Potassium Chloride", Ibid., 38 [2] 900 (1967).
25. K. R. Riggs and M. Wuttig, "Cation Grain-Boundary Diffusion in Sodium Chloride", Ibid., 40 [11] 4682-4683 (1969).
26. J. B. Holt and R. H. Condit, "Oxygen-18 Diffusion in Surface Defects on MgO as Revealed by Proton Activation", Mat. Sci. Res. 3, 13-29 (1966 Edited by W. W. Krigel and H. Palmour. Plenum Press, N. Y.
27. J. B. Lightstone and J. P. Pamsler, "The Effect of Structure on the Mechanism of Zirconium Oxidation" p. 615-630 in "Reactivity of Solids" Edited by J. W. Mitchell et al. Wiley Interscience, N. Y. (1968).
28. D. L. Johnson and L. Berrin, "Grain Boundary Diffusion in Sintering of Oxides" p. 445-466 in "Sintering and Related Phenomena". Edited by G. C. Kuczynski, N. A. Hooton and C. F. Gibbon. Gordon and Breach, Science Publisher, N. Y. (1967).



29. L. W. Barr, I. M. Hoodless, J. A. Morrison and R. Rudham, "Effects of Gross Imperfections on Chloride Ion Diffusion in Crystals of Sodium Chloride and Potassium Chloride", Trans. Faraday Soc. 56 [5] 697-708 (1960).
30. R. E. Mistler and R. L. Coble, "Grain Boundary Diffusion and Boundary Widths in Metals and Ceramics", J. Appl. Phys. 45 [4] 1507-1509 (1974).
31. F. F. Wang "analysis of the Grain Boundary Diffusion Data of  $\text{Ni}^{2+}$  in Polycrystalline  $\text{MgO}$ ", Phys. Let. 18 [2] 101-103 (1965).
32. J. Minkes and M. Wuttig, "Diffusion in Wide Boundaries", J. Appl. Phys. 41 [8] 3205-3209 (1971).
- 33.. B. J. Wuensch and T. Vasilos "Grain Boundary Diffusion in  $\text{MgO}$ ", J. Amer. Ceram. Soc. 47 [2] 63-68 (1964).
- 34.. P. J. Jorgensen and J. H. Westbrook, "Role of Solute Segregation at Grain Boundaries During Final Stage Sintering of Alumina", Ibid., 47 [7] 332-338 (1964).
- 35.. P. J. Jorgensen, "Grain Boundary in Ceramic Materials", in "Proc. 4th Bolton Landing Conf.: Grain Boundaries in Engineering Materials" Eds. J. H. Westbrook, D. A. Woodford (to be published). P. J. Jorgensen and R. C. Anderson, "Grain Boundary Segregation and Final Stage Sintering of  $\text{Y}_2\text{O}_3$ " Ibid., 50 [11] 553-558 (1967).
36. K. S. Kim, "Cation Self-Diffusion in  $\text{ZnO}$ ", Sc.D. Thesis, Dept. of Materials Science and Engineering, M.I.T. (1971).
37. I. M. Lifshitz and Ya. E. Geguzin, "Surface Phenomena in Ionic Crystals", Sov. Phys. -Solid State, 7 [1] 44-52 (1965).
38. I. M. Lifshitz, A. M. Kossevich and Ya. E. Geguzin, "Surface Phenomena and Diffusion Mechanism of the Movement of Defects in Ionic Crystals", J. Phys. Chem. Solids, 28 [5] 783-798 (1967).

39. R. B. Poeppel and J. M. Blakely, "Origin of Equilibrium Space Charge Potentials in Ionic Crystals", Surface Sci. 15 [2] 507-523 (1969).
40. J. M. Blakely and S. Danyluk, "Space Charge Regions at Silver Halide Surfaces: Effects of Divalent Impurities and Halogen Pressure", Ibid., 40 [1] 37-60 (1973).
41. P. Kofstad, "Nonstoichiometry, Diffusion, and Electrical Conductivity in Binary Metal Oxides", Wiley-Interscience, N. Y. (1972).

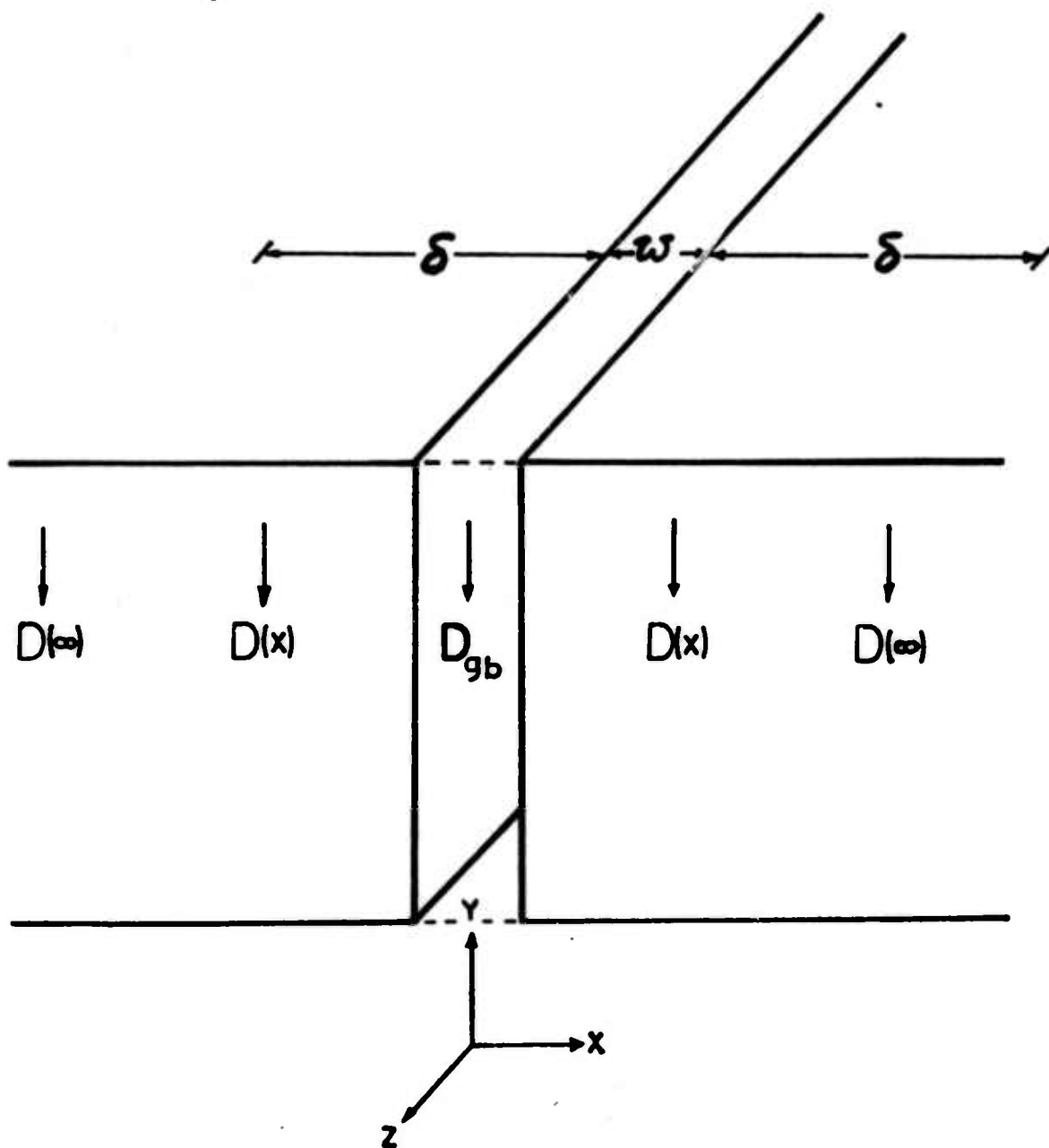


Figure 1. Schematic of the grain boundary region depicting a core region of width  $w$  and a space charge cloud of width  $\delta$ .

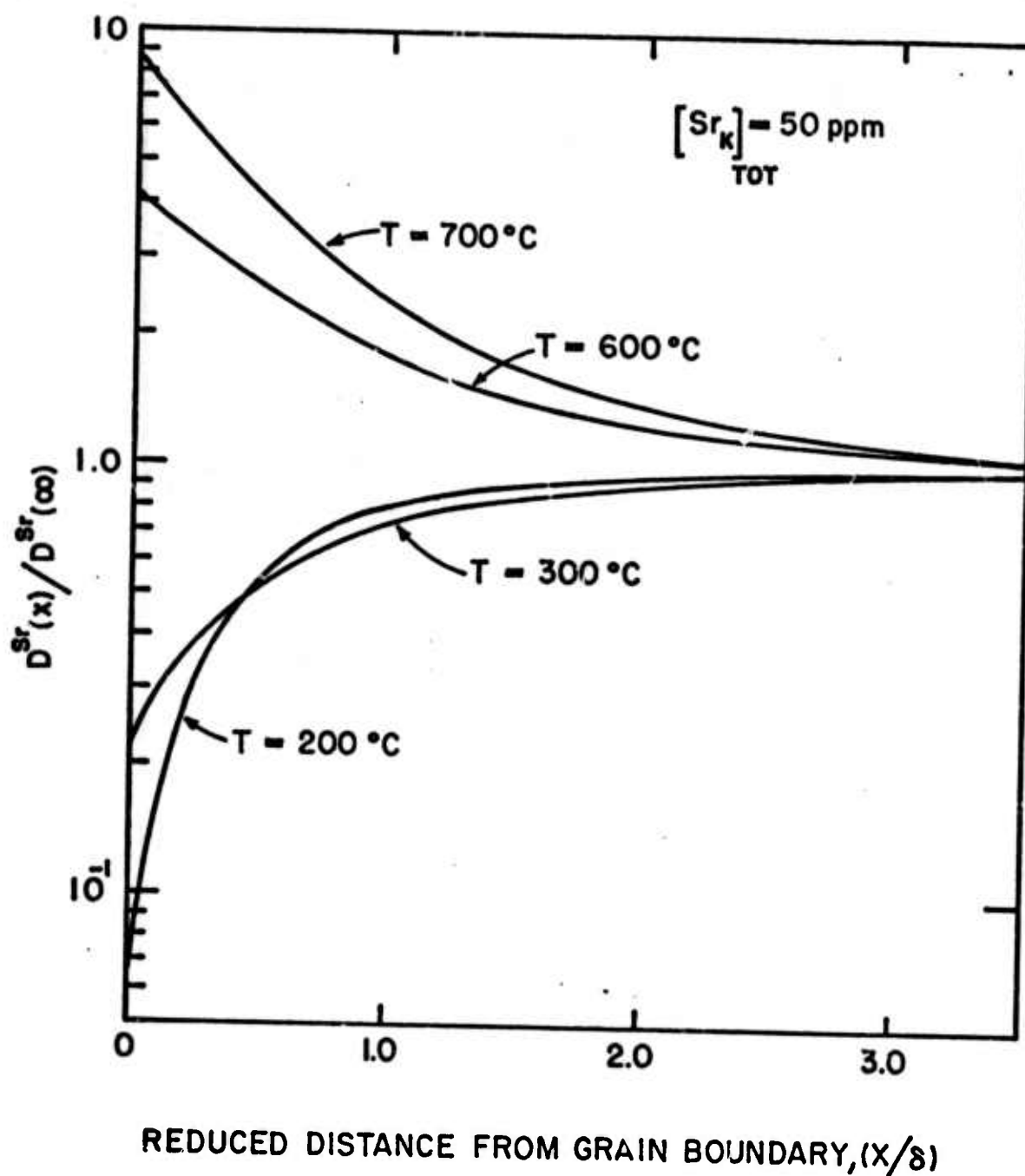


Figure 2. Normalized Sr diffusivities near the grain boundary of Sr doped KCl.

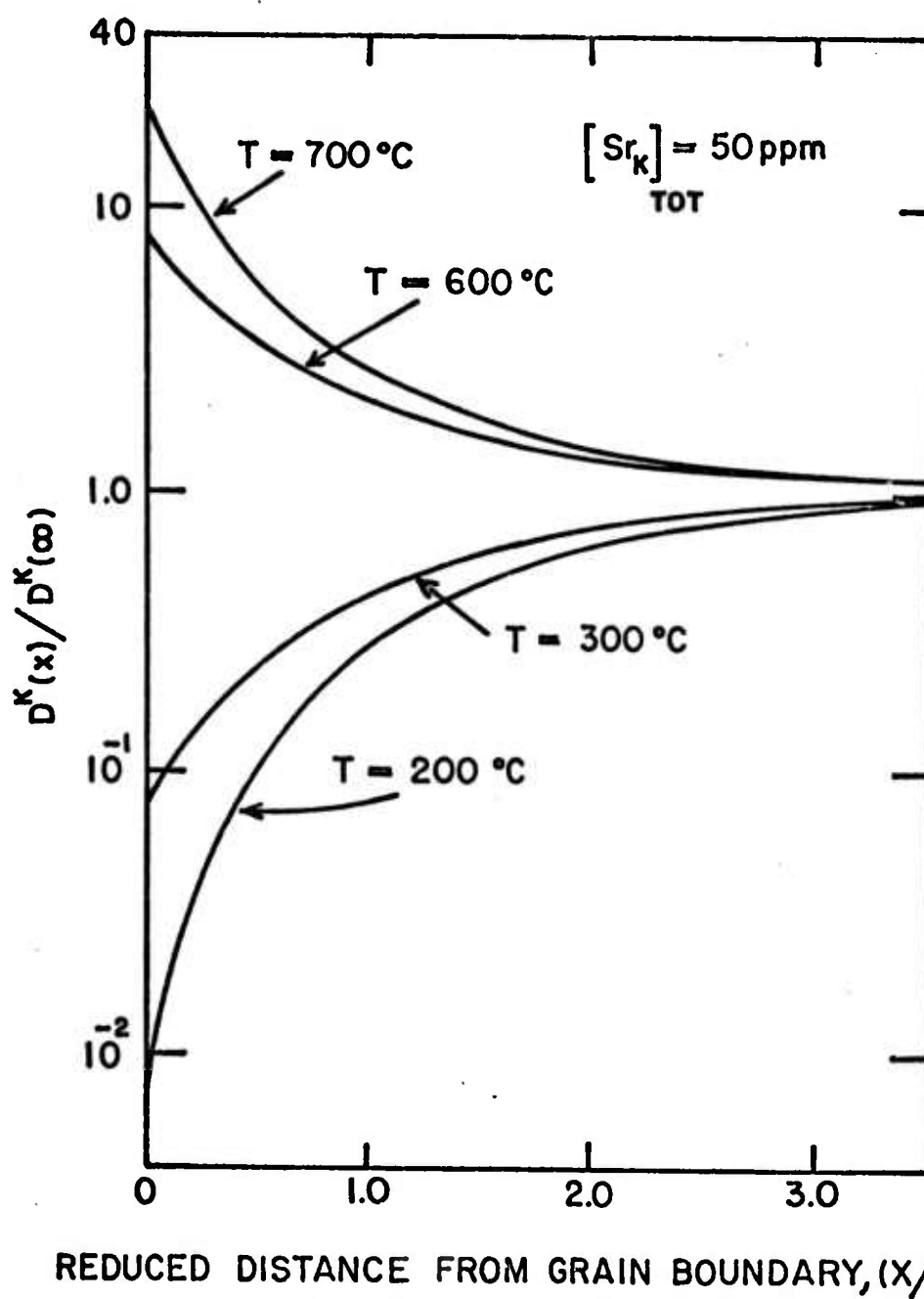


Figure 3. Normalized K diffusivities near the grain boundary of Sr doped KCl.

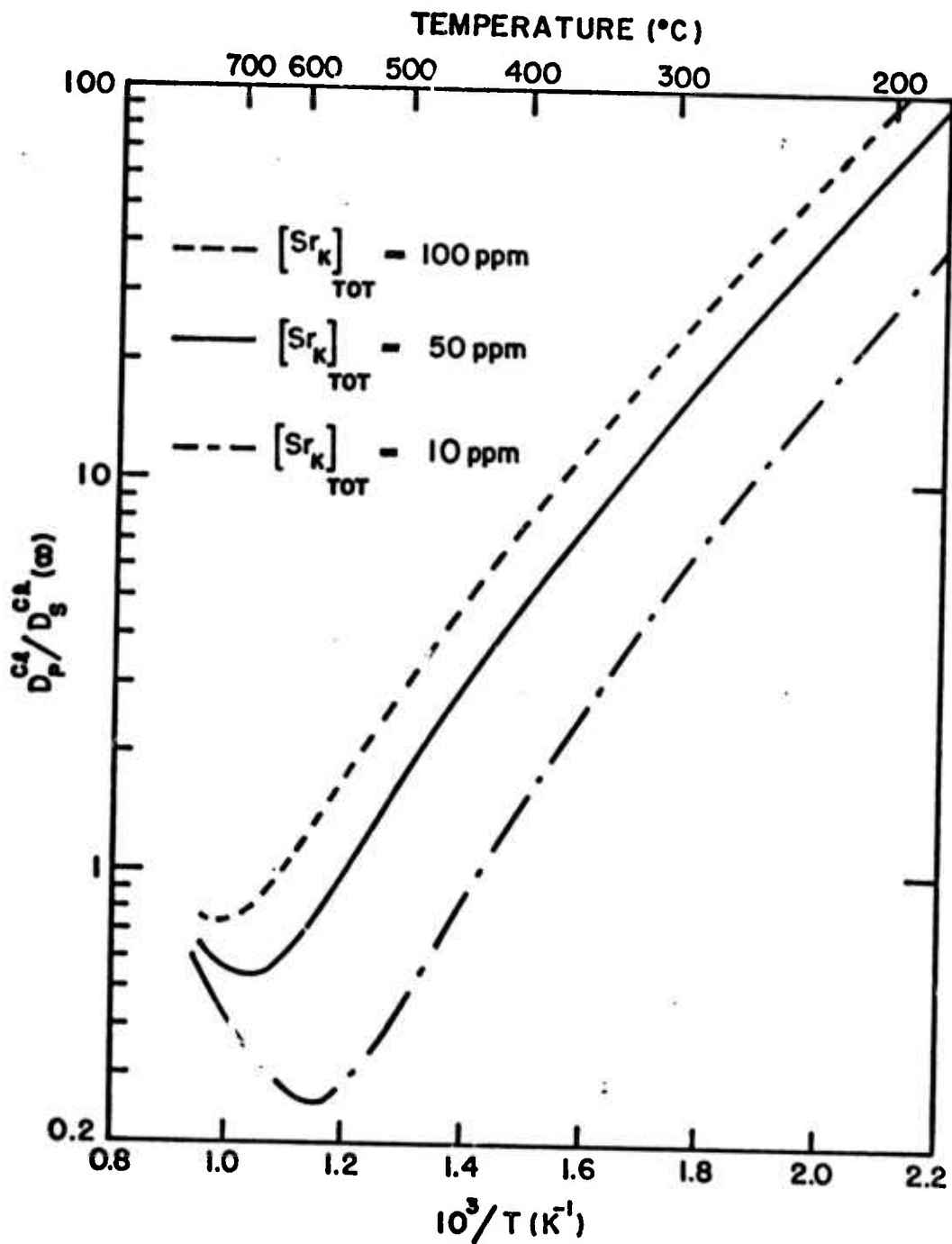


Figure 4. The ratio of the vacancy pair,  $(V'_K V_{Cl}^\bullet)$ , contribution to the single anion vacancy  $(V_{Cl}^\bullet)$ , contribution to Cl diffusion in Sr doped KCl; after Fuller<sup>15</sup> and Fuller et al<sup>11</sup>.

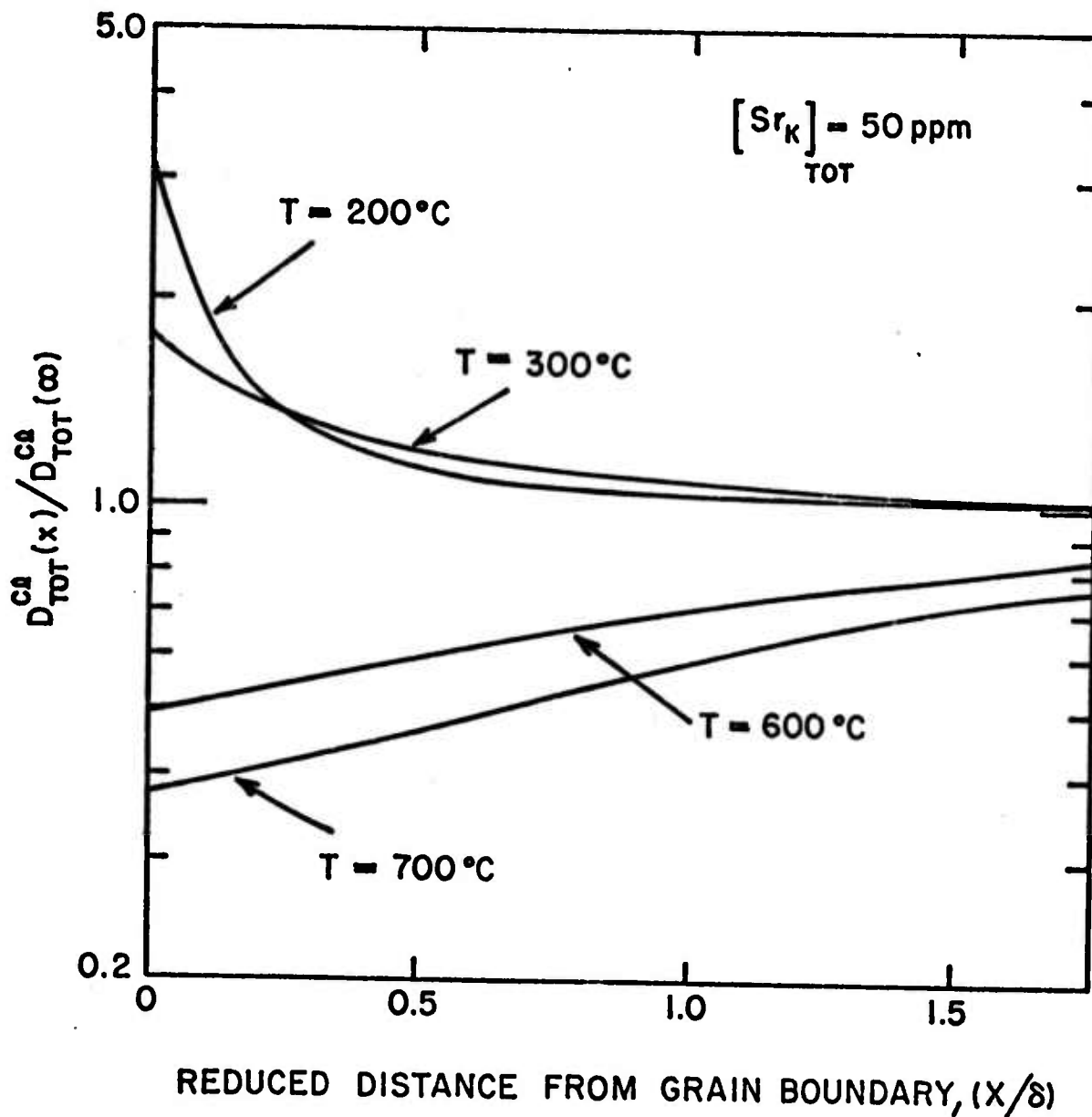


Figure 5. Normalized Cl diffusivities near the grain boundary as contributed by both single anion vacancies,  $(V_{Cl}^\bullet)$ , and vacancy pairs,  $(V_{Cl}^\bullet V_K^\bullet)^*$ .

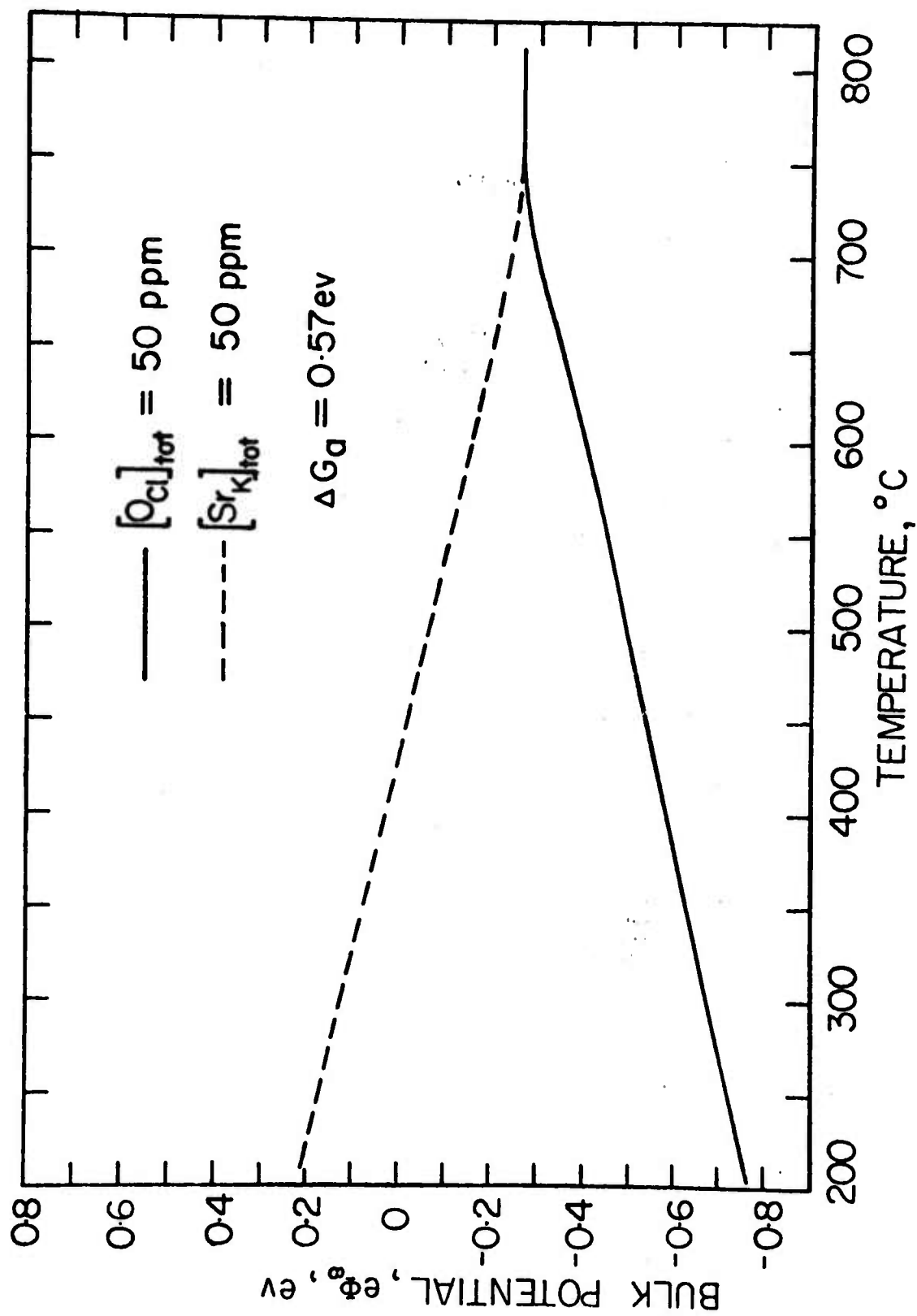


Figure 6. Space charge potential for O and Sr doped KCl.



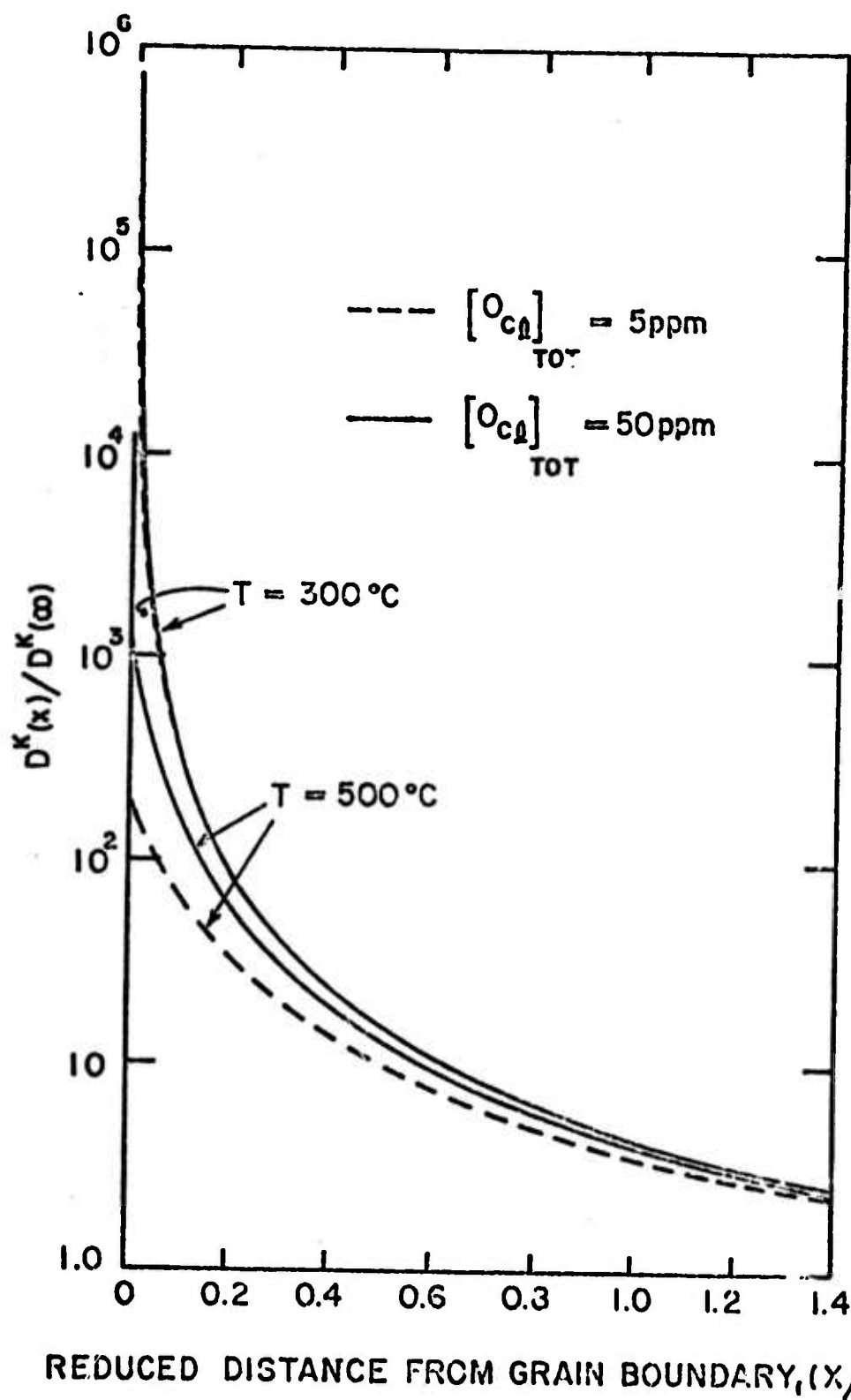


Figure 7. Normalized K diffusivities near the grain boundary of O doped KCl.

## E. DESIGN OF LASER WINDOWS USING FLAW ANALYSIS

Frank A. McClintock  
Professor of Mechanical Engineering  
Walter F. Hahn  
Research Assistant  
Department of Mechanical Engineering

### E.1 INTRODUCTION TO STATISTICAL DESIGN

Laser windows which are to satisfy various service requirements, including strength and success rate standards, must be designed through an iterative process using surface flaw statistics whereby standards are tentatively set until an optimum design is achieved. Figure E-1 shows a general flow chart for such a laser window design procedure.

Although this discussion centers around using flaw statistics as a design parameter for ZnSe laser windows, much of this work can be extended to the design of various brittle components. There are a number of specific benefits of finding flaw distributions:

Possible reduction of flaws through changes in manufacturing processes. By investigating the flaw distributions of brittle materials or of finished components made of those materials, it is possible to determine characteristic flaw concentrations (Fig. E-2). Then it may be possible to determine whether the origin

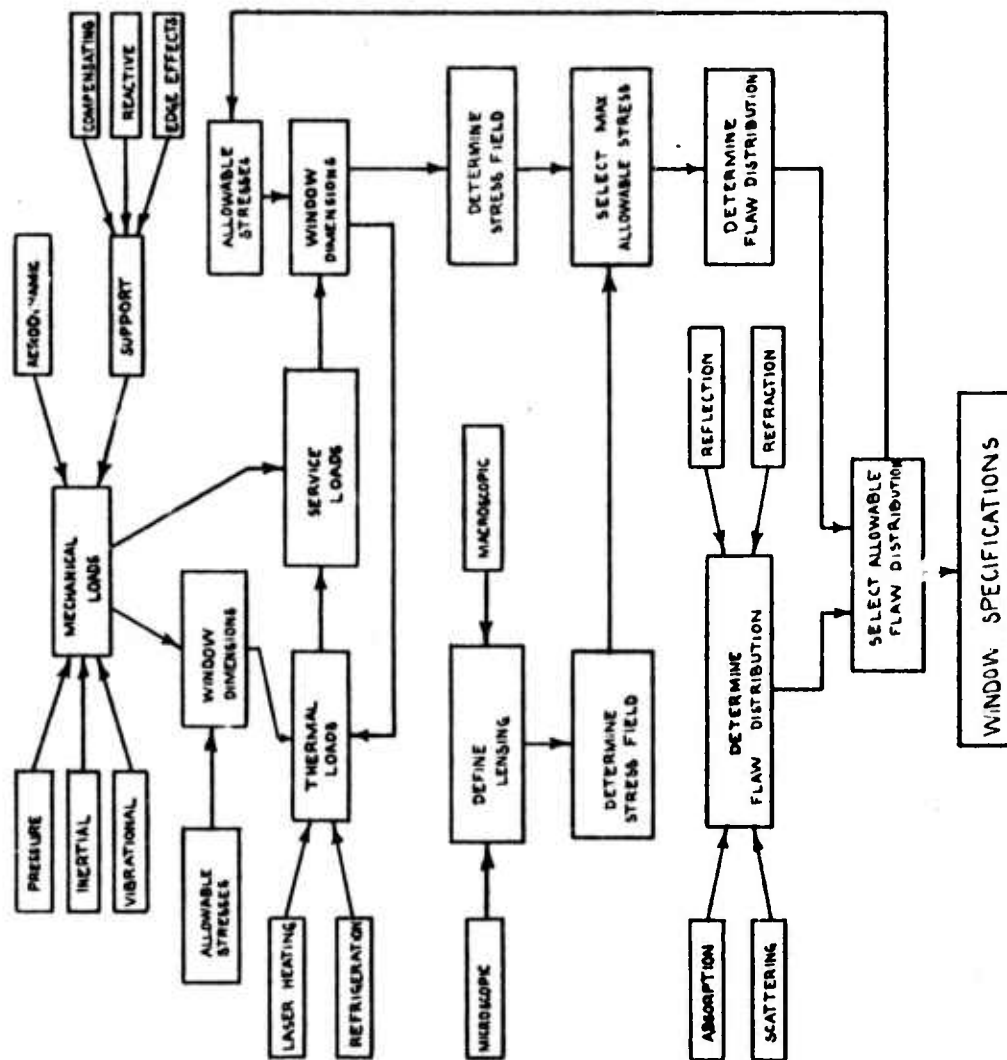


Fig. E-1. Laser Window General Design Procedure

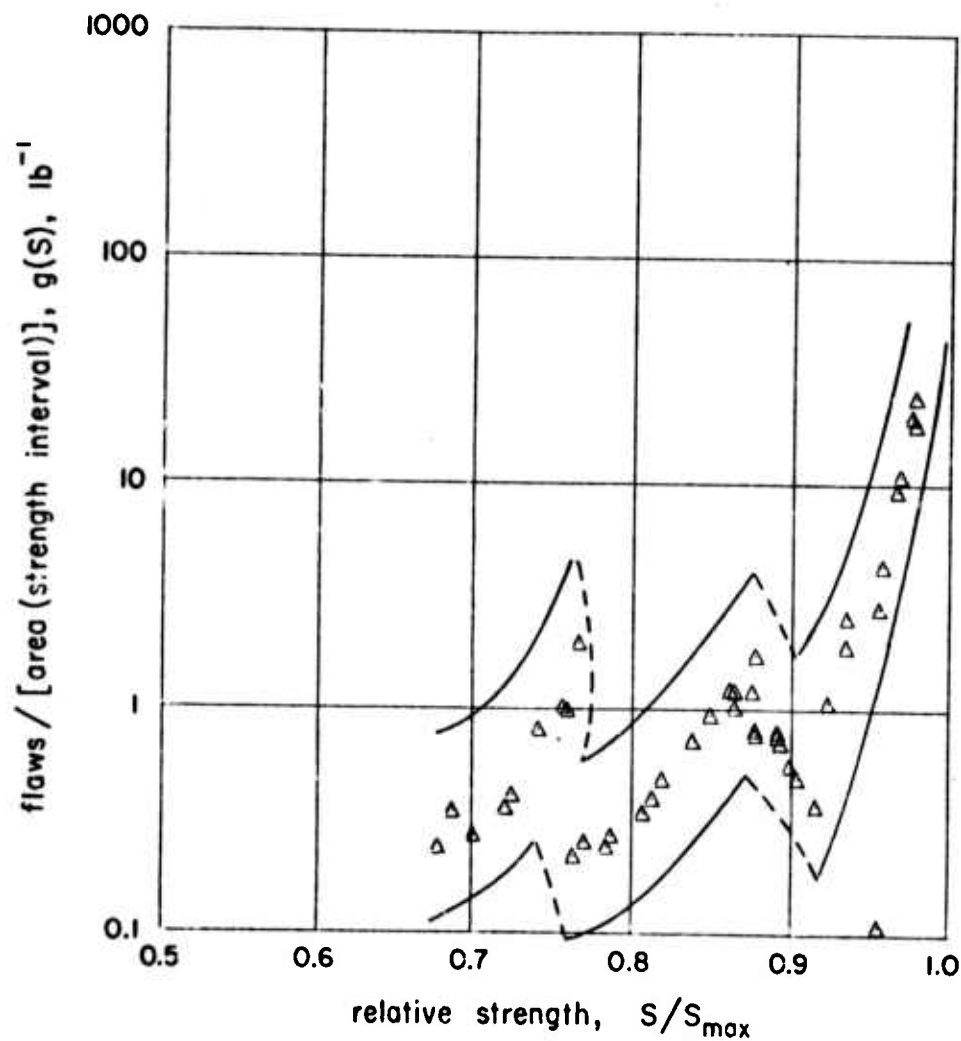


Fig. E-2 Flaw density distribution for window glass  
( 3/16 in. thick,  $S_{\text{max}} = 127,000$  psi) Matthews,  
McClintock and Shack, (1975).

of some flaws arise due to an inherent property of manufacturing of either the raw material or of the finished component. If such characteristic flaws owe their existence to a manufacturing process, it may be possible to change the offending step to reduce the severity of the flaws.

Failure rate predictions using flaw density data.

Flaw density curves of laser windows can be integrated up to a design stress to find the predicted failure rates. Conversely, an acceptable design stress could be found for a given failure rate.

Size effects. From studying the flaw distributions of small specimens it is possible to determine new failure rates for large components by integrating the flaw density curve over the appropriate area. Of course, this is only true if no inherent change in flaw distribution occurs with different size components.

E.2 THEORETICAL ANALYSIS OF FLAW DISTRIBUTIONS

Introduction. Starting with the pioneering work of Weibull (1939), a number of authors have dealt with the strength of parts subject to various stress distributions when the material itself followed one of the three asymptotic forms of extreme value distribution.

See, for example, Gumbel (1958), Dukes (1971), Batdorf and Crose (1973), Buch (1975), and Crose, Buch, and Robinson (1975). In general, however, these authors have not considered the interactions of stress fields of cracks. The interactions are important if several microcracks join together before macro-fracture from an internal site. It then turns out that the distribution of strengths is no longer one of the asymptotic extreme-value types. For this reason, data on the distributions of flaw strengths are needed. Recent progress on these two problems will be summarized here (McClintock and Zaverl, 1975; Matthews, McClintock, Shack, 1975).

Theoretical distribution function for internal fractures. For the strengths of parts as determined by internal flaws, a numerical model was first developed. As shown in Fig. E-3, the grain structure was idealized as a regular hexagonal array of grains whose strengths were randomly assigned from an extreme-value distribution of the third kind (i.e., the strengths vary as some power of the amount by which the stress exceeds some lower limit). The model assumes an elastically homogeneous and isotropic material in which cracking occurs along grain boundaries. The program computes the externally applied stress  $S$  necessary for the

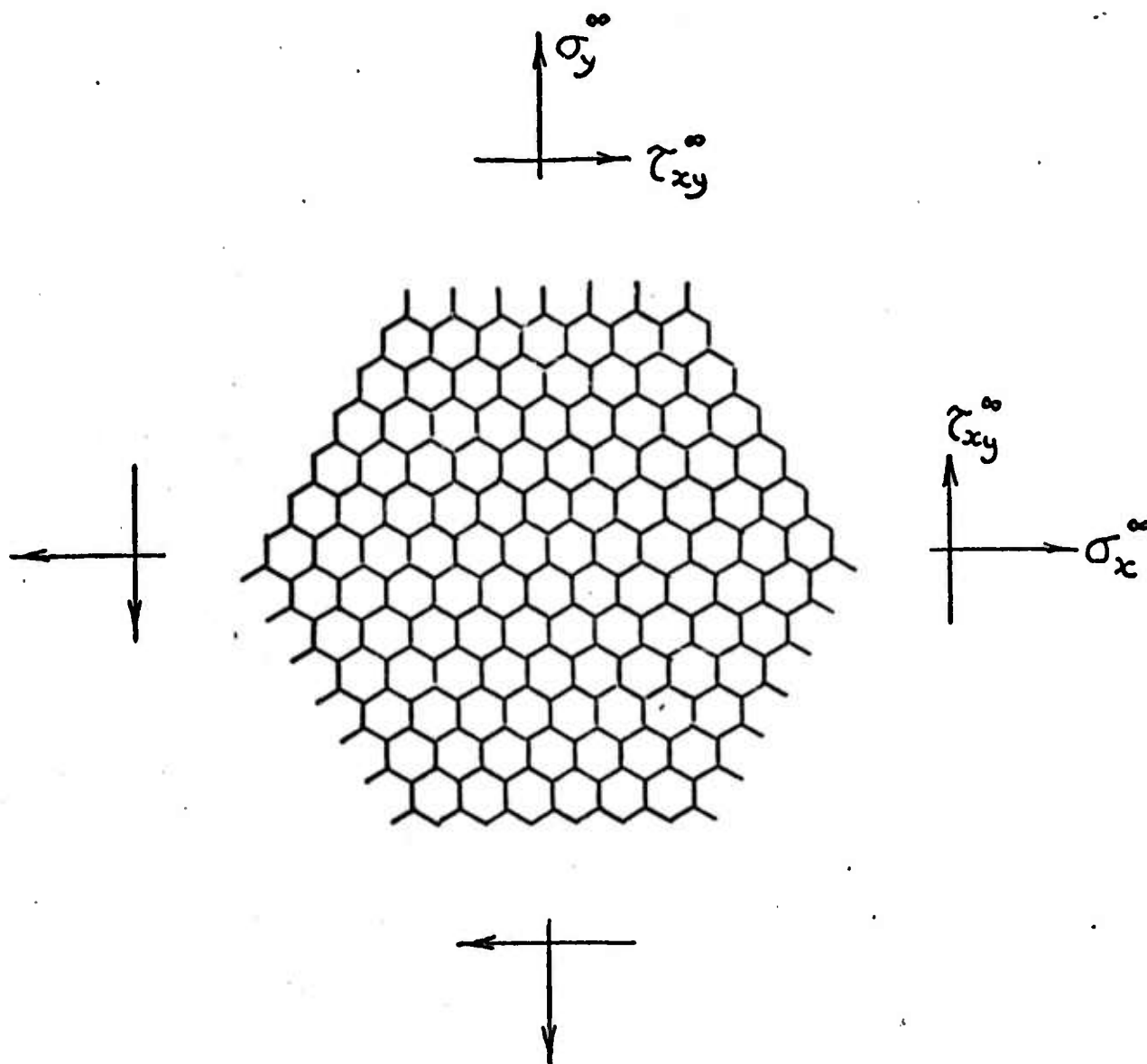


Fig. E-3. Idealized grain structure used in numerical model.

fracture of the weakest grain boundary relative to its locally applied stress, for each cracked segment in turn. More specifically, for applied biaxial tension, the program calculates an elastic solution throughout a periodic grid of hexagonal grains. Fracture is determined by the weakest individual segment relative to the current local stress, or if a crack tip is more critical, by the lowest segment toughness relative to the current local stress intensity. After the most critical segment is found, it is assumed cracked. Then a new elastic solution is calculated, a new most critical segment is found, and so on.

As expected, macro-crack initiation and final instability occur sooner with increasing coefficient of variation and with increasing size of part. The major discovery was that micro-cracking occurs at a lower fraction of the maximum strength in large parts than in small test specimens. Hence, acoustic emission will be more practical in the field than observed in laboratory tests. Also, the load for first cracking is over-conservative by large factors where there is a high coefficient of variation in the grain boundary strengths, and the lower limit of strength approaches zero.



An approximate analytical theory was developed to provide more insight into the numerical results. In an element of volume  $\delta V$ , subject to a uniform stress  $S$ , the probability of fracture below the stress  $S_1$  is:

$$\delta\phi(S_1) = \delta V \int_0^{S_1} g(S) dS. \quad (E-1)$$

Taking the flaw density distribution to increase as some power  $m - 1$  of the amount by which  $S$  exceeds a lower limit  $S_L$  gives, in terms of a single constant (divided into  $V_0$  and  $S_0$  for dimensional clarity):

$$g(S) = m(S-S_L)^{m-1} / (V_0(S_0-S_L)^m). \quad (E-2)$$

Combining (E-1) and (E-2) and solving gives the stress at or below which there is the probability  $\phi$  of encountering the first fracture:

$$S = S_L + (S_0 - S_L) [(V_0/V) n(1/(1-\phi))]^{1/m}. \quad (E-3)$$

Consider now a regular, two-dimensional, hexagonal array of grain boundary segments of length  $2c_1$  in an elastically isotropic material subject to an applied biaxial stress  $S$ . Assume that cracking will continue from an isolated crack either by reinitiation or when the singularity  $k$  of normal stress on one of

the four adjacent grain boundaries reaches that corresponding to the critical stress intensity factor for that boundary under pure Mode I loading. Then, for pure Mode I loading on the original crack, the stress intensity  $k_I (=K_I/\sqrt{\pi})$  on the four neighbor segments will be: (see, for example, Sih and Liebowitz, 1968, pp. 93, 94).

$$k = k_I \left[ \frac{1 + \cos 60^\circ}{2} \cos \frac{60^\circ}{2} \right] = S\sqrt{c_1} \ 3\sqrt{3}/8. \quad (E-4)$$

The statistical parameters governing a possible extreme value distribution of critical stress intensity factors can be expressed in terms of the crack half-length  $c_1$  and factors of proportionality  $f_{kL}$  and  $f_{k0}$ , as well as an exponent  $m_k$ :

$$k_L = f_{kL} S_L \sqrt{c_1}, \quad k_0 = f_{k0} S_0 \sqrt{c_1}, \quad m_k. \quad (E-5)$$

(E-4) and (E-5) are introduced into an expression similar to (E-3) for the statistical distribution of critical stress intensity factors.

Some insight into appropriate choices of the factors  $f_k$  can be obtained by expressing the parameters  $k_L$  and  $k_0$  for the distribution of the stress intensity factors in terms of those for the stress at a distance  $\delta$  beyond the tip of a crack:

$$S_L = k_L/\sqrt{2\delta}, \quad S_0 = k_0/\sqrt{2\delta}. \quad (E-6)$$

Substituting (E-6) into (E-5) suggests:

$$f_{kL} = f_{k0} = \sqrt{2\delta/c_1}. \quad (E-7)$$

At the same time, assume  $m = m_k$ .

Even if the part is large enough for cracks to be stable initially, the applied stress for further cracking will eventually reach a maximum. For very large variability, this maximum might arise from a high density of more or less separate cracks, making a region soft compared to its surroundings. With small to moderate variability, however, the maximum is more likely to be due to the formation of a large crack in generally good material. To estimate the resulting maximum stress and the number of cracked segments at which it is reached, approximate the actual conditions by a linear array of  $N$  grain segments of which the fraction  $p$  are cracked. The longest contiguous crack which has a probability  $\phi$  of forming before a given applied stress  $S$  is given in terms of segment lengths approximately by (McClintock, 1973):

$$N_c = \frac{\ln \left[ \frac{N\sqrt{p}}{(7.5 - 1/\ln p)(-\ln(1-\phi))} \right]}{-\ln p}. \quad (E-8)$$

The fraction  $p$  of segments cracked is taken to be that expected for isolated segments at that stress level; from (E-3) applied to an individual grain boundary,

$$p = 1 - \exp \left[ - \left( \frac{S - S_L}{S_0 - S_L} \right)^m \right]. \quad (E-9)$$

The total number of micro-cracks is  $N_t = N_p$ .

If an applied stress  $S_u$  is required to extend a unit crack through a neighboring segment, then from fracture mechanics, a crack of length  $N_c$  will extend under applied stress  $S$  when:

$$S = S_u / \sqrt{N_c} \quad \text{or} \quad N_c = (S_u / S)^2. \quad (E-10)$$

The strength of a unit crack may be taken to be the median strength for fracture from the weakest of four neighboring grain segments, assuming the unit cracks stop at triple points:

$$S_u = f_{kL} S_L + (f_{k0} S_0 - f_{kL} S_L) \left[ \frac{1}{4} \ln 2 \right]^{1/m_k}. \quad (E-11)$$

Then  $S = S_{\max}$  when the fraction  $p$  of cracked segments from (E-9) leads statistically to a crack of length given by (E-8), and the stress simultaneously allows the propagation of that crack as given by the fracture criterion, (E-10).

The values for  $S_{\max}$  were calculated by an iterative process, bisecting upper and lower bounds for  $S_{\max}$  to see in which region the solution of (E-8) and (E-10) lay. The initial bounds for  $S_{\max}$  were taken as  $S_L$  and  $S_0$ . The results are presented in Table E-1, along with the number of cracked grains at macroscopic fracture,  $N_t$ .

Discussion of theoretical distribution. The strengths for a variety of part sizes and four different grain boundary strength distributions were calculated using both the analytical and numerical models. The boundary strength distributions, having the form of (E-2), are characterized by the lower limit  $S_L/S_0$  and exponent  $m$ . The corresponding coefficients of variation and mean strengths are given in Table E-2. The factors  $f_{kL}$  and  $f_{k0}$  for the critical stress intensities of (E-5) and (E-7) were chosen by taking the distance from the crack tip to the initiation site divided by the segment half-length to be  $\delta/c_1 = 0.125$ .

Fig. E-4 presents the number of cracked segments as a function of applied stress, as obtained from both the analytical and numerical models for  $m = 3$ ,  $S_L/S_0 = 0$ , and a part size  $N = 111$ . According to the analytical model, the maximum stress occurs when the longest

Table E-1 Stress for first fracture and maximum stress as a function of probability  $\phi$ , part size  $N$ , and various strength distribution functions

For  $\phi = 0.5$

	$N$	$S_{2\text{cntg}}$	$S_{1\text{st}}$	$S_{\text{max}}$	$N_t = Np$ at $S_m$	$N_c$ at $S_m$
$m = 3$ $S_L/S_0 = 0$	1.0 E 1	.4293	.4108	.4956	1.146	.750
	1.0 E 2		.1907	.3819	5.418	1.264
	1.0 E 3		.0885	.3269	3.433 E 1	1.724
	1.0 E 4		.0411	.2923	2.466 E 2	2.157
	1.0 E 5		.0191	.2678	1.902 E 3	2.570
	1.0 E 6		.0088	.2492	1.536 E 4	2.968
	1.0 E 7		.0041	.2344	1.280 E 5	3.354
	1.0 E 8		.0019	.2222	1.091 E 6	3.733
$m = 3$ $S_L/S_0 = 0.5$	1.0 E 1	.5996	.7054	.7325	.957	.670
	1.0 E 2		.5953	.6409	2.213	.875
	1.0 E 3		.5442	.5938	6.581	1.020
	1.0 E 4		.5205	.5647	2.164 E 1	1.128
	1.0 E 5		.5095	.5452	7.385 E 1	1.210
	1.0 E 6		.5044	.5317	2.548 E 2	1.272
	1.0 E 7		.5021	.5222	8.752 E 2	1.319
	1.0 E 8		.5010	.5155	2.979 E 3	1.353
$m = 10$ $S_L/S_0 = 0$	1.0 E 1	.6462	.7657	.7934	.941	.663
	1.0 E 2		.6083	.6861	2.285	.887
	1.0 E 3		.4832	.6193	8.264	1.089
	1.0 E 4		.3838	.5713	3.697 E 1	1.279
	1.0 E 5		.3048	.5344	1.898 E 2	1.462
	1.0 E 6		.2421	.5048	1.074 E 3	1.639
	1.0 E 7		.1923	.4803	6.531 E 3	1.810
	1.0 E 8		.1528	.4596	4.204 E 4	1.977
$m = 10$ $S_L/S_0 = 0.5$	1.0 E 1	.7081	.8829	.8931	.863	.629
	1.0 E 2		.8041	.8262	1.387	.735
	1.0 E 3		.7416	.7801	3.039	.824
	1.0 E 4		.6919	.7448	7.911	.904
	1.0 E 5		.6524	.7165	2.317 E 1	.977
	1.0 E 6		.6211	.6931	7.381 E 1	1.044
	1.0 E 7		.5962	.6734	2.516 E 2	1.106
	1.0 E 8		.5764	.6565	9.025 E 2	1.163

Table F-2     The mean and coefficient of variation of grain boundary strengths for the values of  $S_L/S_0$  and  $m$  investigated (evaluated from Eqs. 12 and 13, with  $A_0/A = 1$  ).

$$S_L/S_0 = 0$$

$$S_L/S_0 = .5$$

$m = 3$	$\bar{S}/S_0 = .8930$ $\sigma/\bar{S} = .3789$	$\bar{S}/S_0 = .9465$ $\sigma/\bar{S} = .1794$
$m = 10$	$\bar{S}/S_0 = .9514$ $\sigma/\bar{S} = .1203$	$\bar{S}/S_0 = .9757$ $\sigma/\bar{S} = .0616$

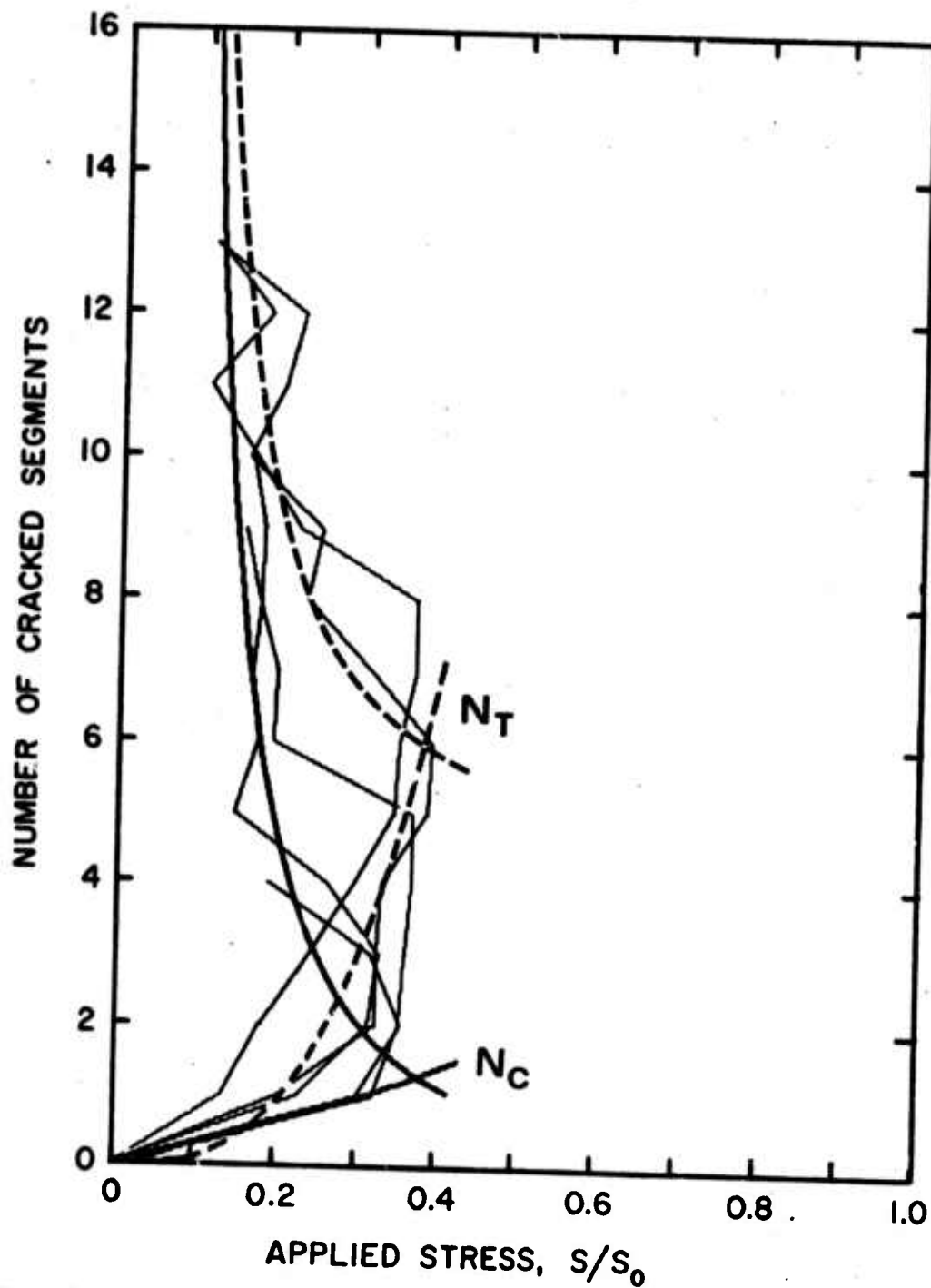


Fig. E-4. Number of cracked segments as a function of applied stress, obtained from the analytic and numerical models. For  $m=3$ ,  $S_L/S_0=0$ ,  $f_k=.77$ , and  $N=111$ .



contiguous crack and the stress satisfy the Griffith criterion. Thereafter, the cracking is more or less contiguous, with a generally decreasing applied stress. The increase in total cracked segments  $N_t$  is some multiple of the increment in crack length, depending on the amount of side-cracking for a growing crack.

The numerical results are in general agreement with the analytical model. There is a large variability in the stress for first cracking, as expected, but relatively little in the maximum stress.

The results for a range of values of  $m$  and  $S_L/S_0$  are presented in Fig. E-5, which gives the strength as a function of part size for the stress for first cracking,  $S_{1st}$ ; the average stress required for contiguous cracking from a unit crack,  $S_u$ ; and the maximum strength,  $S_{max}$  (from (E-3), (E-8), (E-10) and (E-11)). For the numerical model, the maximum strength was taken to be that before an abrupt and continuing decrease in load, which accompanied the formation of contiguous cracking.

#### Finding parameters from acoustic emission data.

Since large numbers of cracks occur before  $S_{max}$  is reached, but these are only a small fraction of all segments (see Table E-1), it may be possible to

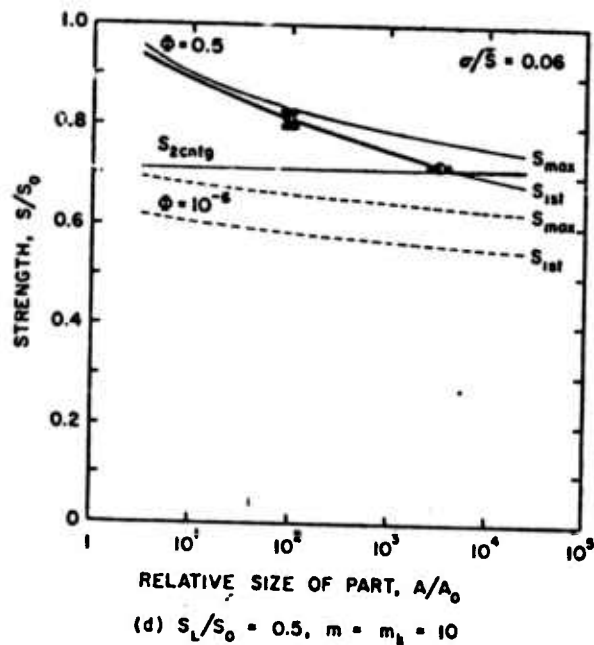
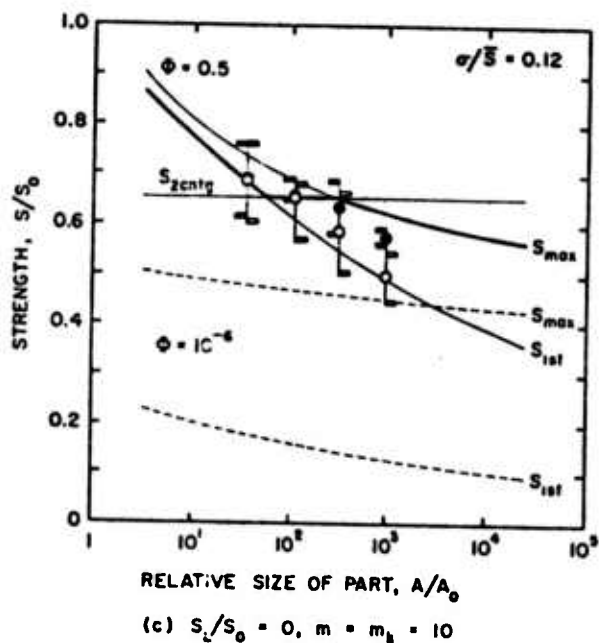
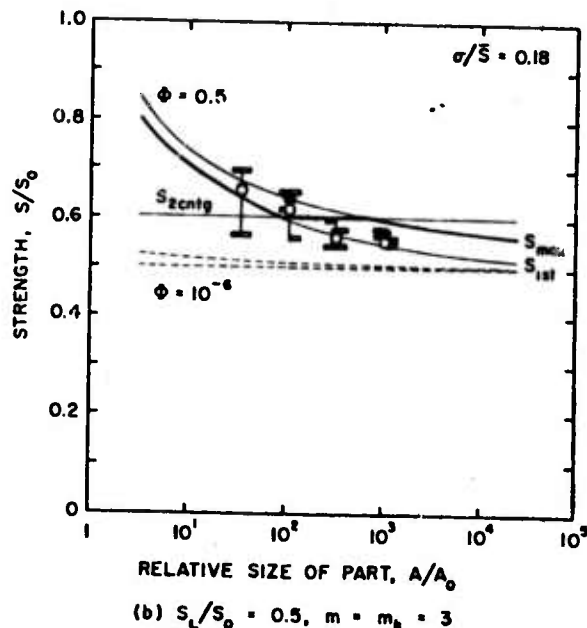
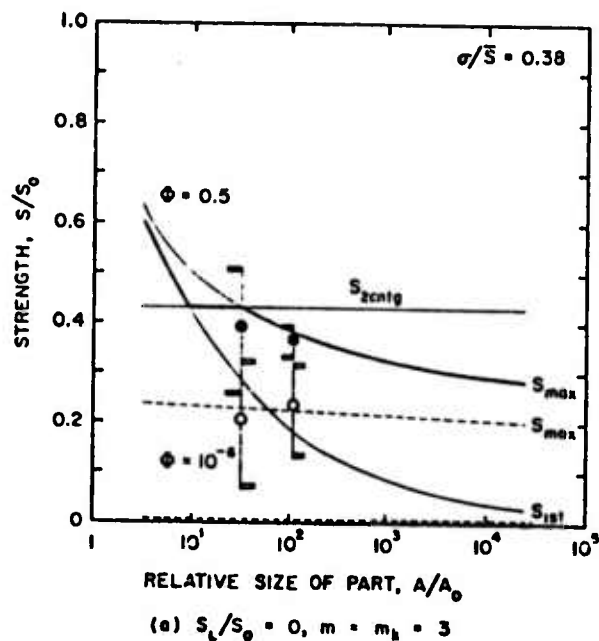


Fig. E-5. Statistical strength as a function of part size for various strength distribution functions characterized by exponent  $m$ , and lower limit  $S_L/S_0$ ;  $f_{k0} = f_{k1} = 0.77$ . (○ first cracking; ● instability)

determine the distribution of crack strengths as a function of stress using acoustic emission as follows:

a. For a small fraction of pre-cracks compared to the total of crack sites, expansion of the exponential of (E-9) gives:

$$n \left[ \frac{N_t}{N} \right] = m \ln \left[ \frac{S - S_L}{S_0 - S_L} \right] . \quad (E-12)$$

The lower limit to crack strength,  $S_L$ , can be varied until a plot of (E-12) gives a linear relation. Alternatively, it may be desired to simply assume  $S_L$  is zero. Assuming the total number of possible fracture sites  $N$  then allows determining the parameter  $S_0 - S_L$ . The exponent  $m$  can be obtained from the slope of the plot.

b. The crack propagation characteristics are all lumped into the strength of a unit crack,  $S_u$  of (E-11). With the other parameters known,  $S_u$  can be found as a function of failure probability in test to complete fracture according to a rearrangement of (E-8), (E-10) and (E-12), neglecting a term of unity compared to  $\ln p$ :

$$S_u = S_{\max} \left[ \frac{\ln \left[ \frac{2N}{\ln(1/(1-\phi))} \right]}{-m \ln \left[ \frac{S_{\max} - S_L}{S_0 - S_L} \right]} - \frac{1}{2} \right]^{1/2} . \quad (E-13)$$

$S_u$  could most readily be evaluated for  $\phi = .5$ , but should remain constant for any failure probability.

A non-constant  $S_u$  may be adjusted by carefully re-evaluating the constants  $m$ ,  $S_L$ , and  $S_0$ .

The maximum strength of uniformly stressed parts subject to proof testing can now be estimated from acoustic emission data, provided it can be assumed either that  $S_u$  is relatively invariant, or that it is related in a constant way to the crack initiation parameters  $m$ ,  $S_0$ , and  $S_L$ . In the latter case,  $S_u$  is found from (E-11). In either case, the probability of failure at any given stress level can then be found by substituting into (E-13).

Conclusions from the analytical and numerical models.

a. The expected decrease in the stress for first cracking with increasing size of part and with increasing coefficient of variation is illustrated.

b. The maximum stress  $S_{max}$  decreases with increasing coefficient of variation and increasing part size, in a fashion similar to that for first cracking but with a much lower dependence on part size for large coefficients of variation.

c. The number of cracked segments at instability ( $N_t$  in Table E-1) increases with increasing part size, while the fraction of cracked segments  $N_t/N$

decreases (more slowly).

d. The agreement of the analytical model with the numerical one is good, considering the number of approximations involved and the small numbers of cases run (the extremes of a sample of 5 represent 93.75% confidence limits for the median of a population). It therefore seems reasonable to use the analytical model to estimate the stress levels for high level of confidence, such as the values for  $\phi = 10^{-6}$  shown by the broken lines in Fig. E-4.

e. The extreme-value distribution is over-conservative by a factor of two to ten as a basis for predicting the mean strength of parts 1000 times larger than the test specimens, when the underlying grain boundary strengths have a lower limit of zero. Furthermore, the variability of the maximum strength is often different from the variability of the stress for first cracking. For these reasons, extreme-value (Weibull) statistics are not appropriate for estimating the maximum strength of statistically homogeneous, polycrystalline material, such as considered here.

f. The above conclusions, along with the fact that 4 significant parameters are involved in the new

theory, and the procedure for estimating them from acoustic emission data, suggest that statistical and acoustic emission data should be obtained for materials of interest which have statistically homogeneous microstructures.

g. Microstructural data are needed for other materials in order to develop a theory that is applicable when inhomogeneities such as holes, micro-cracks, and inclusions already exist.

### E.3 DETERMINING STRENGTH DISTRIBUTIONS FROM EXPERIMENTAL DATA

Analysis of data. For designing laser windows one of the main conclusions reached above is that if the strength is governed by multiple cracks, the distribution function is not of the extreme-value type. On the other hand, if the first crack is catastrophic, the extreme-value theory is still appropriate, whether the crack grows from a pre-existing crack or is formed at fracture.

To predict the probability of fracture in laser windows, we need to know this distribution of strength. Furthermore, the susceptibility to laser irradiation may be changed by sub-critical damage occurring during

operation in rain or fog.

We therefore turn to finding the distribution of strengths in laser windows experimentally by micro-hardness tests, or other tests in which only a small area of material is stressed at any one time. The technique is a generalization of the method of Argon (1959) for finding the distribution of strengths from the distribution of fracture loads on hardness indentures. The complete paper is given in the Appendix, and will only be summarized here.

Let the probability of fracture at or below the stress  $S_1$  in an element of area  $b\delta z$  (the case for an annular element of area  $2\pi z dz$  is considered in the Appendix) be given by:

$$\delta\Phi(S_1) = b\delta z \int_0^{S_1} g(S) dS. \quad (E-14)$$

Assume further that the stress varies with a dimensionless coordinate  $z/l$  and the maximum stress (proportional to load) on the part,  $S_m$ , according to:

$$S_1 = S_m (1 - z/l)^k. \quad (E-15)$$

The exponent  $k$  can be either positive or negative. The probability of fracture of the complete part below the nominal stress  $S_m$  is then given by:

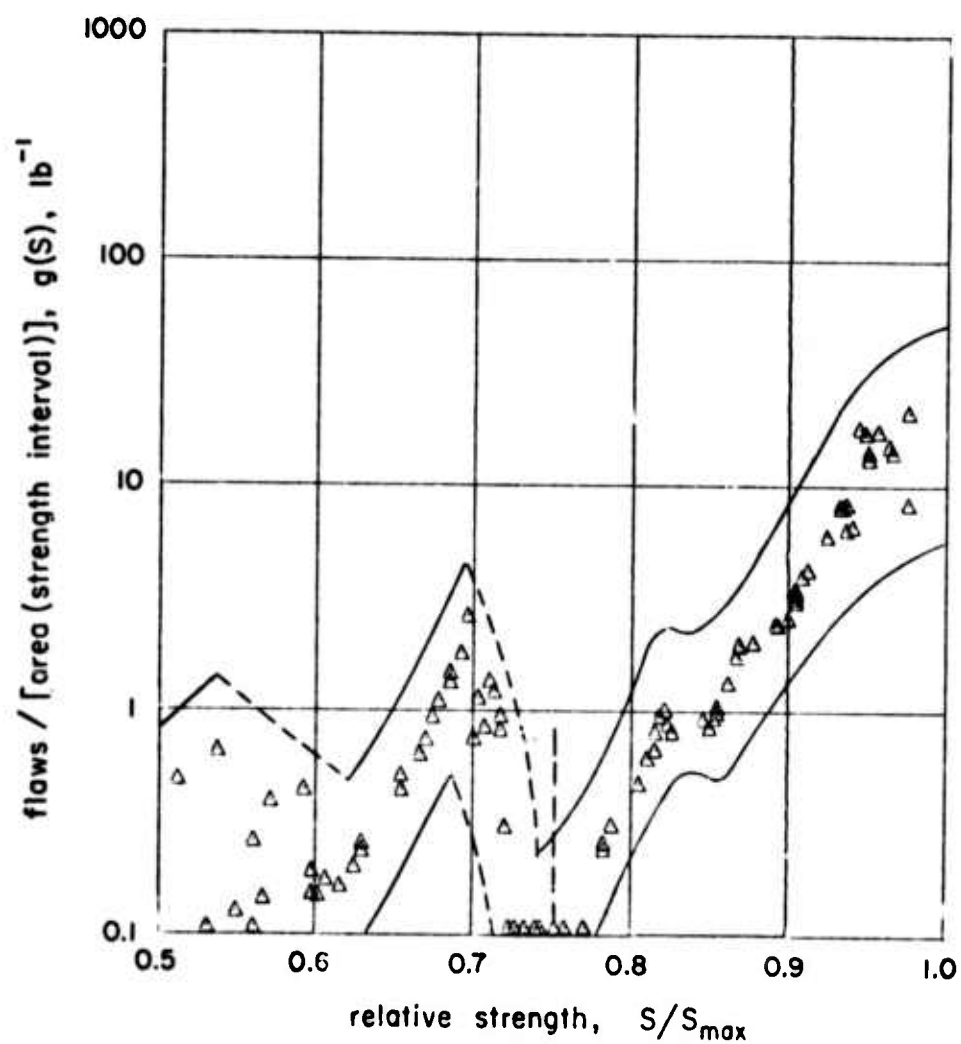


Fig. E-6 Flaw density distribution for sheet glass  
 (  $7/32$  in. thick,  $1/16$  in. indenter,  $S_{\max} = 222,000$  psi)  
 Matthews, McClintock and Shack, (1975).



$$1 - \phi(S_m) = \exp \left( -2b \int_0^{\ell} \int_0^{S_m} \frac{(1-z/\ell)^k}{g(S)} dS dz \right). \quad (E-16)$$

Conversely, as shown in Appendix E-1, the distribution  $g(S)$  can be found from  $\phi(S_m)$  and its first two derivatives:

$$g(S_m) = \frac{S_m |k|}{2b\ell} \left[ \frac{\phi''(S_m)[1-\phi(S_m)] + [\phi'(S_m)]^2}{1-\phi(S_m)} + \frac{(1 + \frac{1}{k})}{S_m} \frac{\phi'(S_m)}{1-\phi(S_m)} \right]. \quad (E-17)$$

Numerical results for the flaw density distribution. A computer program was written to calculate the flaw density distributions according to (E-17), Appendix E-2. The program first generates the cumulative failure distribution function  $\phi(P)$  by ordering the experimentally observed failure loads. A running fit for  $\phi(P)$  in terms of an expansion in Chebychev polynomials was then calculated using a least square criterion. Along most of the curve, a third-order fit was applied to 25 data points, but as few as 7 points were used at the ends. From this interpolating polynomial its derivatives  $\phi'(P)$  and  $\phi''(P)$  were calculated, and then  $g(S)$  was found.

Numerical results for sheet glass as tested by Argon (1959) are presented in Fig. E-6. In order to

estimate the effect of sampling errors on our calculation of  $g(S)$ , twenty sets of new data were generated by random sampling from a smoothed cumulative distribution function and used as input to recalculate  $g(S)$ . The resulting scatter band for  $g(S)$ , about a factor of 3 either side of the mean, was then assumed to represent a 95% confidence limit, and is shown in Fig. E-6.

Figure E-5, showing a 95% confidence limit scatter band for the flaw density of sheet glass, indicates that a definite concentration of flaws exists at  $S/S_{\max}$  equal to 0.7, which suggests that the flaws are from some special source. This then indicates that a change in processing may eliminate this source, as will be shown to be true in Appendix E-1.

#### E.4 THERMAL SHOCK PROOF TESTING OF BRITTLE MATERIALS

Destructive testing has been the only method of locating flaws (see section E.6) in laser windows since, in general, the critical flaws are extremely small (i.e., of the order 100  $\mu\text{m}$  Matthews, 1974) and it did not seem possible to detect them by nondestructive testing methods (Matthews, 1974).

A proof testing system was developed which uses a localized source of thermal shock to propagate flaws

or initiate cracks from imperfections which might make a laser window unacceptable in service. A heat sink rather than a heat source was employed in order to remain below the transition temperature to avoid yielding of the material and hence to minimize effects of proof testing. When the developed stress and strain due to a nitrogen jet (i.e., the heat sink) cause a flaw to become an unstable crack, the crack grows to the extent of the cooled region, which is approximately 1 cm. This saves the laser window from complete destruction. See Appendix E-3 for a detailed discussion of the thermal shock proof testing system.

Calculations for the stresses developed by the thermal shock proof testing system for various materials were made. As shown in Table B-1 in Appendix E-3, the system is most applicable to certain laser window materials (e.g., KCl) as determined by the stress levels achieved. For the materials where the thermal stresses are just insufficient to provide a useful proof test, a known prestress (e.g., three-point bend test) may be superposed with the thermal stress to achieve stresses of the required magnitude.

## E.5 FRACTURE TOUGHNESS OF ZnSe

The mechanical strength of laser windows is primarily determined by their ability to resist fracture. Fracture will occur either at cracks of a critical size, in regions of low cohesive strength, or in regions of plastic-flow induced cracking. In any case, the length of any prior crack, which would have to be eliminated for improved strength, can be found from the fracture or working stress, once the fracture toughness is known.

Some fracture toughness tests performed on ZnSe are described below. The results of these tests, which are consistent with the subsequently published work of Evans and Johnson (1975), and the resulting implications on laser window design will also be discussed.

### Test procedure for fracture toughness test.

A double cantilever beam specimen was used in performing the fracture toughness test. Fig. E-7 shows two .45 mm grooves put into the specimen to insure that the crack would run along the center of the specimen. The crack front remained normal to the grooves indicating that a state of plane strain existed. A good approximation for the fracture toughness is given by Wiederhorn and Bolz (1970) in terms of the crack length  $L$ , the load  $P$ , and the dimensions  $w$ ,  $a$ , and  $t$  of Fig. E-7:

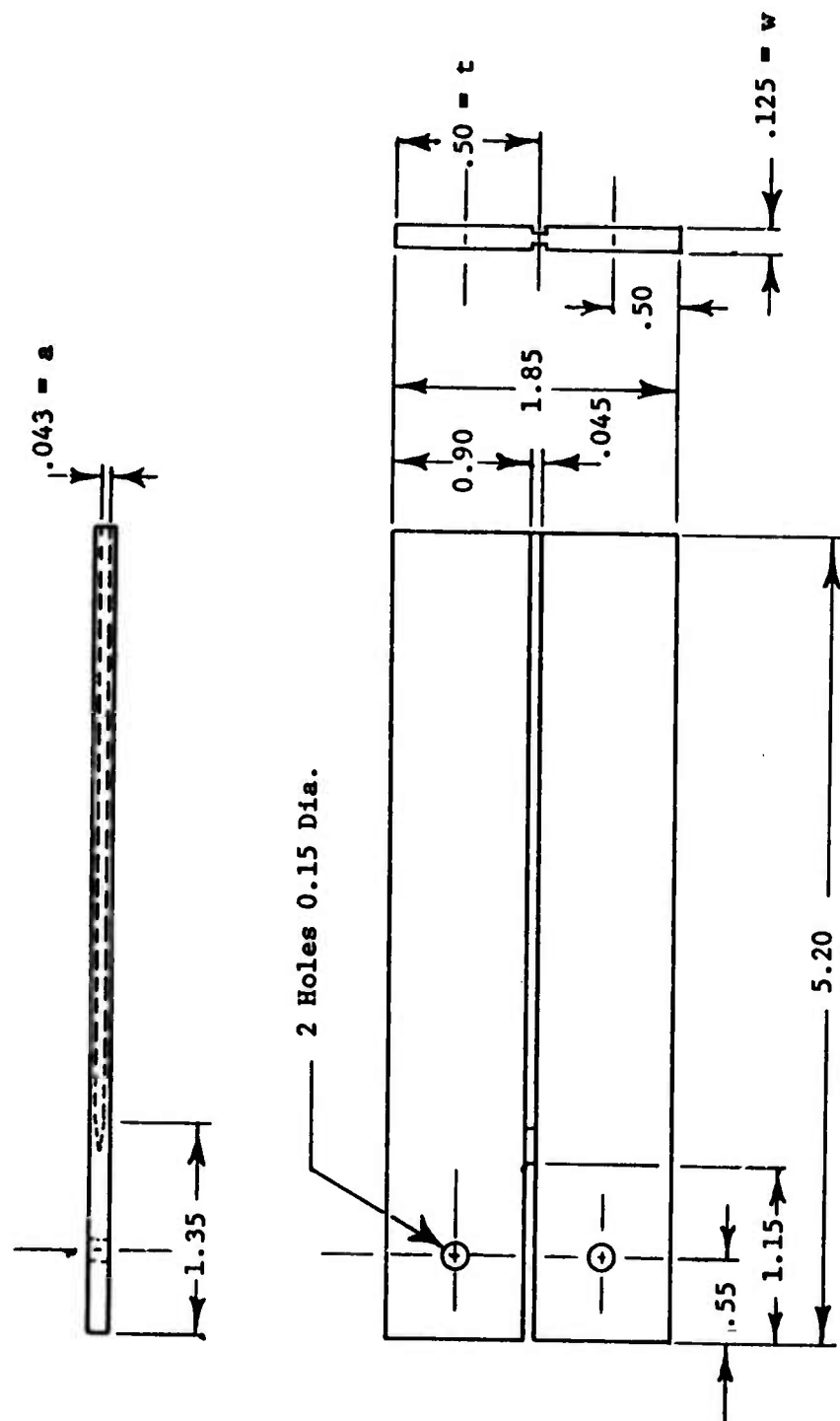


Fig. E-7. Fracture Toughness Test Specimen  
(all dimensions in centimeters)

$$K_{IC} = \frac{PL}{\sqrt{wat^3}} [3.47 + 2.32 t/L]. \quad (E-18)$$

Equation (E-18) was derived by the energy method in which the area moment of inertia of the cantilever beams was used without making any corrections to account for the web (which only produced about a 1% error in the equation for the specimen configuration used).

The fracture toughness test was performed using an Instron Universal Tester with the beam end displacement rate held constant at .0050 mm/min. In order to control any effects of corrosion fatigue (Evans and Johnson, 1975), the test was performed in dry argon gas (e ppm water).

The crack length was measured by aligning a microscope with the crack tip. In most cases the crack would spurt ahead too fast to keep the microscope on the crack tip. Thus, only the positions at which the crack was temporarily stationary were noted. From the data obtained in Fig. E-8,  $K_{IC}$  was calculated to be  $0.75 \text{ MN/m}^{3/2}$  using (E-18), with mean crack velocity of  $10^{-4} \text{ m/sec}$ . This value compares reasonably well with the subsequently published value of  $K_{IC} = .9 \text{ MN/m}^{3/2}$  obtained by Evans and Johnson (1975) for a crack growth rate of about  $10^{-5} \text{ m/sec}$  in a dry atmosphere.

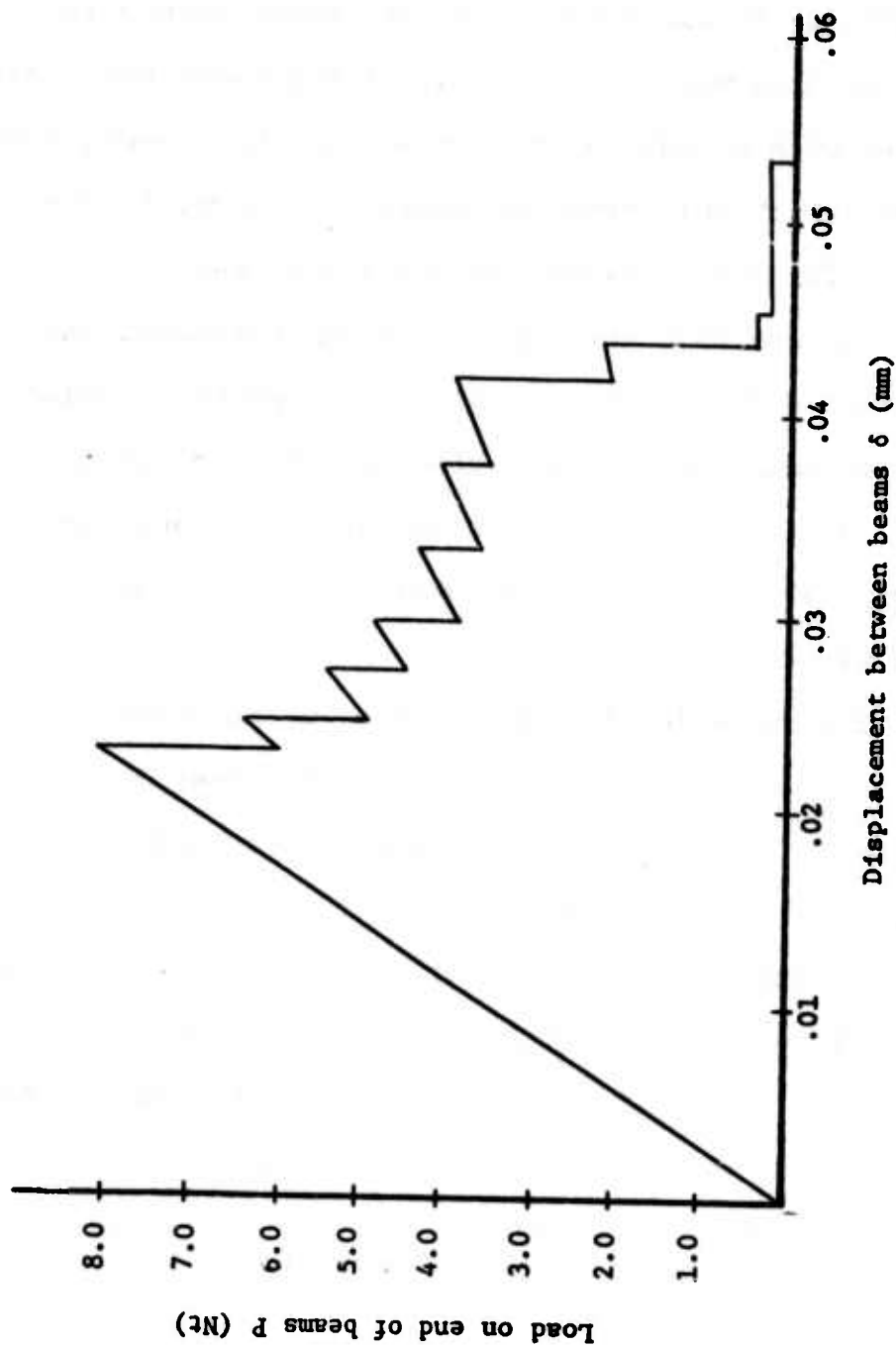


Fig. E-8. Load Deflection Curve of Fracture Toughness Test Specimen.

The value determined for  $K_{IC}$  may have been influenced by the thin web used in the specimen. The web was only fifteen grain diameters thick, which indicates that possibly a true macroscopic  $K_{IC}$  was not determined since the value for  $K_{IC}$  would be susceptible to variations in local strengths of the ZnSe. Furthermore, the particular sample of ZnSe used apparently has a porosity which may have affected the  $K$  value.

#### Implications of $K_{IC}$ test on ZnSe laser window

Design. Data for the mean ultimate strength  $\sigma$  was obtained from Wurst and Kuhl (1973) who found the working stress in polycrystalline ZnSe to be about  $45 \text{ MN/m}^2$ . Using this value for the stress and using  $K_{IC} = .75 \text{ MN/m}^{3/2}$ , the critical crack half-length  $c$  was determined to be about  $90 \text{ }\mu\text{m}$  as found from the applied stress  $\sigma$  and the fracture toughness  $K_{IC}$  by using:

$$c = \frac{1}{\pi} \left( \frac{K_{IC}}{\sigma} \right)^2. \quad (\text{E-19})$$

Since a proposed surface coating on ZnSe laser window materials is about  $2 \text{ }\mu\text{m}$  thick, (Braunstein et al., 1973) the coating would have a negligible effect on the fracture behavior of ZnSe laser windows. It was also



noted that the average grain size in the ZnSe sample used for fracture toughness tests was about  $30\text{ }\mu\text{m}$ . Since the critical crack half-length at  $45\text{ MN/m}^2$  is about  $90\text{ }\mu\text{m}$ , a contiguous crack of about 6 grain diameters must form to be critical. Thus, as discussed in section E.2, a ZnSe laser window is relatively tough and should fail with some warning (i.e., sub-critical cracks distributed through the window).

Determining the required number of tests for predicting failure rates of laser windows. Suppose it is required to predict the stress at which a certain fraction of windows fail (e.g., let  $\phi = 1/1000$ ) without any prior knowledge of the strength distribution  $g(S)$ . Then the question arises, how many tests must be performed to predict the required failure rate.

To find the stress that can be applied to a window while still maintaining the required failure rate  $\phi = 1/1000$ , consider a test where one thousand windows are stressed up to failure and then conclude that the allowable stress is the stress at which the weakest window broke. Generalizing the above argument, it is seen that the total area  $A_T$  of material which must be tested to predict a failure rate  $\phi$  for a window of area  $A$  is:

$$A_T = \frac{A}{\Phi} . \quad (E-20)$$

But, of course, there is always scatter in experimental data (e.g., see Fig. E-6) so the stress at which one window in a set of a thousand windows fails will vary between each set of a thousand windows. Thus, (E-20) is a lower bound to the amount of area which must be tested if the strength distribution  $g(S)$  is unknown.

In general, it is impractical to test a complete surface of a window at one time. Furthermore, it is desirable not to stress the total surface to the stress level of interest because then some cracks may become unstable and go across the whole window. Thus, a localized stress is suggested so as not to ruin the whole window in one test. If we test only a fraction  $f$  of the window surface at a given time, then the total number of tests  $N$  that must be performed is:

$$N = \frac{1}{f\Phi} , \quad (E-21)$$

where (E-21) is a lower bound for the number of tests required for predicting failure rates as was (E-20).

It does not seem probable that strength distribution curves can be extrapolated to low stresses due to the complexity of the strength distributions; the tail

end of the  $g(S)$  curve is unknown. Thus, it is seen that for predicting failure rates, the strength distributions are, for practical purposes, unknown, which was our original assumption and hence (E-20) and (E-21) are valid.

To obtain enough data to predict failure rates, it is seen from (E-21) that many tests must be performed and hence the test method selected is unimportant in reducing the magnitude of the number of tests required.

#### E.6 OPTICAL DETECTION OF FLAWS

A "nonlinear optical" observation technique using second harmonic generation, Hellwarth and Christensen (1974), may prove to be a nondestructive method for locating flaws in laser windows. The operation of the optical system is based on their noting that even though there is little, if any, variation in the refractive indices associated with the structural inhomogeneities, there is invariably an associated large spatial variation in the nonlinear refractive indices. Hellwarth and Christensen relate the intensity  $I$  of the second-harmonic generated to the thickness  $l$  of the structure of interest (e.g., a flaw) and the wave vector  $\bar{q}$  which is inversely proportional to the

wavelength of the incident radiation:

$$I \propto l^2 (\sin ql/2)^2 / (ql/2)^2. \quad (E-22)$$

It is suggested that this method be tried for detecting possible cracks in laser windows. From (E-22) it is seen that the intensity varies with the crack thickness, hence implying that an illuminating laser must be chosen to increase  $\bar{q}$  such that the second harmonic generated can be detected.

Further work must be done to determine whether the other types of flaws such as regions of low cohesive strength can be detected by the optical system described above.

Another technique that may prove useful in detecting flaws optically has yet to be tested. This method for detecting flaws is based on the principle of detecting light which is reflected or scattered by a flaw (Born and Wolf, 1975). In practice, this method may be tested by illuminating a window through one edge and at the same time detecting any possible scattered light.

## E.7 CONCLUSION

1. While strengths limited by surface flaws could follow an asymptotic extreme-value distribution, those governed by the coalescence of subsurface flaws do not. Experiments to find the distribution would therefore be desirable.

2. A new procedure for converting fracture load statistics to strength distributions showed that in glass, at least, concentrations of flaws could be revealed. Too many tests were required to obtain the tail of the  $g(S)$  curve accurately enough to predict desired failure rates of full-scale windows. But, without some prior knowledge of the shape of the strength distribution, improved processing could reduce concentrations of flaws and thus reduce the failure rates.

3. The impracticality of predicting failure rates from strength distribution curves suggests a need for proof testing. A thermal shock proof testing system was developed using a heat sink to avoid yielding the material and to remain below the transition temperature. Besides rapid testing, only about a 1 cm. diameter region was tested at a given time, thus preventing

cracks from growing across the whole window. For some materials, where the induced thermal stresses are just insufficient to proof test the window, a preload can be applied, for instance, by bending.

4. In order to determine the effect of surface coatings on the fracture behavior of laser windows, a critical crack size had to be determined. This was done by performing fracture toughness tests on ZnSe at slow crack growth rates in dry gas to control stress corrosion. The stress intensity was found to be  $.75 \text{ MN/m}^{3/2}$  which is in good agreement with the subsequently published value of  $.9 \text{ MN/m}^{3/2}$  as determined by Evans and Johnson. Using a working stress of  $45 \text{ MN/m}^2$  and  $.75 \text{ MN/m}^{3/2}$  for  $K_{IC}$ , a critical crack half-length was found to be about  $90 \text{ }\mu\text{m}$ . Thus, a window coating of  $2\text{ }\mu\text{m}$  thickness would have a negligible effect on the fracture behavior of a ZnSe laser window.

It is also noted that the average grain size of the ZnSe tested was about  $30\text{ }\mu\text{m}$ , thus a contiguous crack with a length of about 6 grain diameters must form before unstable fracture occurs. Hence the laser window is relatively tough and should fail with some warning such as an unusually high number of subcritical cracks.

5. Two possible methods for optically locating possible flaws were discussed. The first utilized spatial variations in the second-order nonlinear sus-

ceptibility of polycrystalline ZnSe to generate images of its physical structure at the second harmonic frequency of an incident laser beam. Single crystal platelets, about 60  $\mu\text{m}$  in diameter and 1  $\mu\text{m}$  thick were discovered using this method, indicating that this method may be useful in detecting possible cracks whose size is of the order of the platelets. A second method for detecting flaws, which has yet to be tried, is based on the fact the cracks and cavities scatter and reflect light. Thus, it was suggested that possible cracks could be located by dark-field viewing of any light which has been perturbed from the irradiating beam.

E.8      References for Section E.

Argon, A.S., (1959), "Surface Cracks on Glass", Proc. of Royal Society, A, Vol. 250, pp. 422-481.

Batdorf, S.B.; Crose, J.G. (1973), "A Statistical Theory for the Fracture of Brittle Structures Subjected to Non-uniform Polyaxial Stresses", Aerospace Corp. Rep. No. TR-0073 (3450-76)-2 for Space and Missile Systems Organization, Air Force Systems Command, Los Angeles Air Force Station, Report SAMSO-TR-73-162, 34 pp.

Born, M. and Wolf, E., (1975), Principles of Optics, 5th ed., (Pergamon Press, 485 Fitzroy Square, London W.1.), pp. 657-664.

Buch, J.D., (1975), "Mechanistic Model of Graphite Behavior", Extend Abstracts of Proceedings of the 12th Biennial Conference on Carbon, Pittsburgh, Pa., pp. 129-130.

Crose, J.G., Buch, J.D., and Robinson, (1975), "A Fracture Criteria for Anisotropic Graphite", Extended Abstracts of Proceedings of the 12th Biennial Conference on Carbon, Pittsburgh, Pa., pp. 131-132.

Dukes, W.H., (1971), Handbook of Brittle Material Design Technology, AGARD-AG-152-71, pp. 1-16.

Evans, A.G. and Johnson, H., (1974), "A Fracture-Mechanics Study of ZrSe for Laser Window Applications", J. of The Am. Cer. Soc., vol. 58, no. 5-6, pp. 244-249.

Gumbel, E.J., (1958), Statistics of Extremes, chapters 5, 6, and 7, Columbia University Press, N.Y., pp. 156-305.

Hellwarth, R. and Christensen, P., (1974), "Nonlinear Optical Microscopic Examination of Structure in Polycrystalline ZnSe", Optics Communications, v. 12, no. 3, Nov. 1974, pp. 318-322.

Matthews, J.R., McClintock, F.A. and Shack, W.J., (1975), "Statistical Determination of Flaw Density in Brittle Materials", accepted for publication in J. Am. Cer. Soc.



McClintock, F.A., (1973), "Statistics of Brittle Fracture", Fracture Mechanics of Ceramics, R.C. Bradt, D.P.H. Hasselman, F.F. Lange, eds., Plenum Press, pp. 93-114.

McClintock, F.A. and Zaverl, F. Jr., "An Analysis of the Mechanics and Statistics of Brittle Crack Initiation", in manuscript.

Sih, G.C. and Liebowitz, H., (1968), "Mathematical Theories of Brittle Fracture", Fracture, v. 2, H. Liebowitz, ed., Academic Press, N.Y., pp. 93-94.

Weibull, W., (1939), "A Statistical Theory of the Strength of Materials", Ingeniors Vetenskaps Akademien Handlingar, No. 151.

Wiederhorn, S.M. and Bolz, L.H., (1970), "Stress Corrosion and Static Fatigue of Glass", J. of The Am. Cer. Soc., vol. 53, no. 10, pp. 543-548.

Wurst, J.C. and Kuhl, G.E., (1974), "Evaluation of Zinc Selenide for High Power Laser Window Applications", Third Conf. on High Power Infrared Laser Window Materials, vol. II, AFCRL-TR-74-0085 (II), Special Reports No. 174, C.A. Pitha, A. Armington, H. Posen, eds., pp. 733-745.

**APPENDIX E-1**

**Statistical Determination of Surface Flaw Density  
in Brittle Materials**

Statistical Determination of Surface Flaw Density  
in Brittle Materials

by

J. R. Matthews  
F. A. McClintock  
and W. J. Shack

Massachusetts Institute of Technology, Cambridge, Massachusetts 02139

*The density of surface flaws in brittle materials can be determined from the loads in many different kinds of tests. A general method is derived and applied to indentation experiments on crown, plate, window, lead, Pyrex and Solux glass. A knowledge of the flaw density is important for estimating size effect, and differences in the flaw density give insight into the possibility of significant improvements in strength by eliminating a few major sources of flaws.*

I. Introduction

In this paper we develop a procedure for determining the flaw density distribution in a brittle material from fracture tests with fields of varying stress such as indentation tests.

The flaw density distribution function was introduced by Weibull (1939) in the study of the statistical aspects of the strength of materials. Although this work produced valuable insight into the understanding of the size effect in fracture, it treated only certain asymptotic forms of the flaw density distribution function found by Fisher and Tippett (1928) and Frechét (1927). The asymptotic forms do not necessarily characterize the real distributions on various materials surfaces with any accuracy.

Argon (1959) carried out an extensive series of tests on various glasses and was able from his data to deduce flaw density distribution functions. However, his method involved extensive calculations and numerical inversion of Laplace transforms. In this paper we present a much more straightforward procedure. We then use this procedure to find the flaw density distributions from hardness test data for nine different glasses subjected to a variety of surface treatments.

## II. Surface Flaw Density Estimation for Varying Stress Over a Given Geometry

In order to consider the flaw statistics we divide the surface area of the specimen into a large number of small areas of size  $\delta A$ . We assume that: (a) the numbers of flaws giving strengths less than  $S_1$  in nonoverlapping areas are independent; (b) the probability,  $\delta\phi(S_1)$ , that a flaw giving strength less than  $S_1$  occurs in an area  $\delta A$  is proportional to  $\delta A$  when  $\delta A$  is small,  $\delta\phi(S_1) = \lambda\delta A$ ; (c) the probability that more than one flaw giving a strength less than  $S_1$  lies in  $\delta A$  is small compared with the probability that there is only a single flaw when  $\delta A$  is small. These assumptions are known in probability theory as the Poisson postulates. Using these postulates it is a standard result of probability theory (see, e.g., Feller (1957) or Lindgren and McElrath (1959)) that the proportionality constant  $\lambda$  is just the average number of flaws giving a strength less than  $S_1$  per unit area. Thus if we define the flaw density  $g(S)$  such that  $g(S)dS$  is the number of flaws per unit area of strength between  $S$  and  $S + dS$  then  $\lambda = \int_0^{S_1} g(S)dS$ , and the probability that a flaw giving a strength less than  $S_1$  occurs in an area  $\delta A$  is

$$\delta\phi(S_1) = \delta A \int_0^{S_1} g(S) dS \quad (1)$$

In addition to the assumptions on the statistics of crack distribution that we have made we will also assume that: (a) fracture occurs when the stress in  $\delta A$  reaches the nominal strength of any flaw in  $\delta A$ , and (b) failure occurs independently in each element, i.e., interaction effects between cracks are ignored. In this case the probability  $\delta\phi(S_1)$  can also be interpreted as the probability that a failure will occur in  $\delta A$  for a stress less than  $S_1$ . Then the probability that no failure will occur is

$$\begin{aligned} 1 - \delta\phi(S_1) &= 1 - \delta A \int_0^{S_1} g(S) dS \\ &= [\exp(-\delta A \int_0^{S_1} g(S) dS)] [1 + O(\delta A^2)] \end{aligned} \quad (2)$$

We will assume that the variation of stress  $S_1$  with distance  $z$  from the point of maximum stress  $S_m$  is given in terms of a characteristic length  $l$  by

$$S_1 = S_m (1 - z/l)^k \quad (3)$$

Eq. 3 is general enough in form to include the three point bend test.

Let  $\delta A = 2b\delta z$  where  $b$  is a characteristic width. Then since each element fails independently, the probability that the specimen will not fail at a stress less than  $S_m$  is

$$\begin{aligned} 1 - \phi(S_m) &= [1 - \delta\phi(S_1(z_1))][1 - \delta\phi(S_1(z_2))] \dots \\ &= e^{-2bf(z_1)\delta z} e^{-2bf(z_2)\delta z} \dots e^{-2bf(z_n)\delta z} [1 + n O(\delta z^2)] \end{aligned} \quad (4)$$

where

$$f(z) = \int_0^{S_m} (1 - z/\ell)^k g(S) dS \quad (5)$$

Since the number of elements  $n \sim 1/\delta z$

$$1 - \Phi(S_m) = [\exp(-\sum_{i=1}^n 2bf(z_i)\delta z)][1 + O(\delta z)]$$

and in the limit as  $\delta z \rightarrow 0$  the probabilities of survival  $P(S_m)$  or of failure  $\Phi(S_m)$  are

$$P(S_m) = 1 - \Phi(S_m) = \exp(-2b \int_0^{\ell} \int_0^{S_m} (1 - z/\ell)^k g(S) dS dz) \quad (6)$$

for some stress less than  $S_m$ .

Define a new function  $G(S_m)$  of the maximum stress  $S_m$ ;

$$G(S_m) = -\ln(1 - \Phi(S_m)) = 2b \int_0^{\ell} \int_0^{S_m} (1 - z/\ell)^k g(S) dS dz \quad (7)$$

Interchanging the order of integration and inserting a factor of  $\frac{k}{|k|}$ , to make the limits of integration correct, gives an integral equation for  $g(S)$

$$\begin{aligned} G(S_m) &= 2b \int_0^{S_m} g(S) \frac{k}{|k|} \int_0^{\ell} [1 - (S/S_m)^{1/k}] dz dS \\ &= 2b\ell \frac{k}{|k|} \int_0^{S_m} [1 - (S/S_m)^{1/k}] g(S) dS \end{aligned} \quad (8)$$

To solve Eq. 8 we note that

$$\begin{aligned} G'(S_m) &= \frac{dG}{dS_m} = 2b\ell \frac{k}{|k|} \int_0^{S_m} -1/k (S/S_m)^{1/k-1} (-S/S_m^2) g(S) dS \\ &= \frac{2b\ell}{|k|S_m} \int_0^{S_m} (S/S_m)^{1/k} g(S) dS \end{aligned} \quad (8a)$$

Differentiating once more we find

$$G''(S_m) = \frac{2bl}{|k|S_m} g(S_m) - \frac{1}{kS_m} \left[ \frac{2bl}{|k|S_m} \int_0^{S_m} (S/S_m)^{1/k} g(S) dS \right] \\ - \frac{1}{S_m} \left[ \frac{2bl}{|k|S_m} \int_0^{S_m} (S/S_m)^{1/k} g(S) dS \right] \quad (8b)$$

Eliminating the integral terms from (8b) using (8a) and solving for  $g(S_m)$  we obtain:

$$g(S_m) = \frac{|k|S_m}{2bl} [G''(S_m) + \frac{(1 + 1/k)}{S_m} G'(S_m)] \quad (9)$$

(If, instead of (3) we have the more general relationship  $S_1/S_m = f(z/l)$  or solving for  $z/l$ ,  $z/l = h(S_1/S_m)$ , then instead of 8 we obtain

$$G(S_m) = 2bl \int_0^{S_m} [1 - h(S/S_m)] g(S) dS \quad (8^*)$$

However, simple closed form solutions of (8\*) are obtainable only for special forms of  $h(S/S_m)$ , see, e.g. Hildebrand (1952). In general, numerical solutions would be required.)

Using Eq. 7 we can rewrite Eq. 9 directly in terms of  $\phi(S_m)$ ;

$$g(S_m) = \frac{|k|S_m}{2bl} \left\{ \frac{\phi''(S_m)[1 - \phi(S_m)] + [\phi'(S_m)]^2}{[1 - \phi(S_m)]^2} \right. \\ \left. + \frac{(1 + \frac{1}{k})}{S_m} \frac{\phi'(S_m)}{1 - \phi(S_m)} \right\} \quad (10)$$

Eq. 10 gives a straightforward method for calculating  $g(S_m)$  when  $\phi(S_m)$  is known from experimental data.

### III. Determination of Flaw Density Distributions from Indentation Experiments

The ball indenter is ideally suited for investigations of the surface flaw density in glasses, since it stresses only very small areas of the

surface at any one time. When an elastic, spherical indenter of radius  $R$  is pressed with a load  $P$  on to the surface of a semi-infinite elastic solid, a circular contact area is established which increases in size with increasing load. The radius of the contact circle is given in terms of Poisson's ratio and Young's modulus for the indenter and the semi-infinite solid,  $\nu_1, E_1, \nu_2, E_2$  by

$$a(P) = \sqrt[3]{\frac{3PR}{4} \left( \frac{1-\nu_1^2}{E_1} + \frac{1-\nu_2^2}{E_2} \right)} \quad (11)$$

Within the circle of contact, under the indenter, all stress components are compressive. Outside the circle of contact, the radial stress  $S_{rr}$  at the surface is tensile:

$$S_{rr}(r, P) = \frac{(1 - 2\nu_2)}{2\pi} \frac{P}{r^2} \quad (r \geq a) \quad (12)$$

The circumferential stress, on the other hand, is compressive and is of the same magnitude as the radial stress. Thus the stress state in the surface outside the contact circle is one of pure shear. In a brittle material such as glass it is reasonable to expect that Griffith's (1924) fracture condition will hold. This condition states that under biaxial stress, the principal tensile stress governs if its magnitude is greater than one-third of the principal compressive stress. As this is the case in pure shear, fracture occurs at a critical value of the radial tensile stress.

An argument very similar to that which led to Eq. 6 for the strength distribution in terms of the flaw density can now be used to find the probability of fracture for a load less than  $P, \Phi(P)$ , from the surface flaw



density  $g(S)$ . Here, however, the stressed area is a function of load.

The probability of having no fracture in an infinitesimal area

$\delta A = 2\pi r \delta r$  for an indenter load less than  $P$  is

$$1 - \delta\phi(P) = \exp(-2\pi r \delta r \int_0^{S(r,P)} g(S) dS) \quad \text{where } r > a(P) \quad (13)$$

The probability of having no fracture in any of the infinitesimal rings is then

$$1 - \phi(P) = \exp(-2\pi \int_{r_1}^{\infty} \delta r \int_0^{S(r,P)} g(S) dS) \quad (14)$$

and in the limit

$$1 - \phi(P) = \exp(-2\pi \int_{a(P)}^{\infty} r dr \int_0^{S(r,P)} g(S) dS) \quad (14a)$$

Now let

$$S(r,P) = \frac{CP}{r^2}, \quad a = KP^{1/3} \quad (15)$$

where

$$C = \frac{1 - 2\nu_2}{2\pi} \quad K = 3 \sqrt{\left[ \frac{3R}{4} \left( \frac{1 - \nu_1^2}{E_1} + \frac{1 - \nu_2^2}{E_2} \right) \right]}. \quad (16)$$

Using Eqs. 15 and 16 and interchanging the order of integration in

Eq. 14a,

$$\ln(1 - \phi(P)) = -2\pi \int_0^{CP/a^2} g(S) dS \int_{a(P)}^{\sqrt{CP/S}} r dr \quad (17)$$

We find:

$$\ln(1 - \phi(P)) = -\pi a^2(P) \int_0^{CP/a^2} g(S) (1 - (CP/a^2)/S) dS \quad (18)$$

This becomes identical to Eq. 8 after multiplying the right-hand

side by  $\frac{k}{|k|}$  and choosing

$$S_m = CP/a^2, 2bl = \pi a^2(P), G(S_m) = -\ln(1 - \Phi), k = -1 \quad (19)$$

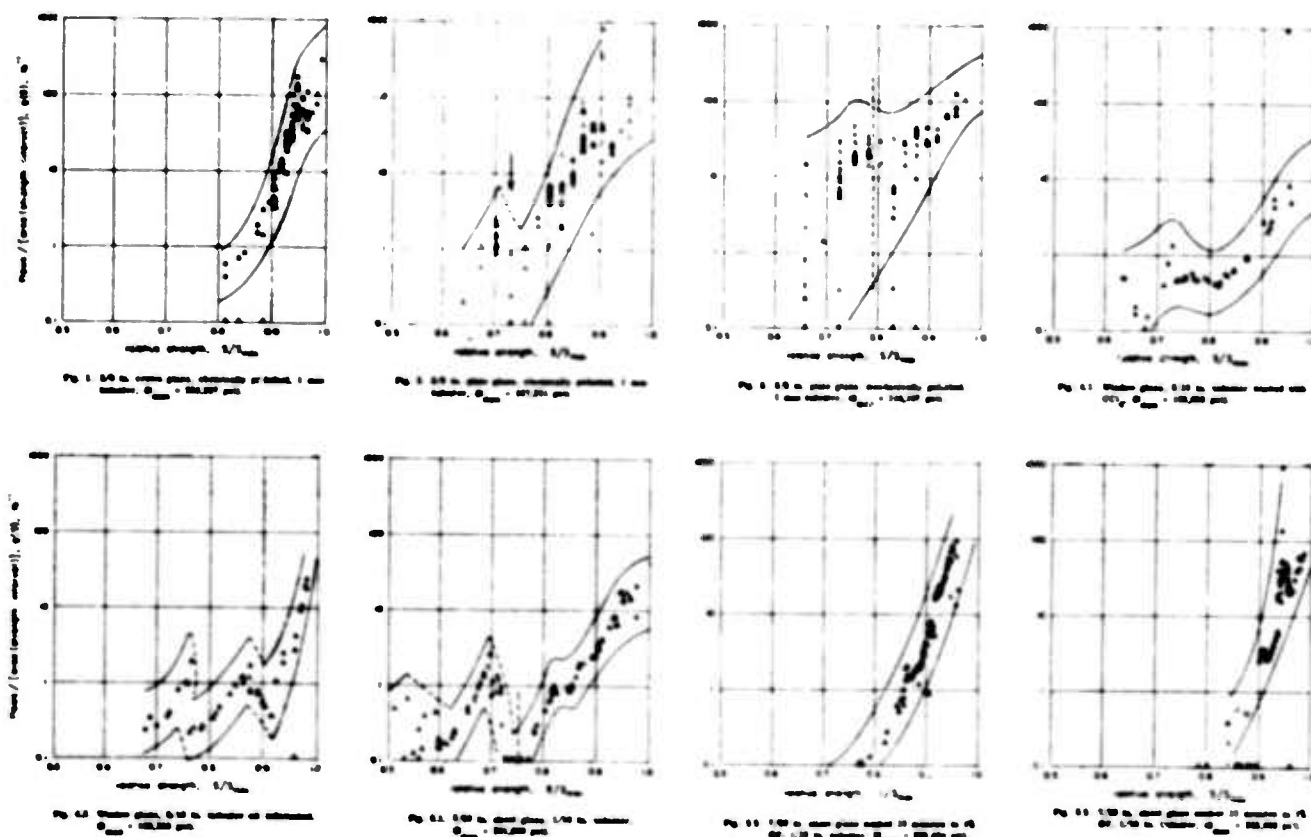
The solution for  $g(S)$  is then given by Eq. 10.

#### IV. Numerical Results for the Flaw Density Distribution

A computer program was written to calculate the flaw density distributions for a series of indentation experiments on various types of glass carried out by Argon (1959). A users manual and copies of the decks are available for a small duplication fee.

The program first generates the cumulative failure distribution function  $\Phi(P)$  by ordering the experimentally observed failure loads. A running fit for  $\Phi(P)$  in terms of an expansion in Chebychev polynomials was then calculated using a least squares criterion. Along most of the curve a third-order fit was applied to 25 data points, but as few as 7 points were used at the ends. From this interpolating polynomial its derivatives  $\Phi'(P)$  and  $\Phi''(P)$  were calculated, and then  $g(S)$  was found using Eqs. 19 and 10.

Numerical results for  $g(S)$  as well as the estimated confidence limits are presented in Figs. 1-8.2 for eight types of glasses subjected to various types of surface treatments. In order to estimate the effect of sampling errors on our calculation of  $g(S)$ , twenty sets of new data were generated by random sampling from a smoothed cumulative distribution function and used as input to recalculate  $g(S)$ . The resulting scatter band for  $g(S)$ , about a factor of 3 either side of the mean, was then assumed to represent a 95% confidence limit, and is shown in Figs. 1 through 8.2.



## V. Discussion

In this paper we have presented a method for estimating flaw density distributions from fracture test data. The required calculations are quite straightforward, with minimal manipulation of the raw data.

We have used the method to analyze flaw densities in several types of glasses which have been subjected to a variety of surface treatments.

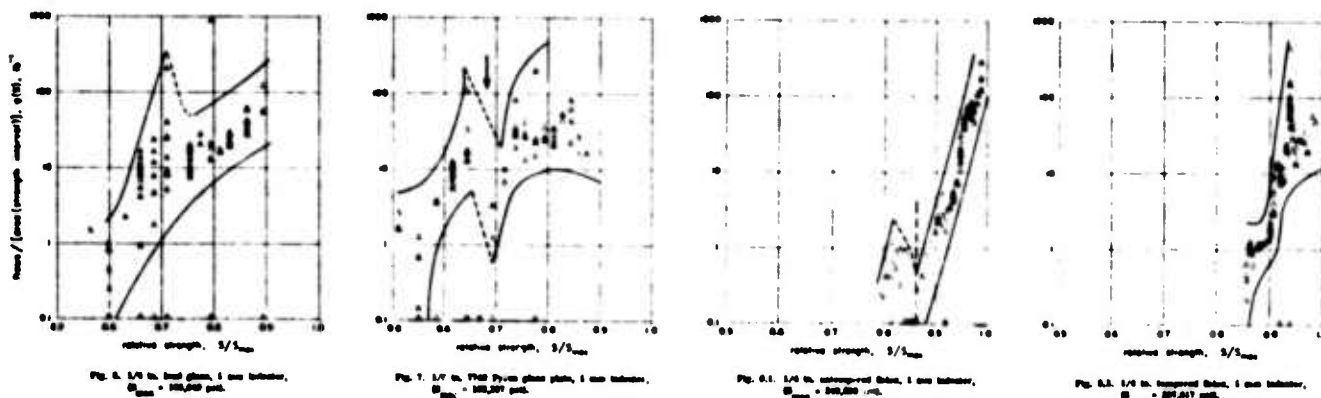
Figures 1, 2, and 3 give flaw density,  $g(S)$ , curves (Fig. 1, crown glass: 71.0  $\text{SiO}_2$ , 8.5  $\text{Na}_2\text{O}$ , 7.56  $\text{K}_2\text{O}$ , 11.3  $\text{CaO}$ , 0.5  $\text{Na}_2\text{SO}_4$ , 1.0  $\text{Sb}_2\text{O}_5$ ; Fig 2 and Fig 3, plate glass: 72.0  $\text{SiO}_2$ , 13.0  $\text{Na}_2\text{O}$ , 12.0  $\text{CaO}$ , 2.4  $\text{MgO}$ , 0.15  $\text{Fe}_2\text{O}_3$ ) showing the differences between crown and plate glasses which have been prepared by mechanical and chemical polishing. Comparing the chemically polished crown and plate glass, it is clear that the best specimens of plate glass are not as strong as the worst of the crown glass. Figure 2 and 3 show the differences between mechanically

and chemically polished surfaces of plate glass. Chemical polishing has removed many of the flaws to the left of the dashed line in Fig. 3. There is an apparent spike in the curve of chemically polished plate glass which suggests that a further improvement in surface preparation could remove the apparent peak indicated by the arrow in Fig. 2. The grouping of flaws below that arrow suggests that they are all due to one specific type of surface flaw.

Figures 4.1 and 4.2 show the flaw density curves for ordinary window glass ( $73.0 \text{ SiO}_2$ ,  $13.0 \text{ Na}_2\text{O}$ ,  $8.6 \text{ CaO}$ ,  $3.6 \text{ MgO}$ ,  $1.3 \text{ Al}_2\text{O}_3$ ,  $0.1 \text{ Fe}_2\text{O}_3$ ) with and without lubrication of the indenter. All other experiments were carried out with a dry indenter. Examination of these figures suggests that the oil has no dramatic effect.

Figures 5.1, 5.2 and 5.3 show the effect of 1% HF etching on the flaw density of sheet glass. The group of flaws up to the dashed line in Fig. 5.1 are removed by the 1% HF etch for 15 minutes. A further etch of 1 hour improves the flaw density curve but the improvement is not really significant since the extra time decreases the magnitude of the flaw density curve in the middle strength range but does not increase the lower limit.

Figure 6 refers to a rouge-polished lead glass, used for protection against X-rays. Figure 7 illustrates the case of rouge-polished Pyrex-brand glass. Both glasses, particularly Pyrex-brand glass, have a distinctly lower strength than ordinary soda glass, corresponding to their weaker bonding forces. In the Pyrex glass there is a possible division of flaw type at the arrow. If this is the case then an improvement in surface by removal of the particular flaw which is



responsible for the lower half of the curve could result in an improved material with flaw density curve chopped off at the arrow.

Fig. 8.1 and 8.2 were obtained from indentation tests on Solex (heat-radiation-absorbing) glass made by the Pittsburgh Plate Glass Company which after conventional grinding, was chemically polished in the research laboratory of the company. Tempering has definitely improved the glass by removing the group of flaws which are responsible for that section of the curve below the dashed line in Fig. 8.1.

### Conclusion

(A) Eqs. 10 and 19 give the flaw density,  $g(S)$ , from fracture tests in which stresses are functions of loading positions. Specific results are given for

(1) a general case when  $S = S_m(1 - z/l)^k$

(2) three point bending where  $S = S_m(1 - z/l)$

and (3) hardness indentation tests where  $S \propto P/r^2$  for  $r > a(P)$ .

(B) Computer programs have been prepared to accept raw data and generate the flaw density curve. An additional computer program was written to generate random sets of data from original data in order

to recalculate  $g(S)$  from the random data drawn on the original data and thereby estimate confidence limits. Programs, users manuals and decks are available for all or individual cases, Research Memoranda 204 and 205.

(C) Actual estimates of  $g(S)$  have been obtained from the analysis of fracture indentation tests on crown, plate, window, lead, Pyrex, sheet and Solex glass. The effects of HF etching, mechanical or chemical polishing, tempering, and friction were examined and their flaw density curves presented.

#### Acknowledgements

This work was sponsored by the Defense Advanced Research Projects Agency under ARPA order number 2055 and Contract No. F19628-72-C-0304 and monitored by Air Force Cambridge Research Laboratory.

Special thanks to Ali S. Argon, of Massachusetts Institute of Technology, who supplied the data for the various glasses and who also pioneered the original analysis of the indentation test in order to obtain the flaw density. His encouragement and help with this present work is also greatly appreciated.

1. A. S. Argon, "Surface Cracks on Glass", Proc. of Royal Society A, Vol. 250, pp. 422-481. (1959).
2. A. S. Argon, "Distribution of Cracks on Glass Surfaces", Proc. of Royal Society A, vol. 250, pp. 482-492. (1959).
3. A. A. Griffith, "Theory of Rupture", Proc. First Intern. Congr. Appl. Mechanics, Delft, pp. 55-63. (1924).
4. F. B. Hildebrand, Methods of Appl. Mech., Prentice Hall, N.J. (1952).
5. H. E. Powell and F. W. Preston, "Microstrength of Glass", J. Am. Cer. Soc., 28, 145-149 (1945).
6. O Reinkober, "Die Zerreissfestigkeit Dunner Quarzfaden", (Tensile Strength and Elasticity of Quartz Fibers), Physik Z., 32, pp. 243-50 (1931).

7. E. W. Sufov, "New Statistical Treatment of Ball Indentation Data to Determine Distribution of Flaws in Glass", J. Am. Cer. Soc. 45, 214-218, (1962).
8. B. W. Lindgren and G. W. McElrath, Introduction to Probability and Statistics, MacMillan, N.Y. (1959).
9. W. Feller, An Introduction to Probability Theory and Its Applications, Vol. 1, 2nd Ed., J. Wiley, N.Y. (1957).
10. R. A. Fisher and L. H. C. Tippett, "Limiting Forms of the Frequency Distribution of the Largest or Smallest Member of the Sample", Proc. Camb. Phil. Soc., Vol. 24, 180-190 (1928).
11. M. Frechet, "Sur la loi de probabilitie de l'ecart maximum", Annals de la Soc. Polonaise de Math, Vol. 6, 92 (1927).
12. J. R. Matthews, User's Manual for Flaw Statistics Programs, Research Memorandum No. 204, Fatigue and Plasticity Laboratory, Department of Mechanical Engineering, M.I.T., Cambridge, Mass. (1975).
13. J. R. Matthews, Generation of g(S) Curves, Research Memorandum No. 205, Fatigue and Plasticity Laboratory, Department of Mechanical Engineering, M.I.T., Cambridge, Mass. (1975).

**APPENDIX E-2**

**Research Memorandum No. 204**  
**User's Manual for Flaw Statistics Programs**

**Research Memorandum No. 205**  
**Generation of  $g(S)$  Curves**



**Research Memorandum No. 204**

**User's Manual for Flaw Statistics Programs**

**by**

**J. R. Matthews**

**July, 1975**

**Fatigue and Plasticity Laboratory  
Department of Mechanical Engineering  
Massachusetts Institute of Technology  
Cambridge, Mass. 02139**

## 7.6 Flaw Statistics Programs

Before we go into the individual programs the subroutines which are common to all will be explained. These are,

- (1) CURFIT sets up coefficient matrices for least squares fit.
- (2) SCALL scales the matrix coefficients so that the maximum coefficient in each row is 1.0
- (3) SIMQ of the scientific subroutine package is used to solve the simultaneous equations for the Chebychef coefficients.
- (4) ORDER orders all the numbers in a vector from smallest to largest.
- (5) INTERP is a linear interpolation routine
- (6) DIFFER this subroutine takes coefficients of Chebychef polynomials as found by calling CURFIT, SCALL and SIMQ and gives back the values  $y$ ,  $\frac{dy}{dx}$ ,  $\frac{d^2y}{dx^2}$ .

### Method of Chebychef Polynomial Least Squares Fitting

The first six Chebychef(Tschebychef) polynomials are

$$T_1 = 1$$

$$T_2 = x$$

$$T_3 = 2x^2 - 1$$

$$T_4 = 4x^3 - 3x$$

$$T_5 = 8x^4 - 8x^2 + 1$$

$$T_6 = 16x^5 - 20x^3 + 5x$$

and the chebychef curve is

$$y = \sum_{i=1}^n b_i T_i \quad n : \text{number of polynomials}$$

To least squares fit we want to minimize all

$$\left[ y_k - \sum_{i=1}^n b_i T_{i,k} \right]^2 \quad k : \text{data}$$

To do this we partially differentiate with respect to each coefficient and set the resulting equations to 0.

$$\sum_{j=1}^n \sum_{k=1}^m T_{i,k} T_{j,k} b_j = \sum_{k=1}^m T_{i,k} y_k \quad m : \text{total number of data points}$$

Solving the set of  $i=1, n$  equations for  $b_i$  gives us our chebychef coefficients and an excellent least squares fit.

Subroutine CURFIT sets up the coefficients of the two matrices , A and B, required to obtain the solution.

$$[A] (b) = [B]$$

where  $A_{i,j} = \sum_{k=1}^m T_{i,k} T_{j,k}$

and  $B_i = \sum_{k=1}^m T_{i,k} y_k$

#### Variables

XX            x data

Y            y data

NPOINT	$M$	total number of data points
N	$n$	number of equations used in chebychev fit
A	$A_{1,j}$	
B	$B_1$	

```

C
SUBROUTINE CURFIT(XX,Y,APOINT,N,A,B)
DIMENSION XX(NPOINT),Y(NPOINT),A(36),B(6),T(6)
      ZEROES A MATRIX
      DO 2 I=1,36
        A(I)=0.0
      CONTINUE
      ZEROES B MATRIX
      DO 4 J=1,6
        B(J)=0.0
      CONTINUE
      DO 1 L=1,NPOINT
        X=XX(L)
        CALCULATES INDIVIDUAL CHEBYCHEF POLYNOMIAL VALUES
        T(1)=1.0
        T(2)=X
        T(3)=2.*X**2-1.
        T(4)=4.*X**3-3.*X
        T(5)=8.*X**4-8.*X**2+1.
        T(6)=16.*X**5-20.*X**3+5.*X
        K=0
        DO 1 I=1,N
          DO 3 J=1,N
            K=K+1
          CALCULATES A COEFFICIENTS
          A(K)=A(K)+T(I)*T(J)
        CONTINUE
      CALCULATES B COEFFICIENTS
      B(1)=P(1)+Y(L)*T(1)
      CONTINUE
      RETURN
      END

```

Subroutine SCALL is used to scale the matrices A and B so that the maximum value of any coefficient is 1.0. It is well known that you can divide any equation by a non zero number. The subroutine searches each row and finds the largest number. It then divides all coefficients in that row by the largest number.

#### Variables

A	A	left hand square matrix
R	B	right hand vector
I4MMX	n	size of square matrix A

Subroutine ORDER takes a vector and orders the values from smallest to largest.

#### Variables

Z	Z	any vector
NMAX	NMAX	number of terms in vector

```

C
SUBROUTINE SCALL(A,R,I4MMX)
DIMENSION SCALE(6),A(36),R(6)
C CALCULATE THE SCALE VECTOR. SCALE LARGEST ELEMENT TO 1.
DO 257 I=1,I4MMX
SCALE(I)=ABS(A(I))
DO 257 J=1,I4MMX
L=(J-1)+I4MMX+1
IF(SCALE(I).GT.ARS(A(L))) GO TO 257
SCALE(I)=ABS(A(L))
CONTINUE
257 DC 258 I=1,I4MMX
IF(ABS(SCALE(I)).LE.10.0E-12) SCALE(I)=10.0E-12
258 SCALE(I)=1./SCALE(I)
C SCALE LOAD VECTORS FOR EACH LOADING
N=1
DC 259 J=1,N
DO 259 I=1,I4MMX
L=(J-1)+I4MMX+1
R(L)=K(I)*SCALE(I)
259 C SCALE THE SQUARE COEFFICIENT MATRIX
DC 260 J=1,I4MMX
DO 260 I=1,I4MMX
L=(J-1)+I4MMX+1
A(L)=A(L)*SCALE(I)
260 RETURN
END

```

```

C
C
C
C
SUBROUTINE ORDER(Z,NMAX)
  DIMENSION Z(NMAX)
  THIS SUBROUTINE ORDERS ALL THE NUMBERS IN A VECTOR FROM
  SMALLEST TO LARGEST
  IT GOES THROUGH CONTINUOUSLY SHIFTING THE LARGEST NUMBER TO
  THE END.
  NM=NMAX-1
  N=NMAX-1
  DO 2 J=1,NM
    DO 1 I=1,N
      IF(Z(I+1).GT.Z(I)) GO TO 1
      AZ=Z(I)
      Z(I)=Z(I+1)
      Z(I+1)=AZ
    CONTINUE
  N=N-1
  CONTINUE
  RETURN
  END
1
2

```



Subroutine INTERP is given two vectors which define a curve ( z,y ) , A value ( y ) of one variable is given and the subroutine linearly interprets with the two vectors finding the corresponding value of the other variable ( z ).

Variables

Z21	any vector	
Y21	any vector	points define a curve
YY	any value of variable y	
YY	corresponding value of variable z	

Subroutine DIFFER takes the chebychef coefficients as found by calline CURFIT, SCALL and SIMQ and then generates the values  $y$ ,  $\frac{dy}{dx}$  and  $\frac{d^2y}{dx^2}$

Variables

B	b	chebychef coefficients
N	n	number of chebychef polynomials used in fit
XXX	x	position of interest
YYY	y	value of y at x
YP	$\frac{dy}{dx}$	slope at x
YPP	$\frac{d^2y}{dx^2}$	value of second derivative at x

C  
SUBROUTINE INTERP(Z21,Y21,YY)  
 DIMENSION Z21(21),Y21(21)  
 THIS IS AN INTERPOLATION ROUTINE.  
 K=IFIX(YY\*20.)+1  
 YY=Z21(K)+(YY\*20.-FLGAT(K-1))\*(Z21(K+1)-Z21(K))  
 RETURN  
 END

```

C SUBROUTINE DIFFER(B,N,X,Y,YP,YPP)
C DIMENSION B(6)
C THIS ROUTINE CALCULATES THE CHEBYCHEF CURVE VALUE, FIRST
C DERIVATIVE AND SECOND DERIVATIVE.
      IF(N.EQ.6) GO TO 1
      DO 1 I=N,5
      B(I+1)=0.0
      CONTINUE
      CHEBYCHEF POLYNOMIAL VALUE
      T1=X
      T2=2.*X**2-1.
      T3=4.*X**3-3.*X
      T4=8.*X**4-8.*X**2+1.
      T5=16.*X**5-20.*X**3+5.*X
      CHEBYCHEF CURVE VALUE
      Y=B(1)+B(2)*T1+B(3)*T2+B(4)*T3+B(5)*T4+B(6)*T5
      FIRST DERIVATIVE
      YP=B(2)+B(3)*4.*X+B(4)*12.*X**2-3.*B(5)*32.*X**3-16.*B(6)*
      1(80.*X**4-60.*X**2+5.)
      SECOND DERIVATIVE
      YPP=B(3)*4.*B(4)*24.*X+B(5)*96.*X**2-16.*B(6)*320.*X**3-120.*
      1X)
      RETURN
      END

```

```

C      SUBROUTINE SIMQ(A,B,N,KS)
      DIMENSION A(1),P(1)
      FPCM SCIENTIFIC SUBROUTINE PACKAGE
      TCL=0.0
      KS=C
      JJ=-N
      DC 65 J=1,N
      JY=J+1
      JJ=JJ+N+1
      RIGA=0
      IT=JJ-J
      DO 30 I=J,N
      IJ=IT+I
      IF(ABS(BIGA)-ABS(A(IJ))) 20,30,30,
20  RIGA=A(IJ)
      IMAX=I
30  CONTINUE
      IF(ABS(RIGA)-TCL) 35,35,40
35  KS=1
      RETURN
40  I1=J+N*(J-2)
      IT=IMAX-J
      DO 50 K=J,N
      I1=I1+N
      I2=I1+IT
      SAVE=A(I1)
      A(I1)=A(I2)
      A(I2)=SAVE
50  A(I1)=A(I1)/RIGA
      SAVE=P(IMAX)
      B(IMAX)=B(J)
      B(J)=SAVE/BIGA
      IF(J-N) 55,70,55
55  IQS=N*(J-1)
      DC 65 IX=JY,N
      IXJ=IQS+IX

```

```

IT=J-IX
DO 6C JX=JY,N
IXJX=N*(JX-1)+IX
JJX=I>JX+IT
60 A(IXJX)=A(IXJX)-(A(IXJ)*A(JJX))
65 B(IX)=B(IX)-(B(J)*A(IXJ))
70 NY=N-1
IT=N*N
DC 8C J=1,NY
IA=IT-J
IR=N-J
IC=N
DC 80 K=1,J
R(18)=B(IR)-A(IA)*B(IC)
IA=IA-N
80 IC=IC-1
RETURN
END

```

### 7.6,2 Relation Between Standard Deviation of Strength and Position of Failure in Three point Bending

This program takes the smoothed  $g(S)$  curve from the previous program and finds the resulting relationship between the standard deviation in strength and position of failure for a three point bend test.

The probability of failure in  $\delta z$  at a stress to  $S_m(1 - 2z/l)$  is

$$\delta\phi(z) = b\delta z \int_0^{S_m(1-2z/l)} g(S) dS$$

The probability of failure in this element and within a  $\delta S_m$  increment is

$$\delta\phi(z, S_m) = b\delta z \delta S_m g(S_m(1 - 2z/l))(1 - 2z/l)$$

The probability of fracture in this element in this increment is the product of this and the probability of no fracture anywhere else ( appendix 7.2 )

$$e^{-bl \int_0^{S_m} (1-S/S_m) g(S) dS}$$

so

$$\delta\phi(z, S_m) = b\delta z \delta S_m g(S_m(1-2z/l))(1-2z/l) e^{-bl \int_0^{S_m} (1-S/S_m) g(S) dS}$$

$$\phi(S_m, z) = \frac{\delta\phi(z, S_m)}{\delta z \delta S_m}$$

The probability of failure in a part is 1.0 and therefore as a check

$$\text{Check} = 1 = 2 \int_0^{S_{\max}} \int_0^{l/2} \phi(S_m, z) dz dS_m$$

The mean failure strength is

$$\bar{S} = 2 \int_0^{S_{\max}} \int_0^{l/2} \phi(S_m, z) S_m dz dS_m$$

The standard deviation in strength is

$$\sigma_{S_m} = \sqrt{\left( 2 \int_0^{S_{\max}} \int_0^{l/2} \phi(S_m, z) (S_m)^2 dz dS_m - \left[ 2 \int_0^{S_{\max}} \int_0^{l/2} \phi(S_m, z) S_m dz dS_m \right]^2 \right)^{1/2}}$$

and the standard deviation in position in failure is

$$\sigma_{z_{\dots}} = \sqrt{2 \int_0^{S_{\max}} \int_0^{l/2} \phi(S_m, z) z^2 dz dS_m}$$

The relationship that we are looking for is now trivial

$$\text{FACTOR} = \frac{\sigma_{S_m} / \bar{S}}{\sigma_z / \frac{l}{2}}$$

## Variables

C1...C6	Chebyshev polynomial coefficients
SL1	Lower cut off of $g(S)$
SL2	Upper end of straight tail of $g(S)$
VSL2	$g(SL2)$
NGRID	integration mesh size
NO PLOT	0 - 1 for plot or no plot of $g(S)$
GMAX	$g(S)$ maximum plotting
S MAX	maximum stress of $g(S)$
S MAX	redefined for upper limit of integration on $S_m$
S MEAN	$\bar{S}$
CHECK	Check
SIGMZ	$\sigma_z$
SIGMSM	$\sigma_{S_m}$
FACTOR	FACTOR
NUMB	integration counter
BB	b width of beam
TL	l length of beam
DELTZ	dz
DELTSM	dS <sub>m</sub>



Input

(1) NGRID , SL1 , SL2      Format (I2,2F4.2)

NO PLOT

S MAX

C1....C6

G MAX                      specify in program

S MAX

B B

T L

Output

one line / card



```

C      SL1  LOWER CUTOFF OF G(S)
C      SL2  UPPER CUTOFF FOR STRAIGHT LINE TAIL OF G(S).
C      C'S CHERBYCHEF POLYNOMIAL LEAST SQUARES FIT COEFFICIENTS,FIFTH
C      ORDER
      C1=.850E-02
      C2=.279E-10
      C3=-.558E-09
      C4=-.271E-18
      C5=.553E-17
      C6=-.262E-22
      GMAX=.02
      G(S)  MAXIMUM PLCTTING
      VSL2=GSS(SL2)
      VSL2  G(SL2)
      *      *      *      *      *
C      COMMENT  ZEROES SUMMATICNS FOR NUMERICAL INTEGRATION
C
      SMAX=10000.
      SMAX  (REDEFINED) FOR UPPER LIMIT OF COUBLE INTEGRATION ON SM.
      YOU SHOULD BE ABLE TO PICK A GOOD VALUE FOR THIS FROM THE G(S) PLOT.
      IF YOU CAN'T THEN USE THREE TIMES THE FIRST SMAX.
      SMEAN=0.0
      CHECK=0.0
      SIGM2=0.0
      SIGMSM=0.0
      FACTCR=0.0
      NUMB=C
      RB=.125
      EG
      TL=.875
      B  WIDTH OF BEAM
      L  LENGTH CF BEAM
      DELTZ=TL/2./FLCAT(NGRIC)
      DELTZ  INTEGRATION INTERVAL
      DELTSM=(SMAX-SL1)/FLCAT(NGRIC)

```

```
C DELTSM INTEGRATION INTERVAL * * * * *
```

CCOMMENT THIS SECTION PLOTS G(S)  
C

```

IF(NCPLOT, EQ, 0) GC TC 80
CALL BEGIN (300, 10)
CALL VECTOR
CALL SCALE(1000., 150., 0., 0.)
CALL AXIS(0., 0., 1., 1., 1., 1., 1., 1., 1.)
DO 80 I=1, 100
  AX=FLCAT(I)/100.
  W=AX*SMAX
  GSSX=GSS(W)/GMAX
  CALL TPLQT(AX, GSSX, 1, 0)
  CONTINUE
GO TC 27

```

80

C  
C  
C

214

```

STOP
END
FUNCTION GSS(W)
COMMON C1, C2, C3, C4, C5, C6, SL1, SL2, VSL2
IF(W.LT.SL1) GO TC 10
T1=W
T2=2.*W**2-1.
T3=4.*W**3-3.*W
T4=8.*W**4-8.*W**2+1.
T5=16.*W**5-20.*W**3+5.*W
GSS=C1+C2*T1+C3*T2+C4*T3+C5*T4+C6*T5
IF(W.FO.SL2) GO TU 20
IF(W.GT.SL2) GO TC 20
GSS=(W-SL1)*VSL2/(SL2-SL1)
GO TC 20
GSS=G.0
RETURN
END
FUNCTION FINT(SM)

```

10  
20

```

COMMON SL1
N=SL1
NINC=1/4
V=(SM-SL1)/FLOAT(NINC)
FINT=0.0
DO 1 I=1,NINC
W=h+V
FINT=FINT+GSS(W)*((1.-h/SM)*V
CONTINUE
RETURN
END
1
C // XEQ 2
C *EL TEKPLT
C * BC 0094
C 400.540.60
C // EJECT
C // END

```

Research Memorandum No. 205

Generation of  $g(S)$  Curves

by

J. R. Matthews

July, 1975

Fatigue and Plasticity Laboratory  
Department of Mechanical Engineering  
Massachusetts Institute of Technology  
Cambridge, Mass. 02139

### 7.6.1 Generation of $g(S)$ from 3 point Bend Test Data

In the paper in appendix 7.2 the derivation for  $g(S)$  from three point bend test data is given;

$$\frac{bl \ g(S_m)}{2} = \frac{S_m}{2} \left[ \frac{\phi''(S_m)(1 - \phi(S_m)) + \phi'(S_m)^2}{(1 - \phi(S_m))^2} + \frac{2 \ \phi'(S_m)}{S_m (1 - \phi(S_m))} \right] \quad 7.6.1$$

$\phi(S_m)$  is the ordered probability of failure directly from the tests.

This program takes the ordered stresses at the center of the beam at failure and generates and plots a  $\phi(S_m)$  curve. A running fit of 11 points using six equations is used to evaluate  $\phi'$  and  $\phi''$  and a new (possibly slightly different)  $\phi$ .  $g(S_m)$  is then calculated using equation 7.6.1 and both  $\phi$  and  $g$  are plotted. One single curve is then put through the  $g(S)$  curve. The resulting smoothed curve is plotted on top of the original  $g(S)$ . The lower tail is cut off this curve and used in the next program.

#### Variables

please see the computer listing



### Input

please see the computer listing

### Output

Fig. 8 of Appendix 7.2 plus tabulated stresses,  $\phi$ ,  $S$ ,  $\phi'$ ,  $\phi''$ , and  $\text{blg}(S)$  and 6 Chebychef polynomial coefficients for continuous  $\text{blg}(S)$  fit. These coefficients are used in Appendix 7.6.2 along with  $SL1$  and  $SL2$  which are chosen arbitrarily from the output plot. ( sample plot at end of listing ).

```

7.6.1 GENERATION OF G(S) FROM 3 POINT BEND TEST DATA
*      *      *      *      *
// FOR
DIMENSION X(31),Y(31),Z(31),A(36),B(6),GS(31),YS(31)
DIMENSION YY(31)
COMMON C1,C2,C3,C4,C5,C6

THIS IS THE FIRST FLAW STATISTICS PROGRAM. IT TAKES DATA
FROM THREE POINT BEND TESTS AND GENERATES G(S). PLEASE SEE
THE PAPER ' DESIGN STRENGTH OF POLYCRYSTALLINE KCL ' BY
F.A. MCCLINTOCK AND JIM MATTHEWS TO UNDERSTAND THE METHOD.

*      *      *      *      *
VARIABLES
Z      MAXIMUM STRESS AT CENTER OF 3-POINT BEND SPECIMEN
Y      OCCURRENCE/N+1
X      MANIPULATED STRESS
A      COEFFICIENTS OF EQUATIONS FOR LEAST SQUARES FIT
B      RIGHT VECTOR FOR LEAST SQUARES FIT
B      CHERYCHEF POLYNOMIAL COEFFICIENTS
GS     FLAW DENSITY
YS     CALCULATED PROBABILITY OF FAILURE BELOW A CERTAIN STRESS
YP     FIRST DERIVATIVE OF YS
YPP    SECOND DERIVATIVE OF YS
*      *      *      *      *
INPUT
GMAX IS FLAW DENSITY PLOTTING SCALE(MAXIMUM)
NMAX IS THE NUMBER OF ORDERED DATA STRESSES

```



```

CALL DIFFER(B,NEQUAT,XXX,YYY,YP,YPP)
YS(I)=YYY
GS(I)=X(I)*((1.5*(YPP*(1.-YS(I))+YP**2)/(1.-YS(I))**2)+
1(YP/(X(I)*(1.-YS(I))))
X(I)=X(I)/Z(NMAX)
WRITE(5,200) X(I),Y(I),YS(I),YP,YPP,GS(I)
FORMAT(/6(2X,E12.3))
200 1 CONTINUE
C

```

```

CCMMENT TC CURVE FIT TO G(S)

```

```

NFIT=NMAX-NPOINT+1

```

```

DC E3 I=1,NFIT

```

```

N=I+NFIRST-1

```

```

X(I)=Z(N)

```

```

YY(I)=GS(N)

```

```

CONTINUE

```

```

CALL CURFIT(X,YY,NFIT,NEQUAT,A,B)

```

```

CALL SCALL(A,B,NECLAT)

```

```

CALL SIMQ(A,B,NEQUAT,0)

```

```

CCMMENT B(1) TO B(6)

```

```

WRITE(5,20)B(1),B(2),B(3),E(4),B(5),B(6)

```

```

FORMAT('O B ',6(2X,E12.3))

```

```

C1=E(1)

```

```

C2=E(2)

```

```

C3=E(3)

```

```

C4=E(4)

```

```

C5=E(5)

```

```

C6=E(6)

```

```

C
C
C
C
C

```

```

FLCTTING

```

```

CALL BEGIN (30000)

```

```

CALL VECTOR

```

```

CALL SCALE(1000.,750.,0.,0.)

```

```

CALL AXIS(0,0,0,1,1,1,1,1,1,1,1,1)
DO 3 I=1,NMAX
  X(I)=Z(I)
  X(I)=X(I)/Z(NMAX)
  Y(I)=FLCAT(I)/FLCAT(NMAX+1)
  CALL TPLOT(X(I),Y(I),0,0)
  CALL TPLOT(X(I),Y(I),1,1)
CONTINUE
GS(NFIRST)=GS(NFIRST)/GMAX
X(NFIRST)=Z(NFIRST)/Z(NMAX)
CALL TPLOT(X(NFIRST),GS(NFIRST),0,0)
NSECAC=NFIRST+1
DO 10 I=NSECND,NCAT#
  GS(I)=GS(I)/GMAX
  X(I)=Z(I)/Z(NMAX)
  CALL TPLOT(X(I),GS(I),1,0)
CONTINUE
X(NFIRST)=Z(NFIRST)/Z(NMAX)
CALL TPLOT(X(NFIRST),YS(NFIRST),0,0)
DO 2 I=NSECND,NCAT#
  X(I)=Z(I)/Z(NMAX)
  CALL TPLOT(X(I),YS(I),1,0)
CONTINUE
CALL TPLOT(U,0,0,0,0,0)
DO 80 I=1,100
  AX=FLCAT(I)/100.
  W=AX*Z(NMAX)
  GSSX=GSS(W)/GMAX
  CALL TPLOT(AX,GSSX,1,0)
CONTINUE

```

3

10

2

80

C  
C  
C

```

STOP
END
FUNCTION GSS(W)

```

COMMON C1,C2,C3,C4,C5,C6

C  
C  
C  
C  
C  
C  
C

THIS IS G(S).  
THE NEXT FLAW STATISTICS PROGRAM CUTS THE TAIL OFF G(S) BEFORE  
USING IT.

\* \* \* \* \*

T1=h  
T2=2.\*W\*\*2-1.  
T3=4.\*W\*\*3-3.\*W  
T4=6.\*W\*\*4-8.\*W\*\*2+1.  
T5=16.\*W\*\*5-20.\*W\*\*2+5.\*W  
GSS=C1+C2\*T1+C3\*T2+C4\*T3+C5\*T4+C6\*T5  
IF(GSS) 10,10,20  
GSS=0.0  
RETURN  
END

10  
20

223

// XEO 2  
\*EL TEK PLOT  
\* BC GC94

C  
C  
C

2796.  
3286.  
3328.  
3384.  
3397.  
3542.  
3565.  
3654.  
3676.  
3845.  
4056.  
4126.  
4158.  
4256.  
4276.

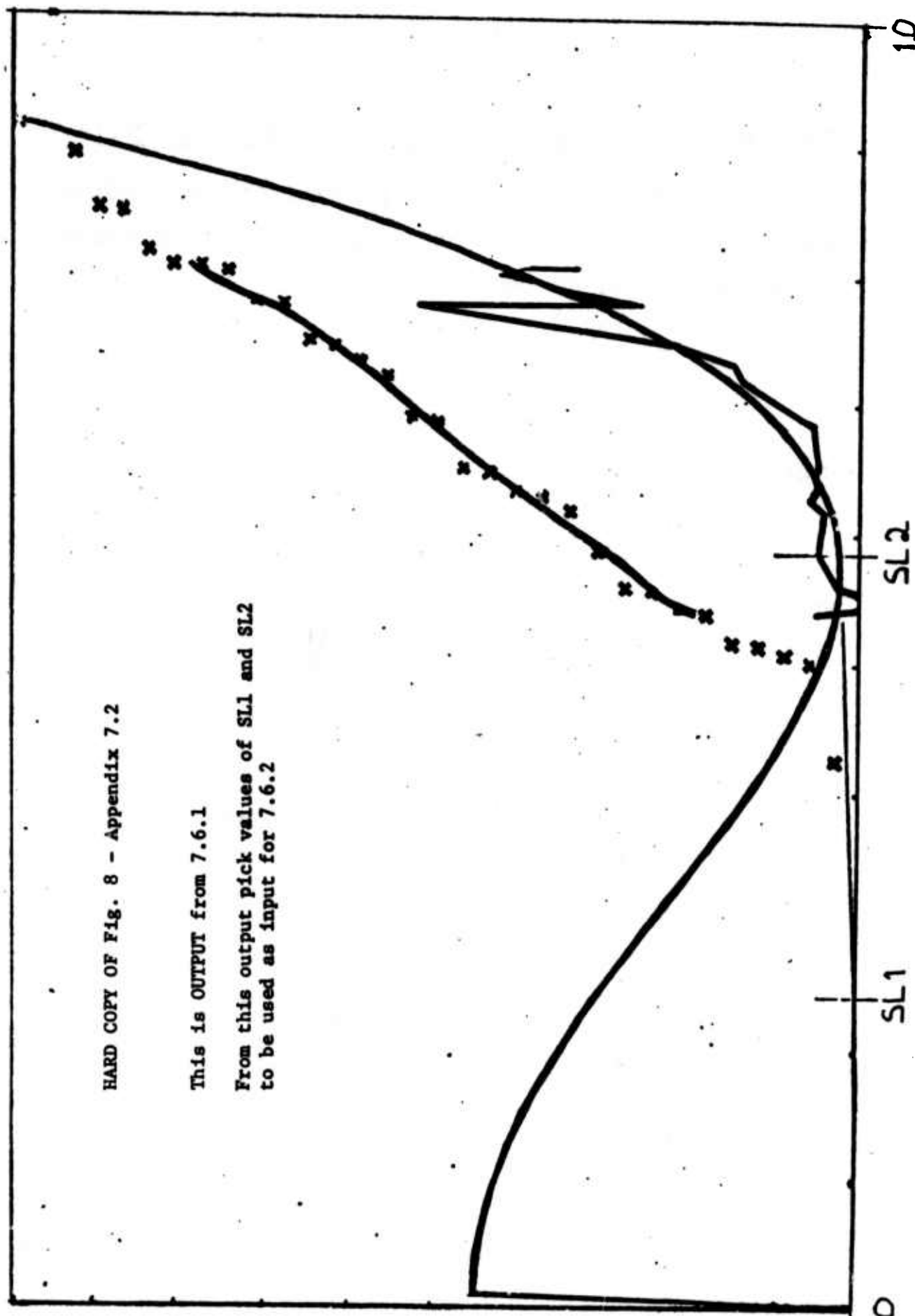
4509.  
4537.  
4740.  
4814.  
4891.  
4922.  
5098.  
5112.  
5265.  
5295.  
5297.  
5372.  
5562.  
5575.  
5863.  
6577.  
C

// END

HARD COPY OF Fig. 8 - Appendix 7.2

This is OUTPUT from 7.6.1

From this output pick values of SL1 and SL2  
to be used as input for 7.6.2





### 7.6.3 Generation of $g(S)$ from Hardness Indentation Tests

The paper in appendix 7.9 derives the required equations for finding the flaw density,  $g(S)$ , from hardness indentation tests. By choosing

$$S_m = CP/a^2$$

$$bl = \pi a^2(P)$$

$$G(S_m) = \ln(1 - \phi)$$

where

$$C = \frac{1 - 2\nu_2}{2\pi}$$

and

$$a = \left[ \frac{3PR}{4} \left( \frac{1 - \nu_1^2}{E_1} + \frac{1 - \nu_2^2}{E_2} \right) \right]^{1/3}$$

then since

$$G(S_m) = bl \int_0^{S_m} (1 - (S/S_m)^{-1}) g(S) dS$$

the solution is given by the general solution with  $k = -1$ .

$$g(S_m) = \frac{kS_m}{bl} \left[ \frac{\phi''(S_m)(1 - \phi(S_m)) + (\phi'(S_m))^2}{(1 - \phi(S_m))^2} + \frac{1 + 1/k}{S_m} \frac{\phi'(S_m)}{1 - \phi(S_m)} \right]$$

This involves input modifications of the program in appendix 7.6.1.

#### Variables

Variables are well documented in computer listing

<u>Input</u>		one/card
40A2	1.	label for graph
F10.4	2.	radius of indenter - R
I3	3.	number of data points - NMAX
F10.4	4.	loads ( kg ) - Z
I3	5.	number of running fits with different - KMAX number of points
I3	6.	number of points used in each of the - NPOINT KMAX fits
I3	7.	for plotting specify lowest NPOINT - NPOINT

In the mainline specify

NU1	v	steel
E1	E	steel
NU2	v	glass
E2	E	glass
NEQUAT		order of fit

### Output

Plots in Appendix 7.9 ; Figs. 1 - 8.2

### 7.6.3 GENERATION OF G(S) FROM HARDNESS INDENTATION TESTS // FCR

```

*      *      *      *      *
      DIMENSION X(100),Y(100),Z(100),A(36),B(6),GS(100),YS(100),YY(100),
      1BL(100)
      REAL NU1,NU2
      INTEGER*2 LABEL(40)

```

## PLCTTING SET UP

```
CALL CALCMP
CALL PLT(2)
CALL SCALE(1000.,140.,250.,155.)
CALL AXIS(0.,0.,.5,4.,1,1.,-1,-1)
CALL TWKITE(7)
CALL TCHAM(12.5,25.,0.)
CALL TPLOT(0.0,-0.1E,0,0)
WRITE(7,27)
FORMAT(5,5,6,7,8)
CALL TPLOT(-.1,4.,0,0)
WRITE(7,28)
FORMAT(1,1000,///,100,/'G(S)')
REAC(8,100) LABEL
FCRMAT(40A2)
CALL TPLOT(-.1,-0.5,0,0)
WRITE(7,29) LABEL
FCRMAT(25A2/15A2)
CALL TPLOT(.41,-.2,0,0)
WRITE(7,30)
FORMAT(10S/SMAX,1)
```

**U U**




























Z LOAD FROM HARDNESS TEST (KG)  
 Z MAXIMUM STRESS AT CIRCUMFERENCE OF INDENTER (PSI)  
 Y OCCURRENCE/N+1  
 X MANIPULATED STRESS  
 A COEFFICIENTS OF EQUATIONS FOR LEAST SQUARES FIT  
 B RIGHT VECTOR FOR LEAST SQUARES FIT  
 B CHERBYCHEF POLYNOMIAL COEFFICIENTS  
 GS FLAW DENSITY (/IN IN PSI)  
 GS CALCULATED PROBABILITY CF FAILURE BELOW A CERTAIN STRESS  
 YF FIRST DERIVATIVE OF YS  
 YPP SECOND DERIVATIVE OF YS  
 X RADIUS OF INDENTER (IN)  
 KMAX NUMBER OF POINTS USED TO GENERATE G(S)  
 NU1 POISSONS RATIO OF INDENTER  
 NU2 POISSONS RATIO OF GLASS  
 EE1 MODULUS CF INDENTER  
 EE2 MODULUS CF GLASS (PSI)  
 POWER DESCRIBING RELATION OF APPLIED STRESS TO POSITION.

**NMAX IS THE NUMBER OF ORDERED DATA STRESSES**

**AFCINT IS THE NUMBER OF POINTS USED IN THE RUNNING**



CHEBYCHEV POLYNOMIAL LEAST SQUARES FIT

C  
C

P=-1.0  
NU1=.3  
E1=30000000.  
NU2=.26  
E2=10000000.

C=(1.-2.\*NU2)/6.2832

READ IN THE ACTUAL STRESSES

1001

CONTINUE

REAC(8,150) R

REAC(8,151) NMAX

FORMAT(I3)

REAC(8,150)(Z(J),J=1,NMAX)

FORMAT(F10.4)

DO 169 I=1,NMAX

CHANGES LOADS FROM KG TO POUNDS

Z(I)=Z(I)\*2.2046

AFAC=.75\*R\*(1.-NU1\*2)/E1+(1.-NU2\*2)/E2

ASQRD=(AFAC\*Z(I))\*666

BL(I)=-ASQRD\*3.1416

CALCULATES STRESS AT INDENTER OUTSIDE RADIUS

Z(I)=C\*Z(I)/ASQRD

CONTINUE

PRINTS CALCULATED STRESSES

WRITE(5,210)(Z(J),J=1,NMAX)

FORMAT('02'/(12F10.1))

REAC(8,151) KMAX

DO 1000 NDJ=1,KMAX

REAC(8,151) NPCINT

C  
C  
C  
C  
C

CALCULATIONS

NEQUAT=6



#### 7.6.4 95% Confidence Limits for $g(S)$ generated from Hardness Test Data

This program takes a set of loads from indentation tests and generates new random sets of loads and from these randomly generated sets of loads calculates the  $g(S)$  curve as in appendix 7.6.3 .

Twenty sets of randomly generated loads are used to calculate and plot a  $g(S)$  curve. The band of this curve is taken as an estimate of the 95% confidence limit for the mean.

There is a TEST in the mainline which can be specified as 1.0 in order to have the program operate on the raw data alone instead of doing the normal operation as outlined above. This makes the program equivalent to the previous one. 0.0 is used to default the test.

This program has additional input specifications;

I3	{	NPLTY	Plotting $\phi(S)$ ( 0 deletes )
each read		NWRTY	Written output ( 0 deletes )
twice		NPLTG	Plotting of $g(S)$ ( 0 deletes )
		NOGS	Calculations of $g(S)$ ( 0 deletes )
F10.4	{	ZMAX	Maximum load for plotting
1/card		ZPLOT	Maximum stress for plotting
		Z21	21 loads taken off at equal intervals of $\phi$ . Appendix 7.6.5 is used to plot raw data in order to fit that data with a curve from which one can pick off at equal increments of $\phi$ the respective loads.



The remaining input is the same as 7,6,4(repeated here),

	R	F10.4
	NMAX	I3
20 sets of (I3)	KMAX	
	NPOINT	
	...	
	NPOINT	
	KMAX of them	
	smallest of the KMAX NPOINTS	

A sample input is given at the end of the listing.



## VARIABLES

Z LOAD FROM HARDNESS TEST (KG)  
Z MAXIMUM STRESS AT CIRCUMFERENCE OF INDENTER (PSI)  
Y OCCURRENCE/N+1  
X MANIPULATED STRESS  
A COEFFICIENTS OF EQUATIONS FOR LEAST SQUARES FIT  
B RIGHT VECTOR FOR LEAST SQUARES FIT  
R CHERYCHEF POLYNOMIAL COEFFICIENTS  
GS FLAW DENSITY (/IN IN PSI)  
YS CALCULATED PROBABILITY OF FAILURE BELOW A CERTAIN STRESS  
YP FIRST DERIVATIVE OF YS  
YFP SECOND DERIVATIVE CF YS  
R RADIUS CF INDENTER (IN)  
KKMAX NUMBER OF NPOINTS USED TO GENERATE G(S)  
NNU1 POISSONS RATIO OF INDENTER  
NNU2 POISSONS RATIO OF GLASS  
E1 MODULUS OF INDENTER  
E2 MODULUS CF GLASS (PSI)  
P POWER DESCRIBING RELATION OF APPLIED STRESS TO POSITION.

美  
美  
美  
美  
美  
美  
美

**NMAX IS THE NUMBER OF ORDERED DATA STRESSES**

NCINT IS THE NUMBER OF POINTS USED IN THE RUNNING  
CPCBYCCHF POLYNCFIAL LEAST QUARES FIT

TEST=1.0  
TEST=C.0  
P=-1.0  
NU1=.3  
E1=3CG0000.  
NU2=.26  
E2=10CU0000.

C=(1.-2.\*N/2)/6.2832

READ(6,150) R

REAC(8,151) NMAX

FORMAT(I3)

FORMAT(F10.4)

151

150

C

C

C

\*

\*

\*

\*

\*

\*

CALL TPLOT(U,0,0,0,0)

Y21(1)=0.0

DO 3002 I=2,21

Y21(I)=Y21(I-1)+.05

IF(NFLT.Y.EQ.0) GO TO 3001

IF(1.EQ.21) GO TO 3001

CALL TPLOT(Z21(I),Y21(I),1,1)

CONTINUE

Z21(I)=Z21(I)\*ZMAX

CONTINUE

IX=26

DO 3000 L=1,20

IF(1.EQ.0) GO TO 3012

DO 3011 I=1,NMAX

Y(I)=FLOAT(I)/FLOAT(NMAX+1)

CONTINUE

GO TO 3005

CONTINUE

DO 3005 I=1,100

IX=899\*IX+3

Y(I)=FLOAT(IX)/65536.0+.5

CONTINUE

CALL CRDER(Y,NMAX)

DO 3008 I=1,NMAX

YX=Y(I)

CALL INTERP(Z21,Y21,YX)

Z(I)=YX

IF(NWRTY.EQ.0) GO TO 3008



```

NFIRST=(NPJINT+1)/2
NCATA=NMAX-NFIRST+1
DO 1 I=NFIRST,NCATA
DO 4 J=1,NPOINT
N=I+J-NFIRST
      FER2/74 STRESS NCRMALIZED TO 1 FOR CURVE FIT
      X(J)=Z(N)/Z(NMAX)
      Y(J)=FLOAT(I-NFIRST+J)/FLOAT(NMAX+1)
4 CONTINUE
      CALL CURFIT(X,Y,NPCINT,NEQUAT,A,B)
      CALL SCALI(A,B,NEQUAT)
      CALL SIMQ(A,B,NEQUAT,0)

C      CURFIT AND SIMQ TOGETHER EVALUATE THE CHERYCHEF POLYNOMIAL
C      COEFFICIENTS(B) FOR A FIT OF NPOINT DATA POINTS
C
C      FER2/74 STRESS NCRMALIZED TO 1 FOR CURVE FIT
      X(I)=Z(I)/Z(NMAX)
      Y(I)=FLOAT(I)/FLOAT(NMAX+1)
      XXX=X(I)
      CALL CIPFER(B,NEQUAT,XXX,YYY,YP,YPP)
      YS(I)=YYY
      FER2/74 STRESS NCRMALIZED TO 1 FOR CURVE FIT
      X(I)=Z(I)
      FER2/74 STRESS NCRMALIZED TO 1 FOR CURVE FIT
      YP=YP/Z(NMAX)
      FER2/74 STRESS NCRMALIZED TO 1 FOR CURVE FIT
      YPP=YPP/Z(NMAX)/Z(NMAX)
      C CALCULATES CHERYCHEF FUNCTION VALUE
      GS(I)=2.*X(I)*P/BL(I)*(.5*(YPP*(1.-YS(I))+YP**2)/(1.-YS(I))**2)+
      1(1.+1./P)/2.*(YP/(X(I)*(1.-YS(I))))
      X(I)=X(I)/Z(NMAX)
      IF(NWRTY.EQ.0) GC TC 1
      WRITE(5,200) X(I),Y(I),YS(I),YP,YPP,GS(I)
      FCPMAT(1/6(2X,E12.3))
200 1
      CONTINUE

```



0.100  
 0.450  
 0.624  
 0.686  
 0.723  
 0.745  
 0.759  
 0.77  
 0.78  
 0.79  
 0.8  
 0.81  
 0.82  
 0.83  
 0.84  
 0.851  
 0.864  
 0.880  
 0.902  
 0.930  
 1.010  
 .0157  
 100  
 3  
 7  
 11  
 25  
 7  
 C

// END



7.6.5 PLOTTING OF LOAD VERSUS ORDERED PROBABILITY OF FAILURE  
FOR EYEBALL SMOOTHING

C  
C  
C  
C  
C  
C

\* \* \* \* \*

```
// FOR
DIMENSION Z(100),X(100),Y(100)
CALL BEGIN(3,0000)
CALL VECTOR
CALL SCALE(1000.,750.,0.,0.)
CALL AXIS(0.,0.,1.,1.,.05,-1,-1)
NMAX=100
READ(6,3000)(Z(J),J=1,NMAX)
FORMAT(F10.4)
DO 3001 I=1,NMAX
  X(I)=Z(I)/Z(NMAX)
  Y(I)=FLUAT(I)/FLCAT(NMAX+1)
CALL TPLCT(X(I),Y(I),0,0)
CALL TPLOT(X(I),Y(I),1,1)
CONTINUE
STOP
END
```

3000

3001

C // XEQ 1  
C \*EL TEKPLOT  
C PLACE THE LOAD DATA CARDS HERE. ONE LOAD PER CARD.  
C // END

**APPENDIX E-3**

**Proof Testing of Brittle Materials by Thermal Shock**

PROOF TESTING OF BRITTLE MATERIALS BY THERMAL SHOCK

F. A. McClintock  
Professor of Mechanical Engineering

J. R. Matthews  
Research Assistant

DEPARTMENT OF MECHANICAL ENGINEERING  
MASSACHUSETTS INSTITUTE OF TECHNOLOGY  
CAMBRIDGE, MASSACHUSETTS 02139

ANNUAL TECHNICAL REPORT  
FOR THE PERIOD ENDING 30 APRIL 1975

SPONSORED BY  
DEFENCE ADVANCED RESEARCH PROJECTS AGENCY  
ARPA ORDER NO. 2055

MONITORED BY  
AIR FORCE CAMBRIDGE RESEARCH LABORATORIES

## ABSTRACT

Proof testing of brittle materials improves their reliability in service by decreasing the expected number of failures and increasing the confidence in the estimated number of failures. For these materials the deformation is elastic and the loading is static or at most applied only a few times. In order to proof test thoroughly and inexpensively, a thermal shock scanning system has been developed. In addition to proof testing, this system gives insight into the frequency of occurrence of the strength-impairing flaws over a large area. The localized nature of the proof test allows isolating the flaws, facilitating their microscopic examination.

### B. PROOF TESTING OF BRITTLE MATERIALS BY THERMAL SHOCK

#### B.1 INTRODUCTION

The work of this report involves proof testing of brittle materials by thermal shock. The object of proof testing of brittle materials is to catch as many problems as possible in the factory instead of in the airplane, on the spacecraft or on the long distance power transmission line.

Our system traverses a small liquid nitrogen jet across a component. This induces a thermal shock that propagates cracks from imperfections

which might make the component unacceptable in service. This localized proof test facilitates microscopic examination of the flawed area. The system has the added feature of providing quantitatively the frequency of occurrence of the strength-impairing flaws for use in design reliability.

If it were possible to detect flaws non-destructively then proof testing would probably not be employed. In brittle materials, the flaws are often too small to detect. A critical flaw size, characterized by the lesser of depth or crack half length, is estimated by taking reasonable values of the stress intensity factor  $K_{Ic}$  and the working stress  $\sigma$

$$c = \frac{1}{\pi} \left( \frac{K_{Ic}}{\sigma} \right)^2 \quad B-1$$

For a brittle material such as polycrystalline KCl, with  $K_{Ic}$  the order of 200 psi  $\sqrt{\text{in.}}$  under stresses of the order of 2000 psi (half yield), the critical flaws are of the order of .003 in. For applied stresses equivalent to the yield strength the critical flaws are 1/4 this size or less (20 $\mu$ ). This is between the grain size and the sub-grain size of polycrystalline KCl. It is suspected that the flaws are actually smaller than this but grow or develop or both during pre-yield plastic deformation. These flaws, if they be cracks, are probably 1/1000 as thin as long. In dealing with brittle materials we are therefore searching for flaws which are orders of magnitude smaller

than the resolution of commercially available flaw detection systems.

Quantitative estimates of the adaptability of this thermal shock flaw detection system to various materials are given by the stress produced in each material by a moving jet of liquid nitrogen. The temperature drop in the surface of the material is found by using the program described in Section B-2. Cooling of only a thin surface layer gives the maximum stress. This is attained at velocities above 1 cm/sec for a 1 cm jet, as explained in Section B-2. The last column of Table B-1 gives these stresses for a variety of candidate materials.

The first group of materials in Table B-1, laser window candidates, can all be effectively proof tested with this system, although a mean bending stress may be necessary in order to get the applied stresses into the range of interest. The mean bending stress can serve another purpose. It will guarantee, if a flaw is located, that the part will be fractured completely and then there will be no doubt as to whether the visual inspection is adequate. The second group of materials in Table B-1, the metals, can not be proof tested with this system. The third group of materials in Table B-1, the glasses, can be effectively proof tested when a mean stress is applied at the same time. An example of this would be proof testing a television tube under vacuum. Few glasses can be effectively proof tested without initial applied stress.

Table B-1 Adaptability of Thermal Shock Flaw Detection System to Various Materials. ( A scanning velocity of 1 cm/sec and an effective source radius of .5 cm was used to calculate the temperature change. The stress is for thin surface cooling.)

MATERIAL	k $\frac{\text{cal}}{\text{cm sec } ^\circ\text{C}}$	$\rho$ $\frac{\text{gm}}{\text{cm}^3}$	$C_p$ $\frac{\text{cal}}{\text{gm } ^\circ\text{C}}$	$\Delta T$ $^\circ\text{C}$	$\alpha$ $\left(\frac{10^{-6}}{^\circ\text{C}}\right)$	E $(10^6 \text{ psi})$	$\sigma$ psi
KBr	.0050	2.75	.104	43.6	40.0	51.5	10000
NaCl	.0167	2.17	.204	19.2	43.0	7.83	9100
KCl	.0156	1.98	.162	23.3	36.0	4.3	5010
MgO	.06	3.58	.221	7.4	9.8	42.6	4340
CdTe	.0098	5.85	.0375	35.5	5.5	7.9	2160
ZnSe	.0633	4.09	.111	9.1	6.0	15.17	1080
Fe	.0164	7.86	.108	14.0	12.25	30.1	7240
Stainless	.0388	7.95	.12	8.6	16.6	28	5600
Ti	.0394	4.54	.129	10.7	9.0	16.5	2230
Ni	.185	8.76	.11	3.5	13.3	30	1960
Brass	.288	8.50	.09	2.7	20.0	16	1110
Be	.38	1.82	.516	2.0	12.4	40	1390
Mg	.38	1.74	.25	2.2	26.0	6.5	520
Al	.515	2.71	.23	1.6	23.6	10.0	530
W	.48	19.2	.034	1.7	4.31	50	514
Cu	.901	8.91	.092	.9	16.7	17.0	360
Ag	1.0	10.4	.056	.7	19.1	10.5	196
Tantalum	.128	16.4	.036	5.2	6.49	27	1260
Gold	.689	19.3	.056	1.2	14.2	10.8	260
Glass	.0015	2.3	.170	67.9	10.6	10.0	10000
Pyrex 7740	.0027	2.35	.25	41.3	3.2	9.8	1810
Vycor 7900	.0022	2.18	.19	54.5	.8	9.7	590
Fused Silica	.0032	2.16	.17	48.0	.504	10.6	360
Slip Cast Silica	.00078	1.90	.22	91.0	.54	10.1	696
Fused Quartz	.0033	2.2	.188	44.6	.55	10.1	346
Pyroceram 9608	.0047	2.5	.19	34.8	.4	12.5	244
Cer-VIT C-101	.00004	2.46	.22	77.1	.144	13.4	208
Invar	.026	8.00	.095	11.7	1.3	21.4	456
Foam Glass	.00014	.14	.20	99.9	8.3	.18	209
ULE Fused Silica	.0031	2.16	.18	47.4	.054	9.8	350
Super Invar	.033	7.95	.12	9.3	.18	21	49
LA-685	.026	8.13	.12	10.4	.1	20	29
Graphite	.289	1.75	.20	2.9	2.52	.7	7

### Background to Development of the Thermal Shock System

Various people have performed thermal shock experiments (Clark (1965), Conrad et al (1969), Kerchner et al (1971), Hasselman (1969), and Cardin et al (1970)). We selected cooling to minimize plastic flow, liquid nitrogen to maximize the effect, and localized cooling to minimize the amount of material wasted (should the remaining portions be of usable size), to locate the strength impairing flaws, to facilitate their examination and to make a study of their density.

The heat transfer between a jet of liquid nitrogen and a plane surface involves both forced convection and a film or nucleate boiling. In spite of the summaries of heat transfer to jets by Gordon (1965) and to boiling liquids by Colver et al (1970), the combination of a jet and liquid nitrogen and the complexity of the surface nucleation necessitated calibration.

Preliminary tests were conducted on KCl and glass slides. Cracks did not initiate in glass slides but cracks induced by other means propagated easily in these same glass slides under the influence of the nitrogen jet. Polycrystalline KCl did not crack easily at room temperature but did crack readily when the sample was first uniformly cooled to a temperature below the unnotched transition temperature.



## B.2 THEORETICAL HEAT TRANSFER, TEMPERATURE AND STRESS CONSIDERATIONS

The heat transfer from a jet to a surface can be estimated either by adding a forced convection flux to a boiling flux or by using the first law of thermodynamics, empirical heat transfer data, and the geometry of the jet and its impingement. The latter approach is discussed in Matthews (1974) but it is simpler and more accurate to avoid both procedures and find the heat flux by calibration. The section then shows how to determine the temperature distribution in a material knowing the scanning velocity, to evaluate stresses using a finite element analysis in three dimensions, and to make approximate stress calculations without costly computer runs.

The net result of this section is a calibration curve of developed stress as a function of the scanning velocity  $U$ . It is evaluated for KCl but the path is clear for developing similar curves for other materials.

### Nitrogen Jet Calibration

A 1/4 inch diameter copper rod with thermocouples 1/2 inch apart and a cartridge heater at the far end was used to calibrate the heat flux from the nitrogen jet. The whole length was well insulated with asbestos and styrofoam and sealed in a plexiglass container with vacuum grease. A drying agent in the container would indicate any moisture leaks.

The heat rate per unit area is found from the thermal conductivity and temperature gradient by

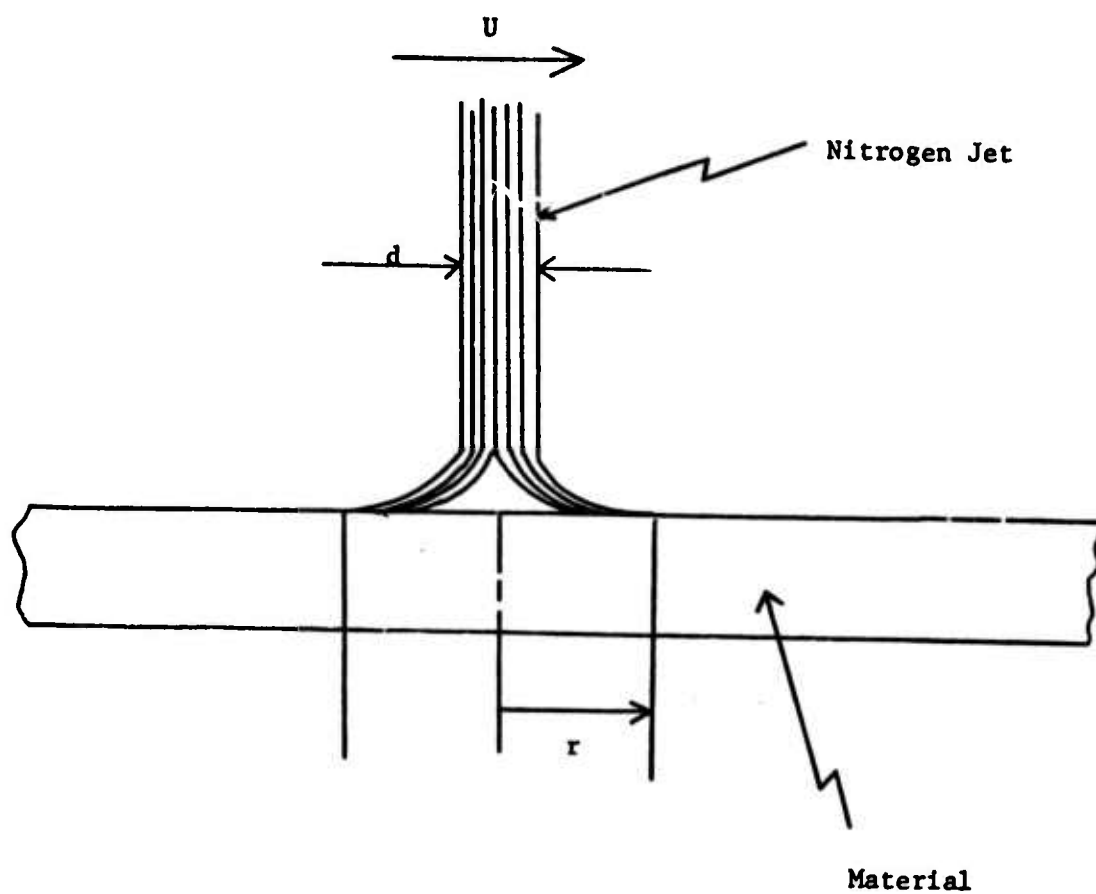


Fig. B -1 Thermal shock flaw detection system.

$$Q = k \frac{dT}{dz}$$

B-2

The resulting value agreed with the wattage drawn by the cartridge heater within 5%.

#### Temperature Distribution Resulting from Finite Moving Heat Sink

The solution for the temperature distribution due to a finite moving heat source in an infinite solid is given in Carslaw and Jaeger (1959). The nitrogen jet is an approximate constant flux sink. In terms of coordinates normalized in terms of scanning velocity  $U$  and thermal diffusivity  $\kappa$ ,

$$X = xU/2\kappa \quad Y = yU/2\kappa \quad Z = zU/2\kappa$$

and normalized source radius  $r$

$$R = \frac{\sqrt{\pi} U r}{4\kappa}$$

the temperature rise is given in terms of the heat rate per unit area on a half-space  $Q$  and thermal conductivity  $k$  by

$$\Delta T = \frac{Q \kappa}{2k U (2\pi)^{1/2}} \int_0^\infty e^{-Z^2/2u} \left\{ \operatorname{erf} \frac{Y+R}{\sqrt{2u}} - \operatorname{erf} \frac{Y-R}{\sqrt{2u}} \right\} \cdot$$

B-3

$$\cdot \left\{ \operatorname{erf} \frac{X+R+u}{\sqrt{2u}} - \operatorname{erf} \frac{X-R+u}{\sqrt{2u}} \right\} \frac{du}{\sqrt{u}}$$

Matthews (1974) reports a computer program which solves this equation.

The primary use of the program was to get nodal temperatures for the finite element stress solution. Results for different velocities and

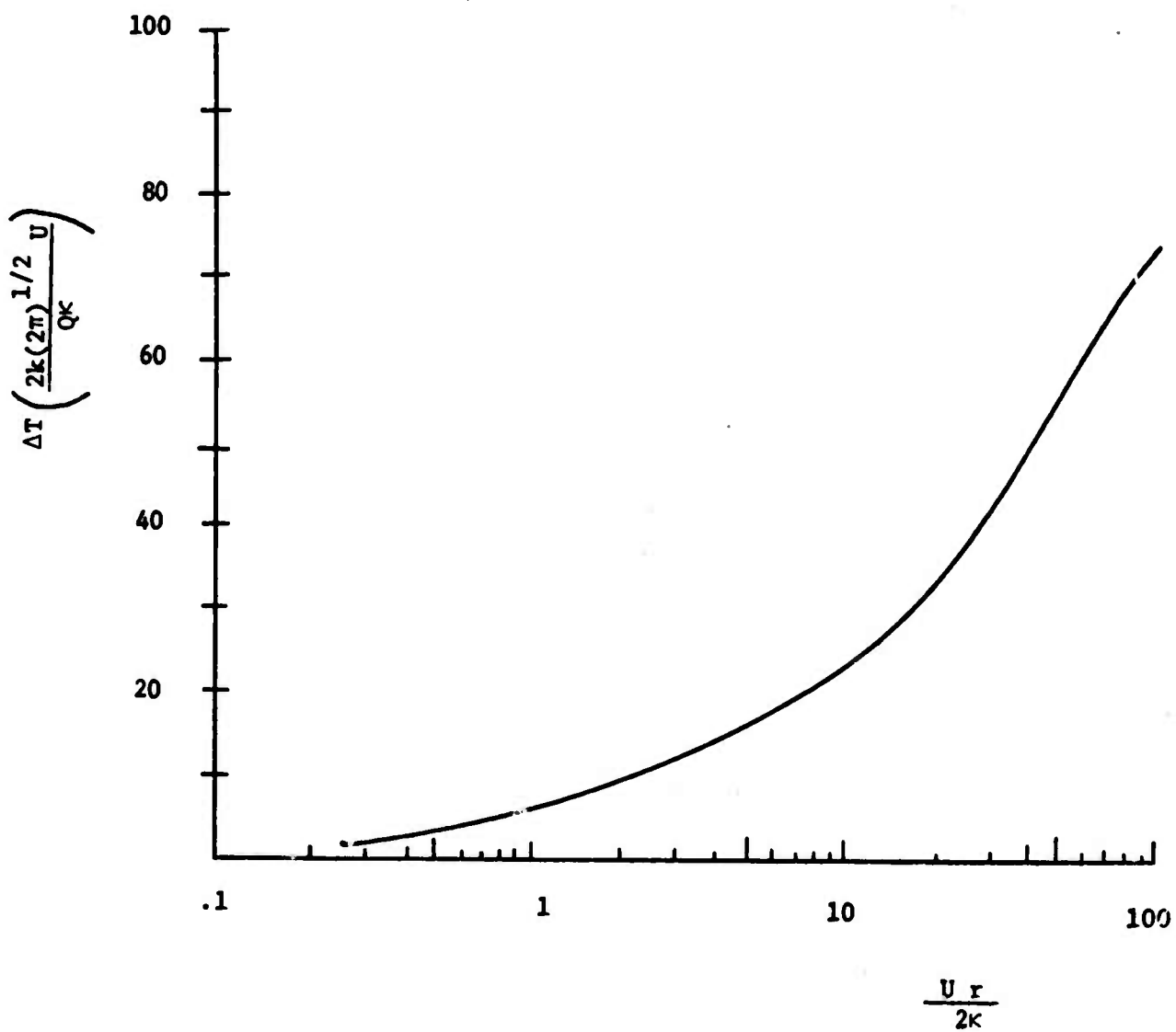


Fig. B-2 Temperature at center of moving heat sink in normalized form.

effective radii of sink are plotted in Fig. B-2. The results of the computer program were within  $\pm .5\%$  of a series of approximate solutions given by Jaeger (1943).

#### Finite Element Stress Solution

A disk of 10 cm diameter and .5 cm thickness with properties of polycrystalline KCl was modelled using finite elements to correlate the stress developed by a scanning nitrogen jet with that approximated by

$$\sigma = K \cdot E \cdot \alpha \cdot \Delta T \quad \text{B -4}$$

which is the general form of both disk cooling (temperature constant through thickness) and thin surface cooling.

For pure surface cooling on an apparently infinite body

$$(\epsilon_x = \epsilon_y = 0, \sigma_z = 0)$$

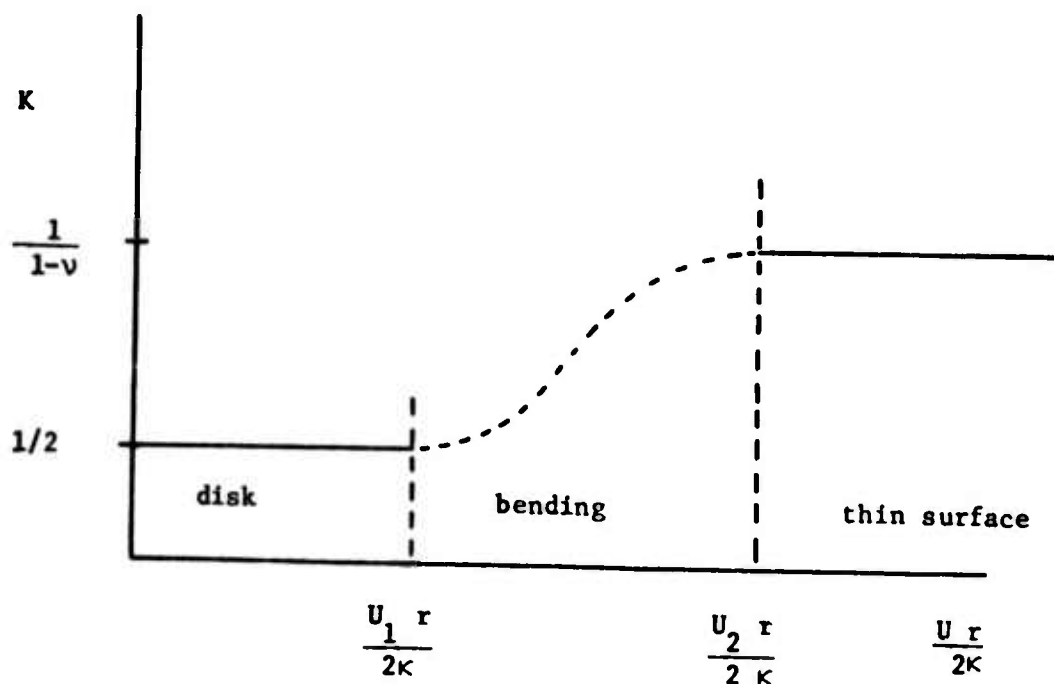
$$\sigma = - \frac{E \cdot \alpha \cdot \Delta T}{1-\nu} \quad \text{B -5}$$

For disk cooling of a relatively thin disk the stress developed in the zone of cooling is (Timoshenko 1970)

$$\sigma = - \frac{E \cdot \alpha \cdot \Delta T}{2} \quad \text{B -6}$$

It is expected therefore that K of Eq. -4 is a function which could be approximated by two horizontal lines and a transition region.

The extremes of the transition are denoted by the normalized velocities  $U_1 r / 2\kappa$  and  $U_2 r / 2\kappa$ .



Stress calculations with the finite element Strudl package were made for tangential scanning velocities of .1 and 1 cm/sec and an effective source radius of .5 cm to accomplish the above correlation. The maximum stress occurred at the same node for each velocity. This was ahead of the jet center. For  $U = .1$  cm/sec the maximum stress corresponded to that for disk heating. For  $U = 1$  cm/sec the maximum stress corresponded to that for simple surface heating. These two velocities were then taken as the break points of  $K$  and on this basis the calibration curve for the moving nitrogen jet sink was generated. This calibration curve is given in Fig. B-3 in a semi-log plot.

Once  $U_2$  and  $U_1$  are established for a specific specimen thickness then  $U_2$ , as a minimum, is valid only for thicker specimens and  $U_1$ , as a maximum, is valid only for thinner specimens. After completing

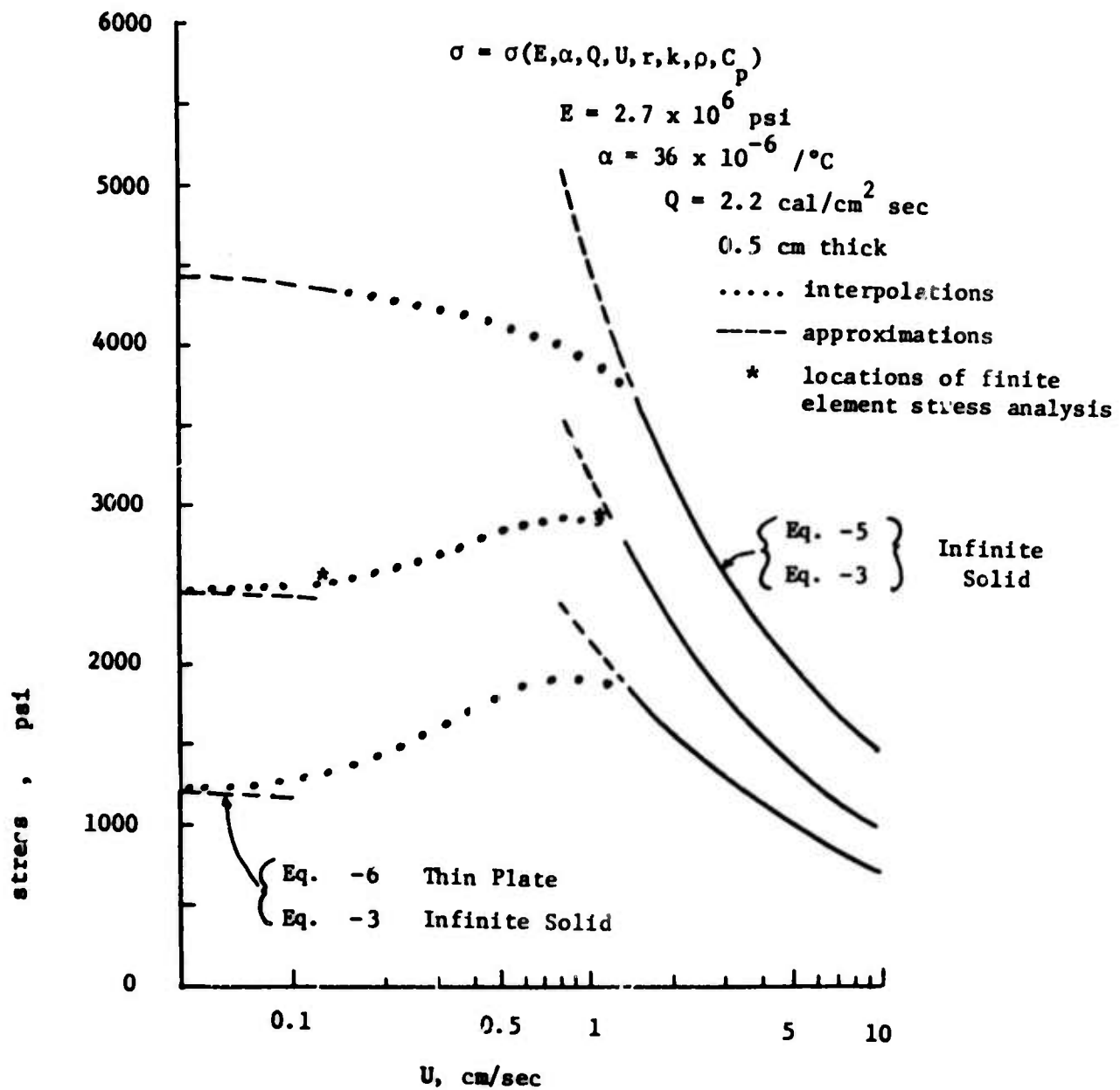


Fig. B-3 Maximum stress developed by nitrogen jet of radius  $r$  and heat flux  $Q$  moving with velocity  $U$ .

the finite element work it became apparent that a wider range of stresses was available for scanning velocities which caused thin-surface stressing. This was found to be the case for all  $U_r/2K > 5$  when the thickness of specimen was 0.5 cm. It is recommended therefore that the system only be used in the range of scanning velocities  $\frac{U_r}{2K} > 5$  and specimen thicknesses greater than .5 cm. Caution should be exercised when using the system calibration when testing parts of thickness much less than .5 cm. (see Matthews 1974 for details).



### B.3 THE NITROGEN JET FOR THERMAL SHOCK

Generation of a reproducible, steady, liquid nitrogen jet was the first equipment requirement. A line with an orifice was unsatisfactory because heat generated causes gas to build up behind the orifice, allowing only gas phase to exit. We found a simple bypass to be unsteady. The nitrogen jet generator therefore must supply adequate cooling to the stream, that is it must maintain the liquid, and second it must have a large enough liquid volume to insure steady output. Both of these requirements are satisfied in the nitrogen jet generator described here.

The liquid nitrogen came from a syphon tank (160 litre dewar) under 20 psig pressure. The connection from the 20 psig liquid nitrogen reservoir to the nitrogen jet generator was made with flexible teflon hose. A copper coil ( Fig. B-4) was constructed from 15 feet of 3/8 inch copper tubing. The coil was placed in a standard one litre dewar and positioned with styrofoam. A 1/8 inch tube at the end of the coil ( 3/8 inch tubing ) ran through the counter flow heat exchanger and contained the nozzle.

The tube from the end of the coil to the nozzle and the nozzle itself must remain at liquid nitrogen temperature or below or else the jet will not exit as a liquid. A second 1/8 in. tube from the beginning of the coil runs parallel to the jet supply tube and has its exit inside a larger tube, which houses both tubes, just behind the nozzle. The flow from this cooling supply tube then goes back

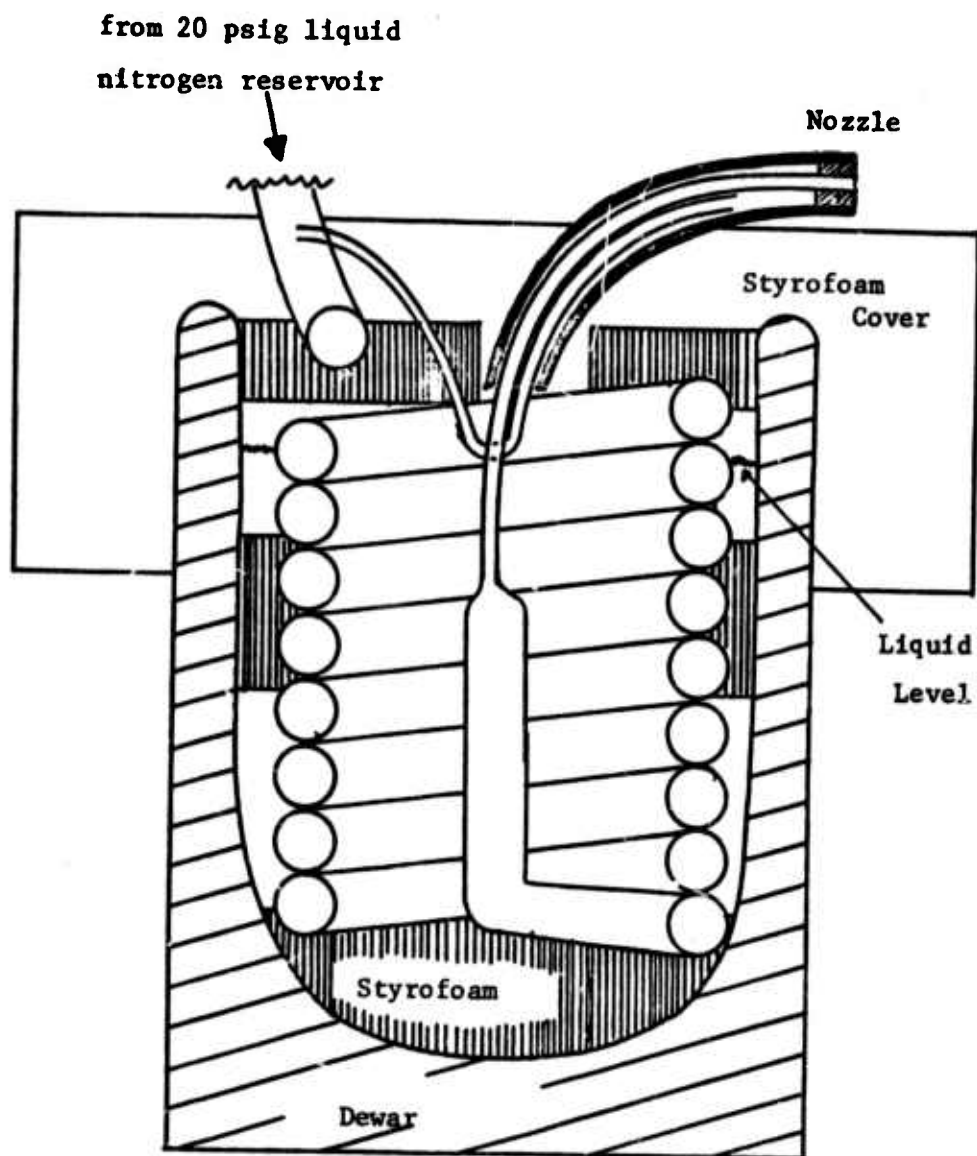


Fig. B-4 Liquid Nitrogen Jet Generator. (Sectional)

along the jet supply tube and exits into the dewar. At this point gas can escape and liquid nitrogen left in the cooling stream fills the dewar. After testing several tube lengths and nozzles we found that a 4 in. dewar length with a .010 in. nozzle worked well, self-filled the dewar 80% of its volume and became stable. This took place in roughly 15 minutes. Thus a steady, reproducible nitrogen jet source was achieved.

The nozzle assembly C ( Fig. B-5 ) was glued with epoxy into the flexible teflon sleeve housing the counterflow heat exchanger and the main tube B ( Fig B-5 ) was glued to the nozzle assembly C. The nozzle itself (A in Fig. B-5 ) was then a replaceable unit. Additional orifices could be placed inside the nozzle tube to add resistance for additional pressure drop.

For our development work we scanned the specimens with the nitrogen jet mounted on a lathe. Specimen temperature was controlled by lightly clamping this to a copper block with an oil film to aid conductivity. ( Matthews 1974) .

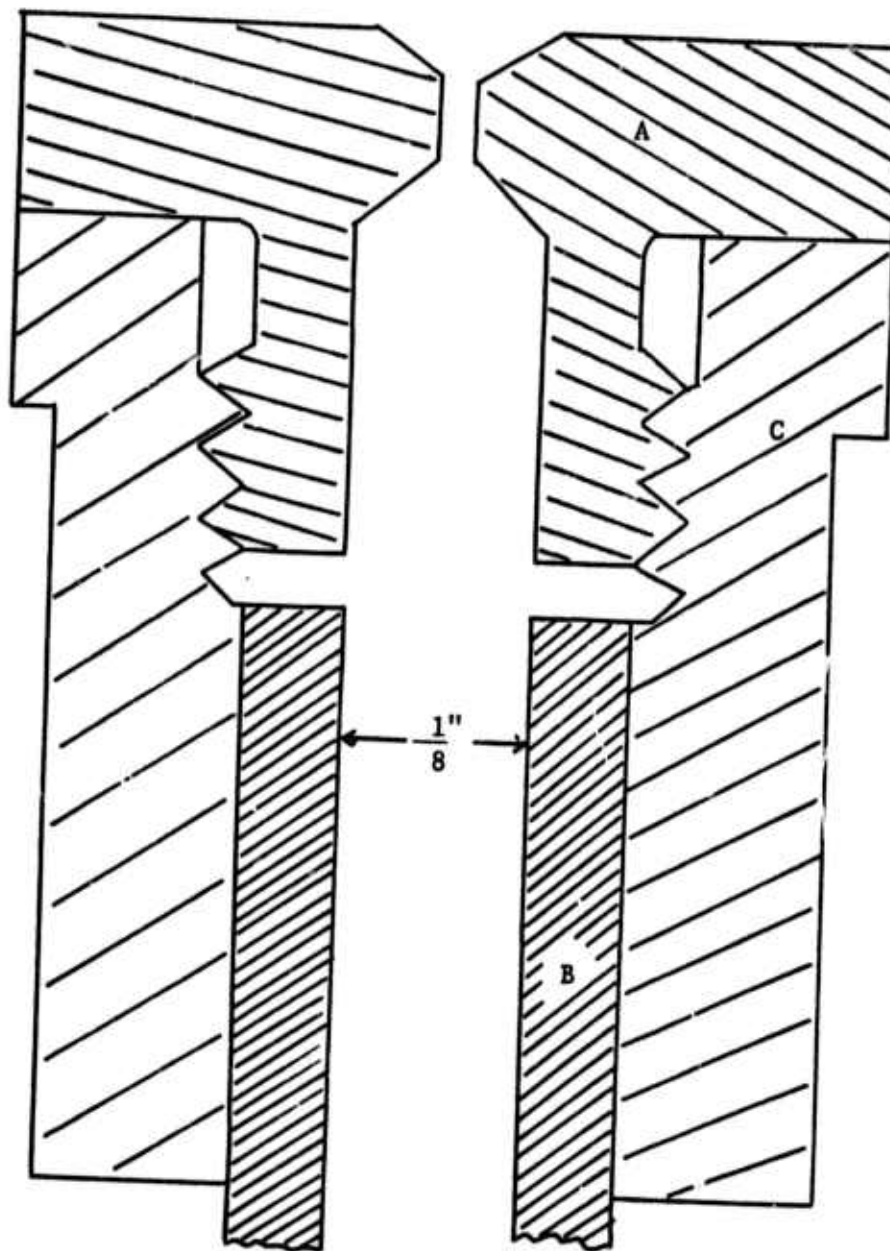


Fig. B-5 Nozzle for Nitrogen Jet Generation ( Scale X 16 )

#### B.4 RESULTS AND DISCUSSION

The object of thermal shock proof testing of brittle materials is to catch as many problems as possible in the factory instead of in the airplane, on the spacecraft or on the long distance power transmission line. We are proof testing in order to truncate the lower end of the flaw density curve and thereby decrease the probability of failure for every stress and at the same time gain more confidence in our estimate of the probability of failure since we have eliminated part of the debatable portion of the flaw density curve. By proof testing to the design stress one theoretically reduces the probability of part failure to zero. Fig. B-6 displays this effect. Since the stress distribution may not be that of service conditions some defective parts may pass.

If  $\delta\phi$  is the probability of failure in a small increment of area  $\delta A$  when stressed to a level  $S_1$  then

$$\delta\phi = \delta A \int_0^{S_1} g(S) dS \quad B-7$$

where  $g(S)$  is the flaw density curve of a particular material. From this basic definition one can analytically derive methods of determining the flaw density curve of different materials from experimental tests. McClintock (1973) shows how to obtain flaw density curves from three point bend tests and Matthews et al (1974) shows how to obtain flaw density curves from indentation tests.

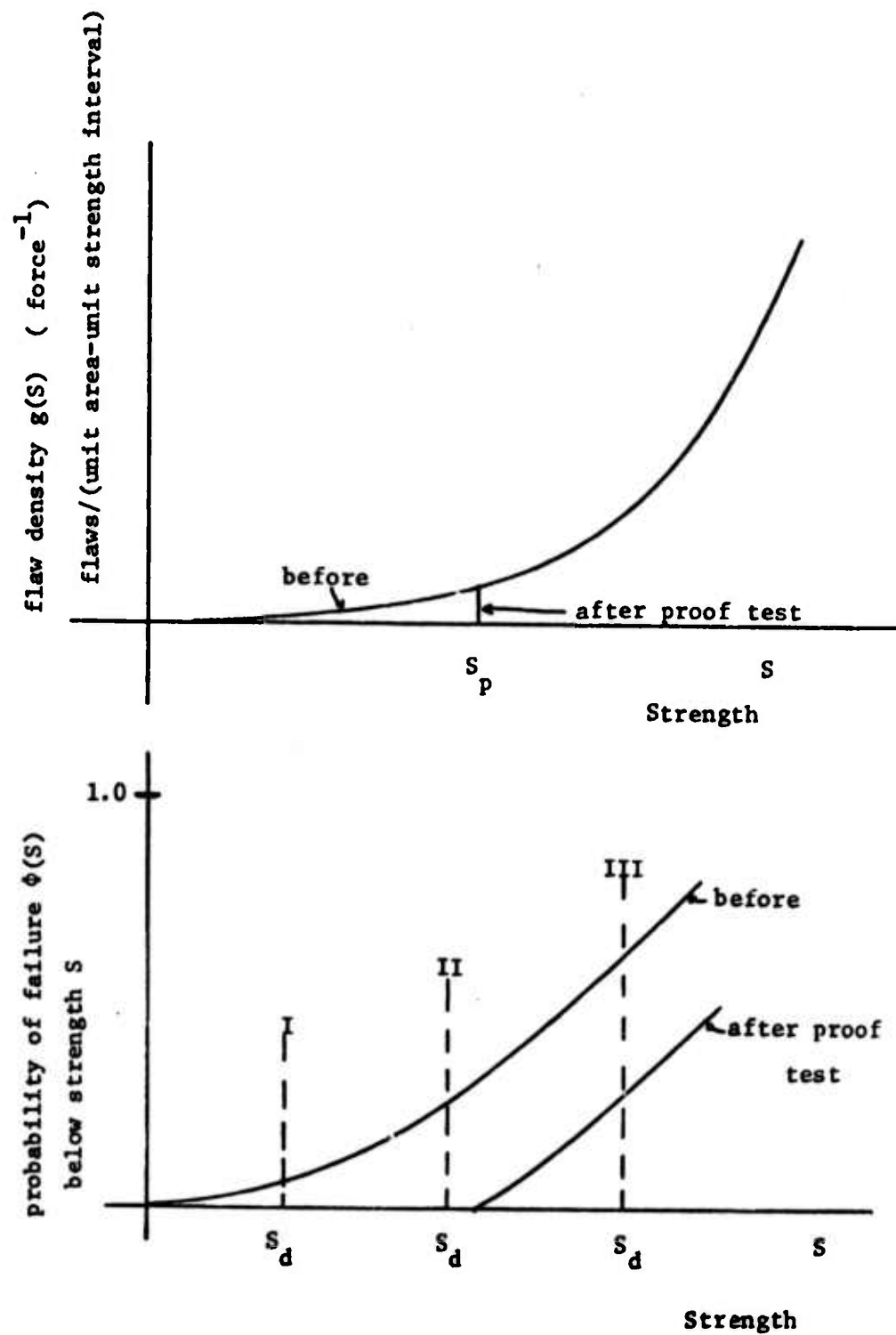


Fig. B-6 Object of thermal shock proof testing of brittle materials.

For a part of size  $A$  which will be stressed uniformly to a design level  $S_d$  the probability of failure is

$$\phi = 1 - e^{-A \int_0^{S_d} g(S) dS} \quad B-8$$

Proof testing to a stress level  $S_p$  cuts off the lower end of the flaw density curve, thereby reducing the integral of Eq. -8 and reducing the probability of failure of the part in service. Furthermore, the lower end of the flaw density curve is the most difficult to obtain and contains a high level of uncertainty. Therefore by eliminating the lower end of the curve (by proof testing) we will be able to estimate the fraction of specimens that will fail in service with better certainty.

For a constant proof stress the largest decrease in the probability of failure comes when the design stress is higher than or equal to the proof stress. At design stresses I and II of Fig. -6 one must worry about damage that may affect the life. This of course varies from material to material ( more relevant to ductile materials ) and therefore if one decides to proof test above the design stress, one should do fatigue tests with and without an initial overstress. All things considered however, proof testing to the design stress is usually the most economical. In light of the work on LiF (McEvily (1959) and Argon (1969))

NaCl (McEvily) and KCl (Pelloux) we did not expect fatigue to be a problem with KCl, in any event. They reported that they could not produce fatigue failure at room temperature in these types of materials regardless of the magnitude of the stress amplitude.

#### Fracture in Polycrystalline KCl

In order to understand the nature of flaws in a material it is necessary to recall the mechanisms of fracture. Fracture near the upper limit of the strength of polycrystalline KCl, at room temperature, is preceded by

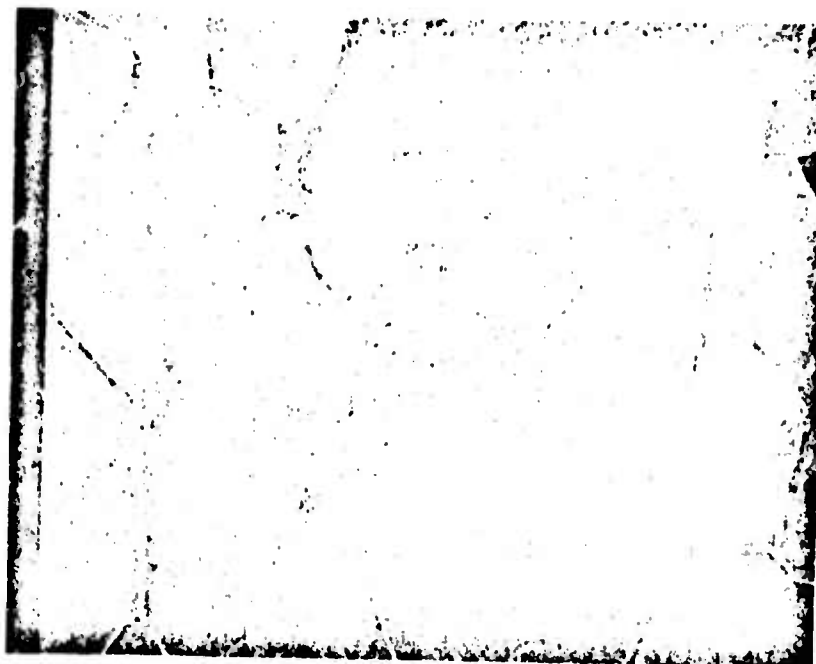
- (1) intergranular decohesion in the absence of slip
- or (2) intergranular or intragranular crack nucleation at grain boundaries due to slip incompatibility.

To explain these it is easiest to describe what the ceramacist is trying to do when he hot works the material to improve the strength.

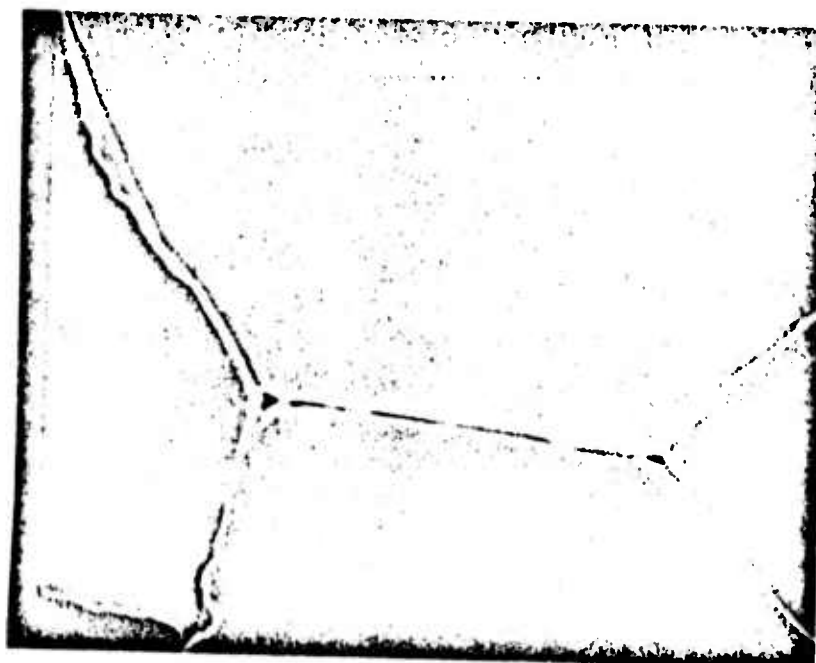
(1) By hot working the grain size is reduced with the object of minimizing the initiation or movement of slip dislocations in dense polycrystalline material. The material would then deform elastically up to the highest stress that the intergranular cohesion can support. An example of this is shown in Fig. B-7. The white line is due to gold coating decohesion.

(2) By hot working the grains receive a strong texture, the net positive effect being a reduced misorientation across grain boundaries. Thus hot working can improve fracture resistance by reducing both slip and elastic incompatibility.





10 $\mu$



1 $\mu$

Fig. B-7 Failure occurs when the intergranular cohesive strength is reached.

When KCl fractures well below the above two strength limits it is usually because of one of the following three agents of fracture initiation:

- (3) porosity
- (4) surface contamination
- (5) mechanical damage

Susuki reported that cracks will form at the edges of small surface crystallites formed by evaporation of water after polishing. This of course is fracture caused by contamination. Most ceramics currently prepared by hot pressing, even those of high density, contain some residual porosity in the grain boundaries. This porosity seriously impairs the intergranular cohesive strength and drops the fracture resistance even further.

In short time tests there is no evidence of stress corrosion cracking in polycrystalline KCl. (Fig. B-8). The specimen was held just under the critical load for 1 week. This corroborates the findings of Singh et al who were trying to obtain slow crack propagation in KCl. The meandering intergranular crack in Fig. B-8 came first, followed by the sharp transgranular crack normal to the plane of loading. It was suspected that a few grain boundary segments failed as in Fig. B-7 and as the load was increased these were connected up until an instability was reached and then a sharp transgranular crack occurred normal to the plane of loading.



1μ



Fig B-8 Meandering intergranular(center) and sharp transgranular (vertical) cracks (1000X). Specimen held just under critical load for one week.

### Proof Tests of Polycrystalline KCl

Section 2 contains the thermal shock calibration curve ( stress vs. scanning velocity ) for polycrystalline KCl. The proof stress can be set by adjusting the scanning velocity. The system works well and proof stresses up to 3000 psi can be readily obtained. This is a realistic design stress for laser window installations. Data are limited because the probability of failure, within the effective area of the jet, when scanning at 1 cm/sec ( a proof stress of 3000 psi ) is 15-20%. Data is also limited because specimens were in scarce supply, independent of the price.

The specimen in Fig. B-9 was scanned at many velocities down to 1 cm/sec, at which point a proof stress of 3000 psi was reached. There was no failure. The specimen temperature was reduced below the fracture transition point and failure occurred at 2500 psi. The crack progressed unstably for 1 cm and halted. Continuation of the test propagated the crack to the extremes shown in the photograph. The halting of the crack is in agreement with the extent of the stress field.

Fig. B-10 contains more results for polycrystalline KCl at room temperature in which additional mean bending stresses ( preloads ) were required to cause failure. The specimen in the second test most likely failed at a stress lower than the stress in the next to last cycle because of low cycle fatigue.

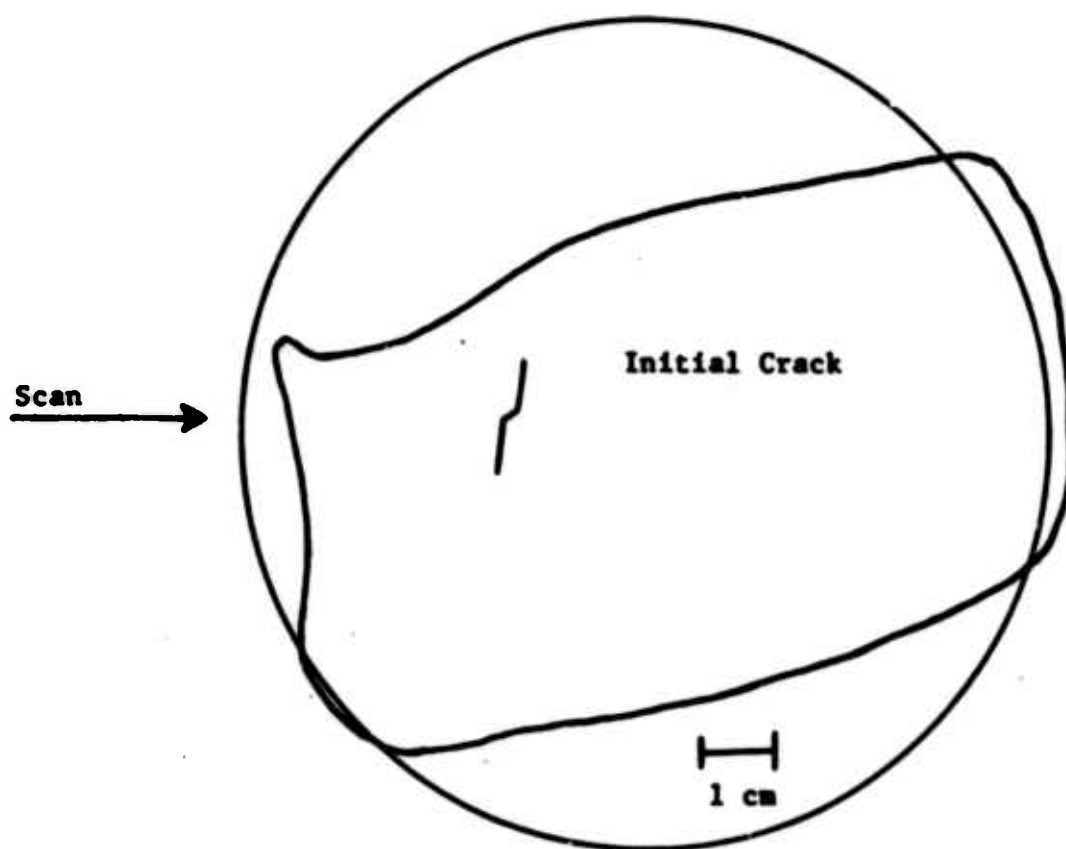
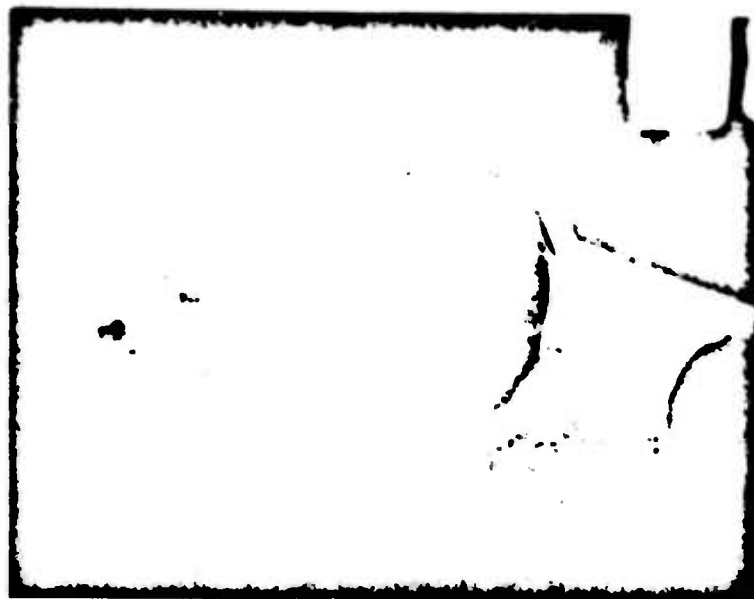
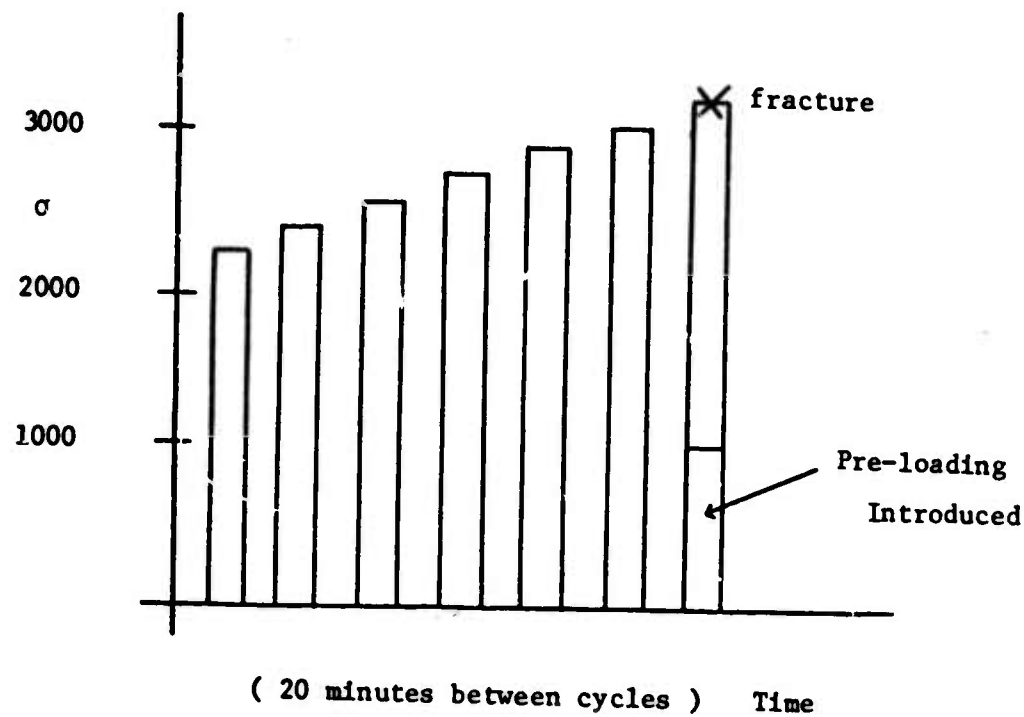


Fig. B-9 Thermal Shock Proof Testing of Polycrystalline KCl



The main goal of this work was the development of a procedure for the evaluation and design of laser window and other brittle materials. A thermal shock scanning system and a statistical analysis seem to have been the best means to this end. The major reason for thermal shock proof testing was to truncate the lower end of the flaw density curve of a material thereby decreasing the probability of part failure in service.

The thermal shock scanning system consisted of a jet source that was steady, reproducible, and very easy to duplicate. It encompassed such characteristics as a 10 cubic inch line of liquid nitrogen to provide steady flow, and was self filling to a level of 80% in fifteen minutes, thereby being reproducible and having a short time constant to steady state.

Even though we have an adequate description of the flaws by the flaw density curve, to perform design and evaluation procedures it is important to know the micro-structural nature of the flaws. Viewing KC1 under load (bending) in the scanning electron microscope has shown two of an expected five modes of fracture initiation: (1) grain boundary separation (along the whole length of a grain boundary segment), and (2) crack formation in the vicinity of surface contamination. The three remaining suspect modes of fracture, from (3) slip incompatibility at grain boundaries and subsequent cracking, (4) porosity and (5) mechanical surface damage, need no proof of possibility.

## B.6

## REFERENCES

- Argon, A. S.  
Godrich, J.A. 1969 "Fatigue in LiF at Elevated Temperature",  
Fracture, Brighton.
- Carden, A.E.  
Andrae, R.W. 1970 "Thermal Stress Crack Initiation Method  
for Ranking Ceramic Materials", J. Am.  
Cer. Soc., v. 53, 339-342.
- Carslaw, H.S.  
Jaeger, J.C. 1946 Conduction of Heat in Solids, Oxford,  
Clarendon Press
- Clarke, F.P.  
Miles, G.D. 1961 "Thermal Shock and Fracture in Crystals  
of MgO", Philosophical Magazine, v. 6  
1449-1452.
- Clements, L.D.  
Colver, C.P. 1970 "Natural Convection Film Boiling Heat  
Transfer", Industrial and Engineering  
Chemistry, V. 62, 26-45.
- Coble, R.L.  
Kingery, W.D. 1955 "Effect of Porosity on Thermal Stress  
Fracture", J. Am. Cer. Soc., v. 38,  
33-37.
- Conrad, C.F. 1969 "An Automated Thermal Shock Chamber  
Designed for MIL STD 202 Test Require-  
ment", Proc. Assurance Conf. and Tech.  
Exhibit, Trans, Hempstead, New York,  
194-196.
- Gardon, R.  
Akfirat, J.C. 1965 "The role of Turbulence in Determining  
the Heat Transfer Characteristics of Im-  
pinging Jets", Int. J. of Heat and  
Mass Transfer, 1261-1272.
- Hasselman, D.P.H. 1969 "Unified Theory of Thermal Shock Fracture  
Initiation and Crack Propagation in  
Brittle Ceramics", J. Am. Cer. Soc.,  
V. 52, 600-604.
- Kirchner, H.P.  
Rishel, P.A. 1971 "Measuring the Tensile Strength of a  
Brittle Material Using a Thermal  
Contraction Loading Device", J. Mater.,  
v. 6, 39-47.



- |   |      |  |
|---|------|--|
| LeClerc, A.                                       | 1950 | "Deviation d'un Jet Liquid Par Une<br>Plaque Normal a Son Axe", Houillee<br>Blanche, 816-821.  |
| McClintock, F.A.<br>Walsh, J.B.                   | 1962 | "Friction on Griffith Cracks in Rocks<br>Under Pressure", <u>Proc. of the Fourth<br/>U.S. National Congress of Appl. Mech.</u> ,<br>1015-1021. |
| McClintock, F.A.<br>Argon, A.S.                   | 1966 | <u>Mechanical Behaviour of Materials</u> ,<br>Addison Wesley, Reading, Mass.   |
| McClintock, F.A.<br>Matthews, J.R.                | 1973 | "Design Strength of Polycrystalline<br>KCl", 3rd Annual Conf. on High Power IR<br>Laser Window Mat'ls., Hyannis, Mass.                         |
| Markowitz, A.                                     | 1972 | "Thermal Control of High Power Laser<br>Windows", <u>Raytheon Co.</u> , Missile Sys. Div.  |
| Matthews, J.R.                                    | 1974 | "Proof Testing of Brittle Materials by<br>Thermal Shock", Ph.D. Thesis, Dept.<br>of Mech. Engr., MIT, Cambridge, Mass.                         |
| Matthews, J.R.<br>McClintock, F.A.<br>Shack, W.J. | 1974 | "Statistical Determination of Flaw<br>Density in Brittle Materials", <u>J. Am.<br/>Cer. Soc.</u> , t.b.p.                                      |
| McEvily, A.J. Jr.<br>Machlin, E.S.                | 1959 | "Critical Experiments on the Nature of<br>Fatigue in Crystalline Materials",<br><u>Fracture</u> , Swampscott.                                  |
| MIT   | 1972 | "Laser Window Quarterly Reports",<br>1, 2, 3, 4  |
| Pelloux, R.M.N.                                   | 1973 | Personal Communications.   |
| Rohsenow, W.M.<br>Choi, H.                        | 1961 | <u>Heat Mass and Momentum Transfer</u> ,<br>Prentice-Hall, 111-116.  |
| Singh, Raj  | 1973 | Personal Communication   |
| Timoshenko, S.P.<br>Goodier, J.N.                 | 1934 | <u>Theory of Elasticity</u> , McGraw-Hill,<br>New York.  |

## F. FRACTURE TOUGHNESS AND FATIGUE

### F.1 GENERAL REVIEW

Fracture Toughness. The brittle behavior of alkali halide ceramics is generally attributed to the lack of five independent slip systems as required for an arbitrary shape change.<sup>1-3</sup> This inability to undergo plastic deformation at the tip of a crack results in high tensile crack tip stresses which lead to fracture by cleavage. Groves and Kelley<sup>4</sup> have shown that only two of the six primary  $\{110\}$   $\langle 110 \rangle$  slip systems of NaCl type structures are independent but that the activation of  $\{100\}$   $\langle 110 \rangle$  secondary systems at high temperatures provide the necessary five slip systems. Gilman<sup>5</sup> has shown by slip line trace analysis that these secondary systems can operate in LiF above 700°K. The activation of secondary slip systems in alkali halides leads to the formation of wavy glide bands which replace the planar glide bands observed on surfaces which are plastically deformed at low temperatures. The appearance of wavy glide has been used by some investigators to identify the onset of ductile behavior. Stokes and Li<sup>6</sup> found that the disappearance of notch sensitivity in NaCl at about 200°C was accompanied by an increase of wavy glide. Carnahan and others<sup>7</sup> found in AgCl a similar ductile-brittle transition at about -100°C.

Stoloff and others<sup>8</sup> reported a very sharp brittle

to ductile transition at 250°C for large grained (350  $\mu\text{m}$ ) polycrystalline KCl. Total elongation increased from 7.5% at 240°C to 69% at 260°C for a strain rate of .0067  $\frac{\text{in}}{\text{in-min}}$ . The fracture stress was relatively insensitive to the test temperature over the range 50°C to 300°C.

Independent of consideration of slip systems, Gorum and others<sup>9</sup> have attributed the brittle behavior of KCl to an embrittling surface reaction of KCl with air. Exposure to oxygen or nitrogen for periods as short as one minute were found to drastically reduce the ductility of freshly cleaved crystals. The presence of water vapor in helium was found to have no effect. Embrittlement was also found to be somewhat controlled by the total impurity content. Previously Dekeyser<sup>10</sup> had shown that a similar surface reaction for rocksalt in air could alter the stress-strain curve and could lead to an increase in surface hardness.

Following the method of Gilman,<sup>11</sup> who first used the double cantilever beam (DCB) specimen to measure fracture energies of ceramics, a number of investigators have studied the fracture surface energy of single crystals of the NaCl type. Westwood and Hitch<sup>12</sup> measure the (100) cleavage strength of KCl at room temperature and found a surface energy,  $\gamma$ , of .11 J/m<sup>2</sup>. If we assume that the only energy absorbing mechanism was the creation of the two fracture surfaces then we may say that the fracture energy,

$G_{IC}$ , is equal to  $2\gamma$ . For an elastic modulus of  $E$  equal to  $4 \times 10^{11} \frac{\text{dyn}}{\text{cm}^2}$  and a Poisson's ratio of  $\nu$  equal to .25 the plane strain fracture toughness,  $K_{IC}$ , may be calculated to

$$K_{IC}^2 = E G_{IC} \frac{1}{(1-\nu^2)}$$

For  $G_{IC}$  equal to .22 J/m<sup>2</sup> this yields a value of about 90 psi  $\sqrt{\text{in}}$ .

Class and Machlin<sup>13</sup> found a value of  $\gamma$  equal to .11 J/m<sup>2</sup>. In addition they studied bicrystals to determine the fracture surface energy as a function of the twist angle between two grains having a grain boundary with a common (100) plane. They found that the energy needed for fracture of grain boundaries with twist angles greater than 10° was only one half the single crystal value.

It is expected that fracture surface energy measurements of single crystals should be only slightly affected by the test temperature so long as plastic flow is small and fracture surfaces do not deviate significantly from one single plane. Tests by Gilman<sup>11</sup> on MgO single crystals over the range temperature from 6°K to 300°K bear this out. Other tests on single crystals of LiF in the same study show a stronger dependence with the fracture surface energy doubling over the same temperature range. In trying to account for the fracture energy absorbing processes, Gilman reports that the scatter in his data correlated well with

the number of cleavage steps observed on the surface of the crystal.

Using MgO bicrystals, Lange<sup>14</sup> investigated the role of grain boundaries as barriers to crack propagation. He found that the angle,  $\alpha$ , between the two intersection lines formed on a grain boundary plane by the intersection with the two respective (100) cleavage planes was an important fracture parameter in this material. Estimates of the energy absorbed during fracture due to the presence of the grain boundary were made and the estimates were found to increase as  $\alpha$  increased from 0° to 45°.

In one of the few reported fracture toughness studies on polycrystalline specimens Clark and others<sup>15</sup> have found that in MgO there is a strong grain size dependence of the fracture toughness. Their data is quite limited but it shows that the work of fracture for a grain size of 38  $\mu\text{m}$  is four times that for a grain size of 7  $\mu\text{m}$  and twenty times that for single crystals of MgO. Work on  $\text{Al}_2\text{O}_3$  by Swanson and Gross<sup>16</sup> has also suggested a grain size dependence of fracture toughness.

Ritchie and others<sup>17</sup> have experimentally and theoretically examined the grain size dependence of  $K_{\text{IC}}$  for cleavage fracture of low carbon steel specimens containing a sharp crack. They concluded that a critical tensile stress for unstable cleavage fracture must be exceeded at

the crack tip over some characteristic length which is dependent upon the grain size. A theoretical analysis of the plastic stress distribution at the crack tip shows that this characteristic distance is of the order of two grain diameters. Their theory also accounts for the temperature dependence of  $K_{IC}$  in the temperature range where cleavage fracture occurs.

Early in this work, Pelloux and Lemaignan<sup>18</sup> provided a limited amount of data from notched three point bend tests which showed that by press forging single crystals of KCl to obtain a fine grain size, the fracture toughness was markedly improved. In a recent similar study Beecher and others<sup>19</sup> also showed an increase of  $K_{IC}$ , however the values of  $K_{IC}$  obtained were much smaller than those obtained by Pelloux and Lemaignan.

In another attempt to improve the fracture resistance of an alkali halide, Forwood<sup>20</sup> has used single crystals of NaCl which were doped with precipitates in the form of 1  $\mu$ m cavities associated with particles of gold introduced by electrodiffusion at 650°C. It was found that when the cavities were spaced 30  $\mu$ m apart the fracture work increased to 100 times that for normal NaCl which is interesting but impractical because the presence of cavities in a laser window material would lead to very poor optical properties.

Since the effects of fracture toughness testing are

sometimes difficult to assess for ceramics, a few investigators have recently tried to evaluate the role of various parameters on  $K_{IC}$ . Swanson and Gross<sup>16</sup> attempted a fairly complete study by correlating experimentally six different parameters and their interactions for DCB specimens of  $Al_2O_3$ . Scatter in the data masked a number of effects but it was found that grain size was the most important factor and that strain rate could be significant. The effect of these parameters on fracture toughness was thought to be ultimately related to the relative amounts of transgranular and intergranular fracture.

Wilshaw and others<sup>21</sup> have shown theoretically that fracture toughness is proportional to the square root of the crack tip radius of a notched bend specimen when the radius is above some critical radius. Using notched three point bend specimens, Bertolotti<sup>22</sup> found experimentally that the critical radius for  $Al_2O_3$  is 70  $\mu m$ . Simpson<sup>23</sup> has recently considered the effect of a notch of finite width containing a short sharp crack at the tip of the notch. He has proposed that the ratio of root crack length beyond the tip of a sawcut notch to notch tip radius be greater than .5 for valid determination of fracture energies in ceramics. The ratio of the notch depth to specimen thickness may also affect  $K_{IC}$  measurements as demonstrated by Hartline and others,<sup>24</sup> with three different ceramic materials.

Fatigue. McEvily and Machlin<sup>25</sup> in some classical studies of alkali halide type materials have suggested that easy cross slip is required for normal fatigue failure. This view was supported by the work of Argon and Godrick<sup>26</sup> on LiF. If this cross slip criterion is accepted the question of whether or not fatigue failure can occur in KCl hinges on the question of what can be called "easy" cross slip. Data provided by Gilman<sup>5</sup> in 1959 would seem to suggest that no cross slip could occur in KCl at room temperature. However, more recently, Backofen and Leseur<sup>27</sup> have stated that critical resolved shear stress for {100} <011> slip is only one to two times that for {110} <110> slip at room temperature. Limited cross slip in some well oriented grains is therefore a possibility.

## F.2 MATERIALS AND TEST PROCEDURES

Test Procedures. The lack of reliable fracture toughness data ( $K_{IC}$ ) for polycrystalline KCl was partially due to processing difficulties to produce adequate test material. Recently, however, press forging of single crystals at elevated temperatures has been shown to be an excellent method for producing fully dense polycrystals of KCl with a fine equiaxed grain structure. Some previous measurements of the fracture toughness of this material by Pelloux and Lemaignan<sup>18</sup> indicated that relatively large specimens were needed in order to comply with specifications



set forth in ASTM E399, "Standard Method of Testing for Plane Strain Fracture Toughness".<sup>30</sup> The specifications require that both the specimen thickness,  $B$ , and pre-crack length,  $a$ , should be greater than  $2.5 \left( \frac{K_{IC}}{\sigma_y} \right)^2$  where  $\sigma_y$  is the yield strength of the material. Also the specimen span is required to be a minimum of  $4W$ . Using Pelloux and Lemaignan's room temperature value of  $K_{IC}$  of 940 psi  $\sqrt{\text{in.}}$  and the .1% offset yield strength of 2700 psi supplied in the same study we find that it is required that

crack length	$a = 2.5 \left( \frac{940}{2700} \right)^2 \approx .3 \text{ in.}$
thickness	$b = .3 \text{ in.}$
width	$W = 2a = .6 \text{ in.}$
span	$s = 4W = 2.4 \text{ in.}$

This means that allowing for a little overhang on the span, the minimum specimen dimensions to be considered were .6 x 3.0 x .3 inches. Since it was intended to also study fracture toughness at temperatures up to 150°C, the following specimen dimensions were selected: (1.0 x 5.0 x .3 inches).

All fracture toughness tests were run in air on notched specimens in three point bending. An Instron tensile testing machine was used to provide constant cross-head displacements from 0.2 in/min to .0002 in/min at temperatures ranging from -50°C to 150°C.

Fracture loads were read off the Instron chart recorder. Since it was assumed that the crosshead displacement was linearly related to the crack opening displacement the load time recordings of the Instron were taken as representative of the load-displacement curves of the tests. Load measurement accuracy was  $\pm 1\%$ .  $K_{IC}$  was calculated to:

$$K_{IC} = \frac{PS}{BW^{\frac{3}{2}}} \left[ 2.9 \left( \frac{a}{W} \right)^{\frac{1}{2}} - 4.6 \left( \frac{a}{W} \right)^{\frac{3}{2}} + 21.8 \left( \frac{a}{W} \right)^{\frac{5}{2}} - 37.6 \left( \frac{a}{W} \right)^{\frac{7}{2}} + 38.7 \left( \frac{a}{W} \right)^{\frac{9}{2}} \right]$$

where  $P$  = fracture load as determined in ASTM-E399  
 $S$  = Span length for three point loading = 4 inches  
 $B$  = Specimen thickness  $\approx$  .3 inches  
 $W$  = Specimen width  $\approx$  1 inch  
 $a$  = Crack length  $\approx$  .5 inch

All measurements of length were made to the nearest .001 inch according to methods described in ASTM E399.

Economic considerations lead to the re-use of the broken halves of a few specimens so that some of the reported data was from specimens having a two inch span rather than the four inch span stated above. Data obtained using the two inch spans appeared to be within the same scatter band as that for the four inch span.

Heating and cooling of the fracture toughness specimens was accomplished using an Instron environmental chamber. Accuracy of the temperature control was considered to be  $\pm 2^\circ\text{C}$ .

Since long times at higher temperatures could lead to grain growth problems, it was desired to use no more than the maximum heat up time necessary. Each specimen run at 100°C and 150°C was held in the chamber environment at 2°C above the recorded temperature for 15 minutes prior to the start of each test. Specimens run at lower temperatures were held only 10 minutes. The heating time did not include the 10 minutes or so which was required to reheat the chamber atmosphere after placing the specimen inside the chamber.

The possibility of strain aging due to heating was investigated using microhardness techniques. Two single crystals with a [100] orientation were tested using a diamond pyramid hardness (DPH) indenter with a 25 gram load. The specimens were tested in four conditions:

1. As received
2. After aging six hours at 125°C
3. After straining to just beyond yield (~300 psi)
4. After annealing 14 hours at 650°C

Both specimens were tested in three locations in each condition and the measured values were averaged. Aging and annealing were carried out in an argon atmosphere. The microhardness tests showed no strain aging effect. However, the hardness values increased by 14 DPH following annealing at 650°C.

Four different methods of preparing a sharp precrack notch in the specimens were tried. The first method was to simply place a razor blade against one edge of the specimen and then gently tap it. The second method was an attempt to locally thermally shock a specimen with a small jet of liquid nitrogen to create a cleavage crack (see work of J.R. Matthews). With both methods, the cracks produced had uneven fronts and were often branched. Thermal shock induced cracks frequently did not go through the entire specimen thickness. Worst of all, cracks produced by both methods always followed the crystallographic direction of the cleavage planes of the surface grains and these directions seldom coincided with the desired fracture plane orientation. Attempts to bias the crack direction by thinning the cross section and by imposing bending stresses did not help.

Fatigue precracking at room temperature with a machine that kept the tip of a prenotch sawcut in compression was the third method attempted. Unfortunately, this failed too as the crack would always propagate through the entire specimen.

It was finally decided that all tests would be run with sawcut notches. A string saw and a jeweler's saw were used to machine notches with crack tip radii of .003 inch.

Fatigue Testing. Following previous fatigue investiga-

tions of ceramics, preliminary testing was carried out using a Sontag SF-2U fatigue machine to apply cantilever loading to notched specimens. However, since this machine was designed for testing thin metal specimens, it did not work well with the large KCl specimens used. The geometry of the test bars was such that large shear stresses were present in addition to the desired bending stress, and a combination of mode I and mode II crack openings resulted. The Sontag machine also imposed a large overload stress during startup which broke a number of specimens during the first few cycles.

To overcome these difficulties a new fatigue apparatus, which imposes three point bending and uses a specimen geometry identical to that used in the fracture toughness study, was developed. Loading was applied by an eccentric shaft and a spring attached to an 1800 rpm synchronous motor. Room temperature tests with  $\Delta K = .4K_{IC}$  were run under  $R = 0$  to propagate fatigue cracks from pre-notched bars.

Materials. Polycrystalline test samples were cut from a large pancake obtained from a [100] Harshaw single crystal compressed 4 to 1 at about 300°C. The pancake, which was one inch thick and 12 inches in diameter, yielded about 40 specimens.

Two separate studies of impurity levels in Harshaw KCl have recently been conducted by Honeywell, Inc.<sup>31-32</sup> The

results of these investigations showed that some significant variations in impurity levels were found, notably for sodium. Since all the fracture toughness specimens were cut from the same pancake the influence of variations in impurity levels should be somewhat minimized. Any local variations due to segregation could not be avoided. All of the specimens tested in fatigue were from a second pancake.

Immediately after processing, the specimens had a 10  $\mu\text{m}$  grain size. However, secondary grain growth at room temperature led to the formation of large flat grains across the surfaces of each specimen. The range of grain size in each specimen was therefore:

fine grain size	10 $\mu\text{m}$ (.0004 in)
coarse grain surface dimension	10-30 mm ( $\frac{1}{2}$ - 1 in)
coarse grain thickness	1 mm (.04 in)

Figure 1 shows an unused etched specimen with a two dimensional surface grain size which is of the order of the specimen size. The surface grains were generally irregularly shaped but Figure 1 shows that some almost square crystals were also present. Figure 2 is a fractured section of a KCl specimen showing the cross section of large surface grains around the edges of the sample. The lower edge of the specimen shows a macroscopic line of demarcation separating the large surface grain from the central 10  $\mu\text{m}$  grain size material. It can be seen that the thickness of the

surface crystals was much less than their surface dimensions. In general there was only one layer of large grained material formed at each surface. However, it can be seen in Figure 2 that the upper surface has two layers of large grains. On the average, large surface grains accounted for about 25% of the specimen thickness.

It is known that exaggerated grain growth is often related to impurities in the matrix of single phase materials. Non-dispersive X-ray microprobe techniques showed that small precipitates containing sodium roughly  $.3 \mu$  to  $1.5 \mu$  in size were present within certain areas of the large grains in some samples and it was thought that the impurities might be the source of the grain growth problem. These precipitates were either square shaped or trapezoidal as observed in two dimensions. They were seldom found in the bulk of the fine grain material but were occasionally found at the grain boundaries in small grain areas near large surface grains.

Experiments were carried out to determine the effect of the sodium precipitates on grain growth. Two specimens were placed in a beaker of water to dissolve away their outer layers of large surface grains and any accompanying precipitates of sodium. The specimens were then dried, placed in a dessicator and held at room temperature. Exaggerated growth of the newly exposed  $10 \mu\text{m}$  grains was not

observed within one week. These same two samples plus two others containing large surface grains were polished using 1  $\mu$ m alumina in methanol to remove etching effects. No further grain growth was observed on the surfaces of the two specimens which had already contained large surface grains. However, exaggerated grain growth did occur within one day on the surfaces of the two specimens which had initially had their large surface grains dissolved away. It was concluded that residual cold work strains helped promote grain growth. It is also possible that removal of grain boundary grooving which would normally inhibit grain growth was a controlling factor. It seems that the sodium precipitates themselves are not the cause of the anomalous grain growth. The precipitates do indicate, however, the presence of extensive sodium impurities in solid solution. This leaves open the question of exaggerated grain growth due to small clusters of sodium particles within the KCl matrix which are not resolvable by the microprobe techniques.

### F.3 RESULTS

Fracture Toughness. Some 70 tests were run and the results are given in Table I. The amount of scatter is reasonable and attributed to the inherent statistical nature of brittle fracture in this material. In two tests run at low strain rate and 150°C, the specimens tended to deform plastically rather than to fracture. Indentation



of the sample at the load jig rollers occurred in both cases. The unreasonable amount of scatter at low strain rate and 100°C was attributed to localized plastic deformation and indicates a brittle to ductile transition for notched specimens at this temperature. As might be expected, K<sub>IC</sub> remains brittle over the range of temperatures investigated and fracture toughness does not change significantly with temperature until the brittle-ductile transition temperature is reached. On the other hand, K<sub>IC</sub> does change significantly with strain rate.

To assess the relative dependence of K<sub>IC</sub> upon temperature and strain rate a general relationship between the two parameters is needed. The usual form of the relationship for a time dependent thermally activated process is

$$\dot{\epsilon} = A e^{-\frac{Q}{RT}}$$

where  $\dot{\epsilon}$  is strain rate, T is temperature, R is the universal gas constant, Q is an activation energy and A is an empirical constant. Taking the derivative of this equation we find that

$$\frac{\Delta \dot{\epsilon}}{\Delta T} = \frac{Q}{R} \frac{\dot{\epsilon}}{T^2}$$

Substituting this into the relationship

$$\frac{\Delta K_{IC}}{\Delta T} = \frac{\Delta K_{IC}}{\Delta \dot{\epsilon}} \frac{\Delta \dot{\epsilon}}{\Delta T}$$

we find that

$$\frac{\Delta K_{IC}}{\Delta T} = \frac{\Delta K_{IC}}{\ln\left(\frac{\dot{\epsilon}_1}{\dot{\epsilon}_2}\right)} \frac{Q}{R} \frac{1}{T^2}$$

where  $\dot{\epsilon}_1$  and  $\dot{\epsilon}_2$  are the two strain rates at which  $\Delta K_{IC}$  is evaluated. The value of  $Q$  can now be evaluated using data from Table II. Using the values of  $K_{IC}$  of 339 and 298 psi  $\sqrt{\text{in}}$  to evaluate the temperature dependence of  $K_{IC}$  near 300°C and the values of 549 and 317 psi  $\sqrt{\text{in}}$  to evaluate strain rate dependence over the range of crosshead displacements from .0002 to .02 in/min,  $Q$  is found to be about  $1400 \frac{\text{cal}}{\text{gm-mole}}$ .

Normally calculated values of  $Q$  for mechanical processes range from 10,000 to 100,000  $\frac{\text{cal}}{\text{gm-mole}}$ . The value of  $1400 \frac{\text{cal}}{\text{gm-mole}}$  found here is therefore quite small. Changes in brittle fracture energy with test temperature are primarily related to the small dependence of the elastic modulus on temperature. The small variation of  $K_{IC}$  with temperature found is therefore expected. The abnormally small calculated value of  $Q$  is consequently attributed to a surprisingly strong strain rate effect on  $K_{IC}$  for KCl.

The plastic zone size ahead of the crack tip,  $R_y$ , was calculated using fracture mechanics according to

$$R_y = \frac{1}{2\pi} \frac{K_{IC}^2}{Y^2}$$

where  $Y$  equals the yield strength of KCl at the appropriate strain rate.<sup>27</sup> The range of values for  $R_y$  at room temperature can be found in Table II. The fact that the calculated plastic zones are seen to be much smaller than the .3 inch test specimen thickness shows that plane strain testing conditions were satisfied.

Fractography. Extensive river markings showed that

transgranular cleavage was the general mode of failure in all tests at all temperatures. Scanning electron microscopy occasionally revealed small, angular cavities, shown in Figure 3, which may have served as fracture initiation sites. The angularity of the sides of the cavities suggests that the trail of voids shown in Figure 3 is perhaps merely the zig-zag trace of a cleavage fracture, adjacent sides of the cavities being orthogonal cleavage planes.

Fracture in the large surface grains followed well defined crystallographic planes oriented near the direction of crack propagation. Figure 4 shows how a crack would zig-zag following cleavage planes at  $90^\circ$  to each other. The extensive secondary cracking surrounding the main fracture path was induced after the test by grinding to show the cleavage planes more clearly.

There was some interaction between the propagating crack and the sodium precipitates mentioned before. As shown in Figures 5 and 6, jagged cracks were sometimes found to follow the precipitates in large surface grains. The fact that the crack would at times go through the precipitate and at times around it suggests that the precipitate and matrix have approximately the same fracture strength.

Fatigue. Data from the fatigue tests run on the

new apparatus appear in Table II. Judging from fracture surfaces it appears that the specimens used in this study had a higher percentage of large grain material than those used in the fracture toughness study. Specimen 3 did not fracture at the notch root as expected but instead broke through an area where the thickness of the specimen was composed of a single grain.

Fractography revealed no fatigue striations on any of the specimens. Instead fatigue fracture surfaces appeared to be quite similar to those of the monotonically loaded fracture toughness specimens. Fractures initiated intergranularly and propagated transgranularly. The extent of intergranular fracture was greater in the fatigue specimens than that in the fracture toughness specimens. As seen in Figure 7, intergranular fracture proceeded to a width of two or three grain diameters. The cleavage fan shown in Figure 8 is in fine grain 10  $\mu\text{m}$  material. Many intergranular fractures can be seen along the line separating the cleavage fan from the sawcut notch in the bottom of the picture. The large step at the left of Figure 8 separates a large surface grain at the far left from the 10  $\mu\text{m}$  material. An enlargement view of the step shows that intergranular fracture occurred along the boundary separating the two regions of large and small grain sizes.

#### F. 4 DISCUSSION

Fracture Toughness. Recently, Beecher and others<sup>19</sup> have published some fracture toughness data for KCl. Their results show that for tests performed in air on polycrystalline material of 6  $\mu\text{m}$  grain size,  $K_{IC}$  ranges from 125  $\text{psi} \sqrt{\text{in}}$  to 300  $\text{psi} \sqrt{\text{in}}$  with an average value of 230  $\text{psi} \sqrt{\text{in}}$ . These values are somewhat lower than the room temperature value of 320  $\text{psi} \sqrt{\text{in}}$  found here. Beecher's data appears to be better since it seems that the specimen notch may have been sharper than ours and it would therefore be a better stress concentrator. On the other hand, it has been shown that fracture toughness measurements are not a function of crack tip radius below a critical radius. The critical radius for KCl has not been established in this investigation, but the 75  $\mu\text{m}$  notch tip radius used in this study is almost equal to the 70  $\mu\text{m}$  critical radius established by Bertolotti<sup>22</sup> for  $\text{Al}_2\text{O}_3$  and so it should be well within the range of critical crack tip radii for brittle ceramics. It may be that the .003 inch crack radius is sufficiently sharp or it may be that damage at the crack tip, much smaller than .003 inch, is concentrating the stresses, but in either case it seems that the data in Table I is quite good.

The tendency with fracture toughness data is generally to accept the lowest measured value. In comparing Beecher's data with ours, it must be remembered

that although we seem to be talking about the same material, in reality there may be some significant differences. Both sets of samples were made by compressing [100] single crystals but there is some question as to whether both processing methods gave equivalent materials. The samples used by Beecher had a finer grain size and a significantly higher yield strength (2700 psi for our material compared to 3000 to 5000 psi for Beecher). There are also important questions concerning the two materials with respect to impurities, types of precipitates, and distribution of precipitates that need to be answered since small amounts of impurities greatly alter the mechanical behavior of ionic solids. It would therefore seem that both sets of data are likely to be valid. The two sets of data are actually in reasonable agreement with each other and may be used to demonstrate the range of properties likely to occur with variation in processing of KCl. It is possible that the differences in the two sets of data are due to the same grain size effects found by Clark and others<sup>15</sup> for MgO.

The relatively strong dependence of  $K_{IC}$  on loading rate is surprising but not unheard of. Swanson and Gross<sup>16</sup> have mentioned that their studies show the possibility of a loading rate effect on  $K_{IC}$  measurements. Class and Machlin<sup>13</sup> have also noted this effect, explaining that values of fracture surface energy for KCl bicrystals were

high with a wide scatter band when tests were run below a critical minimum loading rate. A study by Freiman and others<sup>34</sup> has shown that fracture energy of single crystals of KCl increase by a factor of two as loading rate is reduced from 5 cm/min to .2 cm/min. A dislocation mechanism was given to explain this strong dependence. In view of the relatively weak temperature dependence compared to loading rate dependence found in this study for polycrystals, a simple dislocation mechanism seems unlikely.

The intergranular fracture initiation and transgranular propagation found here supports Stoloff's<sup>8</sup> observations of glide bands meeting a grain boundary to nucleate an intergranular crack which then propagates in a transgranular fashion. The temperature at which cross slip becomes easy is estimated to be about 100°C from the following observations. In Table I the tests at 150°C and .0002 inch per minute crosshead displacement were invalid due to an inordinate amount of plastic slip at the crack tip. Indentation at the rollers of the three point jig was also noted. The scatter at 100°C is felt to be due to the close proximity of the notched specimen brittle-ductile transition temperature. This is rather low compared to Stoloff's<sup>8</sup> result who placed the unnotched specimen transition temperature at 250°C. However, one must remember that the .0002 in/min strain rate is 30 times slower than the strain rate used by Stoloff. Furthermore,

it is known that the quality of commercial alkali halides has improved greatly since Stoloff's work in 1963 and it is possible that what Stoloff called "pure KCl" was really rather heavily doped with impurities that may have increased the transition temperature.

Fatigue. Intergranular cracks at the root of the notch in the fracture toughness tests propagated less than one grain diameter prior to changing to a transgranular fracture. In contrast, the intergranular cracks in the fatigue specimens were observed to have traveled some two or three grain diameters prior to transgranular fracture. The increased amount of intergranular fracture observed in the fatigue specimens is assumed to be an indication of fatigue damage. This damage can be explained by considering the interaction between cross slip and grain boundaries. The stacking fault energy in KCl being high should not limit cross slip. Also, some recent data has shown that the critical resolved shear stress on secondary [100] planes is less than a factor of two times that for the primary [110] planes. Thus, it is conceivable that under cyclic stressing at low stress levels active cross slip will prevent transgranular crack initiation by minimizing the stress concentration due to dislocation pile ups. However, the intergranular cracks do not travel far and cleavage fracture proceeds as the growth rate per cycle increases, or as the crack becomes unstable. Further



studies are needed to clarify what processes are taking place at the crack tip during fatigue. Observations of dislocation arrangements in fatigued single crystals would probably be helpful.

The role of the water vapor in the test environment should also be considered since it has also been observed that natural grain boundary etching on surfaces which have been sawcut is much greater than on cleaved surfaces. Cyclic working could promote a similar enhanced environmental reaction to occur at the tip of the notch in the fatigue specimens. It is, therefore, possible that the increased intergranular cracking observed on fatigue fracture surfaces is due to corrosion fatigue rather than to the mechanism of cyclic hardening and cross slip described above.

The room temperature value of critical fracture toughness at high strain rate was found to be 320 psi  $\sqrt{\text{in.}}$ . Fatigue failure did occur at only 115 psi  $\sqrt{\text{in.}}$ . This low value of  $K_{Ic}$  for fatigue may reflect not only the effect of cyclic stressing but also the effect of a change in crack tip radius. The .003 inch sawcut notch tip radius used in the fracture toughness tests might be larger than the critical crack tip radius for KCl and sharp intergranular fatigue cracks would lead to fast propagation at stress levels below those which would cause failure of the

sawcut notched specimens.

In conclusion it was found very difficult to initiate and propagate a fatigue crack in KCl. The propagation of fatigue cracks under  $K_I = 115 \text{ psi } \sqrt{\text{in}}$  was attributed to corrosion fatigue. The low fracture toughness measured in the presence of a short corrosion fatigue crack remains unaccounted for.

#### F.5 CONCLUSIONS

The fracture toughness index ( $K_{IC}$ ) of KCl was found to vary as a function of strain rate and temperature from 300 to 700  $\text{psi } \sqrt{\text{in}}$ .

A brittle to ductile transition has been observed in notched specimens of KCl at 100°C and at low strain rates.

The effect of temperature on  $K_{IC}$  was found to be small below the brittle to ductile transition temperature. Strain rate effects in the brittle fracture temperature range were found to be significantly larger.

The interaction of the fracture path with grain boundary precipitates of sodium may lead to an increase in the fracture toughness.

Corrosion fatigue crack growth was observed at  $\Delta K$  of 115  $\text{psi } \sqrt{\text{in}}$ . However, initiation of fatigue cracks from a smooth surface is difficult even at a stress amplitude approaching the yield stress in tension.

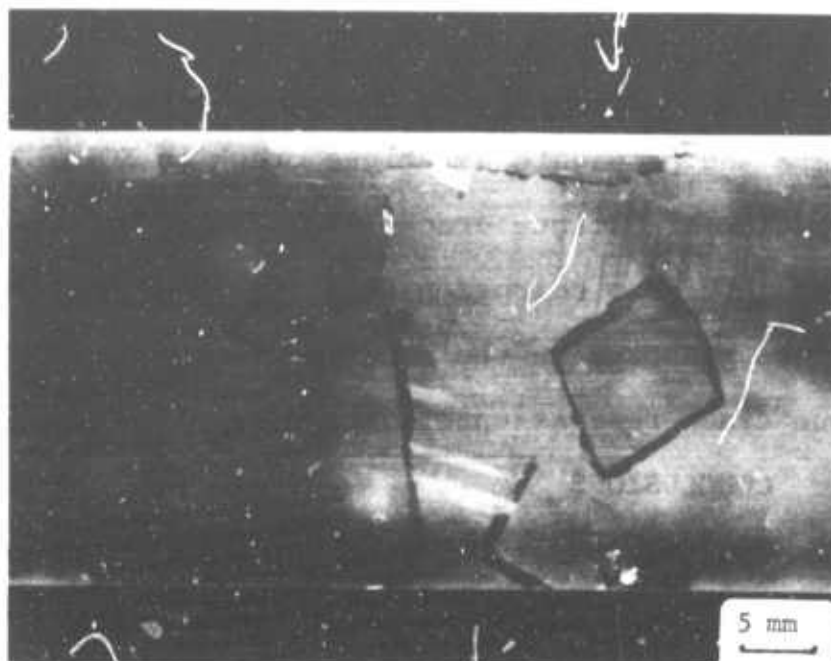


FIGURE 1. Section Of An Unused KCl Test Specimen Showing Large Grains At The Outer Surfaces

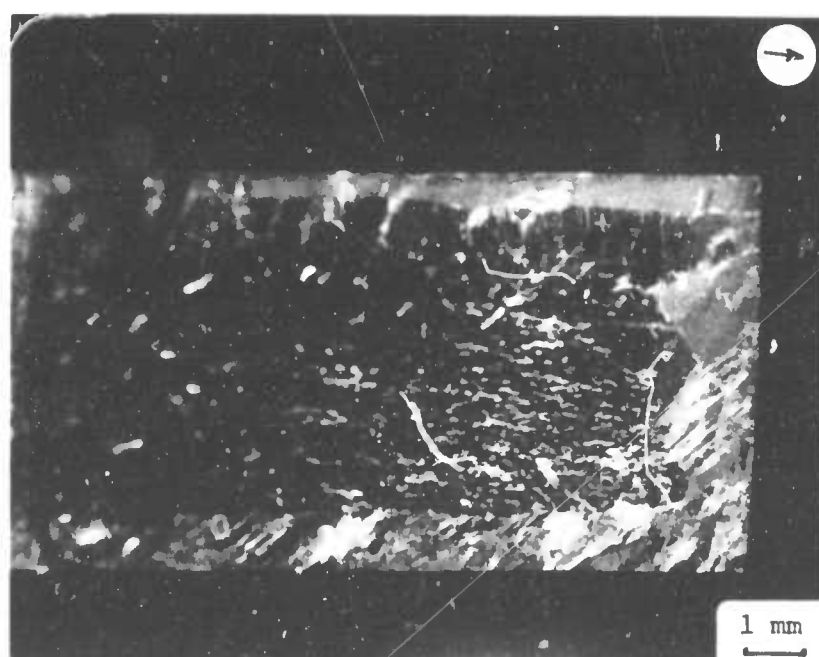


FIGURE 2. Fracture Surface Of A Specimen Cross Section Showing Large Surface Grains Surrounding A Fine Grain Structure (10  $\mu\text{m}$ )

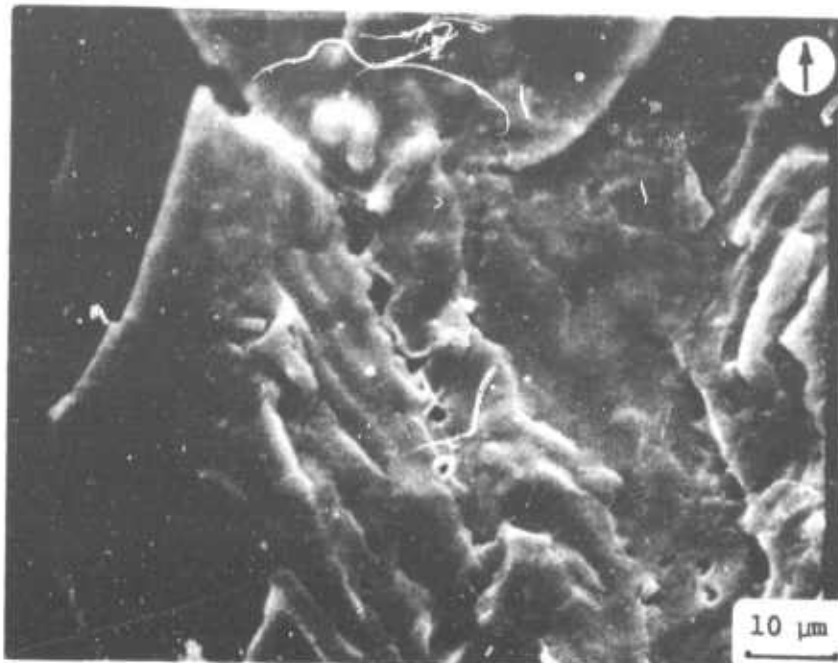


FIGURE 3. Angular Cavities In KCl Fracture Surface

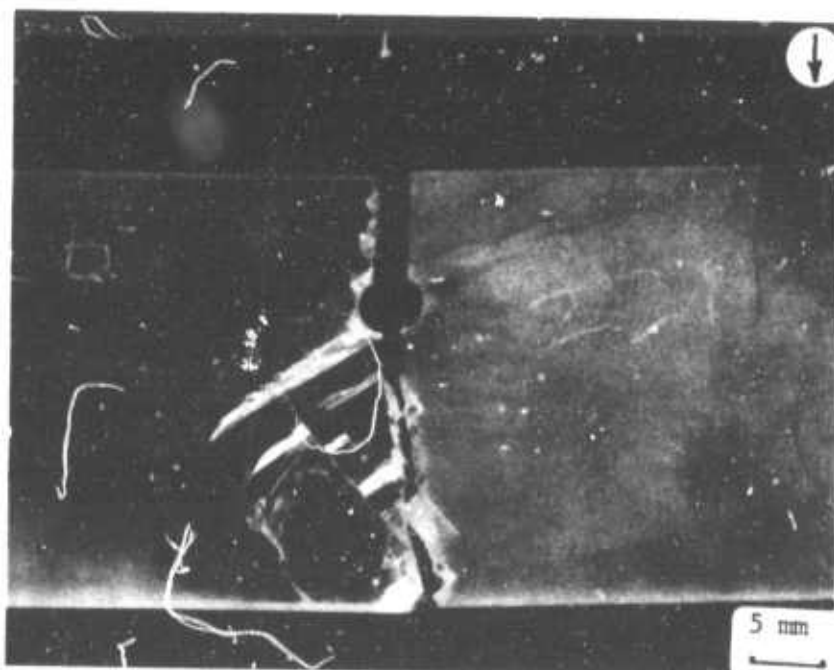


FIGURE 4. Crack Propagation In Large Surface Grains. Secondary Cracking Was Induced After Testing To Reveal Cleavage Planes More Clearly.



FIGURE 5. Crack Following Sodium Precipitates In A Large KCl Surface Grain

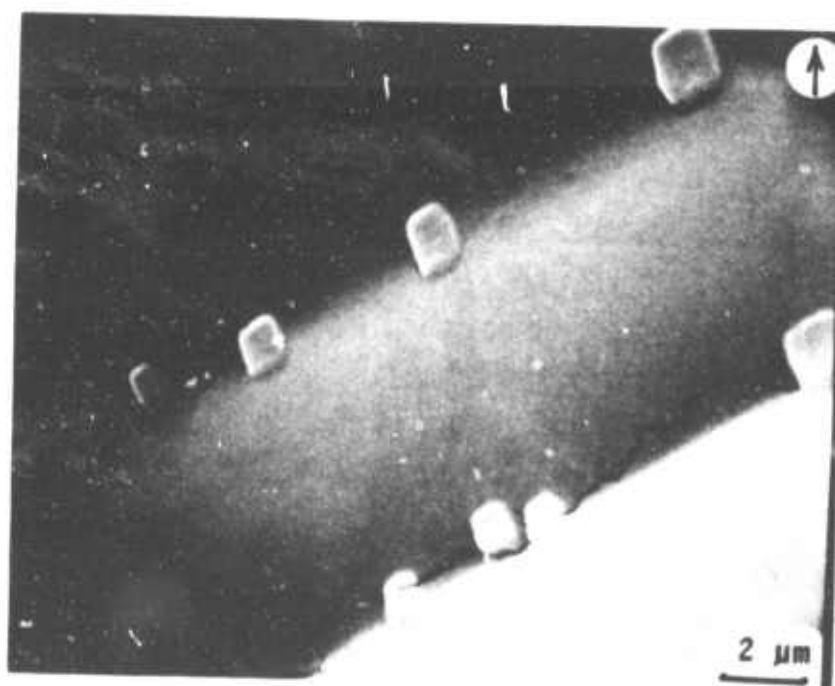


FIGURE 6. Jagged Cracks Penetrating Sodium Precipitates In A Large KCl Surface Grain

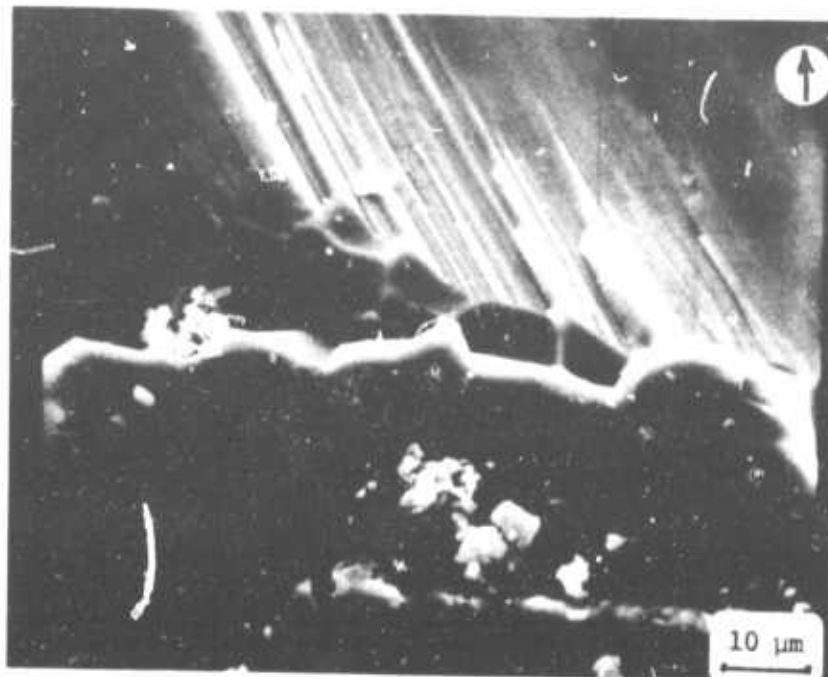


FIGURE 7. Enlarged View Showing Intergranular Fatigue Fracture Initiation

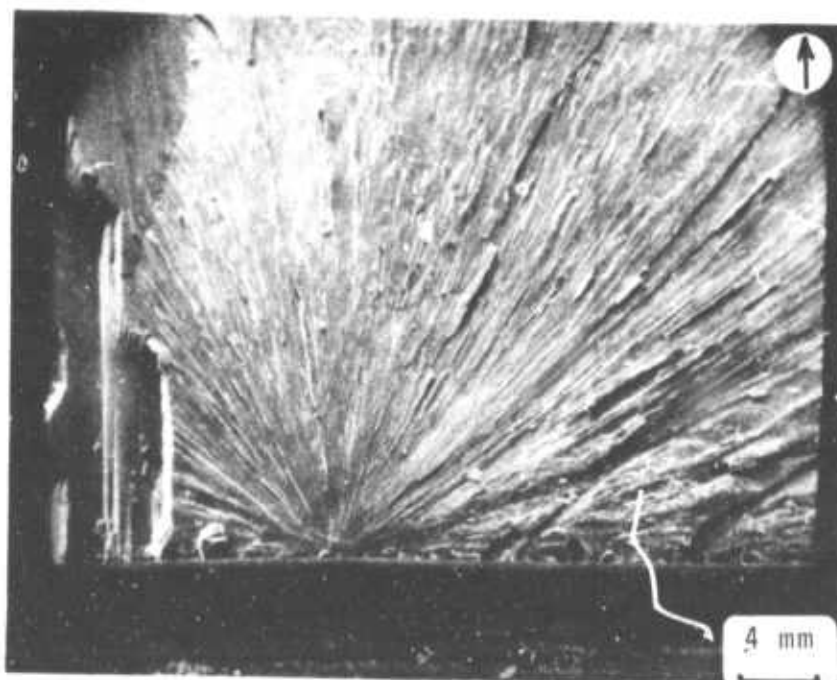


FIGURE 8. Fatigue Fracture Surface Near Origin

TABLE I

Fracture Toughness ( $K_{IC}$ ) of Polycrystalline KCl

Temp.	Crosshead Speed .0002 in./min.		Crosshead Speed .001 in./min.		Crosshead Speed .01 in./min.		Crosshead Speed .02 in./min.		Crosshead Speed .2 in./min.	
	$K_{IC}$ psi	Standard Deviation $\sqrt{in.}$	$K_{IC}$ psi	Standard Deviation $\sqrt{in.}$	$K_{IC}$ psi	Standard Deviation $\sqrt{in.}$	$K_{IC}$ psi	Standard Deviation $\sqrt{in.}$	$K_{IC}$ psi	Standard Deviation $\sqrt{in.}$
-50°C							298 (8)	58		
22°C	549 (7)	69	478 (6)	36	445 (5)	33	317 (8)	37	343 (4)	77
50°C	522 (5)	82					339 (6)	61		
100°C	705 (5)	280					414 (7)	64		
150°C	TESTS INVALID Due To Plastic Deformation (2)						311 (6)	61		

Numbers in parentheses indicate the number of samples tested.

TABLE II

Calculated Range of Plastic Zone Sizes For KCl at 22°C

Rate Of Crosshead Displacement in./min.	$K_{IC}$	Plastic Zone Size, $R_y$ (in.)	Value of Yield Strength Used to Calculate $R_y$
.02	320	.0017	3100
.0002	550	.0066	2700



TABLE III

Fatigue of Notched Specimens of Polycrystalline KCl at Room Temperature

Specimen Number	$K_I$ psi in	$K_I / K_{IC}^*$	Cycles to Failure
1	115	.36	2,979,000
2	128	.40	146,000
3	144	.45	1,857,000

\*  $K_{IC}$  taken at 320 psi in

## IX. BIBLIOGRAPHY

1. S. M. Wiederhorn, Mechanical and Thermal Properties of Ceramics, J. B. Wachtman, Jr. ed., National Bureau of Standards Publication 303, May 1969, 228.
2. R. von Mises, Z. Angew Math. Mech., 8 (1928) 161.
3. G. I. Taylor, J. Inst. Metals 62 (1938) 307.
4. G. W. Groves and A. Kelly, Phil. Mag., 8 (1963) 877.
5. J. J. Gilman, Acta Met., 7 (1959) 608.
6. R. J. Stokes and C. H. Li, Acta Met., 10 (1962) 535.
7. R. D. Carnahan, T. L. Johnson, R. J. Stokes and C. H. Li, Trans. AIME, 221 (1961) 45.
8. N. S. Stoloff, D. K. Lezius, and T. L. Johnson, J. of App. Phys., 34 (1963) 3315.
9. A. E. Gorum, E. R. Parker and J. A. Pask, J. Am. Cer. Soc., 41 (1958) 161.
10. W. Dekeyser, Acta Met., 4 (1956) 557.
11. J. J. Gilman, J. of App. Phys., 31 (1960) 2208.
12. A. R. C. Westwood and T. T. Hitch, J. of App. Phys., 34 (1963) 3085.
13. W. H. Class and E. S. Machlin, J. Am. Cer. Soc., 49 (1966) 306.
14. F. F. Lange, Phil. Mag., 16 (1967) 761.
15. F. J. P. Clark, H. G. Tattersall and G. Tappin, Proc. Brit. Cer. Soc., 6 (1966) 163.
16. G. D. Swanson and G. E. Gross, J. Am. Cer. Soc., 54 (1971) 382.
17. R. O. Ritchie, J. F. Knott, and J. R. Rice, J. Mech. Phys. Solids, 21 (1973) 395.
18. Center for Materials Science and Engineering, M.I.T., Annual Technical Report on Research on Materials for

High Power Laser Windows, 30 April 1973, ARPA Order No. 2055.

19. P. F. Beecher, S. W. Freiman and R. W. Rice, Naval Research Laboratory Semi Annual Report No. 3 on High Energy Laser Windows, 1973 ARPA Order No. 2031.
20. C. T. Forwood, Phil. Mag., 17 (1968) 657.
21. T. R. Wilshaw, C. A. Rau and A. S. Tetelman, Eng. Fract. Mech., 1 (1968) 191.
22. R. Bertolotti, J. Am. Cer. Soc., 56 (1973) 107.
23. L. A. Simpson, J. Am. Cer. Soc., 57 (1974) 151.
24. S. D. Hartline, R. C. Bradt, H. R. Baumgartner and N. B. Rosebrooks, J. Am. Cer. Soc., 56 (1973) 550.
25. A. J. McEvily Jr. and E. S. Machlin, Fracture 1959 (Swampscott), B. Averbach et.al. ed., M.I.T. Press, Cambridge, Mass. (1959) 450.
26. A. S. Argon and J. A. Godrick, Fracture 1969 (Brighton), P. L. Pratt ed., Chapman and Hall Ltd., London (1969) 576.
27. Center for Materials Science and Engineering, M.I.T., Annual Technical Report on Research on Materials for High Power Laser Windows, 31 October 1973, ARPA Order No. 2055.
28. J. J. Gilman and W. G. Johnson, Solid State Physics, 13 (1962) 148.
29. L. M. Brown and P. L. Pratt, Phil. Mag., 8 (1963) 717.
30. American Society for Testing and Materials, 1973 Annual Book of ASTM Standards, ASTM, Philadelphia (1973) 960.
31. Ceramics Center Honeywell, Inc., Interim Technical Report No. 2, submitted to AFML, AFSC WPAFB, Ohio, Contract No. F33615-72-C-2019, May 1973.
32. Ceramics Center Honeywell, Inc., Interim Technical Report No. 4, submitted to AFML, AFSC WPAFB, Ohio, Contract No. F33615-72-C-2019, Feb. 1974.

33. W. D. Scott and J. A. Pask, J. Am. Cer. Soc., 46 (1963) 84.
34. S. W. Fruman, P. F. Beecher and P. H. Klien, Naval Research Laboratory Semi Annual Report No. 4 on High Energy Laser Windows, 30 June 1974, ARPA Order No. 2031.
35. J. P. Holman, Heat Transfer, McGraw Hill, Inc., New York, (1972) 91-101, 205-210.
36. M. P. Holman, Trans. ASME, 69 (1947) 227.
37. J. R. Mathews, "Proof Testing of Brittle Materials by Thermal Shock," Ph.D. Thesis M.I.T., Cambridge, (April 1974).

## G. TRANSMISSION ELECTRON MICROSCOPY OF ALKALI HALIDES

### G.1 INTRODUCTION

Transmission electron microscopy has had a substantial influence on every scientific field in which it has been applied. Without question, the primary reason for the successful widespread utilization of this technique is the fact that it allows for the direct observation of defects with high resolution. However, unlike the fields of metals, oxide ceramics, earth minerals, polymers, and the life sciences, electron microscopy observations of defects in alkali halides are, with few exceptions, virtually nonexistent.

The history of alkali halide electron microscopy spans a quarter of a century (1). However, unlike the transmission electron microscopy of metal foils, the state-of-the-art in electron microscopy of alkali halides has remained in the "primitive" state until very recently. As a result the nature of defects associated with deformation in alkali halides is not nearly as well understood as its counterpart in metals.

The reasons for this relative ignorance concerning dislocation substructures in alkali halides stems from the difficulties associated with electron microscopy of alkali halides. These difficulties arise, to a first

approximation, from two major sources. First, the preparation of a thin, electron transparent foil is more exacting than for most other materials. Additionally, precautions and care must be taken in handling the sample after preparation. Secondly, illumination levels commonly employed for electron microscopy are orders of magnitude higher than those needed to produce substantial radiation damage with the result that the intrinsic microstructure of the sample is obliterated nearly instantaneously upon observation.

The problem of specimen preparation of alkali halides from the bulk stem from the fact that alkali halides are very soft yet extremely brittle. The only completely acceptable method for obtaining undeformed sections from the bulk for subsequent thinning is precision chemical string sawing. Essentially all alkali halides may be sectioned to a suitable thickness using a string saw and various alcohol solvents (2). These same alcohol solvents can be used in a microjet thinning apparatus for preparation of thin foils. Since most alkali halides are insoluble in ketones and ethers (2), these are useful for post-polishing, washing procedures.

Most alkali halides are readily soluble in water and are susceptible to atmospheric moisture attack. A serious

difficulty in chemical polishing for electron transparency is the eventual removal of the solvents used, particularly the washing solvents with high vapor pressures. In this case if the washing solvents are allowed to evaporate in air, the ensuing cooling of the foil will enhance the condensation of water and result in deleterious etching and sample degradation. It is important, therefore, to evaporate these solutions under vacuum.

The problem of radiation damage during electron microscopy observation derives from the electrical and radiolytic properties of alkali halides. In thin foils, where the range of the high energy electrons surpasses the thickness of the foil, the energy loss from 100 kV electrons is uniform through the foil and amounts to about  $10^9$  eV/m. On the average about one displacement in the lattice is produced for every 50 eV of deposited energy (3). However, most of the Frenkel pairs which are produced undergo spontaneous correlated recombination with the result that about  $10^3$  to  $10^4$  eV per Frenkel pair are required for producing stable F-center:H-center pairs. Thus, such stable pairs are produced at a rate of  $\sim 10^6$ /m. With normal illumination levels during electron microscopy the point defect production rate is about  $10^{26}$ /m<sup>3</sup>.sec. Since Frenkel pair saturation is about  $10^{25}$ /m<sup>3</sup> at room

temperature, electron microscopy results in defect saturation in times of the order of seconds. At these high point defect densities extensive aggregation will occur (if the temperature is high enough) to such an extent as to produce extended defects which will obscure pre-existing substructure such as dislocations and dislocation networks.

The sole variable available to microscopists in this situation is temperature. Since the mobility of the defects is thermally activated, reducing observation temperatures below defect mobility thresholds must retard observable defect aggregation. Since the aggregating species is the halogen interstitial (4) microscopy must be done below 30°K. Additional advantage can accrue from the reduction in the efficiency of radiationless decay of excitons in certain alkali halides, such as KI, NaCl, and NaBr, each of which exhibits a depression in defect production efficiency of one or more orders of magnitude at low temperatures. Lastly, impurities are capable of delaying the onset of observable aggregation during low temperature observation.

## G.2 SAMPLE PREPARATION

From the Bulk. It is possible to cleave with a razor blade or similar apparatus alkali halides of the NaCl structure as well as the related alkaline earth



fluorides. Most, but not all, NaCl-type alkali halides exhibit only {100} cleavage. Alkaline earth fluorides cleave on {111}. The two primary concerns when considering cleavage as a mode for the initial phase of sample preparation from the bulk are: 1) the limited orientation flexibility of the cleavage product; and 2) the deformation induced in the cleavage process. Both of these are major drawbacks when one is considering the preparation of samples for eventual use in the transmission electron microscope. First, a complete study of defect arrays, or any three-dimensional feature, requires observation in two, or preferably three, near-orthogonal directions. In a cleaved thin section this is impossible. Secondly, it is desirable to have as thin a cleaved section as possible (to minimize the time of thin foil preparation, the next step in the process) with the result that there is a high probability that cleavage-induced defects will confuse the intrinsic microstructural analysis.

An alternative method, and one which is most desirable when considering samples to be investigated after deformation, is chemical string sawing. This method can produce sections of any orientation and provide them with a minimum of induced deformation. A number of designs have

been described (5,6) all of which function by the action of a string, saturated with a solution that will dissolve the crystal, brought into light contact with the specimen. The apparatus designed for the present study is schematically shown in Figure G-1.

#### Preparation of an Electron Transparent Thin Foil.

A number of techniques have been attempted to produce an electron transparent volume of an alkali halide for transmission electron microscopy. These include a micro-cleaving technique (7,8), thermal evaporation, vapor deposition (9,10), and ion beam thinning (11). For obvious reasons none of these techniques is suitable for the preparation of samples where characteristic dislocation or defect structures are to be maintained as each of these techniques produces some destructive element, with some methods being more destructive than others.

The least destructive thin foil preparation technique is thinning by dissolution. Of the possible chemical thinning techniques available, for reasons of controllability and reproducibility, the twin microjet technique is favored. In this case, one or two jets of solvent (2) are "sprayed" on the sample surface(s). In this way the sample is thinned to perforation with electron transparent area surrounding the perforation. In the present apparatus,

Figure G-2, the sample can be viewed during thinning and in this way the thinning operation can be terminated at the time of perforation. After termination the thinned sample is immersed in the washing solution (ketone, ether) and dried in a vacuum desiccator. The sample is then coated with a thin layer ( $\sim 200 \text{ \AA}$ ) of Al to render the sample conducting (to dissipate charge acquisition) and improve thermal conductance and thermal contact.

### G.3 ELECTRON MICROSCOPY OF ALKALI HALIDES

During routine observation of a thin foil in the transmission electron microscope an electron dose of  $\sim 10^{21} \text{ em}^{-2}$  is delivered at a rate of  $\sim 10^{20} \text{ em}^{-2} \text{ s}^{-1}$ . These fast electrons lose energy in the thin foil almost entirely through ionization losses, i.e., through interactions with the electrons in the solid. Each electron produces stable Frenkel pairs at a rate of  $\sim 10^6 \text{ m}^{-1}$  or an overall displacement rate of  $\sim 10^{-1} \text{ dpa s}^{-1}$ . One or both of the components of the Frenkel defect pair are mobile at room temperature and the agglomeration of these defects leads to associated strain field contrast which can obliterate the intrinsic microstructure of the sample with observation times on the order of seconds. The kinetics of aggregation are temperature dependent since the mobility of defects is thermally activated. At

the defect densities described here, the main influence of specimen temperature is to alter and affect the distribution of defects. At higher temperatures substantial aggregation occurs leading to large defects with long-range strain fields. At lower temperatures numerous small defects with shorter range strain fields are present. In the latter case, image quality is maintained for relatively extensive periods of observation time. Thus very low temperatures ( $\sim 10^\circ\text{K}$ ) can appreciably lessen the observable effects of electron irradiation damage.

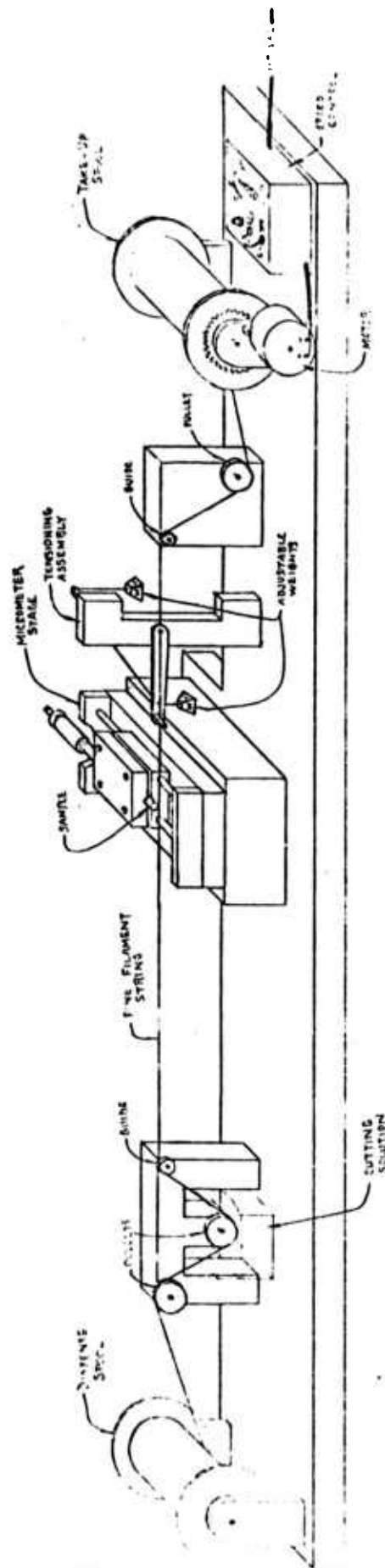
To this end a liquid helium temperature specimen holder has been designed for a Philips EM-300 with goniometer stage. The basic design is based on the standard tilting holder employed in this microscope, Figure G-3. In this case a concentric inlet-outlet tube is used to transport cold helium gas to the sample area. Fused quartz is used for insulation purposes. The sample holder is capable of a  $\pm 20^\circ$  tilt and a  $\pm 45^\circ$  rotation.

#### G.4 CONCLUSION

Equipment has been designed and constructed, at least in part, for the successful transmission electron microscopy of alkali halides. This equipment includes items necessary to prepare samples from the bulk, produce thin foils, and make quantitative observations at high resolution.

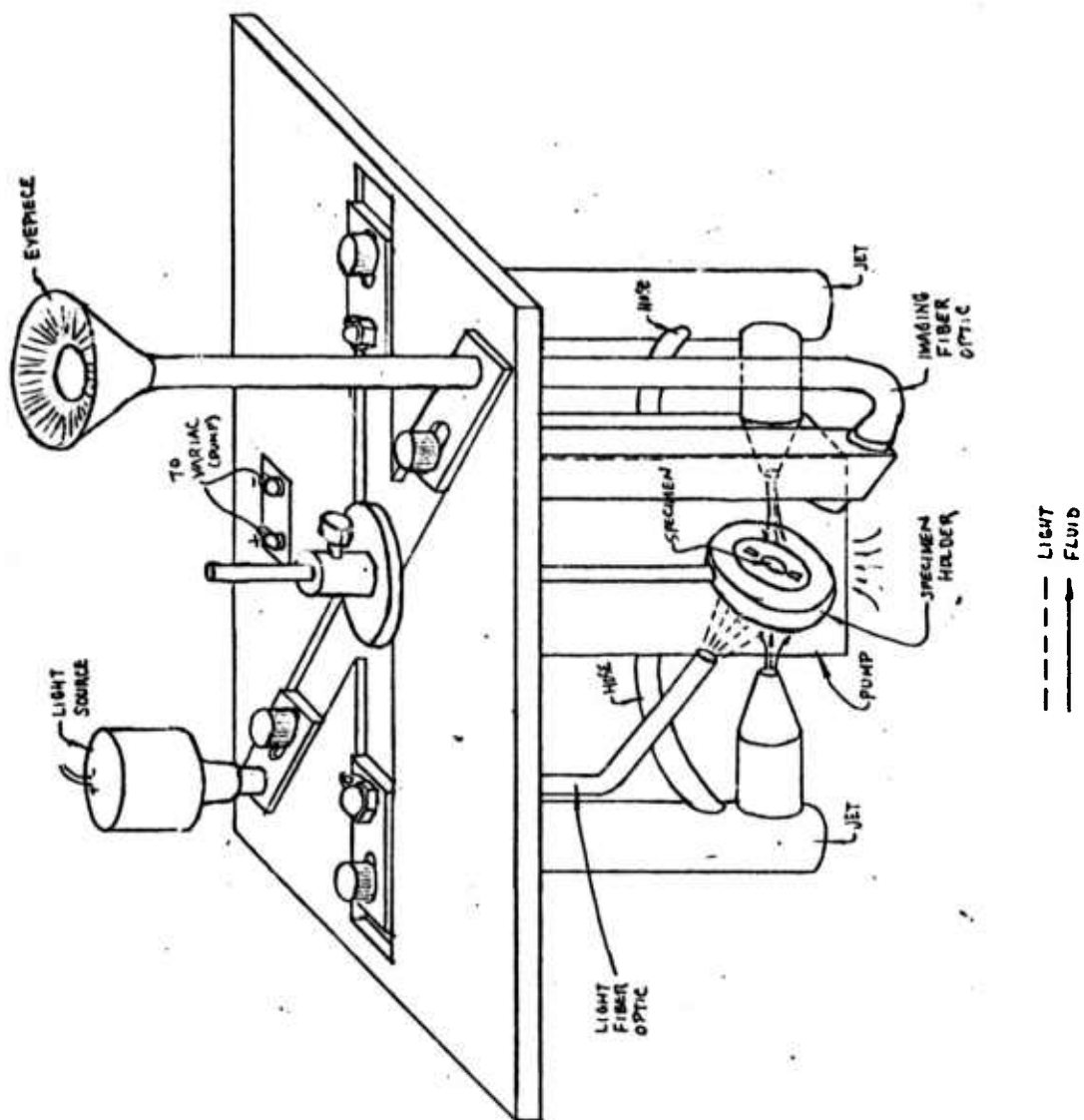
G.5 References for Section G

1. E. F. Burton, R. S. Sennett, and S. G. Ellis, Nature 160, 565 (1947).
2. L. Miravitlles Mille, Anales Fis. y Quim. 41, 138 (1945).
3. E. Sonder, Phys. Rev. B5, 3259 (1972).
4. L. W. Hobbs, A. E. Hughes, and D. Pooley, Proc. Roy. Soc. A 332, 167 (1973).
5. R. W. Armstrong and R. A. Rapp, Rev. Sci. Instr. 29, 433 (1958).
6. F. W. Young and T. R. Wilson, Rev. Sci. Instr. 32, 559 (1961).
7. K. Yagi and G. Honjo, J. Phys. Soc. Japan 19, 1892 (1964).
8. K. Yagi and G. Honjo, J. Phys. Soc. Japan 22, 610 (1967).
9. M. Creuzberg, Z. Phys. 194, 211 (1966).
10. M. Bujor and R. W. Vook, J. A. P. 40, 5373 (1969).
11. L. W. Hobbs, D. Phil. Thesis, Univ. of Oxford, 1972.



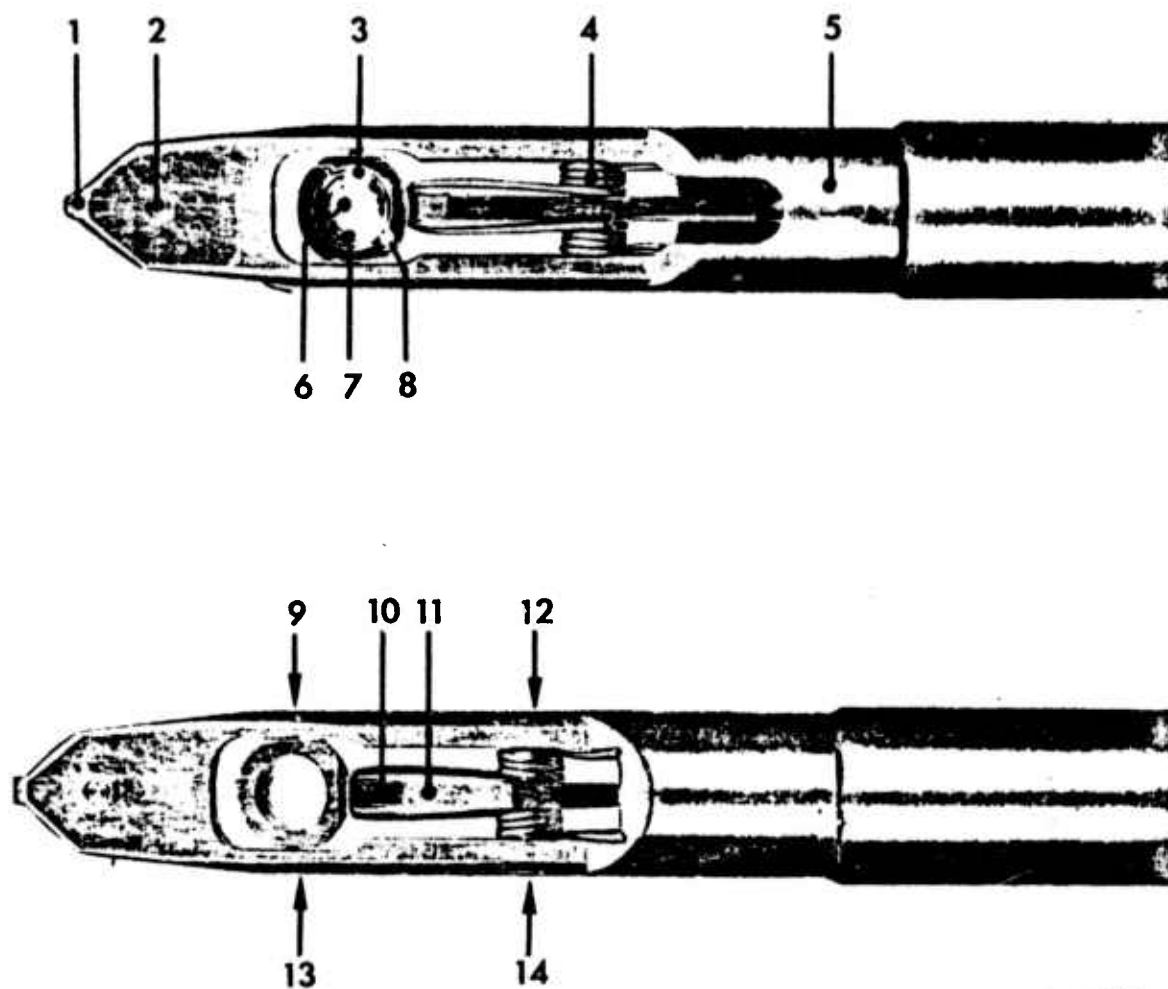
SCALE: 1" = 1"  
 OBlique DRAWING of  
 STRESS SAW

Figure G-1



SCALE 1" = 1/2"  
 OBLIQUE DRAWING of  
 CHEMICAL THINNER

Figure G-2



EM688

Figure G-3



## H. RESULTANT PUBLICATIONS AND THESES

### H.1. PUBLICATIONS

1. H. K. Bowen, "Halide Windows for High Power Gas Lasers", Conference on High Power Laser Windows, October 31, 1972, Ed. C. A. Pitha, published by Air Force Cambridge Research Labs, June 19, 1973, Special Report No. 162.
2. H. K. Bowen, R. N. Singh, H. Posen, A. Armington, and S. A. Kulin, "Fabrication and Properties of Polycrystalline Alkali Halides", Mat. Res. Bull. 8, 1398-1400, (1973).
3. R. N. Singh, H. K. Bowen and R. M. Pelloux, "Strength and Fracture Behavior of Hot-Worked KCl", in Third Conference on High Power Infrared Laser Window Materials, Ed. C. A. Pitha et al., p. 693, [4 February] 1974.
4. F. A. McClintock and J. R. Matthews, "Design Strength of Polycrystalline KCl", in Third Conference on High Power Infrared Laser Window Materials, Ed. C. A. Pitha, et al, p 711, [4 February] 1974.
5. M. F. Yan, R. M. Cannon, H. K. Bowen and R. L. Coble, "Grain Boundaries and Grain Boundary Mobility in Hot-Forged Alkali Halides", Proceedings of the Symposium on Plastic Deformation of Ceramic Materials, Penn State Conference, July 17-19, 1974 Ed. R. E. Tressler and R. C. Bradt, Plenum Press, N. Y. 1975.
6. M. F. Yan, R. M. Cannon, H. K. Bowen and R. L. Coble, "Stabilization of the Grain Size in Hot-Forged Alkali Halides", Proceedings of the Fourth Annual Conference on Laser Window Materials, Ed. C. Robert Andrews and Charles L. Strecker, ARPA, Tucson, Arizona, November 18-20, 1974.
7. R. N. Singh and H. K. Bowen, "Stress-Corrosion Cracking Behavior of Hot-Worked KCl Single Crystals", J. Amer. Ceram. Soc., 58, 342 (1975).
8. M. F. Yan, R. M. Cannon, H. K. Bowen and R. L. Coble, "Space Charge Contribution to Grain Boundary Diffusion", accepted by the J. Amer. Ceram. Soc.

9. J. R. Matthews, F. A. McClintock, W. J. Shack, "Statistical Determination of Flaw Density in Brittle Materials", submitted to the J. Amer. Ceram. Soc.
10. M. F. Yan, R. M. Cannon and H. K. Bowen, "Substructure Formation During Halide Processing", to be presented Fifth Laser Window Conference, Las Vegas, Nevada, [4 December] 1975.

## H.2. THESES

1. J. R. Matthews, Proof Testing of Brittle Materials by Thermal Shock, Ph.D. 1974.
2. R. Schwant, Fracture Toughness and Fatigue of KCl, M.S. 1974.
3. W. F. Hahn, Design of Brittle Components Using Flaw Analysis, M.S. 1975.
4. M. F. Yan, Grain Boundary Mobility in KCl, Sc.D. 1976.